Resistivity of some light - heavy rare earth alloys

Hana Krizek

RESISTIVITY OF SOME

LIGHT - HEAVY RARE EARTH ALLOYS

by

Hana Krizek

Dipl.Physicist (Praque)

Presented in candidature for the degree of

DOCTOR OF PHILOSOPHY

JUNE 1973

A B S T R A C T

Measurements have been made of the electrical resistivity of four light-heavy rare earth alloy systems, ie La-Dy, Nd-Dy, Nd-Y, Pr-Tb in the temperature region 2.7-300(400°K).

The resistivity variation with temperature in the different crystallographic phases has been explained as follows:

1) in the hcp phase - the main contribution comes from spin disorder scattering which may be described theoretically by the RKKY theory. The parameters which are most likely to vary in the series are discussed.

2) in the d-hex phase there are two contributions to the resistivity which are of the same order, $\rho_{phon.}$ and $\rho_{c.f.}$. These are due to phonon scattering and crystal field scattering. The phonon resistivity $\rho_{phon.}$ has been approximated to ρ_{La}, $\rho_{c.f.}$ has been calculated theoretically for Pr, and Pr-Tb in the d-hex structure and qualitatively discussed for Nd, Nd-Y and Nd-Dy.

3) in the Sm-phase, the resistivity can be discussed in a similar way to the resistivity in the hcp phase or in the d-hex phase, depending on the effective Fermi surface area and the magnetic moment. La and La-Dy alloys in the d-hex phase have been explained in terms of rapid changes of the density of states at the Fermi energy.

The residual resistivity in the hcp phase has been found to agree, at low concentrations of the light rare earths, with the previously published results, being dependant of ΔS^2_{eff}, suggesting that the magnetic scattering varies as S(S+1) at these concentrations rather then

Resistivity variation with temperature of Pr-Tb.

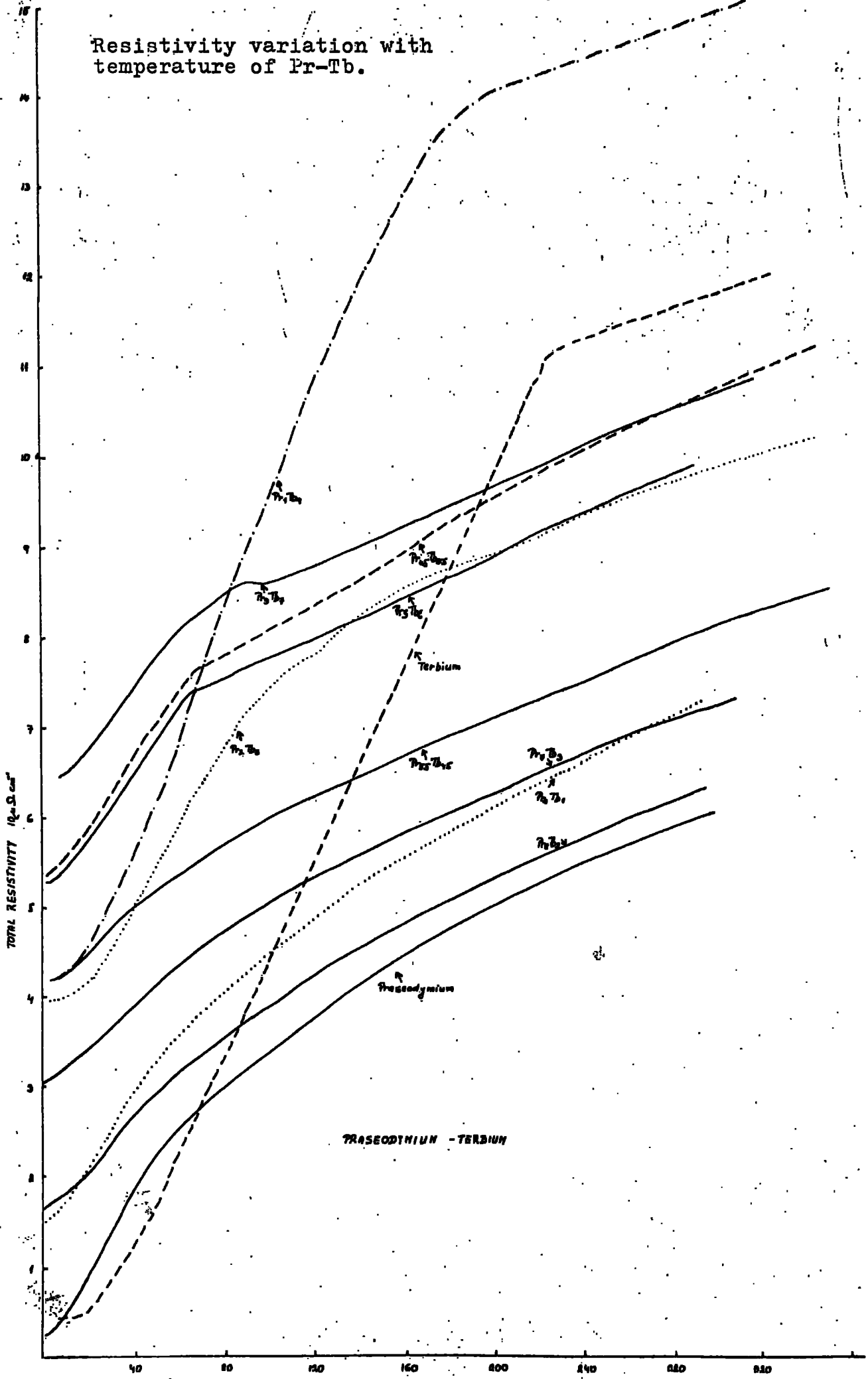

Fig. 1

$(g - 1)^2 J(J + 1) . \rho_{residual}$ has been found to change only slightly in the Sm phase while in the d-hex structure it shows a normal behaviour for nonmagnetic alloys but becomes anomalous for those alloys which order or become superconducting.

The variation of the total resistivity with temperature is presented for all the alloys measured on the following four figures.1-4.

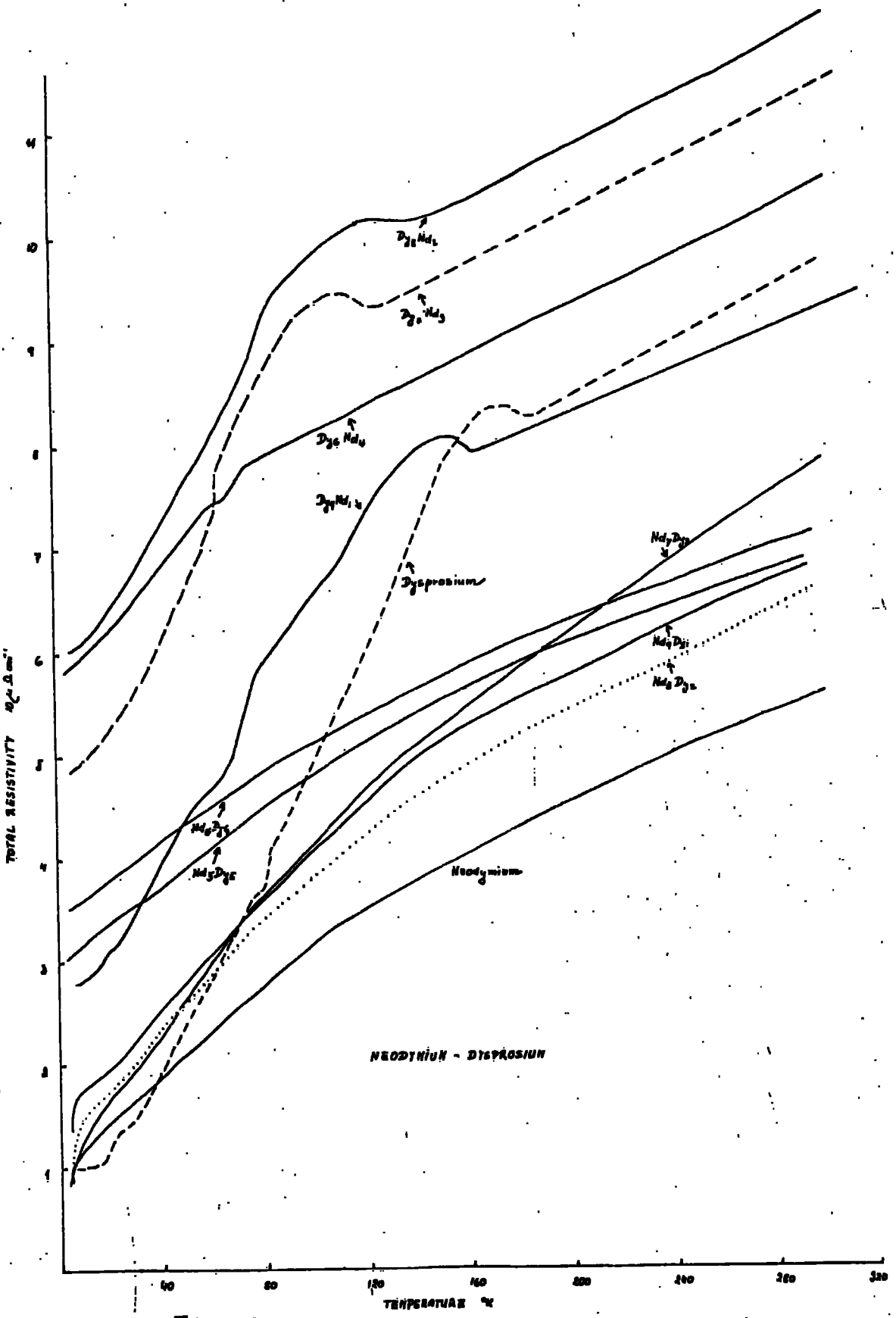

Fig. 2 Resistivity variation with temperature of Nd-Dy.

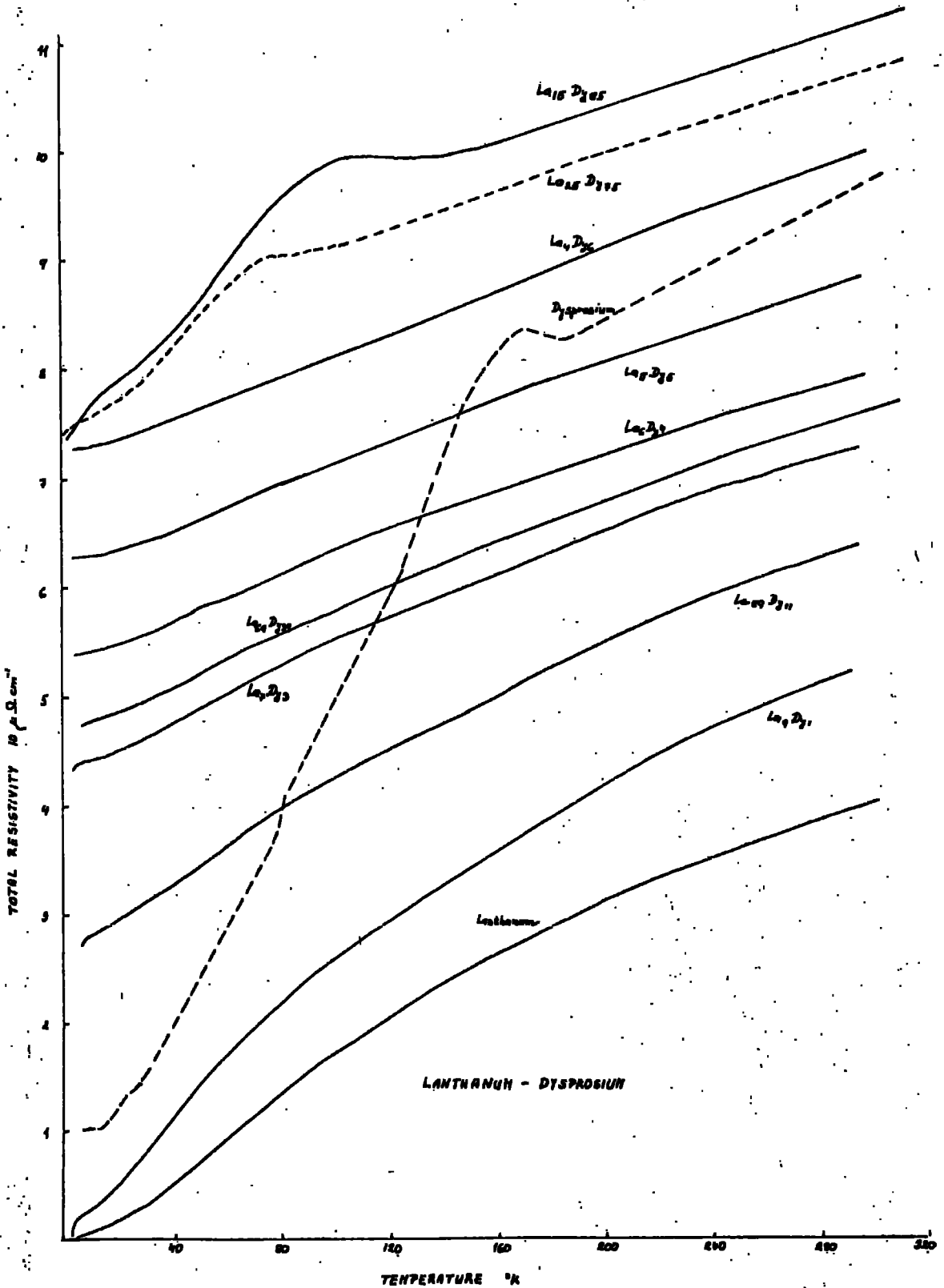

Fig. 3 Resistivity variation with temperature of La-Dy.

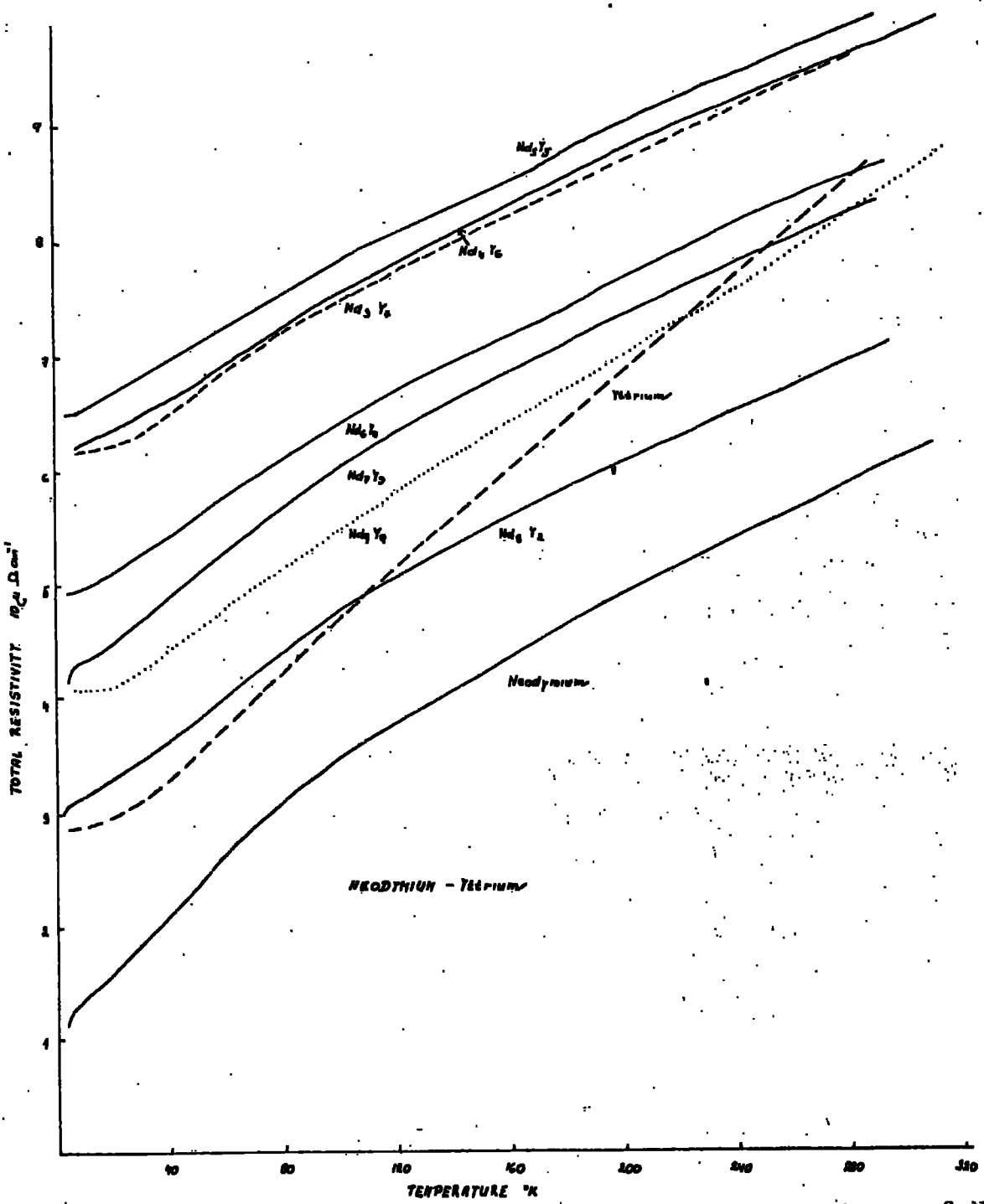

Fig. 4 Resistivity variation with temperature of Nd–Y.

P R E F A C E

This study is concerned with the structural and transport properties of the rare earth intermetallic alloys La-Dy, Pr-Tb, Nd-Dy, Nd-Y.

Apparatus, experimental techniques and results, relevant theory and discussion are the subject of individual chapters arranged as follows:

Chapter one contains a brief introduction to the problem dealt with in more detail in chapter 3,4,5,and 6 both from a historical and a physical point of view.

In chapter two are described in detail the experimental methods employed including the specimen preparation, structure determination, contact preparation for the resistivity measurents, apparatus, measurements procedure and construction of the cryostat.

Chapter three is devoted to the description of the experimental results of the structures and lattice parameters, and the temperature variation of the resistivity between 2.7-400^{o}K.

In chapter four is summarised the theory relevant to the resistivity results presented in chapter three.

A discussion of the experimental results, in terms of the theory given in chapter four is presented in chapter five .

General conclusions about the findings are given in chapter six, together with suggestions for further study.

The references to the literature are for brevity given in the text only by numbers and a list of them appears at the end of the thesis divided according to the different chapters.

A C K N O W L E D G E M E N T S

I wish to express my gratitude to my supervisor, Dr. K.N.R.Taylor, for his guidance and encouragement. My appreciation goes to the entire Physics Department of Durham University, particularly to Professor G.D.Rochester, F.R.S., the Head of the Department, to the staffs of the workshops for their cooperation, and to my colleagues in the solid state group, mainly to my husband Jiri Krizek for his encouragement and fruitful discussions. Finally, I would like to thank Mr.R.Phillips of Geology Department for his understanding.

C O N T E N T S

C H A P T E R O N E

STATEMENT OF THE PROBLEM

1.1. Introduction

The study reported in this thesis is part of the research programme of the Rare Earths Solid State Group of the Durham University into the structural, electrical and magnetic properties of the rare earths.

Historically only for the last ten years have the rare earths been available in a reasonably pure form. The first detailed investigations of their physical properties were carried out by F.H.Spedding and his coworkers at Ames Laboratory, Iowa.

Because of the similarity and dissimilarities in their physical properties the pure rare earth elements may be divided into three groups:

a) heavy rare earths, Gd-Tm,

b) light rare earths, La, Pr, Nd, sometimes Ce and Pm are included as well and

c) the anomalous rare earths, Ce, Sm, Eu, Yb and to a certain degree La.

1.2.Electronic structure

Lanthanum is the first element in the 5d transition metal series with an electron structure having the Xenon core ($1s^2$ $2s^2$ $2p^6$ $3s^2$ $3p^6$ $3d^{10}$ $4s^2$ $4p^6$ $4d^{10}$ $5s^2$ $5p^6$) plus $4f^0$ $5d^1$ $6s^2$. The energy of the 4f shell in the La is higher than the $5d^1$ state and is therefore unoccupied. The addition of a further electron (and proton) to form the element Cerium finds the 4f state preferable, so beginning the progressive population of the 4f level which occurs across the series (1a).

One of the unusual features of these electronic structures is the variation of the radii of the 4f wave functions with increasing atomic number. As electrons are added to the 4f shell the simultaneous increase in nuclear charge results in the appearence of a large electron energy decrease in the vicinity of the nucleus. This causes the electrons of the 4f shell to be drawn towards the interior of the atom. At Lanthanum the empty 4f shell is situated outside the Xenon core $5s^2$ $5p^6$ shell, but for the remainder of the series the 4f electrons lie within these xenon shells. This phenomenon is known as the lanthanide contraction and arises because the electron distribution in the 4f shell is such that an electron added to this shell cannot completely screen the remaining 4f elecrons from the added positive nuclear charge. As a consequense the radius of the outer shell is decreased because of the increased electrostatic attraction.

This contraction has important consequences in many of the properties of the rare earths, eg. structural, electric, magnetic. As for instance, it is the 4f electrons which give rise to the magnetic properties of the ions and the appearence of the ferromagnetism in elements such as gadolinium or terbium or antiferromagnetism in the majority of the other rare earths. However, because of the small orbital radius the 4f electrons are deeply buried within the atom and the coupling mechanism between different ions necessary for the magnetic order to exist cannot occur by the direct everlap of the electrons in the incomplete shell, as it does in the 3d metals, Fe, Ni and Co and some other

exchange mechanism is essential.

1.3 Magnetic properties

With the succesive addition of the 4f electrons to the lanthanum core in going from cerium to lutetium, an ionic moment is developed whose magnitude may be given in an elementary way using Hund's rules. The total moment is calculated as J=L-S for a less than half-filled shell and J=L+S for a more than half-filled shell. Provided that the lowest 4f energy levels of the ions are well separated, the magnetic susceptibility of a solid containing these ions will be given by the relation

$\chi = N^2 g^2 \mu_B^2 (J (J+1))/3 K T$

derived by Hund. If , however, the level splitting is not sufficiently great, then electron excitation into these higher levels will occur so making second or higher terms necessary. The additional susceptibility terms have been evaluated by Van Vleck.

If the observed effective ionic moments μ_{eff} (proportional to $g\mu_B [J (J+1)^{\frac{1}{2}}]$) for the rare earths are compared with the Hund and Van Vleck theories one finds that in general a simple treatment of the ionic moment is adequate to describe the observed susceptibility, although in the cases of samarium and europium appreciable additions of the first excited states have to be included for satisfactory agreement.

Three of the elements, namely lanthanum, ytterbium and lutetium are found to be paramagnetic, with temperature independant susceptibility. In the metallic form lanthanum and lutetium are in a trivalent state with zero and 14

electrons, respectively. Ytterbium, however, is divalent, having gained an electron into the 4f shell from the valence electrons, and consequently it has a complete 4f shell. The remaining rare earths are trivalent with the occasional exeption of Ce and show in general some form of collective magnetic behaviour.

The most thoroughly studied of the rare earth elements have been the heavy metals. Their strong magnetic behaviour display a variety of spin structures from element to element as well as with temperature changes. This has made them interesting from a theoretical as well as an experimental point of view as will be discussed in more detail below. Below room temperature the development of a cooperative phase is evident in ten of the pure metals. The four light metals, cerium, neodymium, samarium and europium order antiferromagnetically, while six heavy metals, gadolinium to thulium, show the existance of either ferromagnetism or anti-ferromagnetism, depending upon the temperature.

Gadolinium is purely ferromagnetic with a Curie temperature of 293°K and a saturation moment of 7.55 μ_B. The remaining five elements show various changes in the type of order, with correspondingly complex magnetization-temperature behaviour.

In dysprosium the magnetization increases on cooling to a cusp like maximum, at 179°K (the Neel point), indicating the onset of antiferromagnetic order which persists to a Curie point (T_c) of 85°K, when a transition to a ferromagnetic state occurs in a small measuring field. The temperature of the second transition is found to be highly dependant on the

applied field. With increasing field strength it approaches the Neel point T_N.

To solve the magnetic moment configuration in the remaining elements neutron difraction studies had been done. These revealed a much more complex situation than could have been anticipated. In the antiferromagnetic phase the most commonly found structure is the helical spin system. In this ordered state the magnetic moments of the ions in any one plane of hcp structure are aligned ferromagnetically (i.e. parallel to one another). However, the direction of these moments with respect to the crystal lattice changes from one plane to the next with a constant angle ω between the spins in successive planes. This 'turn-angle' is temperature dependant and decreases with increase in temperature. The existence of the'turn-angle' leads to an oscillatory variation of the moment direction in the crystal, the periodicity of which is not in general a simple multiple of the crystallographic lattice parameter.

Holmium is similar to both terbium and dysprosium in the antiferromagnetic range, but below the Curie temperature it develops a ferromagnetic component of the moment parallel to the c axis of the crystal while maintaining the helical structure in the basal plane. This structure is essentially ferrimagnetic.

Erbium changes from having a sinusoidal variation of the magnitude of the magnetic moment parallel to the c axis just below the Neel point to a second antiferromagnetic structure in which a helical plane component exists in addition to a square wave variation of the c axis component.

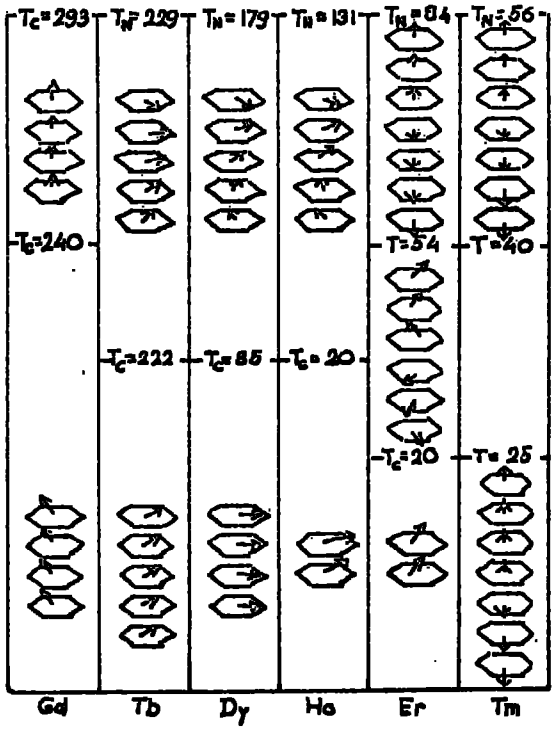

Fig. 1.1 Zero-field moment configuration of the heavy rare earth metals in the anti-ferromagnetic and ferromagnetic states with the Néel and Curie temperatures.

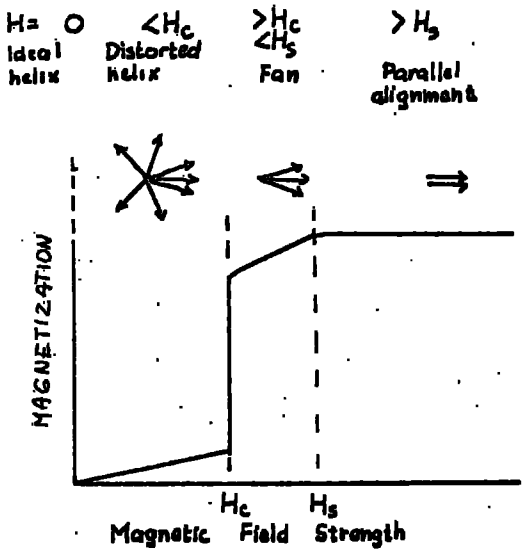

Fig. 1.2 The destruction of the ideal helical structure by an applied field and the resultant variation of the observed magnetization.

Below the Curie point the structure is very similar to that of holmium.

Thulium also shows a series of changes from the sinusoidal c axis moment variation to a rectangular wave variation in which there are more spins parallel to the c axis than antiparallel to it, in the ratio of 4:3.

The existance of helical spin structures can be interpreted very simply in terms of an exchange interaction whose magnitude is an oscillating function of distance. An exchange mechanism which satisfies these requirements is the indirect exchange interaction derived originally by Rudermann and Kittel in connection with nuclear resonance investigations and extended by Kasuya and Yosida to the case of coupled ionic spins in a metallic lattice.

The spin configurations and their change from element to element (and within an element over a wide temperature region, $4^{o}K$-T_N, T_C) are displayed on fig. 1.1. Applying a magnetic field to the helical spin configuration leads to a continuous distortion of the helix until the field strength is sufficient to cause a rotation of those spins in the reverse direction into the field direction. Further increase in the field strength then brings about a slow collapse of the 'fan' structure which is formed once the critical field is exceeded, and consequently the magnetization approaches saturation. This change in the order of the magnetic moment is shown in fig 1.2 along with the corresponding idealized magnetization curve which compares favourably with the observed results. Saturation magnetization measurements have proved to be extremaly difficult

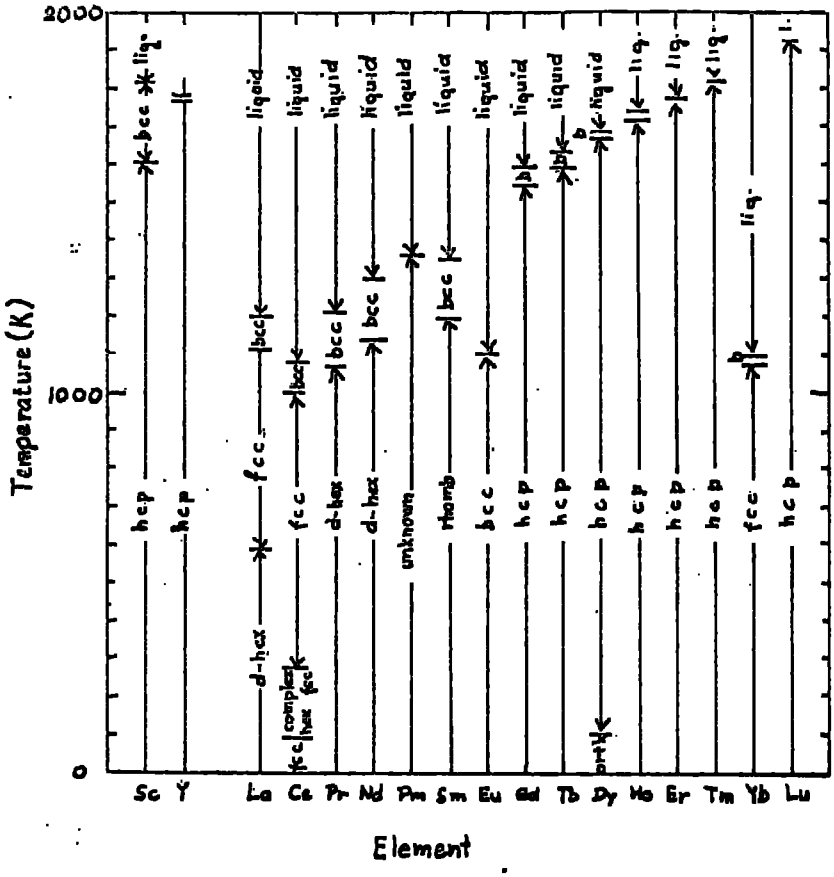

Fig. 1.3 The temperature ranges over which the various phases of the rare earth metals and Sc,Y are observed at atmospheric pressure.

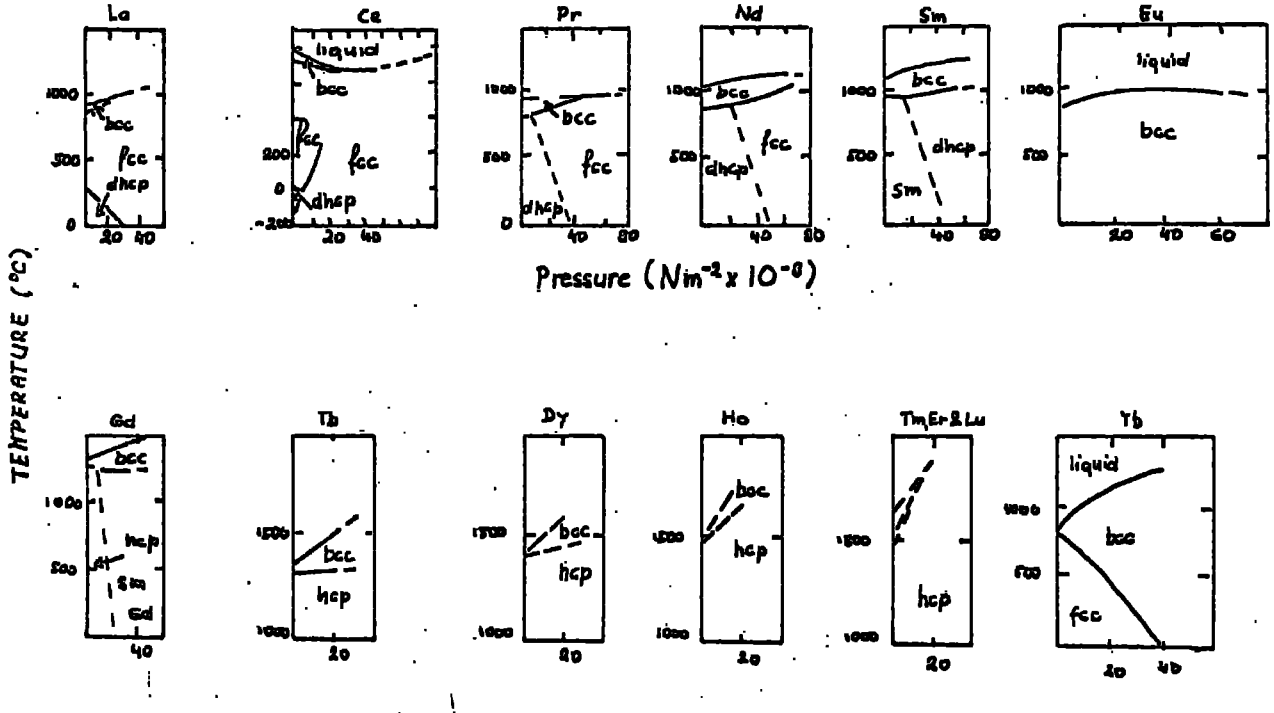

Fig. 1.4 The p-T phase diagrams observed for the pure metals.

in polycrystalline specimens of the heavy rare earth metals because of the very large values of the magnetocrystalline anisotropy which inhibits the saturation of the magnetic moments away from the easy direction of magnetization. This in general coincides with a principal crystallographic axis.

1.4 Effects of temperature, pressure and alloying

Interesting results have been found in investigations of the effect of temperature, pressure and alloying on the structure of the metals (10), mainly heavy rare earths. Raising the temperature in general leads to a phase transition from the hexagonal room temperature structure to the bcc structure. The eceptions to this are mainly alloys formed from the anomalous rare earths: europium (bcc at all temperatures), ytterbium (fcc-bcc transition), erbium, thulium and lutetium (no observed transitions) and finaly cerium in which structural behaviour is very complicated. Fig 1.3 displays graphically the different transitions in the rare earths .

Structural transitions have also been observed by subjecting the metals to high pressure. The first of these were observed in gadolinium and samarium for which it was found that after heating the metals to 400° and 300°C, respectively, at a pressure of 4×10^9 Nm^{-2} an appreciable percentage of a second phase was present in the specimen on subsequent return to normal conditions of temperature and pressure. The second phases had been retained in a metastable state after removal of the pressure and were the samarium and doublehexagonal structures, respectively. Subsequent observations showed that similar transitions could be

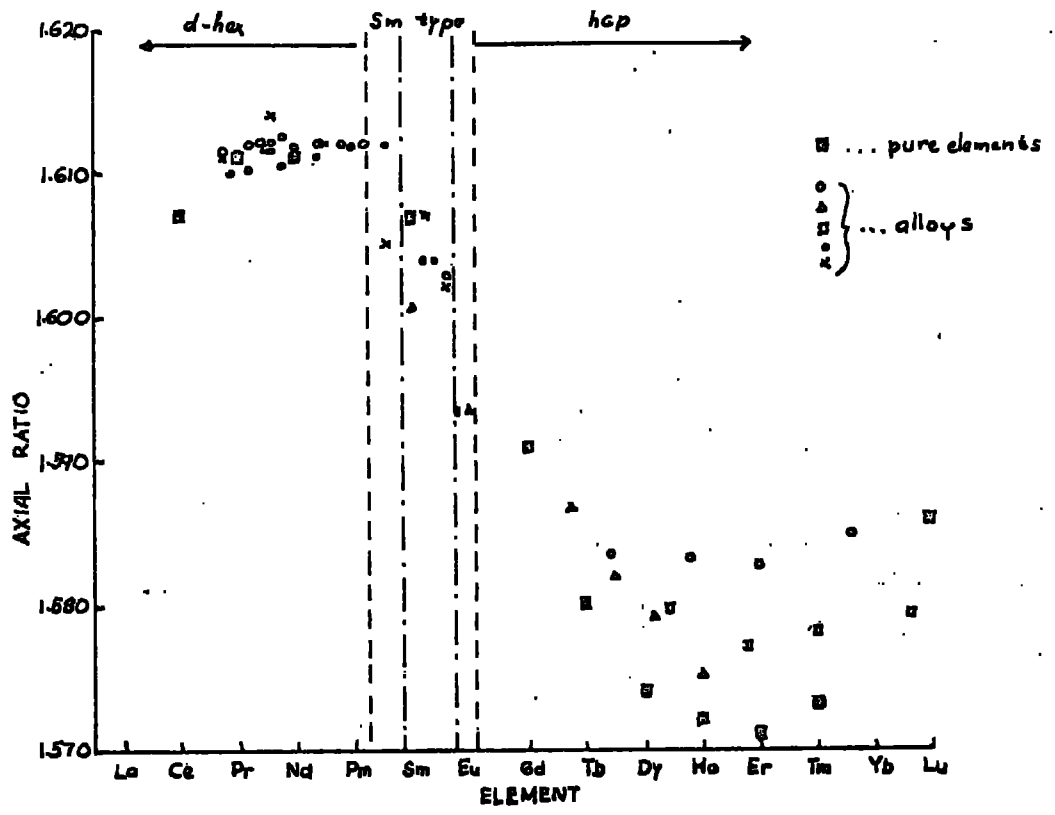

Fig. 1.5 The variation of the axial ratio (c/a) with atomic number for pure metals and various alloy systems.

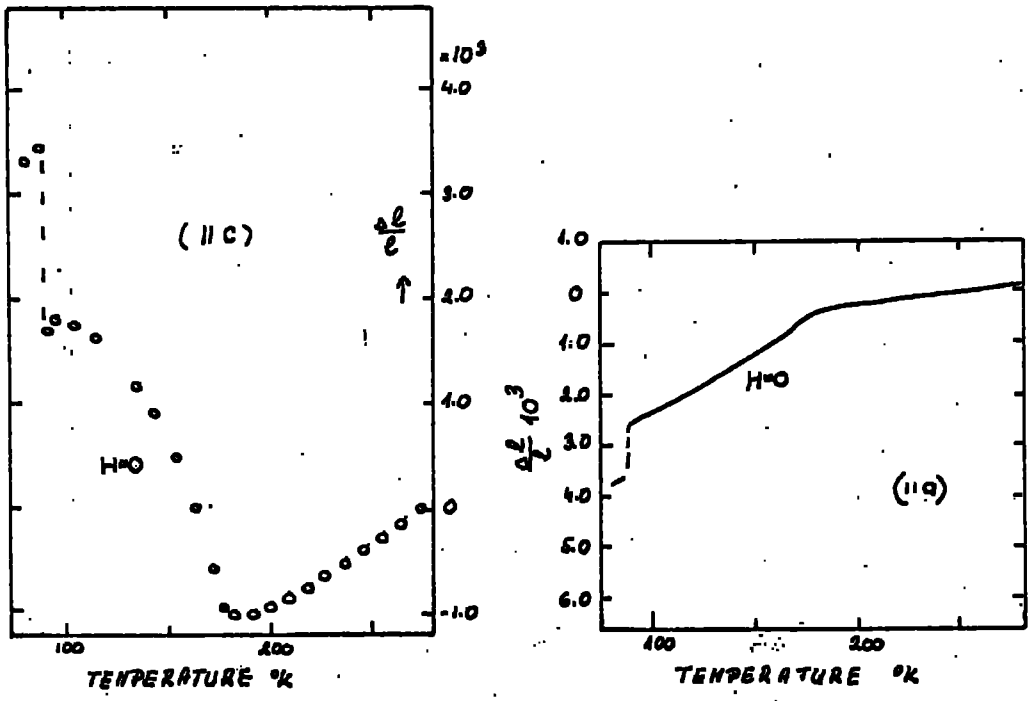

Fig 1.6 Thermal expansion data for single crystal dysprosium.

produced in most of the other metals and that with increasing pressure the structure changes occured in a definite sequence identical with the structure sequence observed for the rare earth metals themselves with decreasing Z. That is, with increasing pressure, the structures occur in the order, hcp - Sm type - d-hex - fcc. Some evidence also exists that these transitions may be related to the variation of the $^{c}/_{a}$ ratio in the same way as the alloy behaviour.

The high temperature bcc phase is also affected by applied pressure, the range over which it exists decreasing for the heavy metals and increasing for the light metals, as the preasure is increased. This is clearly seen from the $\wp$ - T phase diagrams shown in fig 1.4, as well as the structure sequence mentioned above.

By alloying any two rare earth elements the observed room temperature structures of the alloys are found to pass through the intermediate structures found between the component metals in the rare earth series. For example in the praseodymium-terbium system the observed structural changes from hcp to the samarium type at a composition $\cong$ 67% Tb and from samarium type to the double hexagonal structure at $\cong$46% Tb. Few such changes have been observed (29 and ref. there in) experimentally.

Correlation of the occurence of the samarium structure has been made with the $^{c}/_{a}$ value of the pure elements fig1.5, average atomic number and the radial extent of the 4f wave function. The internal consistency in the region to the left of gadolinium for all alloy systems investigated is remarkably good, although in the vicinity of

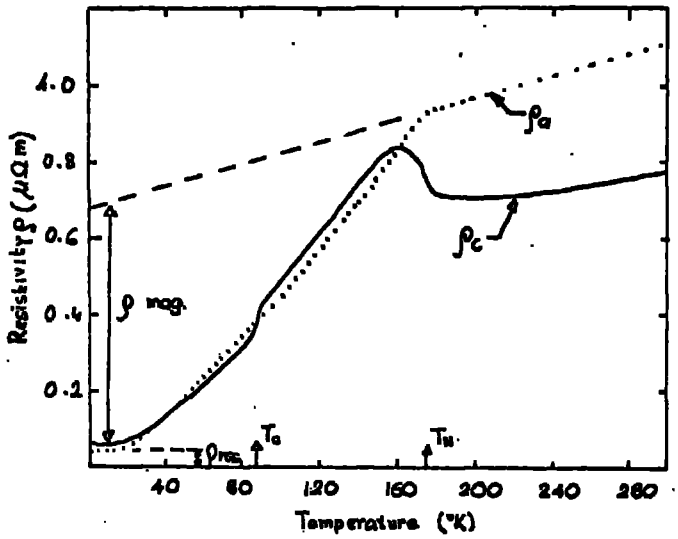

Fig 1.7 Resistivity of Dysprosium single crystal

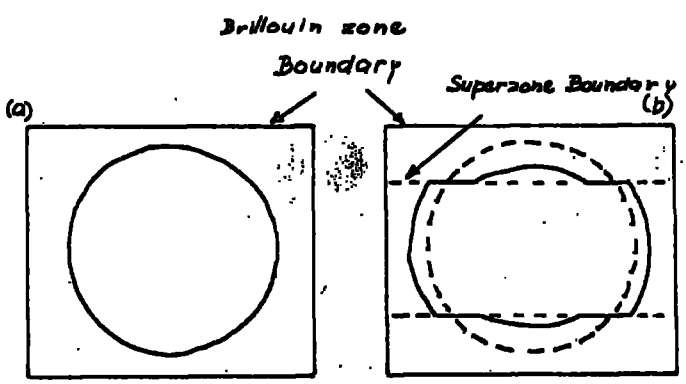

Fig 1.8 The effect of introducing superzones on a spherical Fermi surface
(a) simple metal, (b) the intersection of the surface by superzones

the heavy rare earths there does appear to be some dependance of the behaviour on the atomic number of the heavy rare earths involved. It is possible that the magnetic interactions are here contributing to the observed lattice parameters.

1.5 Thermal expansion

Thermal expansion measurements have shown that for temperatures well in excess of the magnetic ordering temperature the metals are reasonably well behaved and exhibit anomalies only in the vicinity of the solid-solid phase changes. However there have been numerous reports of very large changes of lattice parameter and consequently of the expansion coefficient both at the Neel and Curie point. In dysprosium these changes are sufficiently great to lead to a structure change from normal hcp to an orthorhombic modification, fig 1.6.

Associated with these dramatic changes in lattice parameters are correspondingly large values of magnetostriction arising from the detailed variation of the magnetic (exchange and anisotropy) energy as the observed state of the metal changes.

1.6 Resistivity

The variation of the total resistivity of the heavy rare earth elements can best be summarized by reference to single crystal dysprosium results, see fig 1.7. The total resistivity ρ_{Tot} may be divided into various components(for inst.in basal plane) $\rho_{Tot} = \rho_{phonon} + \rho_{residual} + \rho_{spin\text{-}disorder}$ assuming validity of Matthiessen's rule. The $\underline{c}$ axis specimen shows one important feature not present in the basal plane resistivity, namely, with increasing temperature the resistivity rises suddenly at

Element	Phonon coefficient C ($\rho = CT$), ($\mu\Omega$m 10^2) basal plane	c axis	Spin disorder resistivity, ρ_{mag} ($\mu\Omega$m 10^2) basal plane	c axis
La*	complex		no ordering	
Ce*	0.06-0.09		-	
Pr*	0.13		27	
Nd*	0.13		20	
Pm	-		-	
Sm*	0.21		46	
Eu*	0.134		50	
Gd	0.085	0.03	105	105
Tb	0.130	0.056	83	83
Dy	0.145	0.08	63	50
Ho	0.19	0.110	41	24
Er	0.185	0.122	18	8
Tm	0.22	0.123	22	7.4
Yb	complex		no ordering	
Lu	0.026	0.012	no ordering	

Table 1.1 The magnitude of the resistivity contributions in the rare earth metals.

the Neel point and then again at the Curie point. With certain exceptions the behaviour of the other heavy elements, which are magnetically ordered, is adequately described by that of dysprosium, the magnitudes of the various components are of course different and are listed in table 1.1. Gadolinium and thulium represent the two exceptions, the former having no antiferromagnetic phase and consequently the observed resistivity shows no discontinuities at T_C. Thulium, on the other hand, is never ferromagnetic, passing from the complex antiferromagnetic phase to a ferrimagnetic structure, and while the resistivity shows a sharp rise at T_N no corresponding decrease is observed at the antiferromagnetic transition temperature.

The spin disorder contribution to the resistivity has been approached in several ways, which deal with different aspects of the observed magnetic component.

The exchange interaction between the localized magnetic moments and the conduction electrons leads to a scattering process which is dependent upon the ionic spin. Viewing this process in terms of a scattering cross section A_m per scattering centre, the contribution to the resistivity in a metal containing N centre and n conduction electrons is given by

$$\rho_{mag} = (k_f N / n q^2) A_m ,$$

where k_f is the wave vector representing the conduction electrons. In the high temperature, paramagnetic state, for which all possible moment orientations are equally probable, the cross section A_m is given by

$$A_m = (m / 2 \pi h^2) \mathcal{J}^2 (g-1)^2 J (J+1) ,$$

leading to a spin disorder resistivity for these conditions

$\rho_{mag.} = (3\pi N m / 2 h q^2 E_f) \mathcal{T}^2 (g-1)^2 J (J+1)$.

This contribution to the total resistivity is independant of temperature in this high temperature limit and may be derived experimentally from the difference between the low temperature residual resistivity and the intercept on the resistivity axis of the extrapolated high temperature phonon scattering contribution. Comparison of the observed $\rho_{mag.}$ values with the spin dependant function $(g-1)^2 Jx (J+1)$ shows that for these metals it is a good approximation.

In the temperature range $T < T_C$ the magnetic contribution may be calculated for a ferromagnetic material both on the basis of a molecular field model and a spin wave model, the latter applying at low temperatures and the former when T approaches T_C. The scattering of the conduction electrons by spin waves in a ferromagnet has been shown to lead to a magnetic contribution to the resistivity which varies as T^2 for low magnetocrystalline anisotropy. However, for the rare earths, whose magnetic behaviour is highly anisotropic, a finite amount of energy Δ is necessary to create a spin wave. Under these conditions the spin diorder resistivity takes on the form

$\rho_{mag} \cong T^2 \exp (-\Delta / k T)$.

Of course, the form of the equation is dependant on the spin-wave spectrum, the T^2 term being replaced by T^4 when the dispersion relation changes from a square law to a linear one. Dysprosium has been shown to obey this equation for $10 < T < 30^{\circ}K$ with $\Delta \cong 1.5 \times 10^{-3}$eV, as also have thin films of the heavy rare earths. 'Δ' for various heavy rare earth metals is difficult to extract, reliably, as the range of

observation is severely limited by the fast rise in the phonon resistivity at low temperatures and the occurrence of the magnetic transition temperatures in the range 20-100°K.

1.7 Resistivity near T_N - superzones

The sharp discontinuity in the resistivity at $T_{N,C}$, fig 1.7, have been explained by examining the effect of the change in the types of order in the ferro and antiferromagnetic regions (50 and ref. there in). In normal metals, the electron states in which the conduction electrons exist are surrounded by Brillouin zone boundaries whose separation is a function of the reciprocal of lattice parameters. In the simplest case the Fermi sphere is completely within a Brillouin zone, as is shown in fig 1.8. The electrons available for conduction are those at the surface of this sphere, and consequently are dependant on the area of the surface. If other periodic features occur within the metallic lattice, whose wavelength is not equal to that of the lattice, than other zone boundaries will occur which may intersect the Fermi sphere. Since these boundaries will bring with them an associated energy gap, the intersections will result in a transfer of electrons from the cut-off, energetically less favourable, part of the Fermi sphere to more favourable regions. In fig. 1.8 is shown the effect of such intersections on the electron redistribution, associated with a periodicity approximately twice that of the lattice. Since the electrons on the plane of energy discontinuity cannot contribute to the conductivity it is clear that the effective surface area of the Fermi sphere in (b) is appreciably less than that in (a) and

consequently there will be a resistivity increase from (a) to (b).

This is very important when explaining the electronic behaviour of the heavy rare earths with helical and conical spin structures. These have a periodicity in the c axis direction which is appreciably greater than that of the lattice, and once formed on decreasing the temperature from the paramagnetic to the antiferromagnetic phase, will lead to the introduction of several new 'superzone' boundaries within the fundamental Brillouin zone, some of which will intersect the Fermi surface causing the observed increase in resistivity at T_N. For temperatures $T < T_N$ slight modifications will occur due to the temperature dependance of the turn angle and the resultant shift in the positions of these boundaries. For $T \leq T_C$, e.g. in ferromagnetic phase, the resistivity will fall rapidly due to the disappearence of the periodic moment structures. The magnitude of these changes may be estimated using the free electron model.

1.8 Light rare earths

The study of the magnetic properties of light rare earth metals has lagged behind that of heavy rare earths partly because of metallurgical difficulties of preparing good single crystals, which are needed to elucidate the widely differing roles played by exchange and crystal fields in these metals and partly because they lack strong magnetic behaviour. Consequently they have been studied much less (9,10,12-18,36-39,49).

1.9 Magnetic properties of light rare earths

The light rare earth metals which order magnetically,

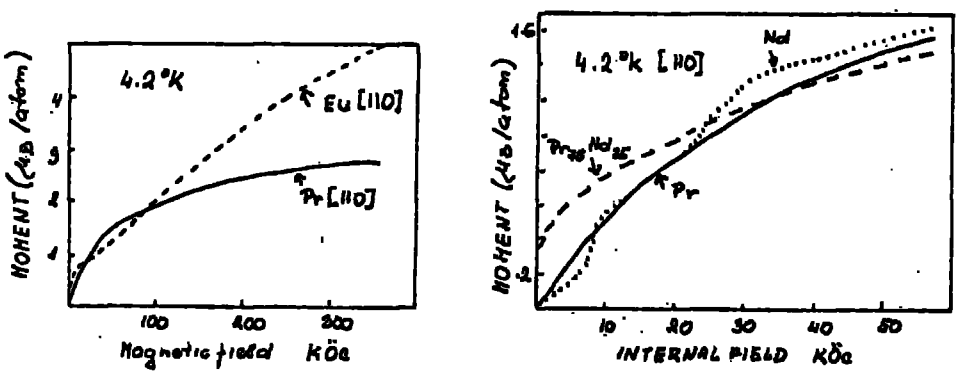

Fig. 1.9 The magnetization of Eu, Pr, Nd, and $Pr_{75}Nd_{25}$ at 4.2°K for field applied in the [110] direction.

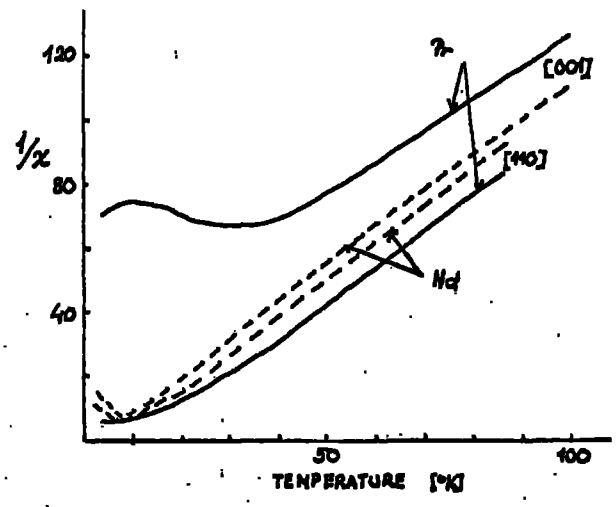

Fig. 1.10 The low field susceptibility (MKSA) of Pr and Nd in the [110] and [001] directions as a function of temperature.

Nd, and Ce also show marked anomalies at the transition temperatures but the measurements have been, until recently, limited to polycrystaline materials. Praseodymium single crystals do not appear to order (46,51), although polycrystalline results in the early work suggested an antiferromagnetic state below ~20°K. (37) have recently studied the magnetic ordering of Pr and Nd single crystals by neutron diffraction in magnetic fields up to 46 KOe, so establishing the separate contributions to the magnetic anisotropy from the cubic and hexagonal sites. (46) have carried out magnetization experiments on single crystals of Eu, Pr, Nd. In divalent bcc Eu the crystal field is very small compared with the exchange contrary to the case in Pr and Nd. The magnetization and susceptibility curves of Pr and Nd may be understood by assuming that Pr is an induced moment system in which the large magnetic anisotropy is dominated by the anisotropy of the effective exchange, [001] being the hard direction and [110] easy one, fig 1.9, 1.10. Nd on the other hand is an ordered moment system in zero field at low temperatures and the abrupt changes in the magnetization by an applied magnetic field may be due to the crossing of crystal field levels similar to the observations of (47) on $(Gd,Nd)Co_2$. This seems to be supported by theoretical calculations made by (45) on the basis of the resistivity measurements made by (16).

1.10 Crystal field energy

The light rare earths also show evidence for crystal field level splitting as was accounted for by (14,51) in inelastic neutron scattering experiments, or by (45)

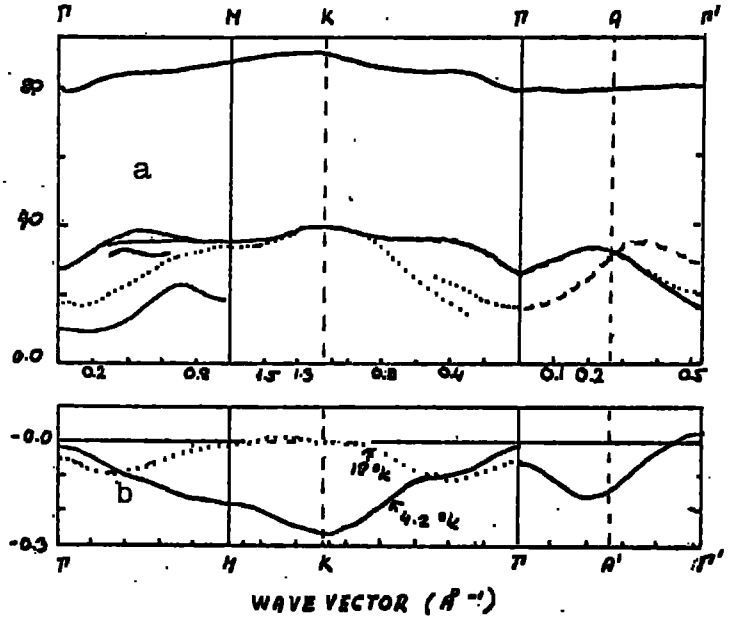

Fig 1.11 (a) The dispersion relations for magnetic excitons in Pr at 4.2° and 18°K.
(b) $\mathcal{J}(q)$ (full line) and $\mathcal{J}(q)'$ (doted line for the hexagonal sites.

theoretically through the electrical resistivity behaviour and by (44) on the basis of specific heat measurements or from EPR and Mössbauer spectroscopy by (48 and ref there in). The crystal field interactions in the light rare earth metals are comparable in magnitude to the exchange forces. Very interesting mapping of low lying magnetic energy levels split by the crystal field have been made by (14) on Pr single crystals by means of inelastic neutron scattering at 4.2°K, fig 1.11. In the light rare earths as the effective exchange is weaker and comparable in magnitude to the crystal field forces, the ordered moment is reduced from the free ion value $g\mu_B J$ so much that is possible to have complete suppression of magnetic order as is believed to be the case in Pr (51). In this case the magnetic excitations have the nature of magnetic excitons in which a transition between single ion crystal field states is propagated through the crystal by the exchange interactions between neighboring ions. For each symmetry direction investigated the dispersion curves for these excitons have three branches. A single branch lying between 8 and 9meV has been provisionally assigned to a mode propagating on the cubic lattice sites, since these lie on a simple hexagonal lattice with one atom for unit cell. The lower branches, optic and acoustic, have a larger dispersion and correspond to a mode propagating on the hexagonal sites. There are two branches because the hexagonal sites lie on a hcp lattice, the upper mode being an 'acoustic' one , the lower an 'optic ' one. This indicates that the exchange interactions between B and C layers which gave rise to the Davydov

splitting the modes are antiferromagnetic . This has been recently verified (51) experimentally. Because the energy gap between different levels is of the order 10–100°K there is good reason to believe that the electronic properties of the metals would be to some extent governed by this mechanism too, as has already (45) been considered for the resistivity measurements made by (16).

1.11 Rare earth alloys

Rare earth elements readily form intermetalic alloys of any stoichiometry (1). The properties of these alloys resemble the pure rare earth elements. As there are still many outstanding problems concerning the rare earth elements it was hoped that some insight into their electronic and structural behaviour might be obtained through a study of these alloy systems.

To state the problem it is necessary to make a brief summation of the characteristic features of rare earths more fully described above.

Heavy-heavy and heavy -Y alloys have already been studied by many workers together with the heavy rare earths owing emphasis to their strong magnetic behaviour (2-10,19) . Heavy rare earths are stable in their hcp structure up to transformation temperature, which is high (~1400°K), their valency is stable at 3, not influenced by alloying, their f-shell is buried deeply into the electron core of atom, (or ion in the solid state) and is isolated by the outer, fully occupied, shells. These elements are well described by a localized electron model. In the temperature range studied (4-300°K) they are generally magnetically ordered

so that the most important energy comes from the exchange interaction.The complex magnetic structures in the ordered states which occur because of the interaction of the exchange and crystal field effects can be seen through the appearence of magnetic superzones effects (33).

Alloys formed from the light rare earths have been also occasionally studied (21-27) but alloys formed between heavy and light have been essentially neglected (28-30,36). The light rare earths have twice as large an elementary cell in the d-hex modification as the heavy rare earths but at normal and low temperatures they exist also in a cubic modification (38). Their structure is comparatively unstable with decreasing atomic number, the a and c lattice parameters increase and the crystals are softer. The binding of neighborough atoms seems to get less tight. Spedding (32) suggested that the atoms are 'anisotropic' as a and c are both smaller than theoretically expected from a given structure. With the increasing lattice parameters a and c towards the light rare earths the exchange interaction becomes smaller, virtually vanishing because of the lack of f-electrons in the case of La. In Pr and Nd this is a second order energy term. The decreasing importance of the exchange energy enables other effects to develop , e.g. crystal field effects, but in a different way than it happens in heavy rare earths.

The exchange interaction is far from being negligable for all rare earths and at the same time in the light rare earths is comparable to other energies. This enables us to make an estimate of its size.There seems to be some evidence for the

f-shell emerging to the vicinity of the Fermi level, (Ce, La (43)) towards the lighter rare earths (11). This means that at the vicinity of E_f there will be three types of electrons s, p, f instead of two, s and p as is the case in other rare earths.

To describe electronic properties of these elements, with three different types of electrons at E_f, the resonant scattering machanism, is a more covenient model than the model of localized electrons. Comparing the behaviour of normal and 'anomalous' rare earths (Ce, La, Eu, Sm, Yb) and from known changes in density of states $\eta(E_f)$ near E_f (34-5) it might be possible to deduce to which group this particular alloy belongs to.

Samarium (and Europium) is, currently of interest to the rare earths physicist because of its similarity with the transuranic elements. Their magnetic behaviour is similar to the heavy rare earths but the change in the number of conduction electrons with pressure, temperature and nature of the host metal resembles to some extent Ce, Yb, and La (also called anomalous rare earths (11)). The smallest group , in number, of the rare earths exist in the Sm-structure whose primitive cell is 4.5 times bigger than that of the heavy rare earths having $\underline{c} \sim 4.5\ \underline{c}_{hcp}$. Their f-shell seems to be in the vicinity of the Fermi level but mechanisms of changes in its position relative to E_f seems to be more compicated than for instance at Ce where resonance scattering model or metal-insulator model (40) are suitable. In Sm a combination of them or a semiconductor-metal model (41) would be necessary to account

for the experimental behaviour. In a very crude approximation one can talk in the case of normal rare earths in terms of density of states $\eta(E_f)$ near E_f as a constant as the other effects are stronger, while in the case of 'anomalous' rare earths the most important mechanism or one of the most important one's is connected with changes in $\eta(E_f)$ as was simply described by (42).

It is the purpose of this thesis to collect some experimental evidence as well as to provide a possible explanation of some of the features reported and to deduce from them a qualitative or quantitative conclusion concerning the rare earths.

C H A P T E R T W O

EXPERIMENTAL METHODS, APPARATUS

2.1 Introduction

This chapter will be devoted solely to the description and discussion concerning the experimental method, techniques used for the sample preparation, choice and construction of the apparatus together with the actual experimental procedure.

The main purpose of this work was to study some light-heavy rare earth alloys namely their electrical properties and their dependence on structure.

The chapter is ordered so as to start with the description of the alloy making process as far as the shaping of the sample for the resistivity measurements on one side and powder X-ray analysis on the other side are concerned. The description of the apparatus for the temperature dependent resistivity follows next, giving details of the D.C. method used and the electronic and cryogenic part of the apparatus. The chapter ends with the description and discussion of the resistivity measuring procedure.

2.2 Specimen preparation

Ingots of Dy, Tb, Y, La, Pr and Nd with a purity of 99.9% obtained from Koch-Light Laboratories, were used as the raw material for the preparation of all the materials studied. These included the alloys Dy-Nd, Tb-Pr, Nd-Y, and Dy-La at all concentrations as well as specimens of the pure rare earth elements themselves.

The ingots were cut to appropriate quantities, approximately 3gms weight, for preparing samples. The components of any-one alloy were weighed to an accuracy of ± 0.05mg on a balance kept in argon atmosphere in the glove box where all the metal cutting was performed.

The 3gms specimen buttons were melted by standard arc furnace techniques. This consists of melting together the desired quantities of the required metals on a water cooled copper hearth under an atmosphere of pure argon at a reduced pressure (~250 torr) using a controllable electric arc with a non-consumable tungsten electrode. The lower face of the melted button is, of course, in contact with the cold copper so that it is necessary to turn the specimen over and remelt it several times to obtain a homogeneous mixture.

The argon was obtained as 'Pura gon' with an oxygen content of no more than 3 p.p.m. The arc furnace was pumped down to 10^{-3}torr then flushed with purargon to 700torr, pumped down to 10^{-3}torr again and then filled to 250torr with 'Pura gon'. Any remaining oxygen was removed as far a as possible by gettering for about one to three minutes with molten tantalum before melting the sample components together.

The sample melting was done at as low a temperature as possible to minimise the loss of material by evaporation. Weight loss was always checked after melting which was of the order of 0.1% of the total weight. Surface oxidation was checked visualy. If present it was filed carefully off before annealing.

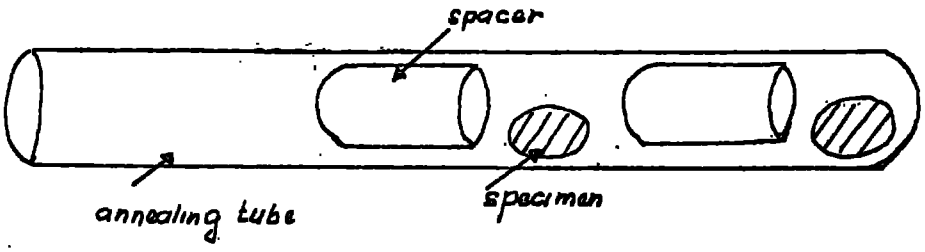

Fig. 2.1 Annealing tube.

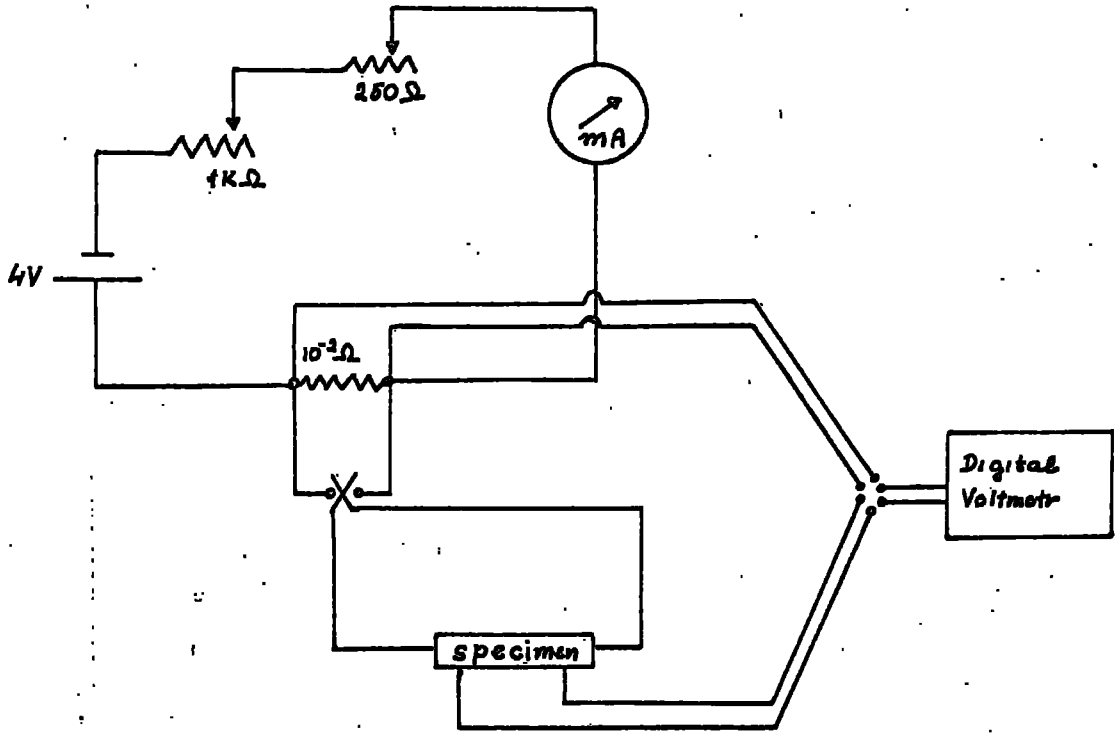

Fig. 2.2 Circuit of the D.C.power supply.

2.3 Annealing

Most of the specimens were annealed previous to any measurement, at a slightly lower temperature (50-100°) than the expected phase transition temperature (3.4, 1.4) to ensure phase purity. The length and temperature of annealing are given in table 2.2.

Table 2.1.

specimen	Dy-Nd	Y-Nd	Tb-Pr	Dy-La
temperature	≧ 800°C	≧ 700°C	≧ 700°C	≅ 200°C
time (days)	42	71	60	14

Annealing of the samples was done on half buttons wrapped in molybdenum or tantalum foil and placed in a quartz tube. Several samples of the same alloy where placed in one annealing tube, each being spaced from its neighbour by a short length of quartz tube at one end which fitted freely inside the annealing tube, see fig 2.1. The annealing tube was filled with 'Pura gon' and gettered by the same procedure as described above for preparing a sample button. The argon was then pumped out to 10^{-3} torr and the samples isolated from each other by collapsing the quartz tube on the spacers.

2.4 Determination of crystal structure and lattice parameters

The phase purity as well as the lattice parameters of the samples were examined by X-ray diffraction from a rotating powder sample using a Phillips 360mm circumference Debye-Scherrer X-ray camera and usually cobalt K_α radiation. The films obtained by this method were analysed in the usual way using a Bunn chart in conjunction with previously published data about the constituent metals of each alloy

series. Two computer programmes were used (Appendix 1,2) in the structure determinations one simply giving smallest interplane distances d derived from Bragg's law $\sin\theta = \lambda/2d$, where θ is angel of incidence of X-rays, λ is their wavelength in Å and d for hexagonal structure is given by the following equation

$$1/d^2 = 4/3\ (h^2 + hk + k^2)/a^2 + (l/c)^2$$

The other programme carried out calculations of the lattice parameters 'c', 'a', the axial ratio 'c/a' and the elementary cell volume from a given set of θ and h,k,l (reciprocal planes parameters known as the Miller indices).

2.5 Samples for resistivity measurement

The samples for resistivity measurement were cut from the arc melted buttons in the form of rectangular prisms with approximate 1mm x 2mm x 10mm.dimensions. The cutting was performed with a high speed diamond saw in the Department of Applied Physics at Durham University. The surfaces obtained by the saw were sufficiently good and flat that only filing on a fine emery paper was necessary to remove any surface oxide layers before applying the electrical contacts to the sample. Specimens were taken from the centre of the button as this was considered the region of the higher homogenity; the powder needed for X-ray analysis was also obtained from this area.

2.6 Specimen dimension and contacts

The specimens in the form of rectangular prisms enabled easy appication of the electrodes. The dimension, 1a x 2a x na (where $n \gg 1$), where so chosen to enable us to minimise the effect of size and shape (1) on the

measured resistance (i.e. resistivity). The same reason, discussed in (2) limits the suitable points for attaching probes on a specimen of a given shape. The probes were attached 2mm from the edges 1-2mm apart on each end of the specimen. Spot welded contacts were used as these proved to be the best ones from several different types used in preliminary examinations. These included arc-welded, soldered and ultrasonicaly bonded contacts but in general only the former were consistently reliable. Arc welded contacts were made using a 'Hirst' resistance welding machine. Standard thermocouple quality copper wires insulated with PTFE sleving were used as the electrodes. Contacts formed this way make an intimate contacts with material and so avoid a complex of intermediate layers at the contact which lead to unwanted transitions. The lower faces of the prepared specimens, mounted three at a time, were glued by Varnish (G.E.7031 supplied by Oxford Cryogenics) to an al uminium block (1.5cm x 1.5cm x 1cm) to minimise the temperature gradiant along the samples. This varnish maintains a good thermal contact in the required temperature region and at the same time works as an electricaly insulating medium between the sample and the supporting aluminium block.

2.7 Resistivity measurement

A conventional four probe D.C. method was chosen to carry out the measurements, the basic block scheme for which is shown in in fig 2.2. The circuit diagram of the D.C. power supply is given in fig 2.2. A stabilised direct current of the order of 0.1 Amp was passed through the end

electrodes and the appropriate voltage was measured across the inner potential electrodes. In the early observations a precision ($1\mu V$) potentiometer was used with an external galvanometer. This proved to be a slow and tedious method of recording. In the majority of the results presented a digital voltmeter, 'Schlumbergen Solatron 200' was used. The accuracy of the reading was 5×10^{-4}mV on the 10mV scale. To minimise the error of the resistance determined this way current was observed for each 'voltage' reading. For each value of the resistance R(T) the current was reversed and the reading repeated thus eliminating thermo-electric effects. The resistance $R_i(T)$ for each temperature was then calculated simply using Ohm's law:

$$R_i(T) = (V_i^+ + V_i^-)/(I_i^+ + I_i^-)$$

where $V_i^{\pm}$ was the potential drop across the specimen measured between 'voltage' contacts for current in + and - direction, $I_i^{\pm}$ current in + and - direction. To obtain the resistivity values the dimensions of the samples were measured by repeated observations with a micrometer and the readings averaged. The distance between the 'voltage' electrodes were measured with a portable microscope with a built in micrometer screw to a standard accuracy of 0.005mm. The resistivity $\rho_i(T)$ at a given temperature is then given by the well known formula:

$$\rho_i(T) = R_i(T)\ (a \times b)/L$$

$(a \times b)$ being the cross section of the sample, L the separation of the voltage electrodes. No correction has been made for the length contraction with temparature. As many as 600 $R_i(T)$ points on average have been taken for each

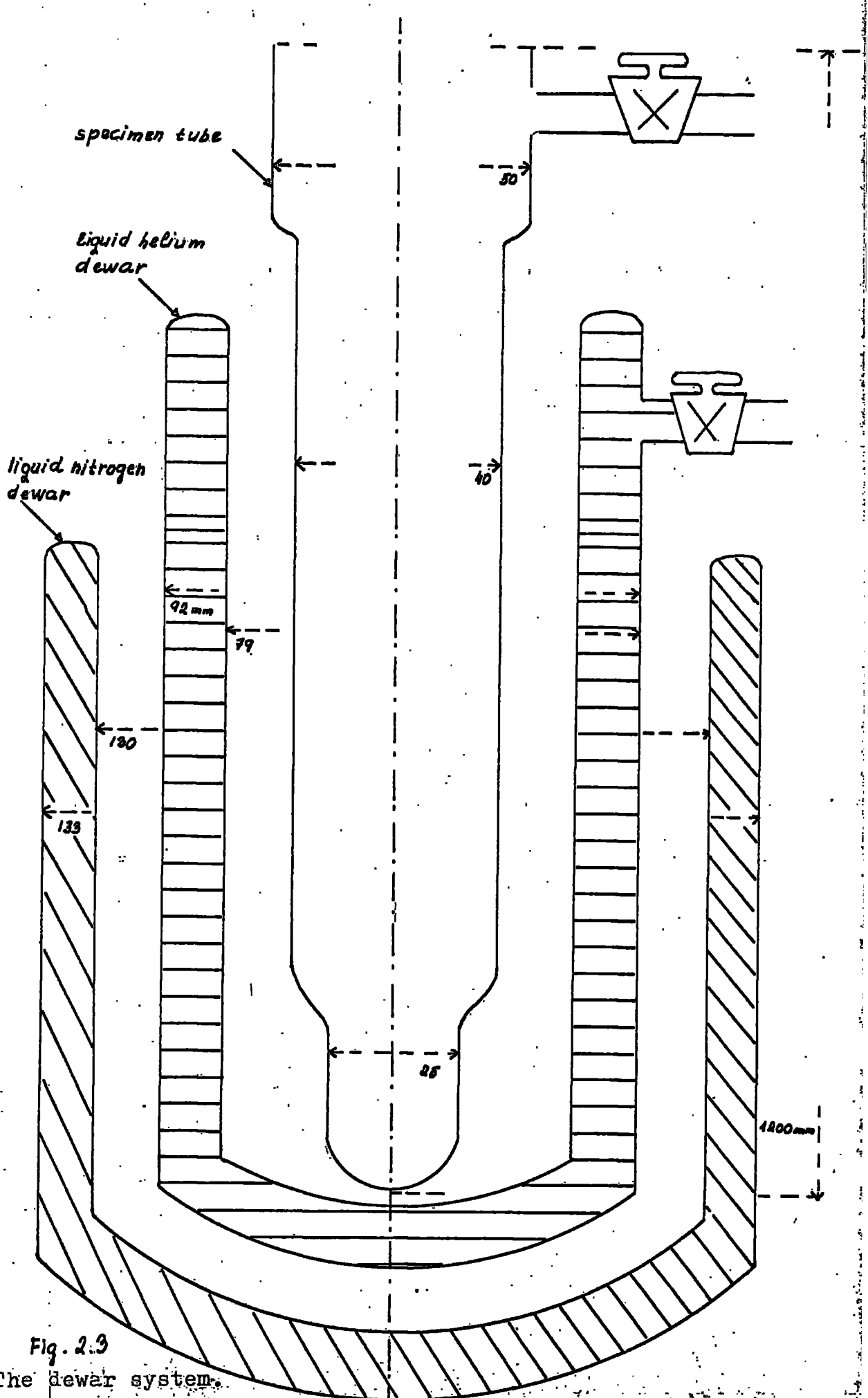

Fig. 2.3
The dewar system.

sample over the observed temperature region. A computer program was used (Appendix 3) to get the numerical values for $\varrho_i(T)$ as well as the drawing of the graphs $\varrho_i(T)$ vs T. The computations were carried out on the IBM 360/67 computer instaled at Durham University.

2.8 Cryostat

To obtain any temperature between ~2 .7 and 400°K for the time necessary to allow thermal stability of the specimen during the measurements at a given temperature a conventional cryostat was constructed as is shown in fig2.3. It consists of a specimen chamber, helium dewar and nitrogen dewar. The dewars were made from Pyrex glass. The nitrogen dewar was evacuated and permanently sealed. The inner helium dewar is flushed and pumped each time it was used to remove any helium gas, which had diffused through the inner wall into the vacuum space. The tube forming the specimen chamber was made of quartz. The dimensions of the system are shown on the schematic diagram of dewar system, fig 2.3. A vacuum system was attached to the cryostat as indicated on the schematic representation in fig 2.4 and 2.5.

The purpose of the system are as follows:

1) To enable evacuating and filling the inner specimen chamber with He-gas .
2) To allow evacuating and flushing of the helium dewar with He-gas and the collection of any He-gas boiled off.
3) To flush and evacuate the helium dewar wall space and
4) to allow pumping over liquid gas es (nitrogen and helium) to assist attaining the desired temperatures.

2.9 Heater

A heater coil made of constantan wire, isolated by

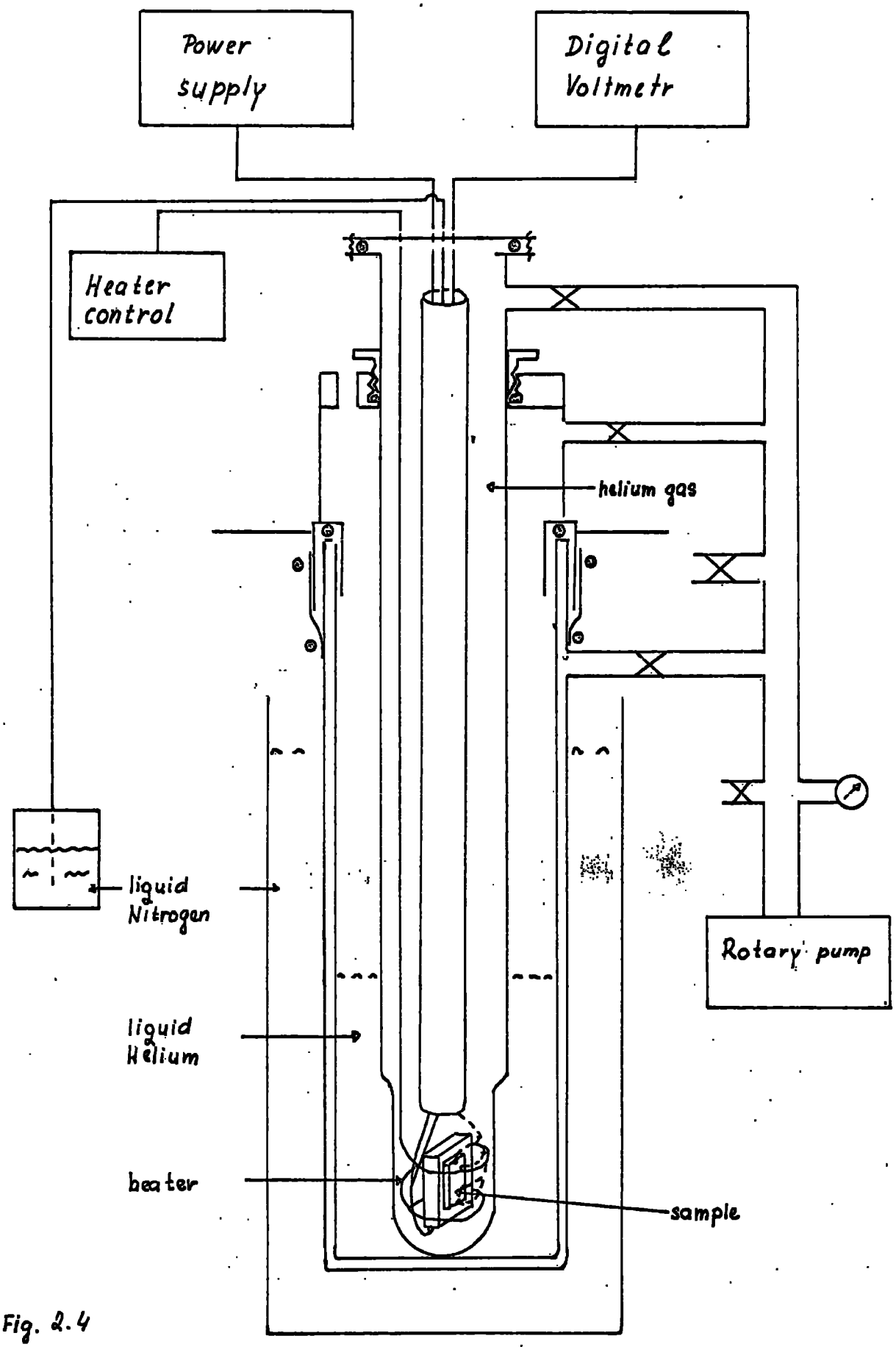

Fig. 2.4
Schema of the apparatus.

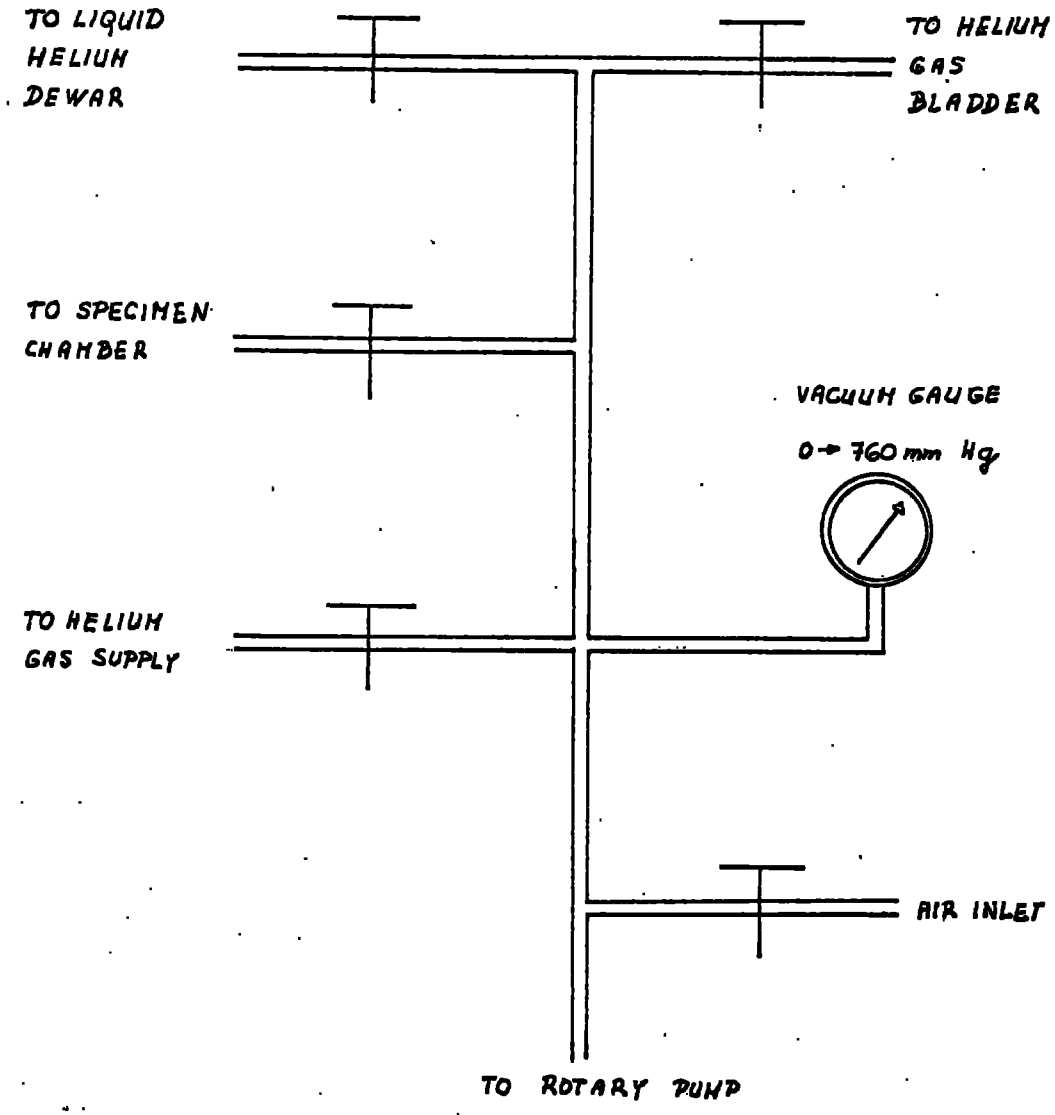

Fig. 2.5 Vacuum System

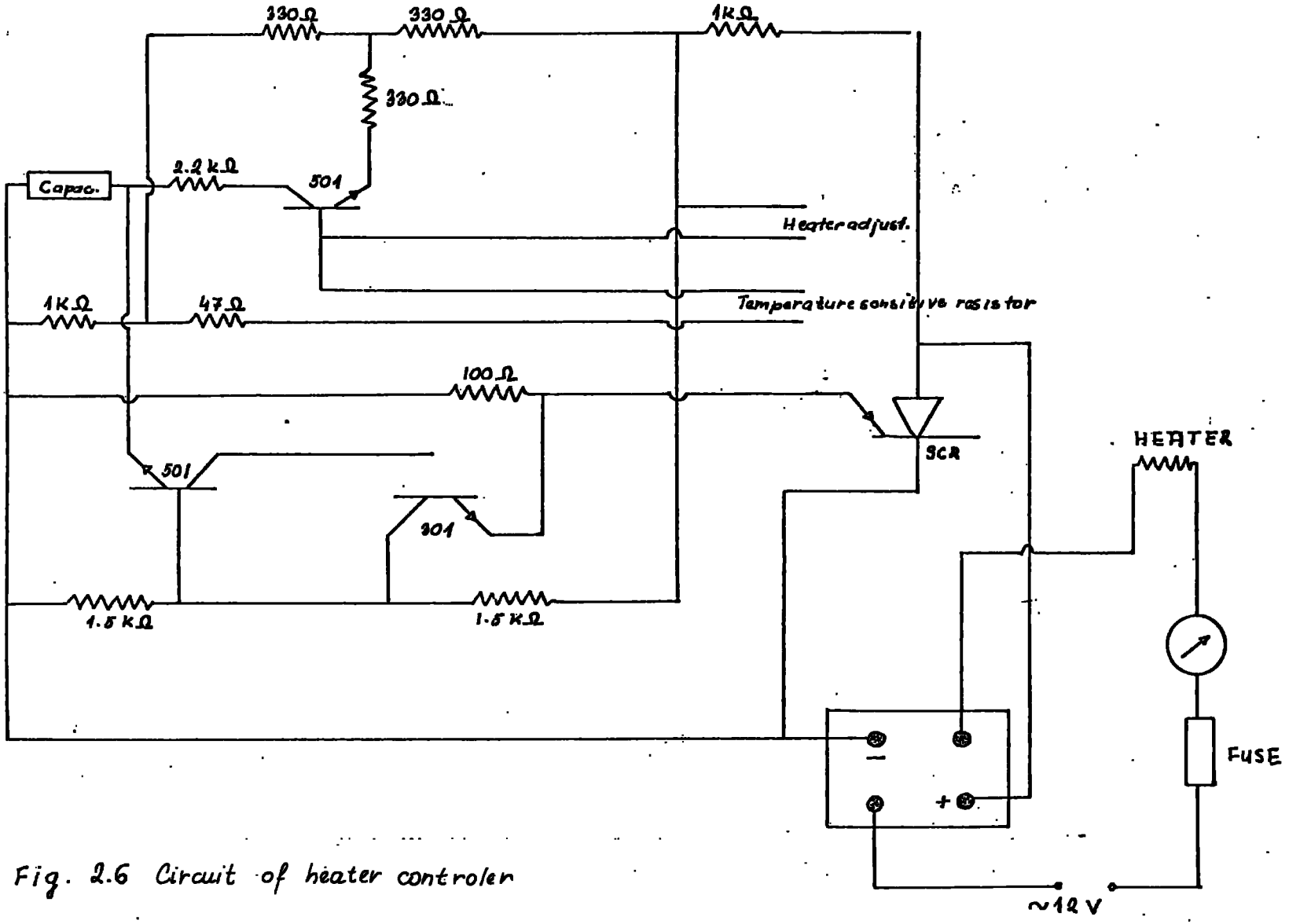

Fig. 2.6 Circuit of heater controler

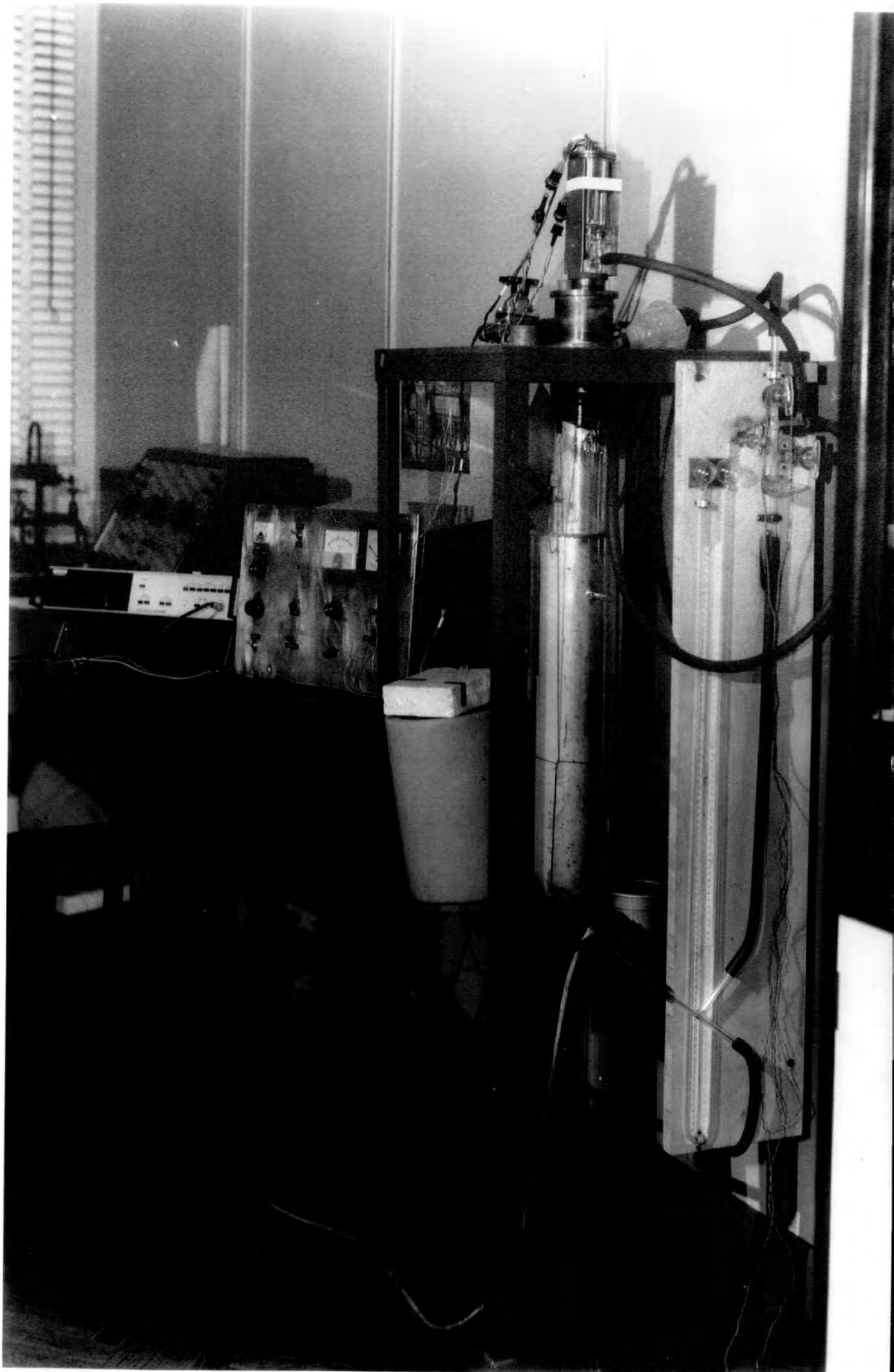

fig. 2.7 Resistivity apparatus

'Refrosil' sleeving, was wound around the aluminium foil covering the samples. The voltage for the heater coil was obtained from a 12-Volt filament transformer controlled by the circuit shown in fig 2.6. This could be manually controlled by the potentiometer (250Ω) as well as by the carbon resistor sensing element placed next to the specimen. The manual adjustment was used to set the temperature at which the measurements were to be made. The circuit then automaticaly adjusted the current to reach the chosen temperature.

2.10 The dewar head

The dewar head rested upon the top of a steel bridge as shown in fig 2.7. To the top of the head was attached a brass mechanism (the height adjuster) whose function was to adjust the vertical position of the quartz tube serving as a sample chamber. The top of this tube was fitted into a brass tube, fig 2.8 and secured to this by araldite to give a vacuum tight seal. The upper end of the sample tube was attached from the outside to the brass tube and sealed by an O-ring. The external brass tube could be evacuated via the side tube thus evacuating the helium dewar prior to filling with helium as an exchange gas. The sample chamber had its own gas inlet valve on the side of the quartz tube as the same process has to be followed for this chamber as for the inside He-dewar previous to any temperature run.

2.11 Support of the sample

The samples were glued, fig 2.10 (as mentioned above) to an aluminium block which was attached to a stainless stel

tube. The tube covered all the wires from the specimens as well as the thermocouple wires and supported also the sample holder and heater and temperature sensing element providing the electronic temperature controller with information about the temperature at the sample. The upper end of the stainless steel tube was fixed, fig 2.8, by a brass mechanism to a top brass plate. The plate was vacuum sealed to a brass ending of quartz tube (sample chamber) using the O-ring, supported by 6 screws. The top brass plate also contained the vacuum lead through for all the necessary wiring.

2.12 The temperature measurements.

In the region between 70°K and 400°K, temperatures we were measured using a copper - constantan thermocouple in contact with the aluminium block to which specimens were attached as mentioned before. Standard thermocouple quality copper and constantan wires were used, insulated with PTFE sleeving and the junction made by melting the wires together in a normal bunsen flame. The thermoelectric emf's were measured using the same digital voltmeter as was used for the resistivity measurements.

The thermocouple calibration was checked periodically at several fixed points and compared with the standard references tables.

For temperatures below that of liquid nitrogen (~77°K) a gold-iron vs copper thermocouple was used. The gold wire, available from Oxford Instruments Cryospares Division, has a small (0.2%)) iron addition, giving a thermoelectric power of about 10μV per degree at liquid helium temperature, compared with the 1μV per degree of a copper-constantan

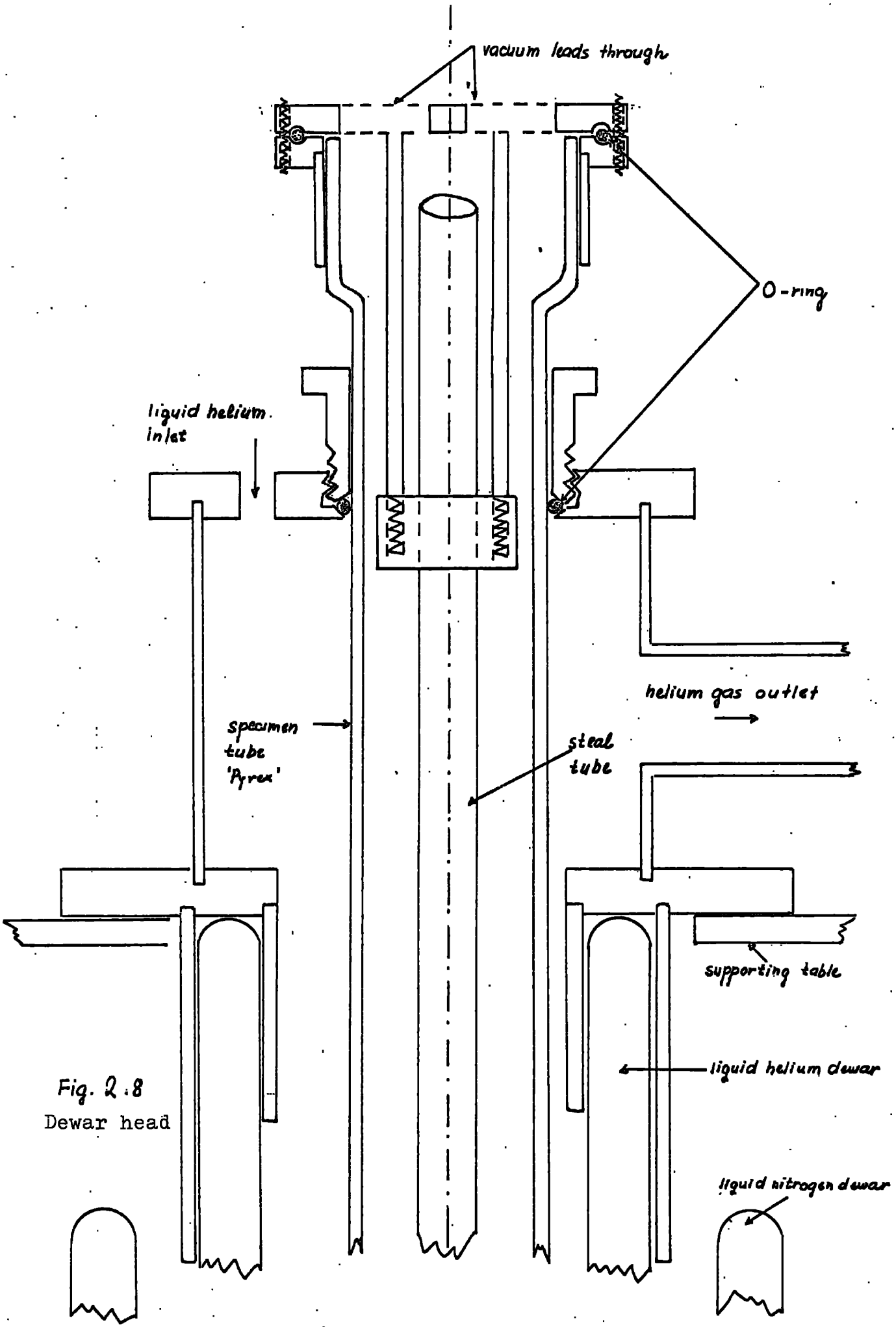

Fig. 2.8
Dewar head

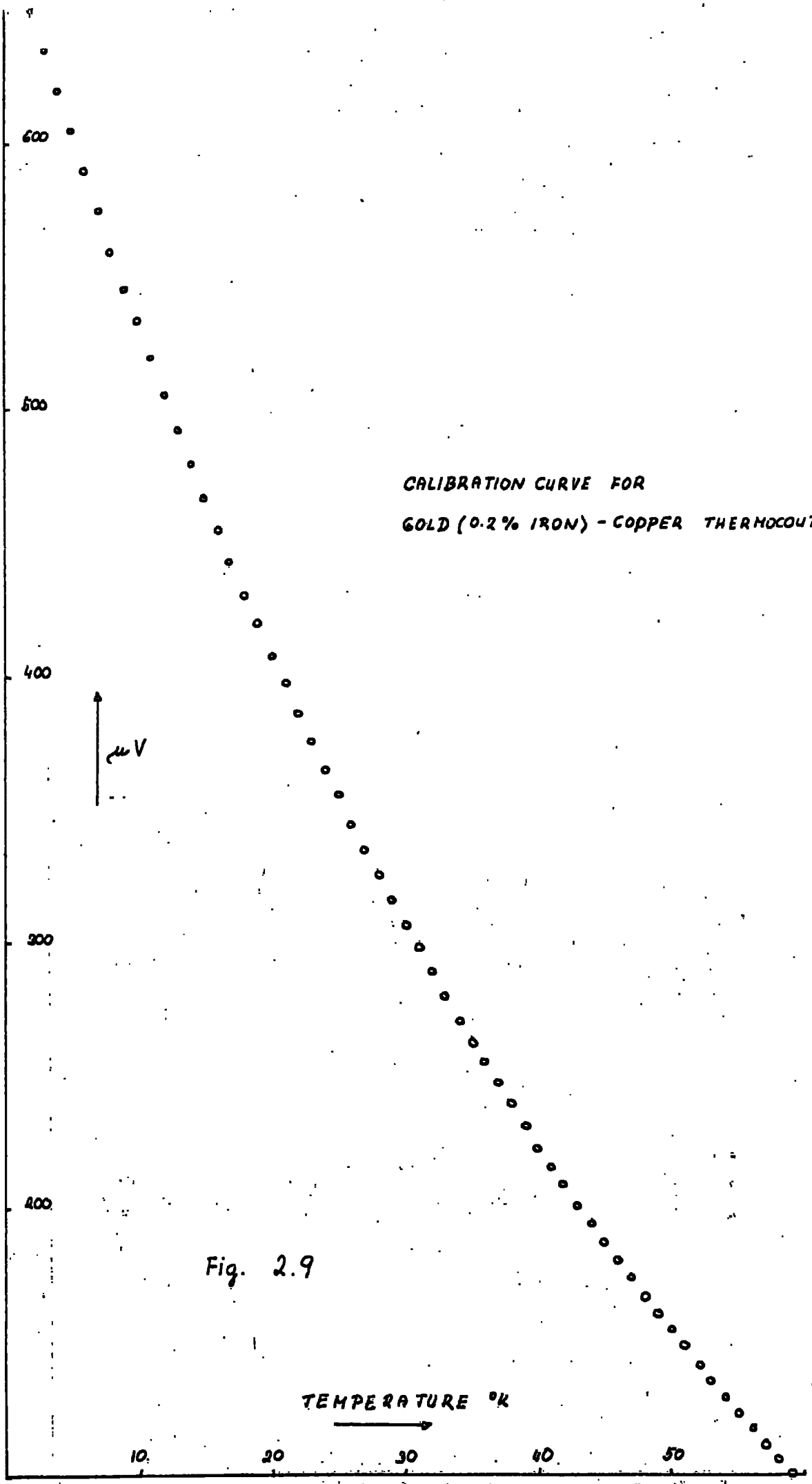
600
500
400
300
400
μV
CALIBRATION CURVE FOR
GOLD (0.2% IRON) - COPPER THERMOCOUPLE
TEMPERATURE °K
10.
20
30
40
50

Fig. 2.9

thermocouple. Since there are no standard tables available the thermocouple was calibrated using measurements made at liquid nitrogen (~77°K), pumped nitrogen (3mm pressure; 54.5°K), liquid neon (27°K) and liquid helium (4.2°K) temperatures. A computer programme was used to fit the observed calibration points to a third degree polynomial and from the results the emf vs temperature were calculated. The calibration obtained in this way is shown in fig 2.9. The thermoelectric power falls rapidly above 4.2°K (and below) to ~70°K. Both thermocouples were permanently attached to the aluminium block holding the specimens, fig 2.10. The reference junctions of both thermocouples were at liquid nitrogen.

2.13 Temperature runs

The usual cooling time of the apparature from the room temperature to the temperature of liquid nitrogen (~77°K) was 3-4 hours. The controlled heating process (from 4.2°K or below that temperature to 300-400°K) took on average 12-15 hours. As it was difficult to attain the whole cycle of cooling and heating (300°K-4.2°K-300°K) in one day the temperature region studied (300°) was usually measured in three stages. This introduced a systematic error appearing as a step in the ρ vs T curve in some of the samples measured, the origin of which is not fully explainable. Changes in the residual resistivity, as well as the random error were usually much smaller. An explanation involving magnetic hysteresis or any other form of hysteresis, is not supported by the experimental evidence and so the origin of this systematic error remains open.

Temperatures below 4.2°K were obtained by pumping on

Fig. 2.10 Sample holder

the liquid helium, In this way ~2.7°K was obtainable. Temperatures between 4.2°K and 77-100°K were realized with the help of the electronically controlled heater described earlier. Thus it was possible to take readings every 0.05-0.1° in the region of very low temperatures (≲20°K) and every degree above 20°K with an accuracy better than 0.1°K. Readings were taken, below 4.2°K, both on the cooling and heating cycles. Between 4.2°K and 80°K measurements were made only while the sample was warming, as the temperature was uncontrolable otherwise. In the temperature region (80°K-300°K) measurements were readily made while the sample was warming as well as cooling. Occasionally a mixture of acetone and 'dried ice' (solid CO_2) was employed to obtain selected temperatures between 200° and 300°K. The temperatures above room temperature up to 400°K were obtained by the use of the heater described previously.

2.14 Temperature equilibrium

Each change of the quasi equilibrium temperature state of the sample resulted in an increase in the random error of the measuremens. A very long time was found necessary to reach thermal equilibrium when liquid helium is transfered to the system. This could be followed on an enlarged plot of ϱ vs T (of the region 0°-40°K). By reaching the thermal quasiequilibrium the random error, otherwise quite big, could be decreased by two orders of magnitude. This enabled us to study changes in the behaviour of ϱ vs T in low and very low temperature regions which is very important for distinguishing different scattering mechanisms in the alloys studied since the magnetic spin disorder contribution as the normal phonon contribution are negligible in this temperature region.

C H A P T E R T H R E E

EXPERIMENTAL RESULTS

3.1 Introduction

Experimental results from the powder X-ray analysis of all the elements and alloys studied are presented and discussed in the first part of the chapter. Second part is devoted to the measured resistivity variation with temperature of all alloys whose structure is presented in the first part.

In the both parts the results are divided into four groups as four alloy systems have been studied, namely Pr-Tb, Dy-Nd, Y-Nd, Dy-La.

The resistivity results are subdivided according to the crystallographic groups to which the actual samples belong because this factor seems to be largely responsible for the major differences in the resistivity behaviour. For each alloy system the behaviour at very low temperature is discussed separately as this is believed to be of special importance in distinguishing the scattering mechanism fromatheoretical point of view.

3.2 Structure

All the alloys studied, La-Dy, Pr-Tb, Nd-Dy, Nd-Y, have been shown to possess a structural sequence with increasing light rare earths concentration (1-4). This has the form hcp → Sm-type → d-hex and is similar to the structure sequence observed in crossing the rare earth group from Lu to La as well as to the sequence of pressure induced phase transitions which have been reported (5,6) for the pure elements and for limited number of alloys. Beaudry (7) reported the existence of two additional mixed

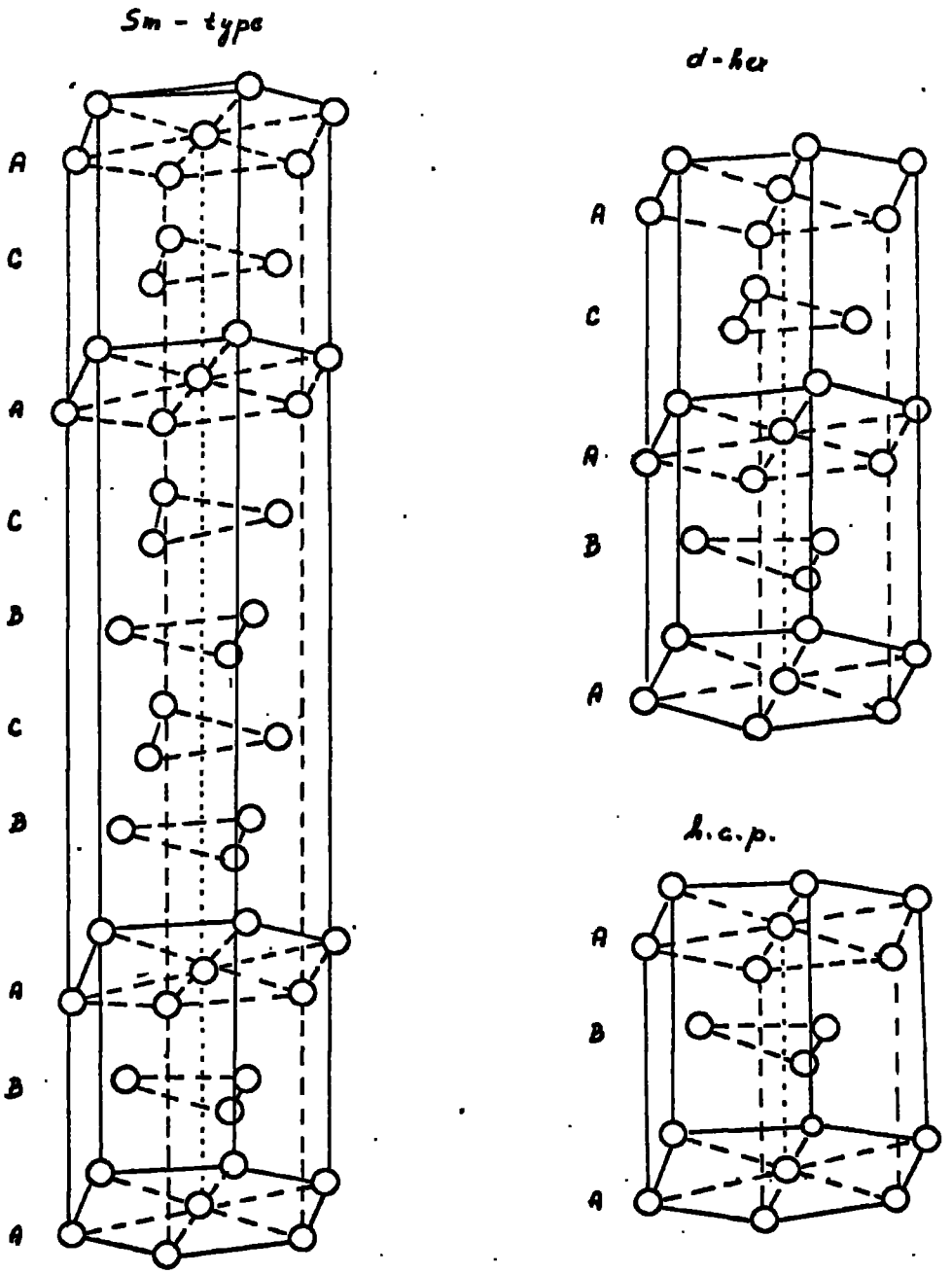

Fig. 3.1 Schematic representation of the crystallographic structures of the rare-earth metals in terms of three basic layers.

phase regions in the Nd-Y system. These existed over narrow (5-10%) concentration ranges surrounding the samarium phase. These are known to be a mixtures of the two adjacent phases, either Sm and d-hex or Sm and hcp depending on the alloy concentration. The lines of the X-ray powder diffractogram are broad in this phase and the intensities very sensitive to concentration and to both thermal and mechanical treatment. Indexing of the diffraction lines was always very difficult and sometimes impossible.

Very few structural characteristics of light-heavy rare earth alloys have been reported in the press. Speight et all (8) gave details for Pr- Tb, Chatterje and Taylor (9) included structural data for Dy-Nd in their discussion of the magnetic properties of these alloys. Varied systems have been studied by Lundin (10) particularly in the samarium phase. Structural properties of Y-Nd have also been published by Beaudry et all (7). Properties of the La-Dy alloys to our knowledge have been reported only for 10 and 20% of La, i.e. in hcp phase.by (18).

One of the studied structures (hcp structure) has the smallest volume of the primitive cell, fig 3.1. It is also the only one with simple a and c, lattice spacings corresponding to these structures. Its primitive cell may be considered to be formed from two basic stacking layers A and B. The stacking sequence being ABABA...

The Sm-phase has the biggest 'elementary' cell and can be viewed in terms of three different hexagonal stacking layers A,B and C ordered in nine layers sequence ABABCBCAC... The lattice parameters a and c change discontinuously

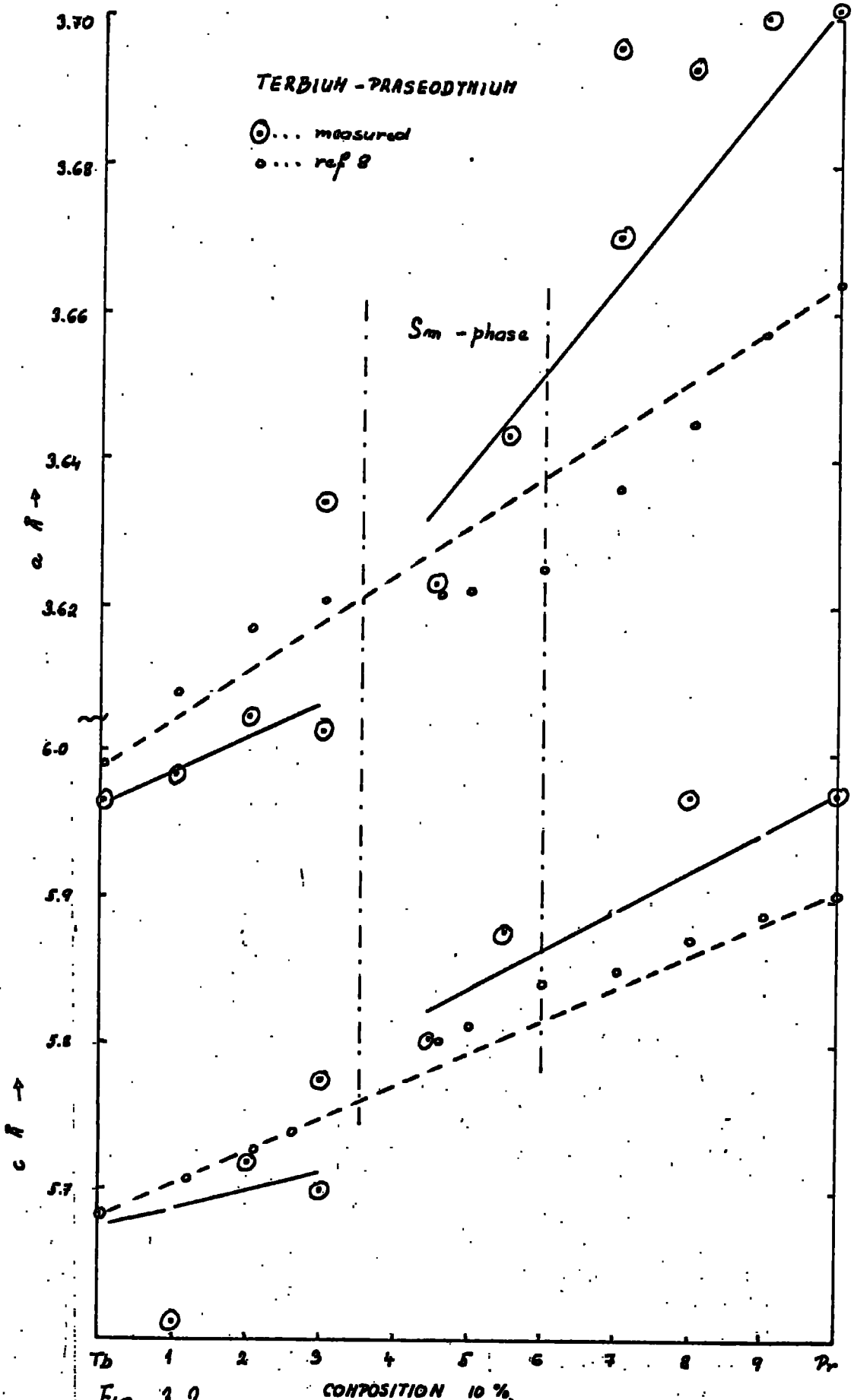

Fig. 3.2 Lattice parameters a and c of Tb-Pr.

between hcp and the Sm structure as well as between Sm and d-hex structure.

The d-hex structure is formed from two hcp primitive cells. They differ by means of a translation symmetry being applied on the central layer of the hcp primitive cell. Thus the d-hex structure could be viewed in terms of three different hexagonal stacking layers A,B and C ordered in a four layer sequence ABAC A ...

3.21 Praseodymium-Terbium system

The values for the lattice parameters a, c, axial ratios c/a (c/a for hcp, c/4.5a for Sm-structure, c/2a for d-hex structure) and atomic volume V determined by means of X-ray powder diffractometry (described in Chapter2) are consistent with the results obtained by Speight et all (8). The changes, especialy in a and c are somewhat bigger in the d-hex phase than those obtained by these workers, thus giving biger values of V, the volume of the primitive cell. The corresponding c/a values agree well with those previously reported suggesting that there has been a slight increase in overall cell size in our materials. This may result from a difference in the puruty of the starting materials..

Examining the behaviour of a with composition in the hcp phase, fig 32 most of the experimental values have a negative deviation from the ideal behaviour as represented by the straight line joining the a spacing of the pure elements whereas Speight's alloys showed a slight positive deviation even in the region of the hcp phase. The c values, fig. 3.2, seems to be consistent with those of Speight in the hcp and Sm phase and show a negative deviation from the ideal

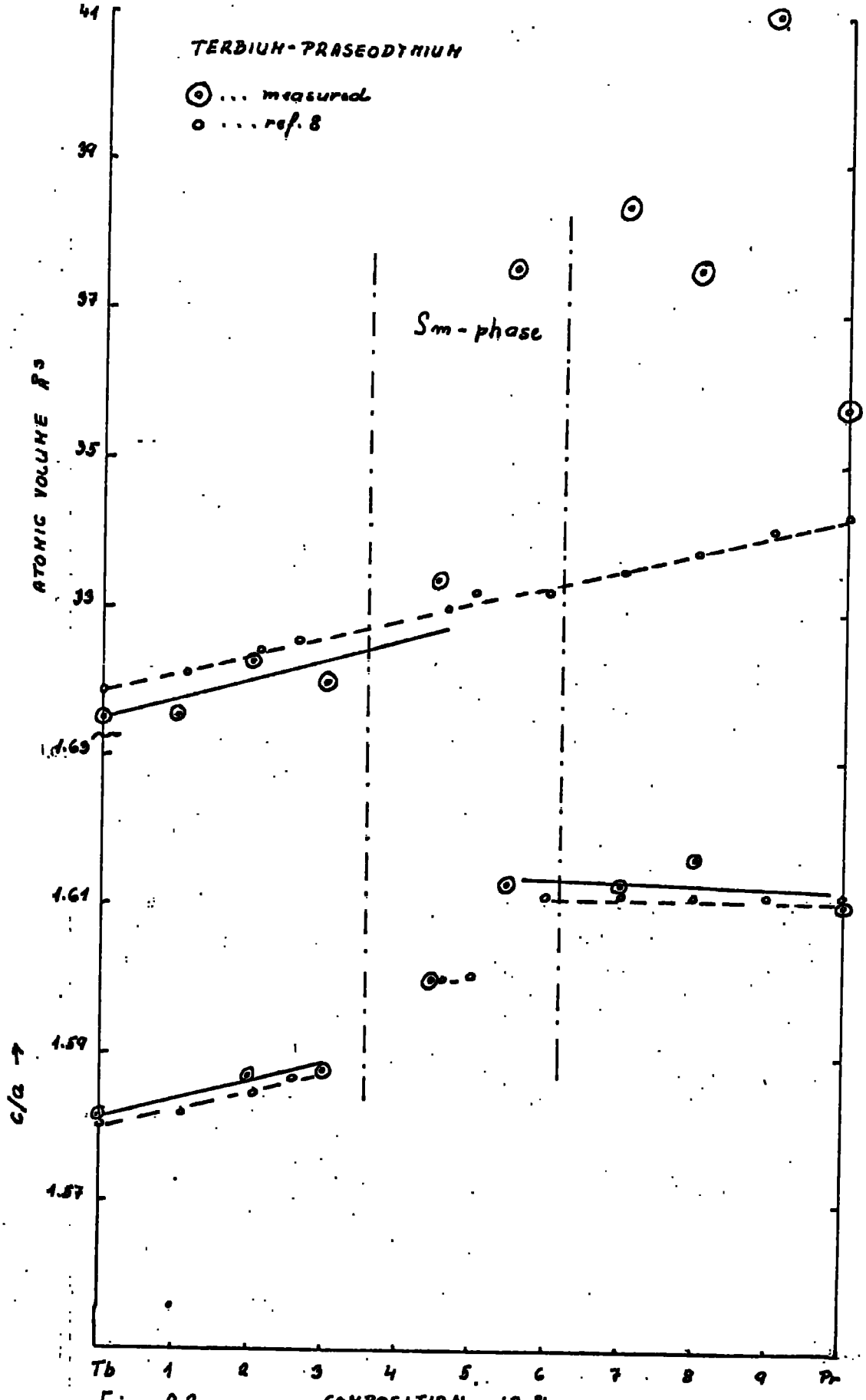

Fig. 3.3 Axial ratio c/a and atomic volume V of Tb-Pr.

behaviour as indicated in the table 3.1. In the d-hex phase they are, on average, 1-2% bigger than those reported by Speight. The behaviour of the axial ratio c/a, fig 3.3, is similar to that reported by Speight. In the hcp phase the experimental values deviate negatively from the ideal behaviour and positively in the Sm and d-hex phase. In the d-hex the ratio is nearly constant. The deviations from the values reported by Speight are best seen by looking at the experimental values for the atomic volume V, fig 3.3. The V values agree very well in hcp and Sm phase but the atomic volume reported here is greater than Speight's by some 13%.

For the explanations of these discrepencies one should look at the history of each particular specimen. It is known (11) that rare earth elements made by a different manufacturer generally show slightly different lattice spacings. The alloys reported in this work have been made from rare earth elements supplied by Koch-Light Laboratories whereas Speight's alloys were prepared from elements purchased from Messrs. Johnson, Matthey and Co.

Even though most of the examined alloys have been annealed for several days (or weeks) see Chapter 2, table 2.1, the metal filings from these were not annealed. Mechanical pressures induced when filing can induce another phase in the powder specially in the d-hex region and to a smaller extent in the Sm phase too as these are less stable than the hcp phase (12,13). Also the additional lines on the X-ray diffractograms could be explained this way.

This all stresses the

importance of the use of highly pure elements and phase-stabilized specimens for precise crystallographic study (12).

3.22 Neodymium-Dysprosium system

The structural (along with the magnetic and electrical) properties of this alloy have been examined in this laboratory (9,14). The samples reported in this study are mostly identical with those used for previous measurements and so their lattice spacings a, c, axial ratio c/a and atomic volume V are presented only in the summarising graph, fig 3.9. They generally display the same behaviour as discussed for other alloys which have or will be mentioned here.

3.23 Neodymium-Yttrium system

The values of the lattice parameters a, c, axial ratios c/a and atomic volume V measured for the purpose of this study are in reasonable agreement with the values reported previously by Beaudry at all (7). Beaudry also presented the phase diagram for this alloy, fig 3.4. From this and from table 3.2 the phase boundaries are defined in the following way: Y-Y_5Nd_5 is in the hcp phase. The parameter a and consequently the atomic volume V are smaller by approximately 1% than the alloys of a similar composition reported by Beaudry. According to the work of (7) Y_4Nd_6 should be a mixture of hcp and Sm-phase. When indexed (on Bunn chart) as the hcp phase the lattice parameters a and c seem more consistent with a and c for other compositions, than the corresponding a and c values when indexed as the Sm-phase. Y_3Nd_7 lies in the next region of mixed phases showing a tendency towards the d-hex phase. The data reported here and in (7) for d-hex phase agree very well. The discrepancy in the lattice

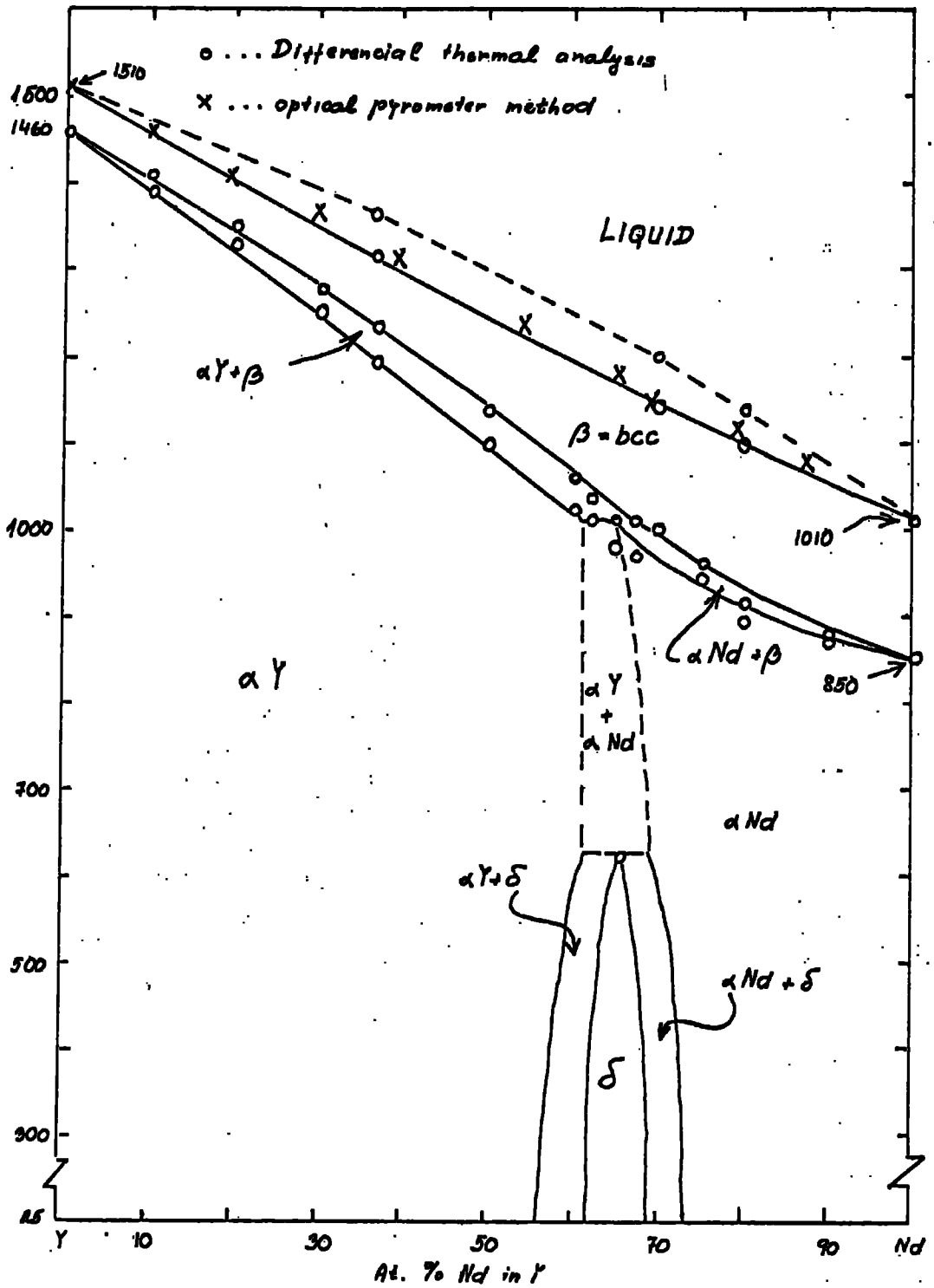

Fig. 3.4 Phase diagram Nd - Y

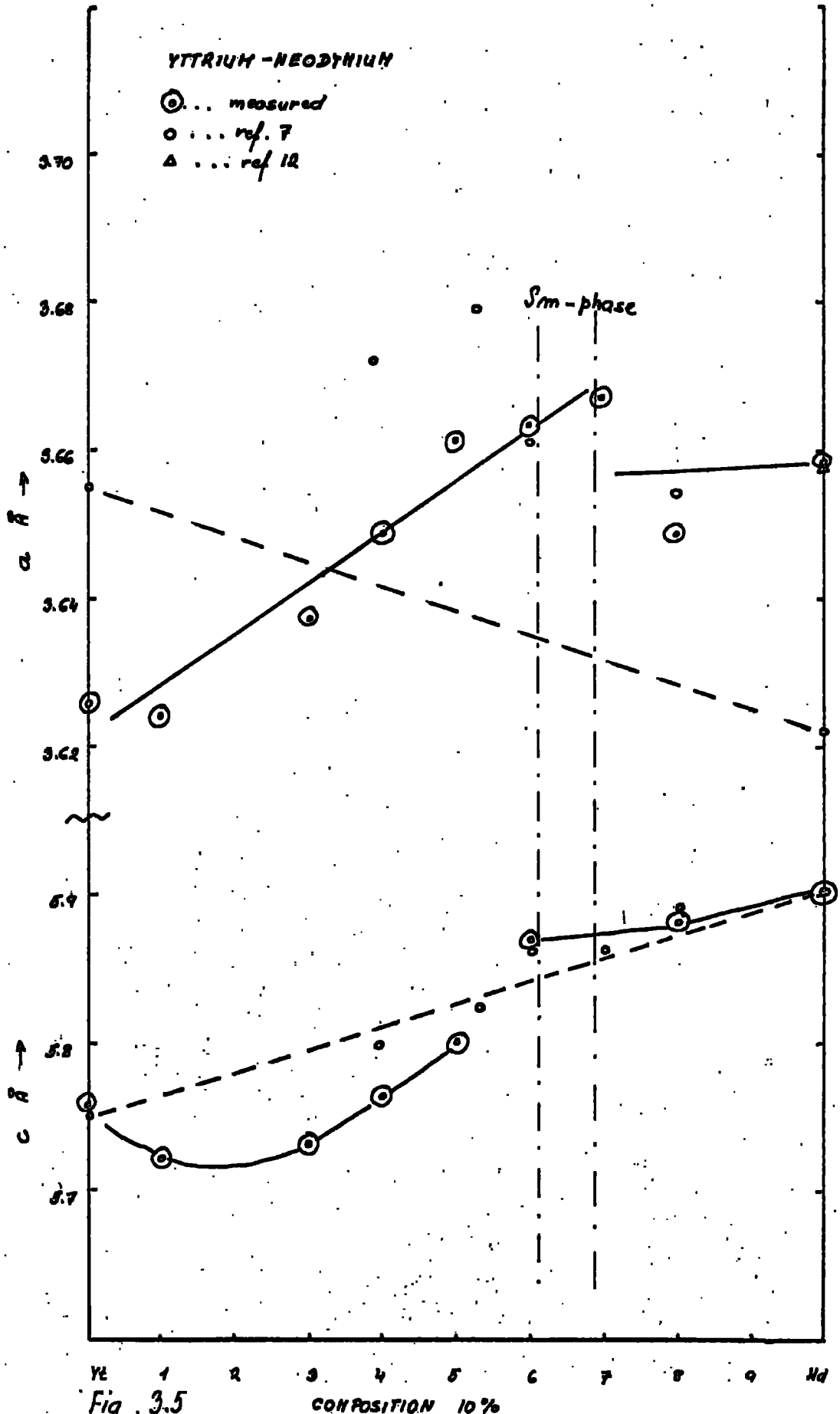

Fig. 3.5 Lattice parameters a and c of Y-Nd.

parameter values could again be explained if we make an allowance for the different manufactures of the pure elements and also slightly different thermal treatment of the cast samples. The alloys used by (7) were annealed under the following conditions: Y-Y_5Nd_5 at 950°C for 200 hours, Y_5Nd_5- Nd at 900°C for 20 hours. The samples used in this work were annealed at ~700°C for 74 days . The X-ray apparatus allowed them (7) to work in an atmosphere of inert gases, which is important especially for light rare earths, which are subject to easy oxidation; whereas this work was done in the open air. No evidence was found for oxide lines however in the present study.

The experimental values of a, fig 3.5, seem to have an overall positive deviation from the ideal curve. The c values, fig 3.5, show a negative deviation from the ideal curve in the hcp phase and positive in both the Sm and d-hex phases. The axial ratio c/a, fig.3.6, behaves in the same way as in Pr-Tb case, the hcp phase displaying a deviation in a negative direction while in the Sm and d-hex phases it is positive. In the latter case c/a seems to be almost constant. The atomic volume V shows, fig. 3.6, mostly a positive deviation from the ideal curve part from a part of the hcp phase. Again this is similar to the results for Pr-Tb described previously.

3.24 Lanthanum- Dysprosium system

This alloy has not been reported previously. From the behaviour of similar alloys mentioned above and elsewhere, it could be expected that this alloy would undergo phase changes as the composition is changed from La→Dy in the

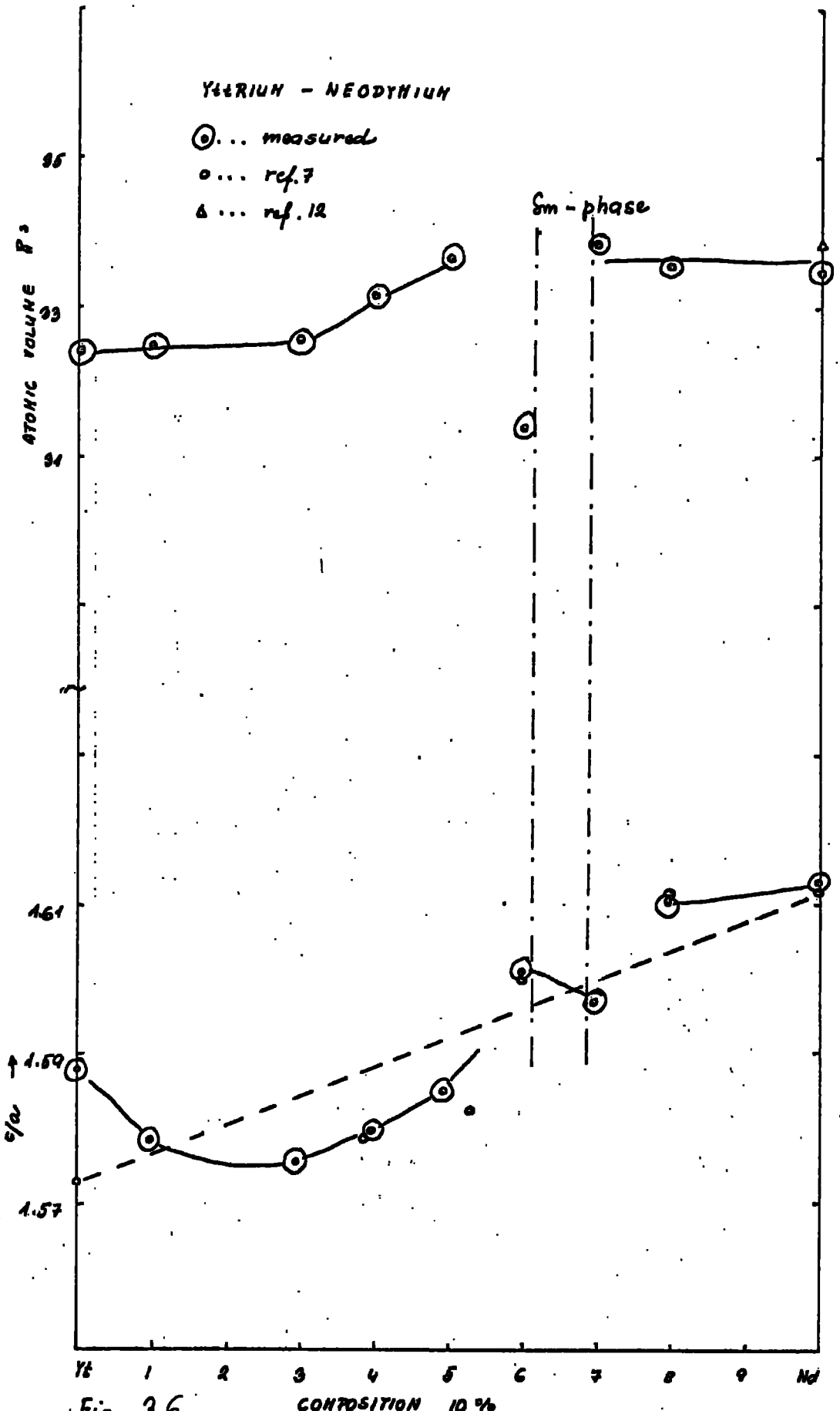

Fig. 3.6 Axial ratio c/a and atomic volume V of Y-Nd.

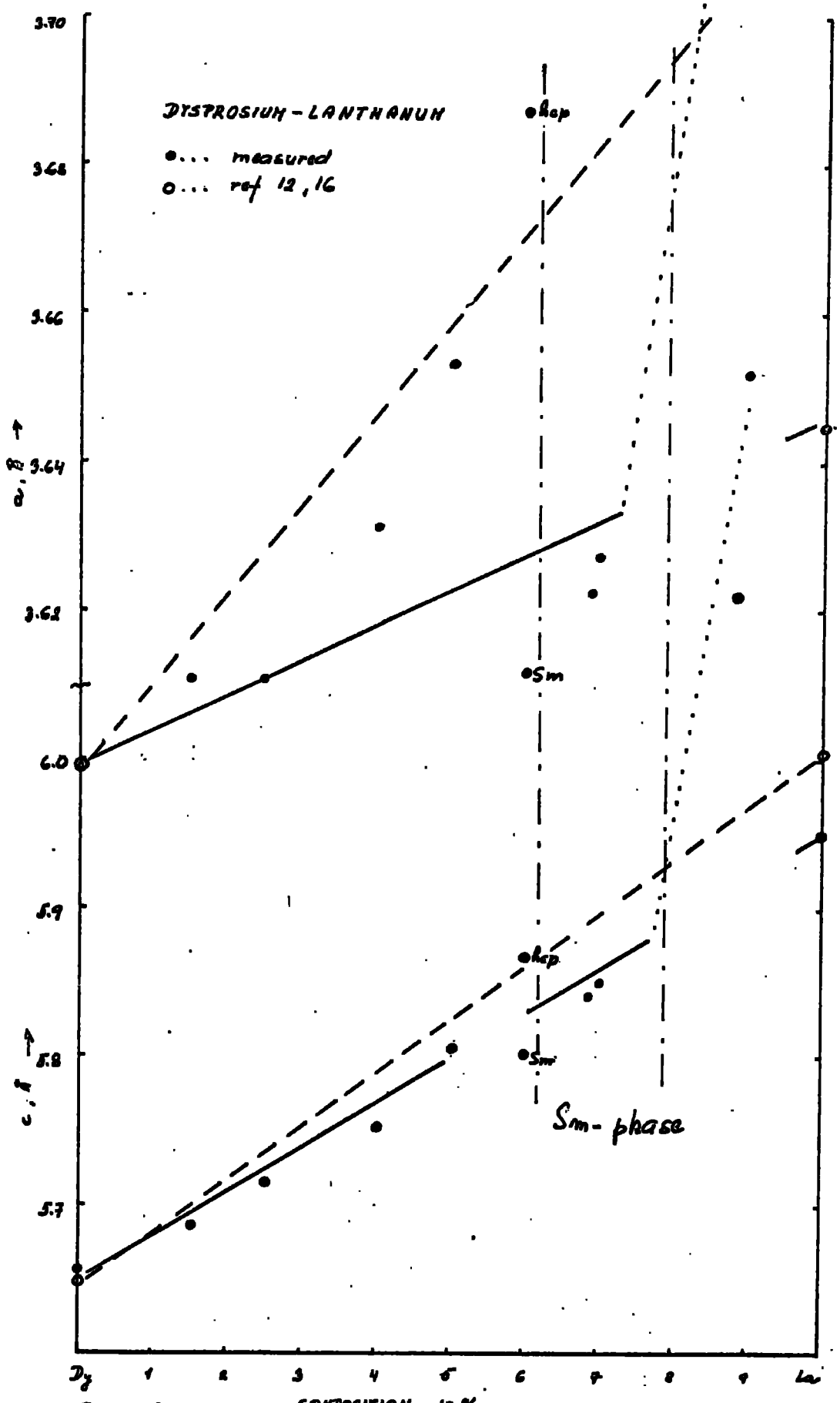

Fig. 3.7 Lattice parameters a and c of Dy-La.

sequence d-hex → Sm → hcp phase. The existence of each different phase is obvious (7,15) from the discontinuity of the c/a parameters: ⟨1.58⟩ for hcp, ⟨1.63⟩ for Sm phase and ⟨1.63⟩ for the d-hex phase, (measured in Å). Rough phase boundaries have been estimated from the X-ray powder diffractogramms at room temperature, see table 3.3. Dy_1La_9-La forms the d-hex phase at room temperature only when given a proper thermal treatment to stabilize d-hex phase and thus abolish the fcc structure. The bulk samples of the alloys used in this study have been annealed for 14 days at a temperatures of 290°C. This thermal treatment seems to be sufficient for the hcp and Sm phases but not for the d-hex phase as could be seen from comparison with the structural parameters of the pure elements measured previously (16,17,1,12,9,14) as well as with other inter rare earth alloys. Most likely the mechanical stress applied when filing could be sufficient to induce another phase even if the bulk sample has been previously annealed. The metal (alloy) filings require additional annealing especially when in the d-hex phase. The a and c values, fig. 3.7, vary in a similar way to the a and c values for Pr-Tb presented by Speight, apart from the d-hex phase as discussed above. The axial ratios c/a, fig 3.8, deviate negatively in hcp phase and follow the ideal curve in the Sm phase. They are probably constant in the d-hex phase as in the case for other alloys mentioned above.

3.25 Conclusion

It seems to be rather a general rule, as pointed out for the particular cases mentioned above and other results published in literature for inter rare earth alloys, that:

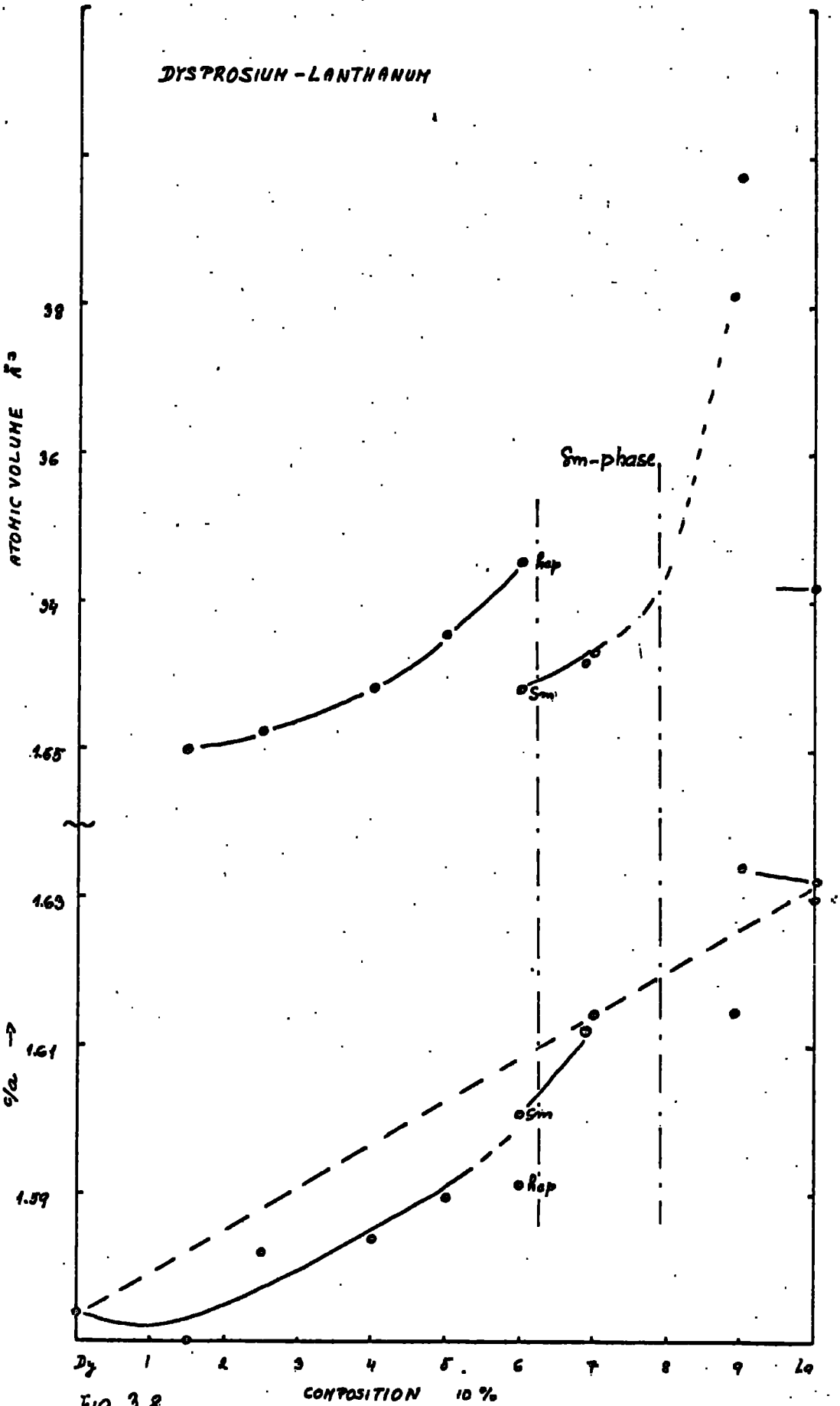

Fig 3.8

Axial ratio c/a and atomic volume V of Dy-La.

1) They, like the pure elements withthe exeption of Ce, Eu, and Yb), exist in the three different crystallographic phases forming a sequence, from light to heavy rare earths, d-hex → Sm-type → hcp.

2) The stability of the crystal structure, when subjected to a mechanical or thermal treatment, seems to decrease with increasing atomic volume.

3) It is consequently necessary to take great care to thermaly stabilize the d-hex phase as a basis for reliable results when the X-ray powder method is used. This can be seen from the difference in results for Y-Nd alloy which was well thermally stabilized (annealed for a long period) and results in d-hex phase of La-Dy alloy, which was annealed for a considerably shorter period and so did not ensure phase purity (18).

4) The value of the a parameter changes discontinuously at phase boundaries.

5) The c values lie close to the ideal curve, connecting the c values of pure elements.

6) The values of the axial ratios c/a lie below the ideal curve in hcp phase, close to it in the Sm-phase and remain constant, at the value of the pure light elements in the d-hex phase.

7) The atomic volume V should closely follow the ideal line.

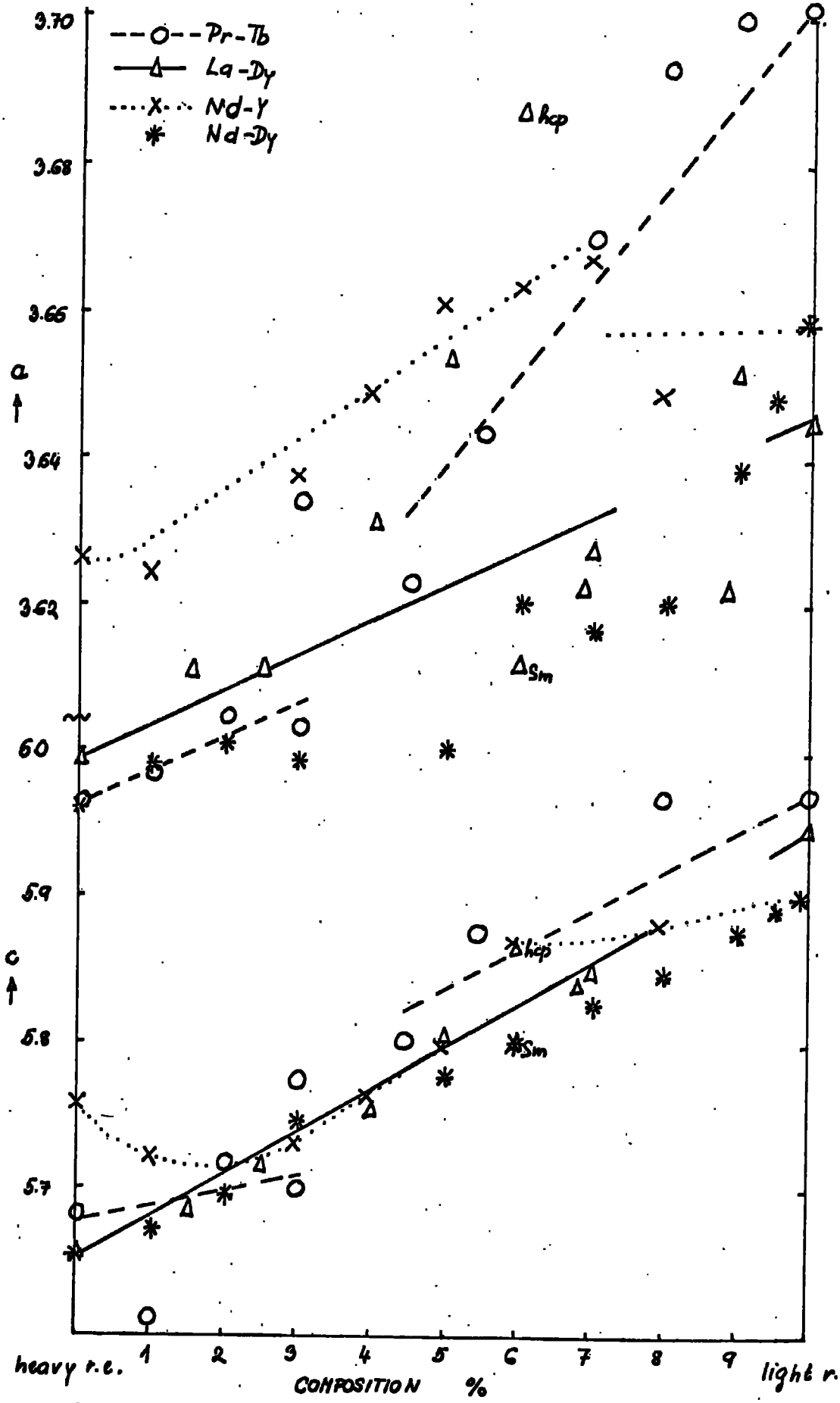

Fig 3.9a Lattice parameters a and c of some light-heavy rare earth alloys.

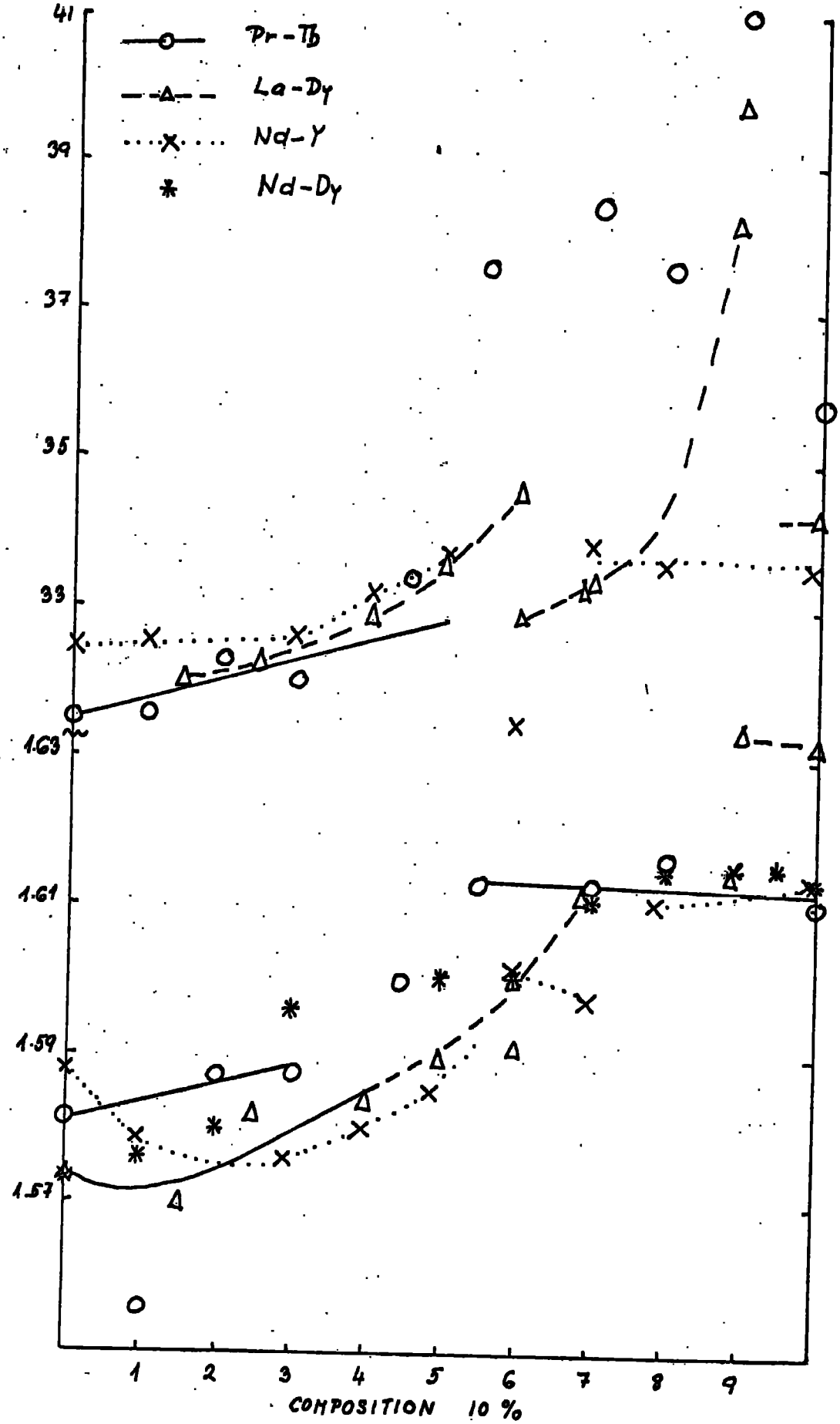

Fig. 3.9b Axial ratio % and atomic volum V of some light - heavy rare earths.

Tb_xPr_{1-x}	a (Å) ±0.005	c (Å) ±0.005	c' (Å)	c/a ± 0.01	c'/a	V $(Å)^3$
1.0	3.5938	5.6837		1.5815		32.503
0.9	3.5972	5.6098		1.5595		31.550
0.8	3.6047	5.7206		1.5869		32.301
0.7	3.6029	5.7012		1.5878		32.000
0.67	3.6391	11.7394	5.8697	3.2259	1.6129	33.659
0.55	3.6235	26.1237	5.8052	7.2088	1.6021	33 418
0.45	3.6436	11.7562	5.8780	3.2265	1.6132	37.652
0.3	3.7050	12.9603	6.4801	3.4980	1.7490	38.466
0 2	3.6937	11.9415	5.9707	3.2329	1.6164	37.600
0.1	3.7016	13.3244	6.6622	3.4866	1.7432	42.133
0.0	3.7140	11.9448	5.9724	3.2216	1.6108	35.732

Table 3.1 Lattice parameters of Tb-Pr alloys.

Y_xNd_{1-x}	a(Å) ±0.005	c(Å) ±0.005	c'(Å)	c/a ±0.01	c'/a	V (Å)³
1.0	3.6259	5.7589		1.5883		32.450
0.9	3.6239	5.7206		1.5785		32.500
0.7	3.6377	5 .7311		1.5755		32.600
0.6	3.6489	5.7648		1.5798		33.230
0.5	3.6607	5.8046		1.5856		33.680
0.4	3.6840	5.8295		1.58236		34.250
	3.6332	26.3565	5.8700	7.2541	1.6120	31.400
0.3	3.6710	26.3844	5.8632	7.1889	1.5975	33.890
0	3.6553	11.8197	5.9098	3.2336	1.6168	34.055
0.2	3.6484	11.7609	5.8804	3.2235	1.6177	33.860
0.0	3.6580	11.8000	5.9000	3.2260	1.6130	33.585

Table 3.2 Lattice parameters of Y-Nd alloys.

Dy_xLa_{1-x}	a(Å) ± 0.005	c (Å) 0.005	c'	c/a ± 0.01	c'/a	V (Å)³
1.0	3.5920	5.6550		1.5740		
0.85	3.6108	5.6860		1.5703		32.060
0.75	3.6110	5.7150		1.5826		32.270
0.6	3.6315	5.7529		1.5841		32.850
0.5	3.6534	5.8071		1.5895		33.580
0.4	3.6872	5.8694		1.5918		34.550
	3.6119	26.1257	5.8050	7.2379	1.6084	32.820
0.31	3.6225	26.2863	5.8414	7.2562	1.6124	33.190
0.3	3.6275	26.3301	5.8510	7.2641	1.6143	33.370
0.11	3.7896	12.2369	6.1185	3.2291	1.6145	38.141
0.1	3.8199	12.5210	6.2605	3.2682	1.6341	39.790
0.0	3.6445	11.8977	5.9488	3.2645	1.6323	34.215

Table 3.3 Lattice parameters of La-Dy alloys.

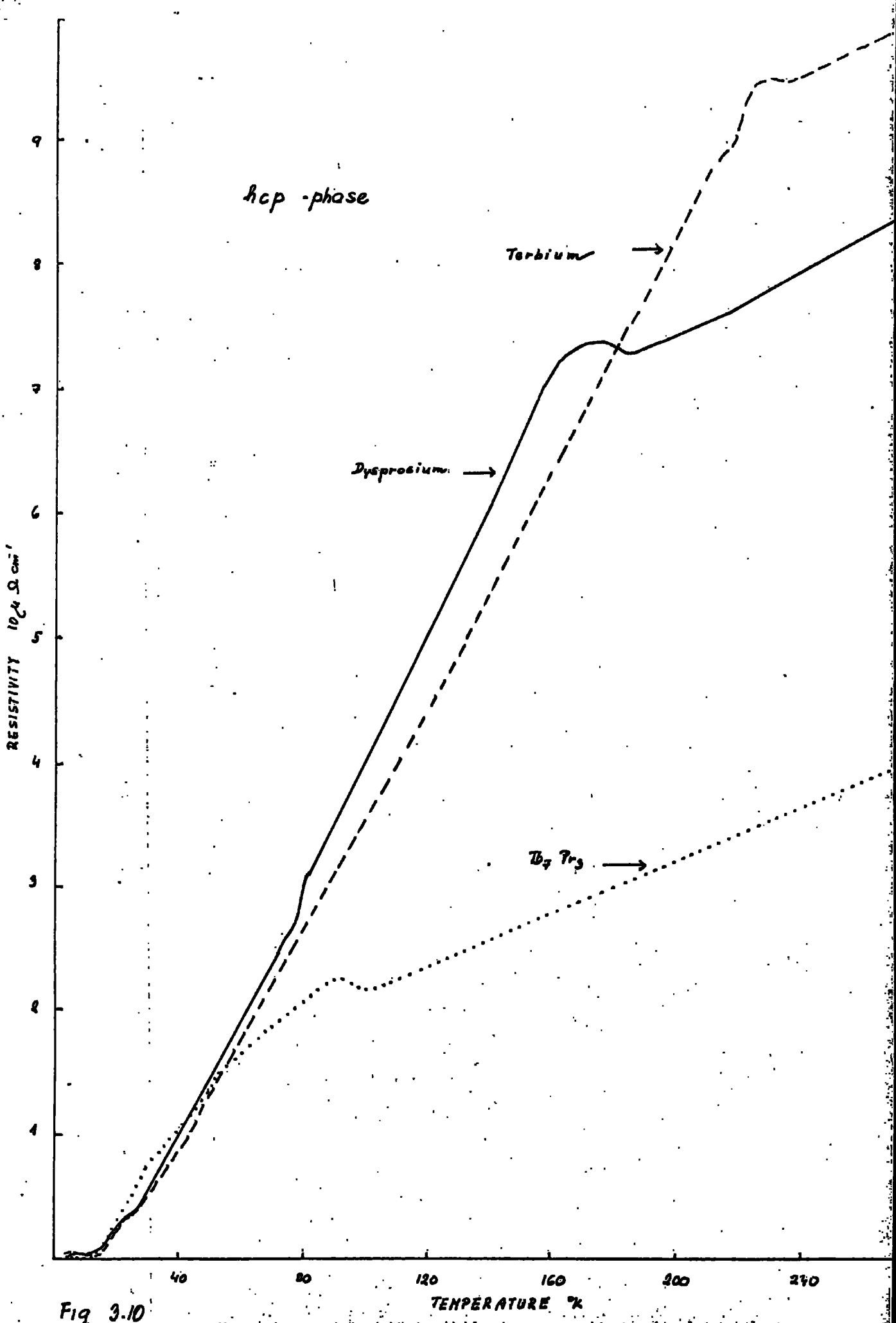

Fig 3.10 Resistivity variation with temperature in hcp phase.

3.3 Resistivity

The resistivity of the four light-heavy inter-metalic series of alloys, La-Dy, Nd-Dy, Nd-Y, Pr-Tb, have been measured in the temperature region ~2.7°-400°K using the experimental methods described in Chapter 2. The results of the measurements in the form of the resistivity variation with temperature for the four series are described in the following. The observed variations for the series studied have many features in common apart from some obvious variations which will be pointed out later when discussing each particular series.

3.31 The general behaviour

The hcp phase: The resistivity behaviour for all the alloys containing heavy rare earth in the hcp structure is similar. The observations can be devided into three clearly distinguishable regions:

1) 0-20°K where the residual resistivity dominates and in which the measured resistivity could be regarded as temperature independant.

2) ~20°K- the Néel point T_N. This temperature region is characterized by a sharp increase of the resistivity with temperature mainly due to the growth of a spin diorder resistivity contribution ρ_s, but also due to the increasing phonon resistivity ρ_{phonon}. These two resistivity contributions in this temperature region are very difficult to separate. Within the pattern described, some variety still remains in the observed resistivity behaviour for particular cases as shown for example in fig3.10. The increase in the anti-ferromagnetic region is not so rapid as that found in the

Fig 3.11 Resistivity variation with temperature in Sm-phase.

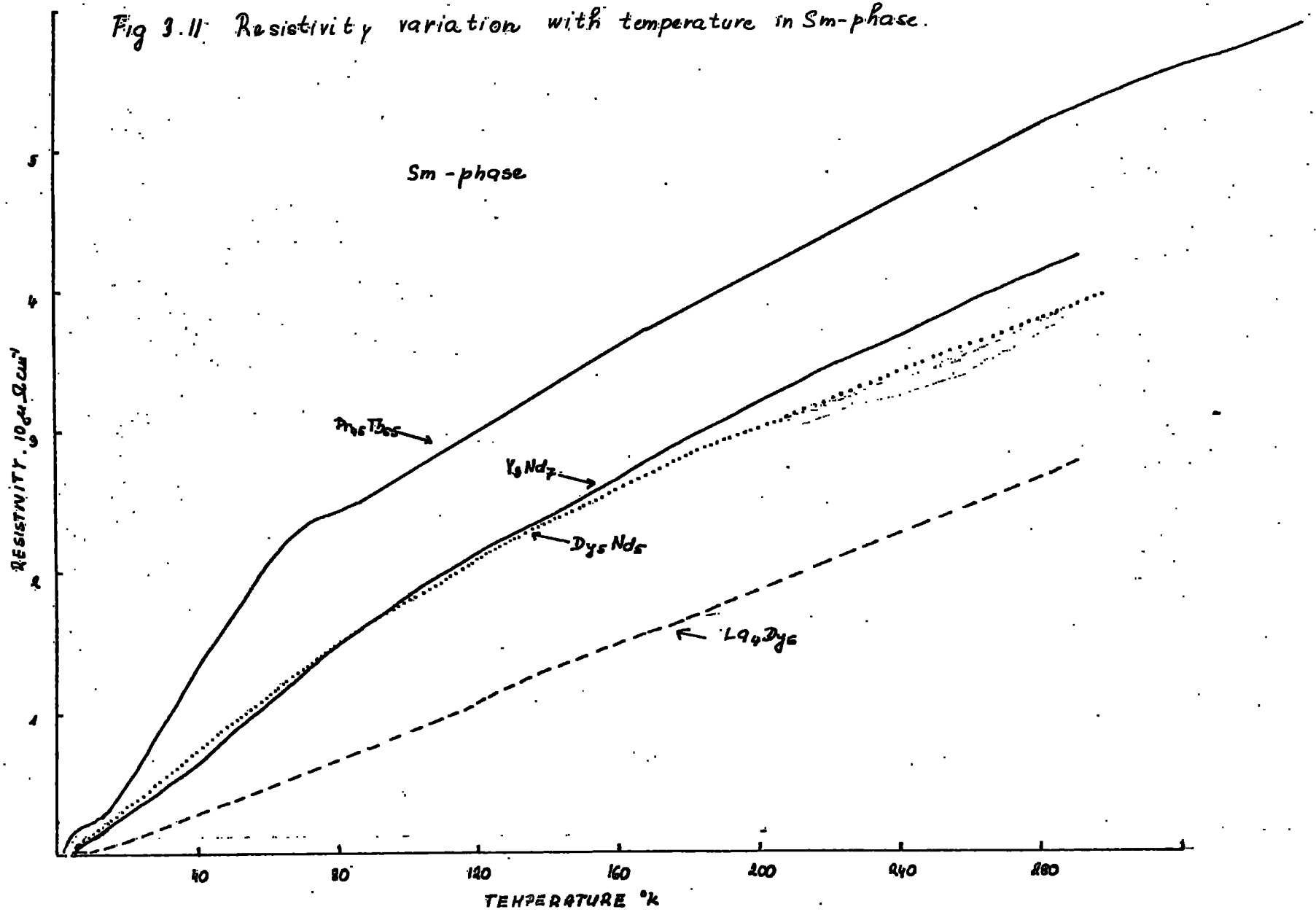

ferromagnetic region. Near T_N the resistivity reaches a maximum which is followed by a shallow minimum covering some 10-30° in the temperature region in which the metal is known to be in the paramagnetic phase from magnetic measurements (21,1-28-9). It seems most likely that short range ordering is responsible for this resistivity decrease.

3) The paramagnetic phase ($T>T_N$) is characteristic by a linear increase for which one can assume that all the temperature dependance is associated with phonon scattering. ρ_{phonon} is generally accepted to be linear with temperature above the Debye temperature T_D which is of the order of 180°K for the metals studied(1-19,20). The difference $\rho_{300°K} - \rho_{4.2°K}$ generally decreases with an increase of light rare earths content in all the alloys in the hcp phase.

All the anomalies connected with phase transitions are well defined on the resistivity curve and are in general in reasonable agreement with those reported on the basis of magnetic measurements. The transition temperatures are given in tables 3.5, 3.7, 3.9, 3.11.

Sm-phase: This narrow concentration range can be characterized in some of the cases in a similar way to the hcp phase. Usually the resistivity curve is divided into temperature regions. Sometimes the division is less obvious and in a few cases it vanishes altogether, see fig 3.11. The Néel point T_N, defined from the resistivity as that temperature at which an anomaly or abrupt gradient change is seen, does not agree well with the T_N observed in the magnetic measurements. In most of the cases $(T_N)_{resist} < (T_N)_{mg}$ suggesting some discrepancy in the definition of $(T_N)_{resist}$

Fig. 3.12 Resistivity variation with temperature in d-hex phase

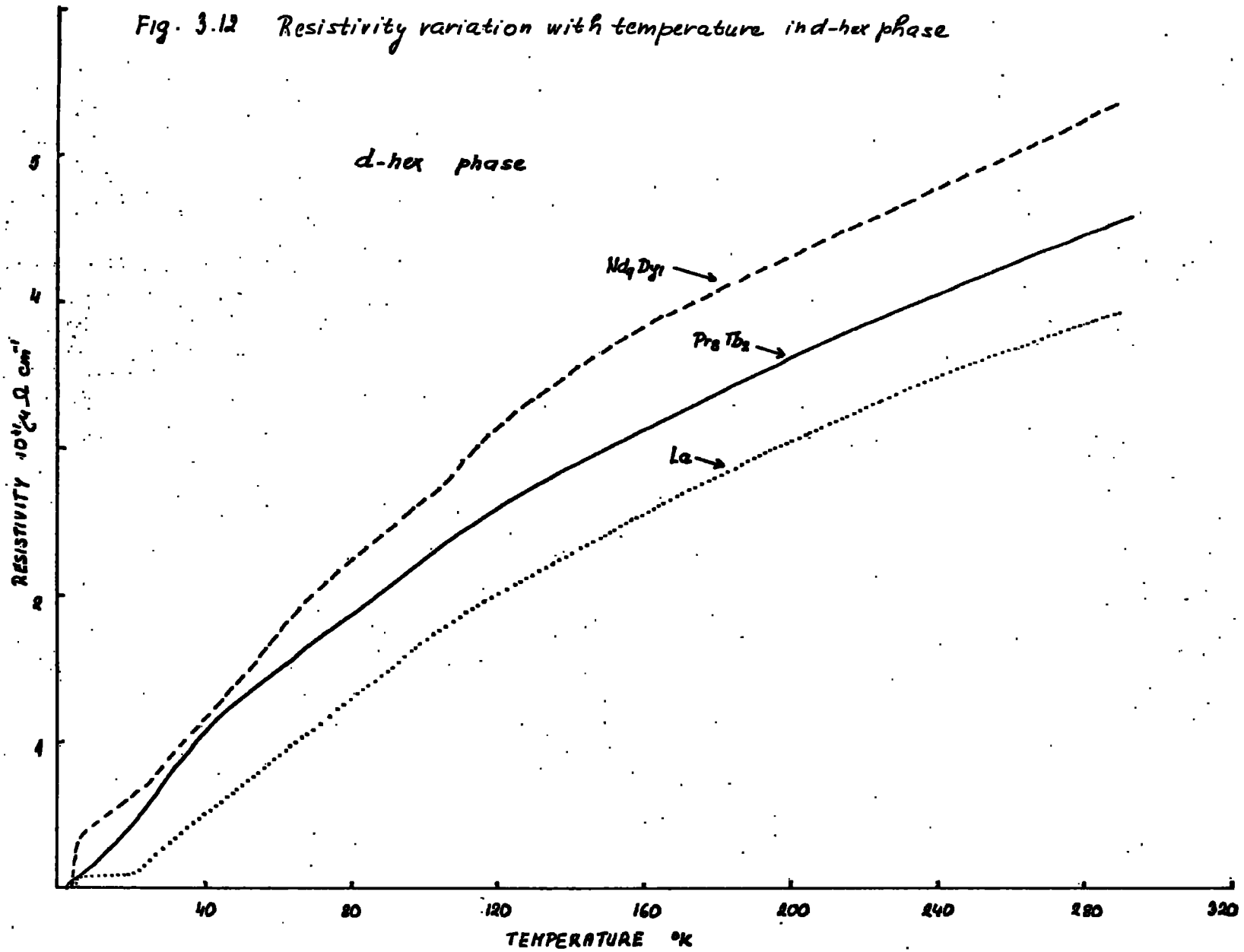

which will be discussed later.

d-hex phase: The resistivity variation with temperature in this phase could be described as a convex upwards curve from ~30°K onwards as shown in fig.3.12 This is supported by measurements done by (1-13) up to the transition temperature for the majority of the light rare earths. The low temperature behaviour can be shown to fit a T^2 dependance and in cosequence ρ_{res} is difficult to estimate and has been taken here to be identical with $\rho(4.2°K)$. The difference in the resistivity behaviour for different alloy systems in this temperature region are caused by the presence or absence of magnetic ordering (Nd, Pr), for discussion see (1-37), or superconducting transitions (La) in the specimens. Above 30°K there is no obvious anomaly on the resistivity curve for any material even though the $d\rho/dT$ vs T is not a monotonic curve, fig.3.13-16 The difference in the overall form of the resistivity variation with temperature, we believe, is mainly dependent on the distribution of crystal field levels (1-44,14,36) in each particular alloy as will be discussed in the later chapters.

3.4 Specific alloy systems

3.41 Praseodymium-terbium

hcp phase: The resistivity variation of the pure Tb and Tb with 10% of Pr are very similar, fig. 3.13. The temperature independant residual resistivity ρ_{res} of Tb covers a relatively wide temperature range ,~20°K, whereas ρ_{res} of Tb_9Pr_1 as well as the ρ_{res} of other alloys in the hcp phase extends only over about 10°K. The temperature region immediately following the temperature independant ρ_{res} region is

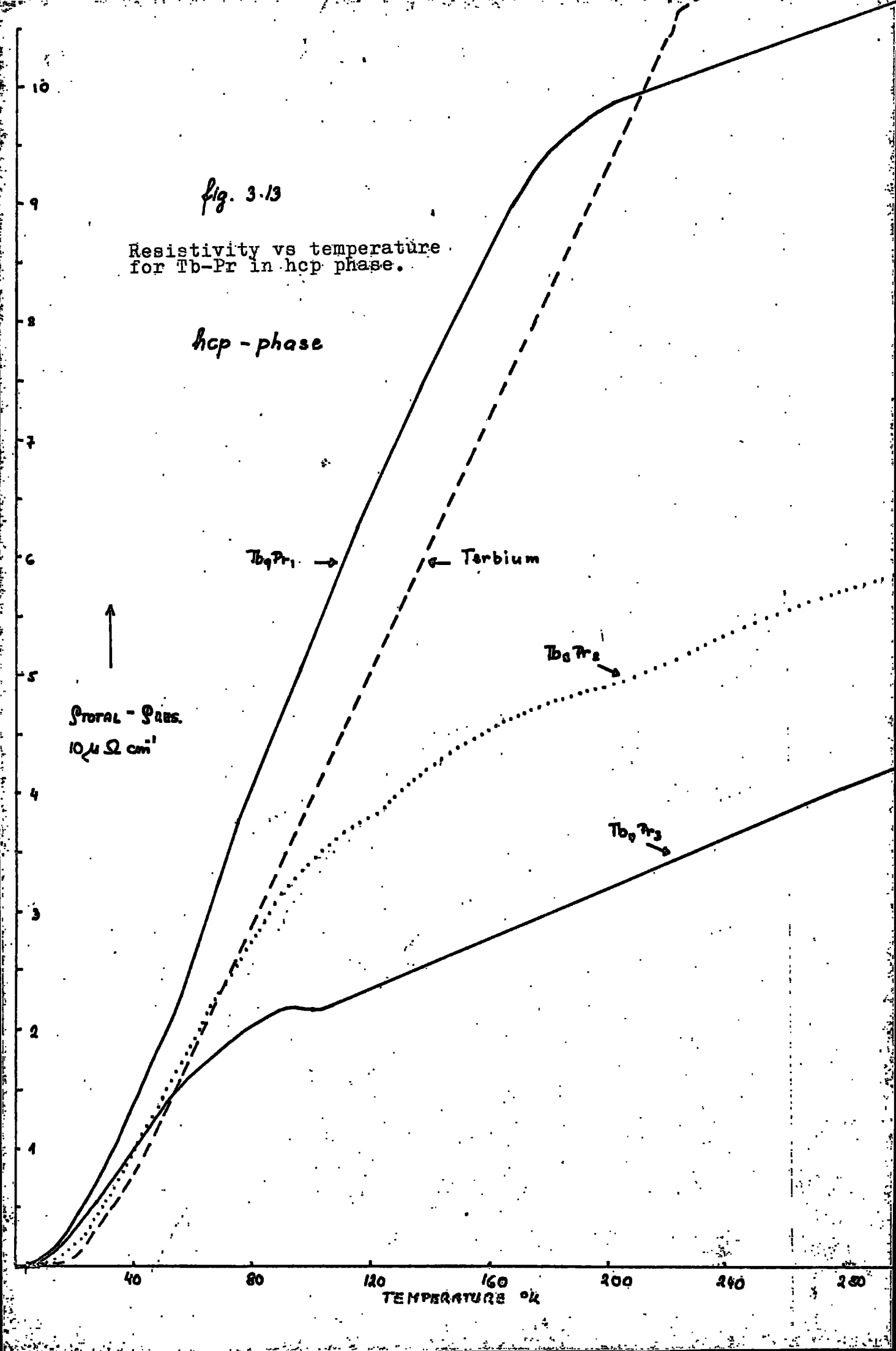

fig. 3.13

Resistivity vs temperature for Tb-Pr in hcp phase.

hcp - phase

characterized by a sharp increase of resistivity as a power law in temperature, $\rho \propto T^n$, the coefficients n being given in table 3.4. This behaviour continues to the temperatures close to the ordering temperature T_{N1} and is followed by a small region showing relatively little change in resistivity until the upper temperature T_{N2} is reached. Above T_{N2} there is a shallow resistivity minimum suggesting that short range order or superzones effects are important in the paramagnetic region close to the ordering temperatures. The resistivity increase in the higher temperature region is essentially linear and values of $d\rho/dT$ are given in table 3.4.

Only one transition temperature could be distinguished clearly on the curve of Tb_9Pr_1 which is in agreement with the results of the magnetic measuremens performed on the same samples (1-29). The sharp gradient change near T_N becomes less obvious with increasing Pr content and covers a much bigger temperature region especially in Pr_2Tb_8, fig. 3.13, between 85-168°K. The spin disorder resistivity decreases very sharply with composition, table 3.5, fig. 5. Generally the variation becomes more curved below T_N with increasing Pr content.

Sm-phase: On the resistivity curve for $Pr_{45}Tb_{55}$ can be seen all the three regions mentioned above, fig. 3.14. On adding 10% more of Pr the transition between the para and antiferromagnetic phase becomes very broad and T_N is difficult to define from the resistivity measurements. This is perhaps some evidence for an early collapse of the long range ordering, replaced by a short range ordering over a broad temperature range, which could be a reason for the difference

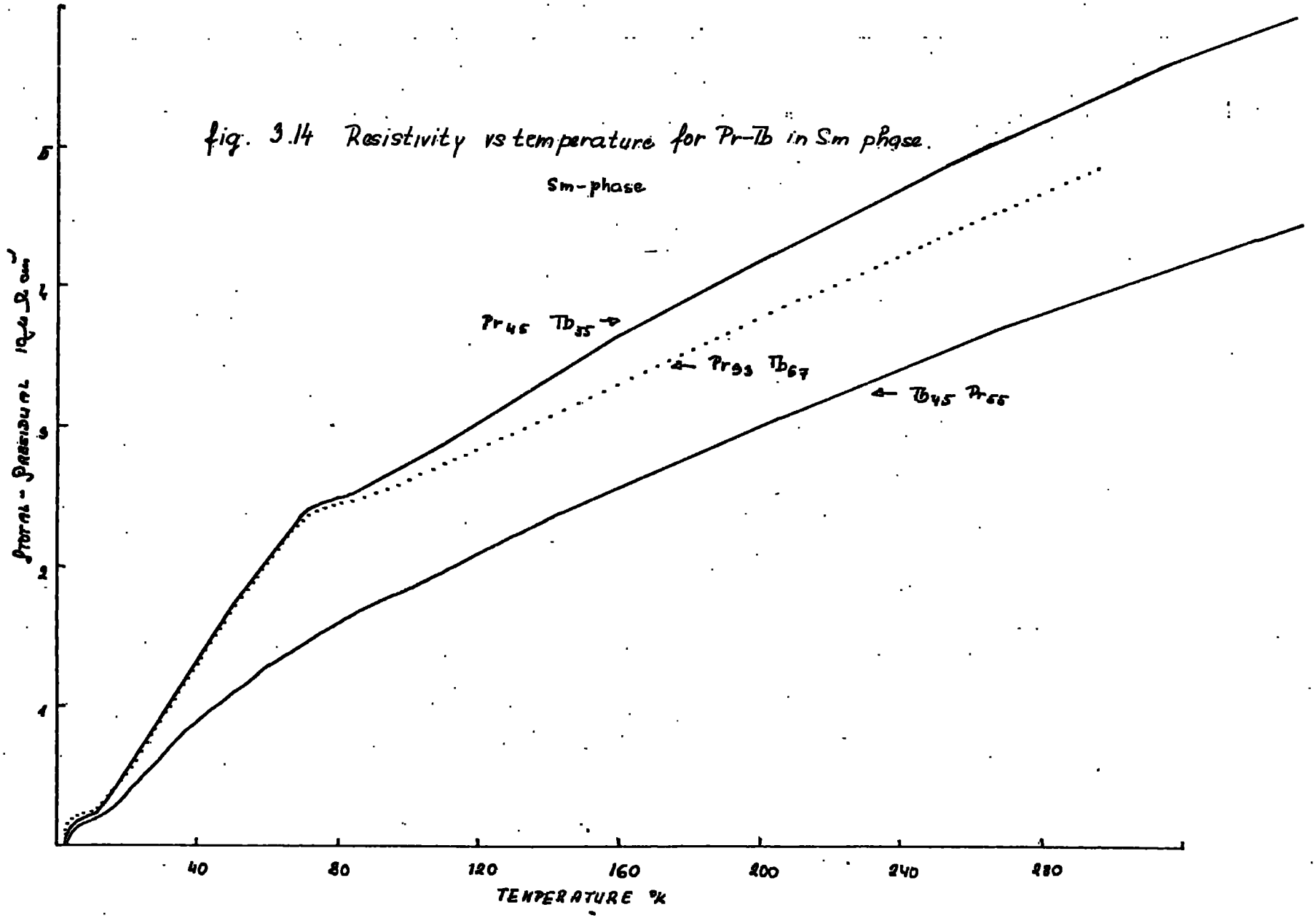

fig. 3.14 Resistivity vs temperature for Pr-Tb in Sm phase.

between $(T_N)_{resist.}$ and $(T_N)_{mag.}$. In the latter composition the temperature dependent part of the resistivity makes the smallest contribution to the total resistivity of all the alloys in this series. The resistivity curves for $Pr_{55}Tb_{45}$, in the Sm phase, and Pr_7Tb_3, in the d-hex phase are rather similar, however the scattering mechanisms involved should be different as $Pr_{55}Tb_{45}$ is known to be magnetically ordered ($T_N \sim 80^oK$ as follows from magnetic measurements) while there is no evidence in ρ vs T observations for magnetic ordering in Pr_7Tb_3. The curved ρ - T variation occurs in this latter case because of the presence of strong crystal field effects which are comparable to or greater than the exchange energy in this alloy.

d-hex phase: At very low temperatures the resistivity is strongly temperature dependent ($\rho_{res} \sim T^n$, where $n>1$), fig.3.15. The n is biggest for pure Pr and decreases with increasing Tb content but does not become constant for any composition in the d-hex phase. The temperature variation $d\rho/dT$ increases, especially in the region of low temperatures, with inceasing Pr concentration so that Pr forms a covering curve to all others in this phase, see fig.3.15. This is consistent with the changes in the crystal field levels with composition (1-36), discussed later. No obvious anomalies suggesting magnetic ordering have been detected for temperatures above 2.7^oK. A summary of some of the parameters derived from the resistivity curves just described is presented in the tables 3.4, 3 5.

3.42 Low temperature resistivity

From the enlarged graph of the resistivity between 2.7^oK

fig. 3.15 Resistivity vs temperature for

PRASEODYMIUM - TERBIUM in d-her

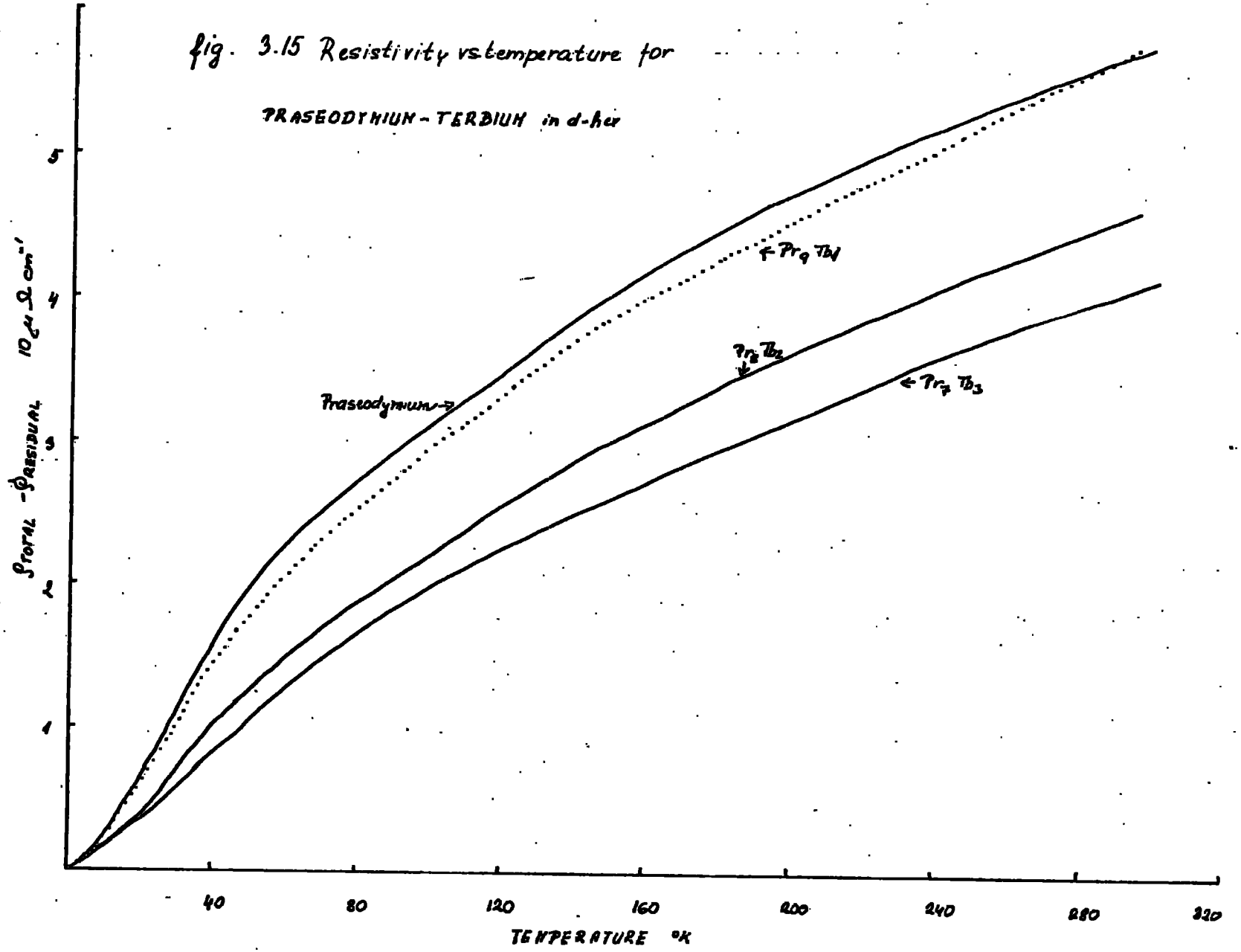

fig. 3.16 Resistivity vs temperature, between 0-40°k for Tb-Pr in d-ha phase.

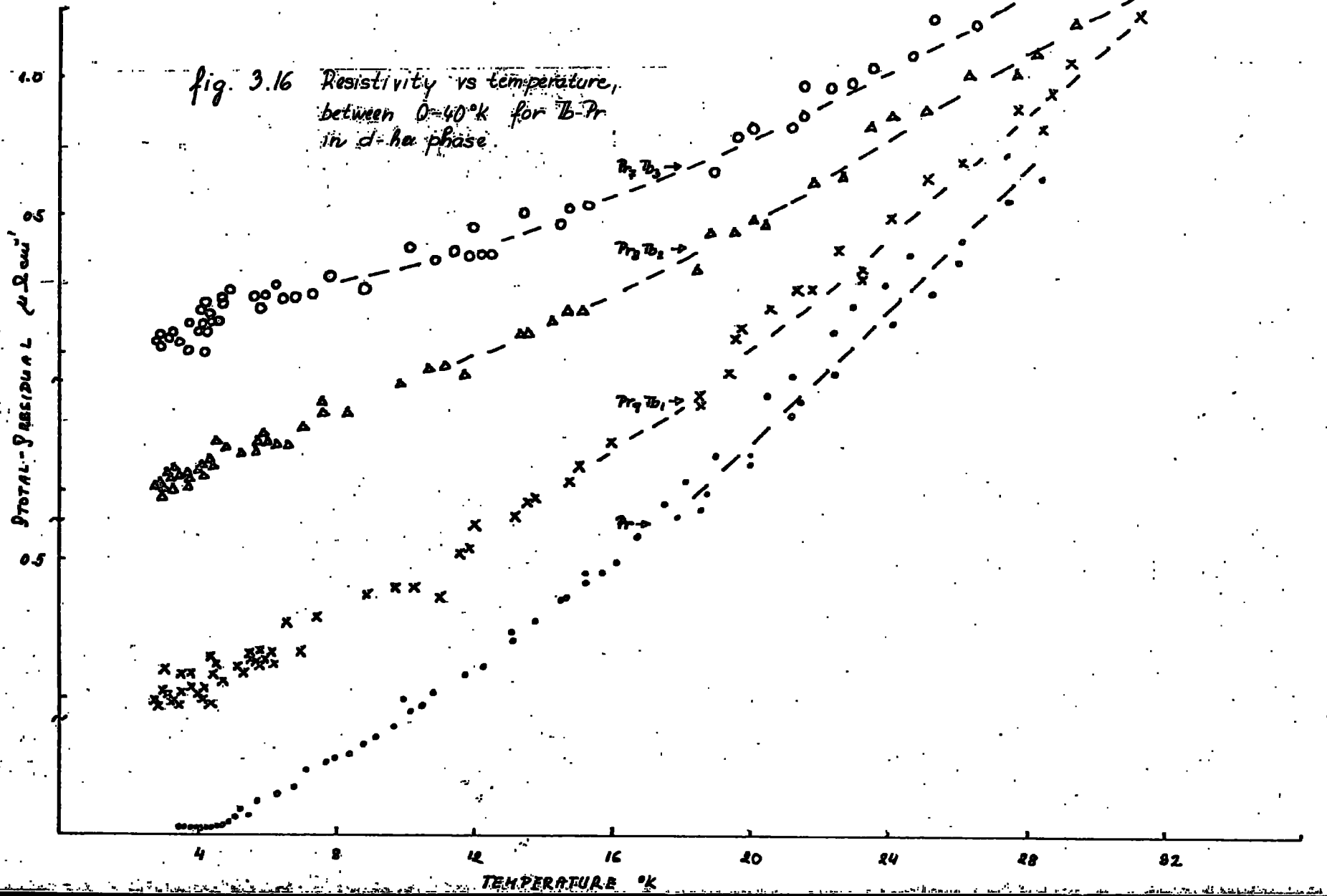

fig. 3.17 Resistivity vs temperature, between 0-40°K, for Tb-Pr in Sm-phase.

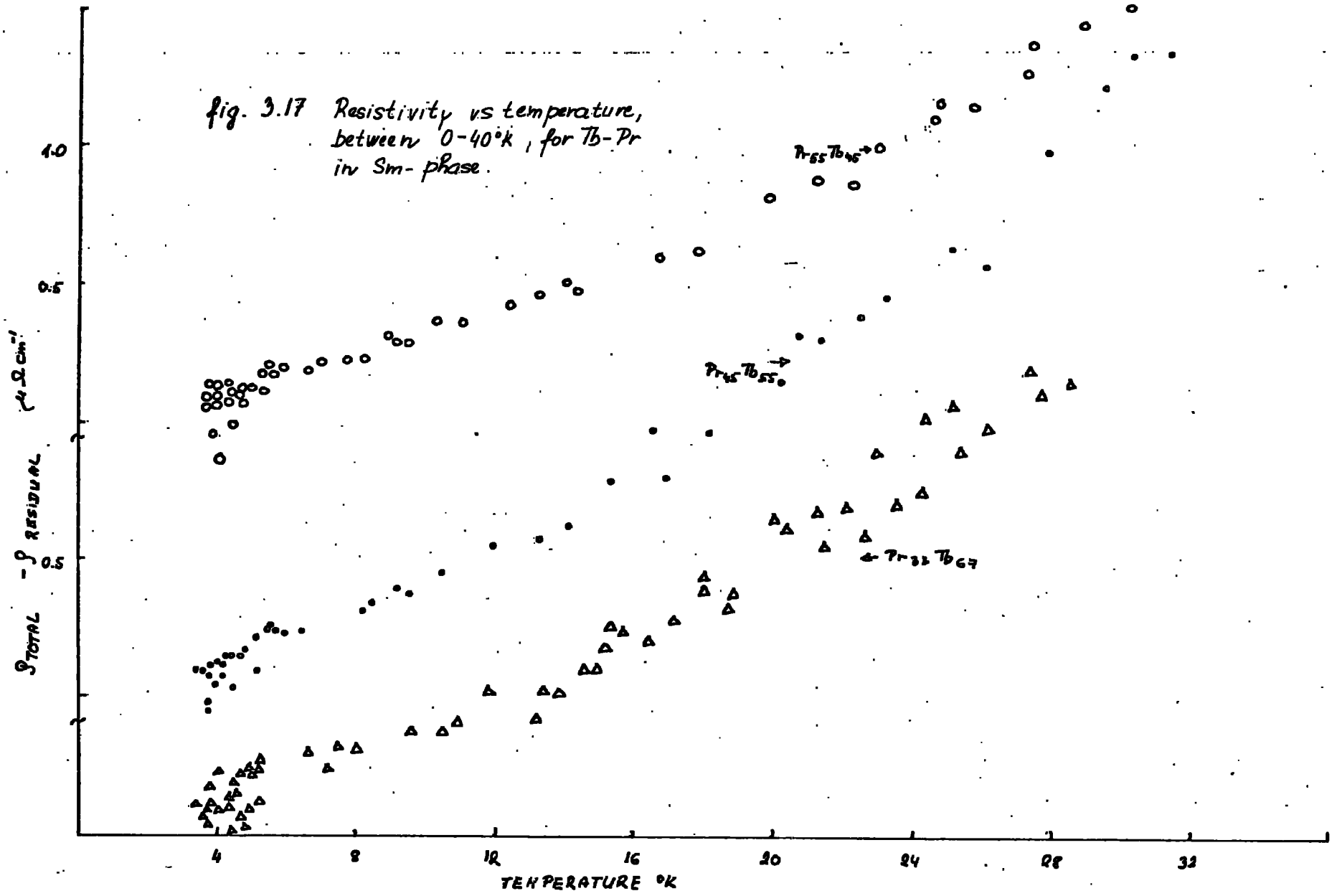

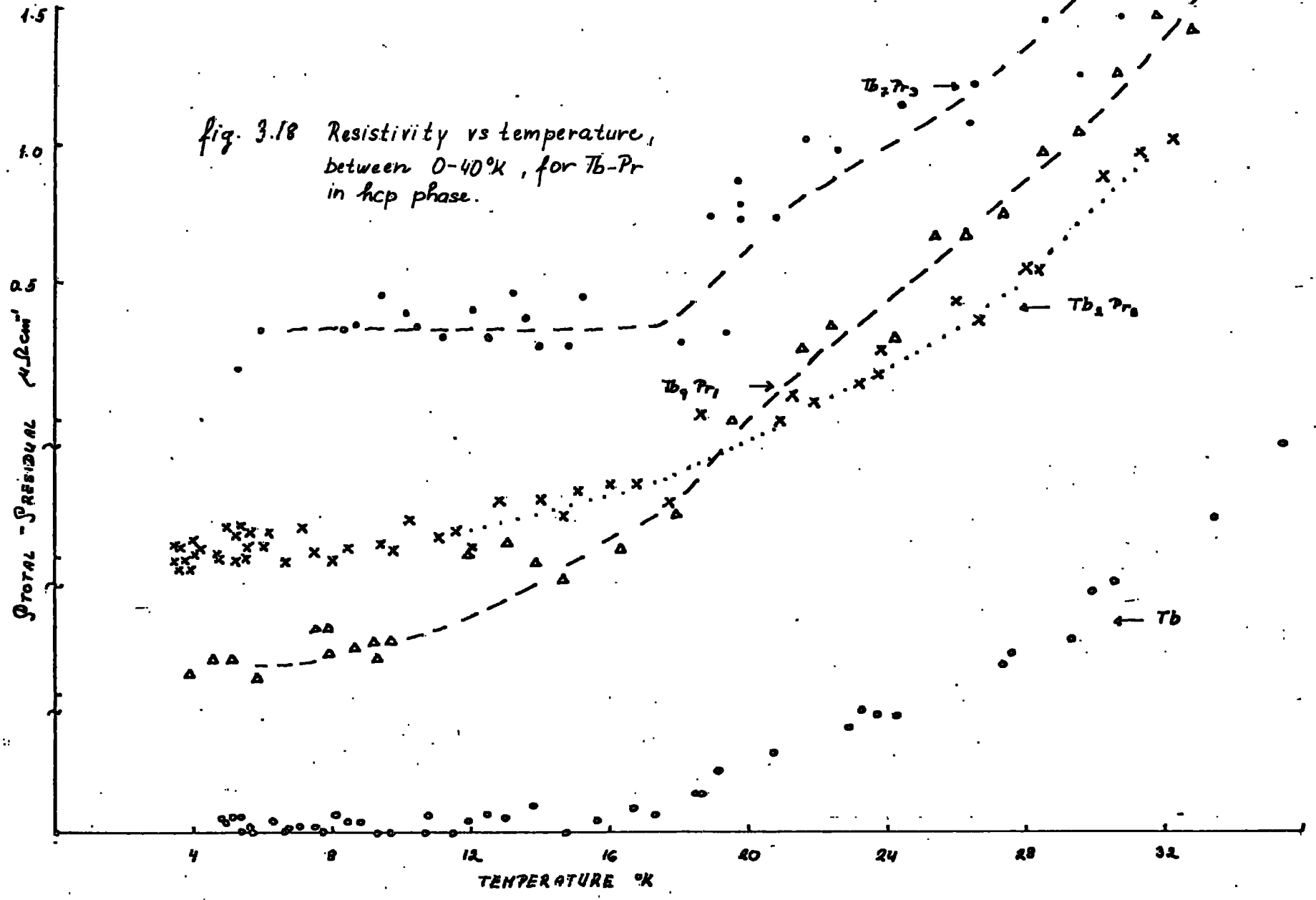

fig. 3.18 Resistivity vs temperature, between 0-40°K, for Tb-Pr in hcp phase.

Resistivity vs temperature
for Dy-Nd in hcp phase.

fig. 3.19

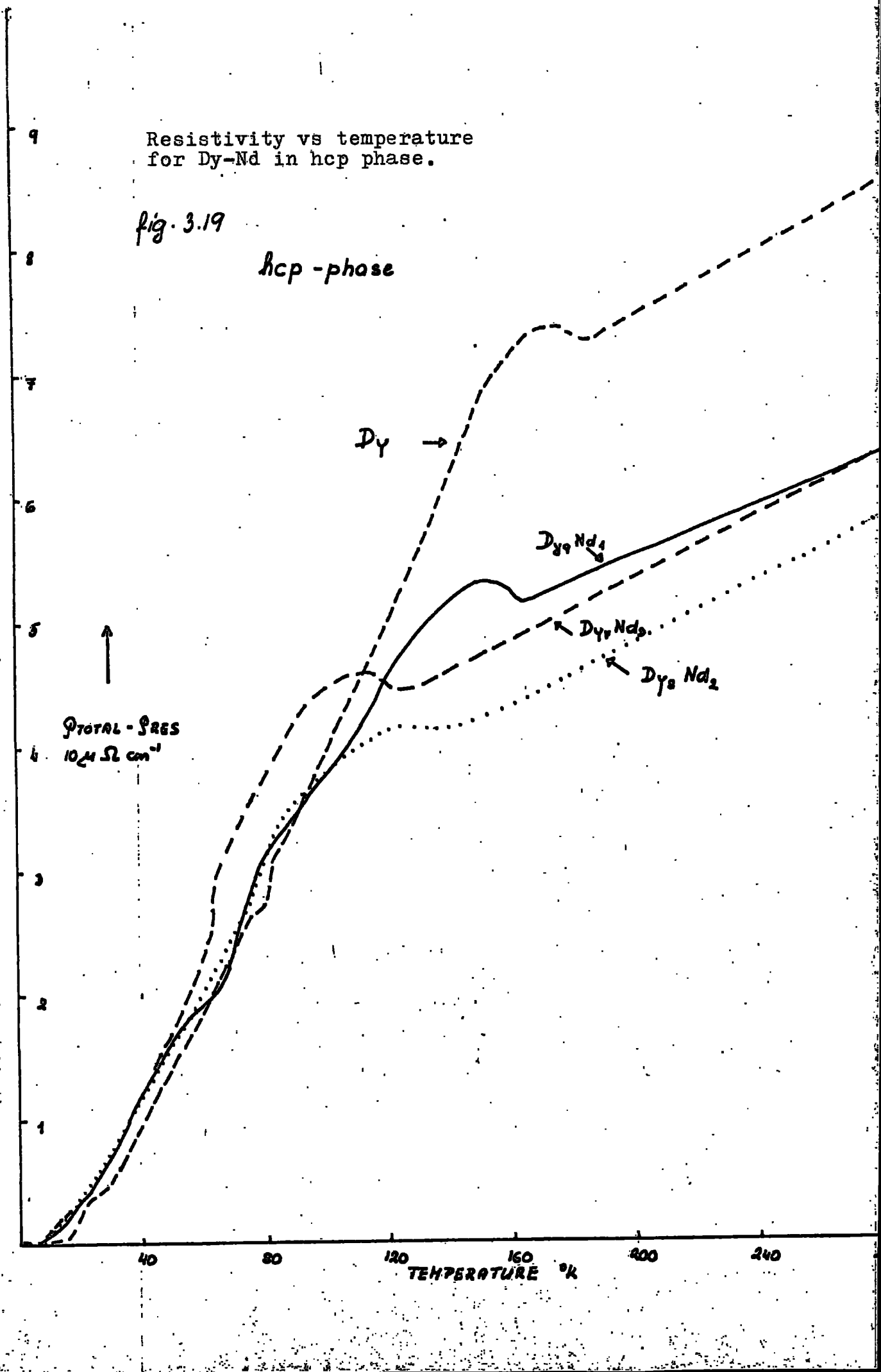

and 40°K the following features are obvious which have been mentioned briefly above:

1) existence of $\rho_{res}(T)$=constant only in the hcp phase, fig .3.18

2) gradual increase of $\rho(T)$ from 2.7°K to ~40°K for all alloys in the d-hex phase and some in the Sm-phase, fig.3.16-17.

3) in the case of $Pr_{55}Tb_{45}$ and $Pr_{33}Tb_{67}$ there is some evidence for the existence of an anomaly between 5-10°K caused most likely by some type of magnetic ordering, fig.3.17 which is not found in magnetic or neutron difraction studies.

3 43 Neodymium-dysprosium

hcp phase: There is a much bigger resemblance in the resistivity behaviour for all the alloys of this series in hcp phase than in Pr-Tb system. They all follow closely the pattern outlined for the hcp phase in the introduction, fig. 3.19 . After an initial temperature region (smaller for bigger concentrations of Nd) of temperature independent residual resistivity ρ_{res} a temperature region follows where the resistivity increases sharply with the temperature until the magnetic ordering temperature T_N is reached. Above T_N the resistivity increases slowly and almost linearly. The sharp resistivity rise, caused by magnetic and phonon scattering is subdivided by T_C into two regions (in Dy and Dy with 10, 20 and 30% Nd) by an anomaly caused by the ferro-antiferromagnetic transition. In Dy_6Nd_4 only one transition is obvious presumably T_N (the antiferro-paramagnetic transition) as follows from magnetic measurements repeated by (1-29). This alloy is a mixture of the Sm and hcp phases. In all other alloys both transition temperatures T_C and T_N are well defined even though they are consequently lower.

fig. 3.20 Resistivity vs temperature for Dy-Nd in Sm-phase.

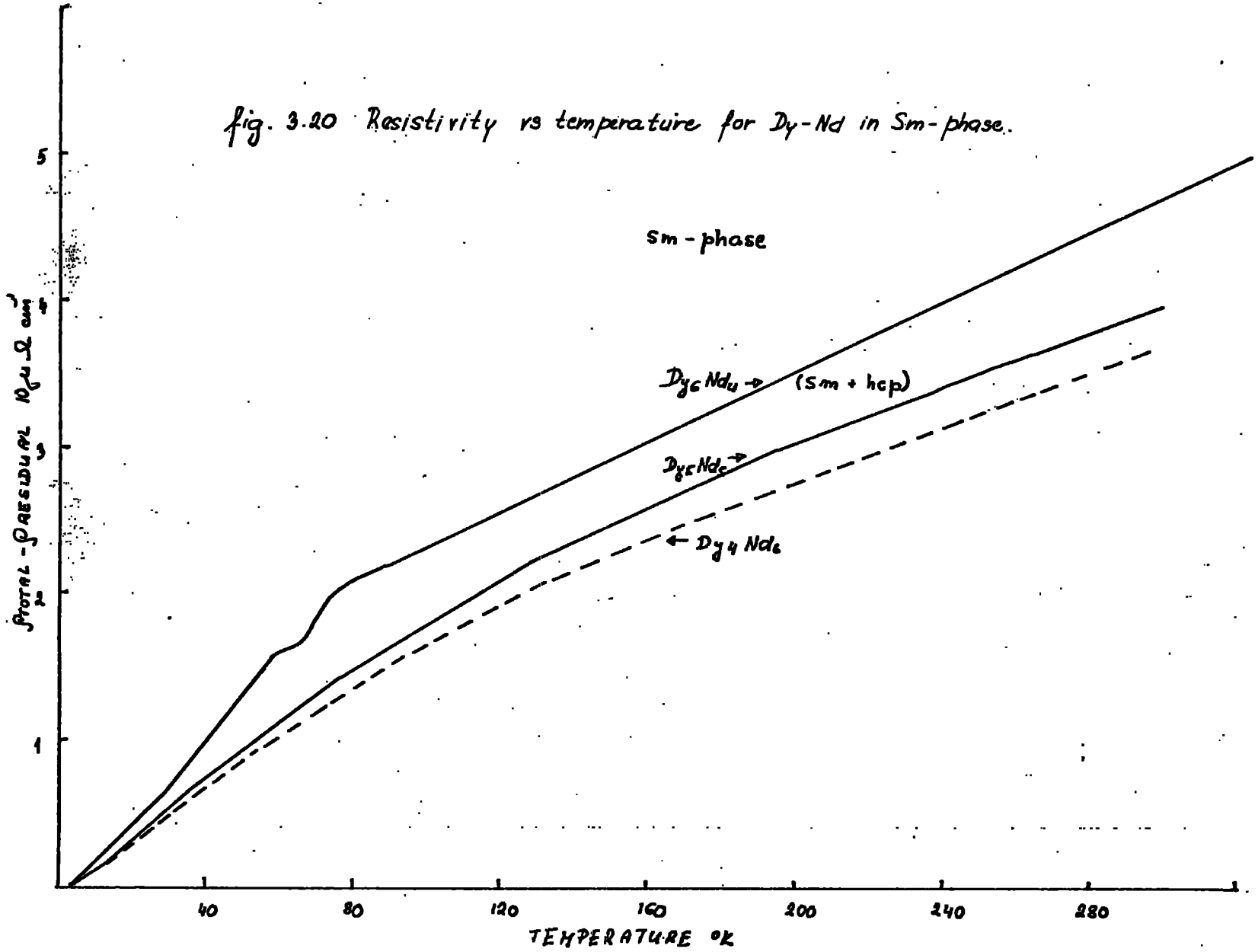

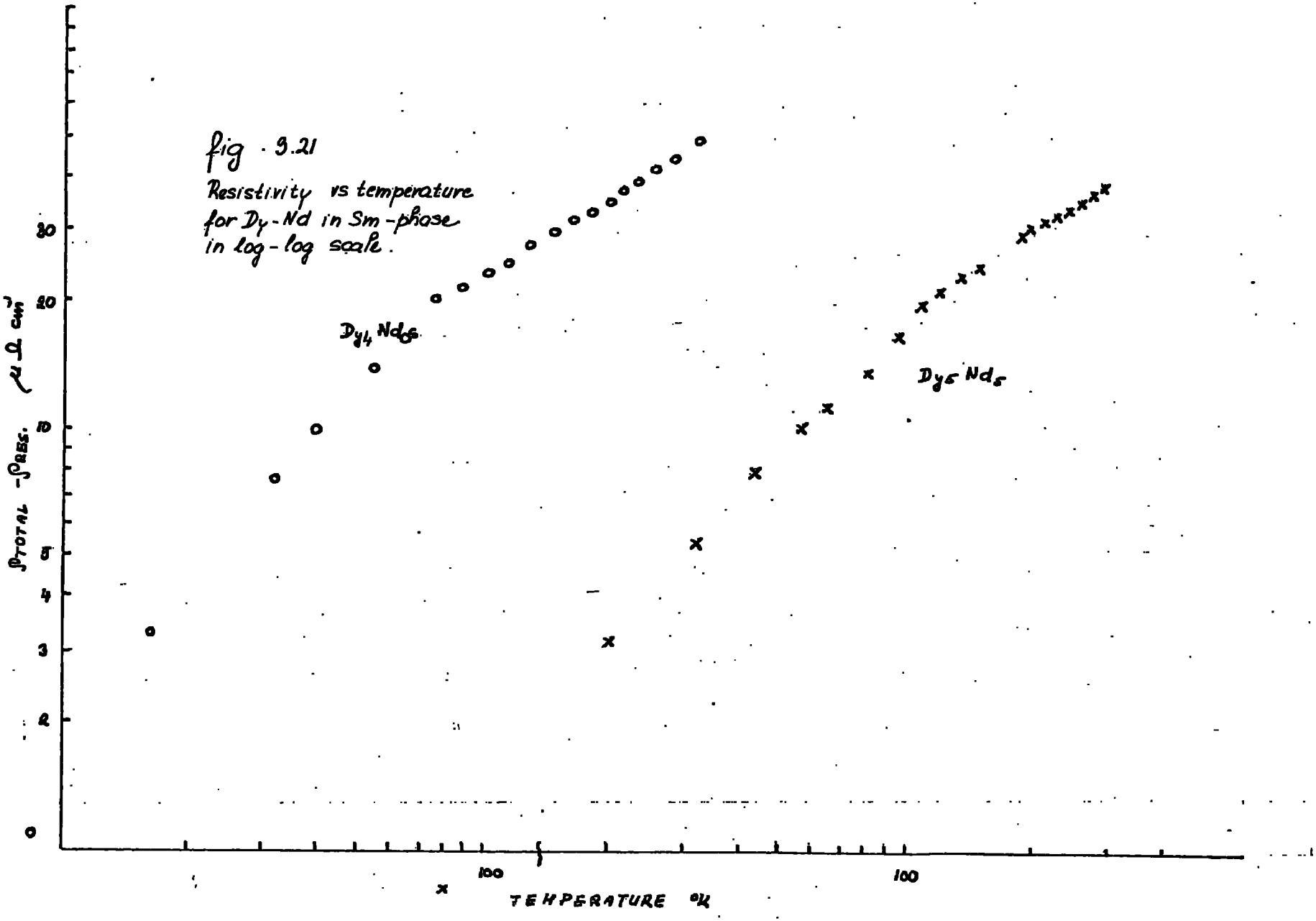
fig · 3.21
Resistivity vs temperature for Dy-Nd in Sm-phase in log-log scale.
Dy4 Nd6
Dy5 Nd5
ρTOTAL - ρRES. (μ Ω cm)
TEMPERATURE °K
100
100
0
2
3
4
5
10
20
30

Resistivity vs temperature
of NEODYMIUM - DYSPROSIUM } in d-hex
NEODYMIUM - YTTRIUM

fig. 3.22

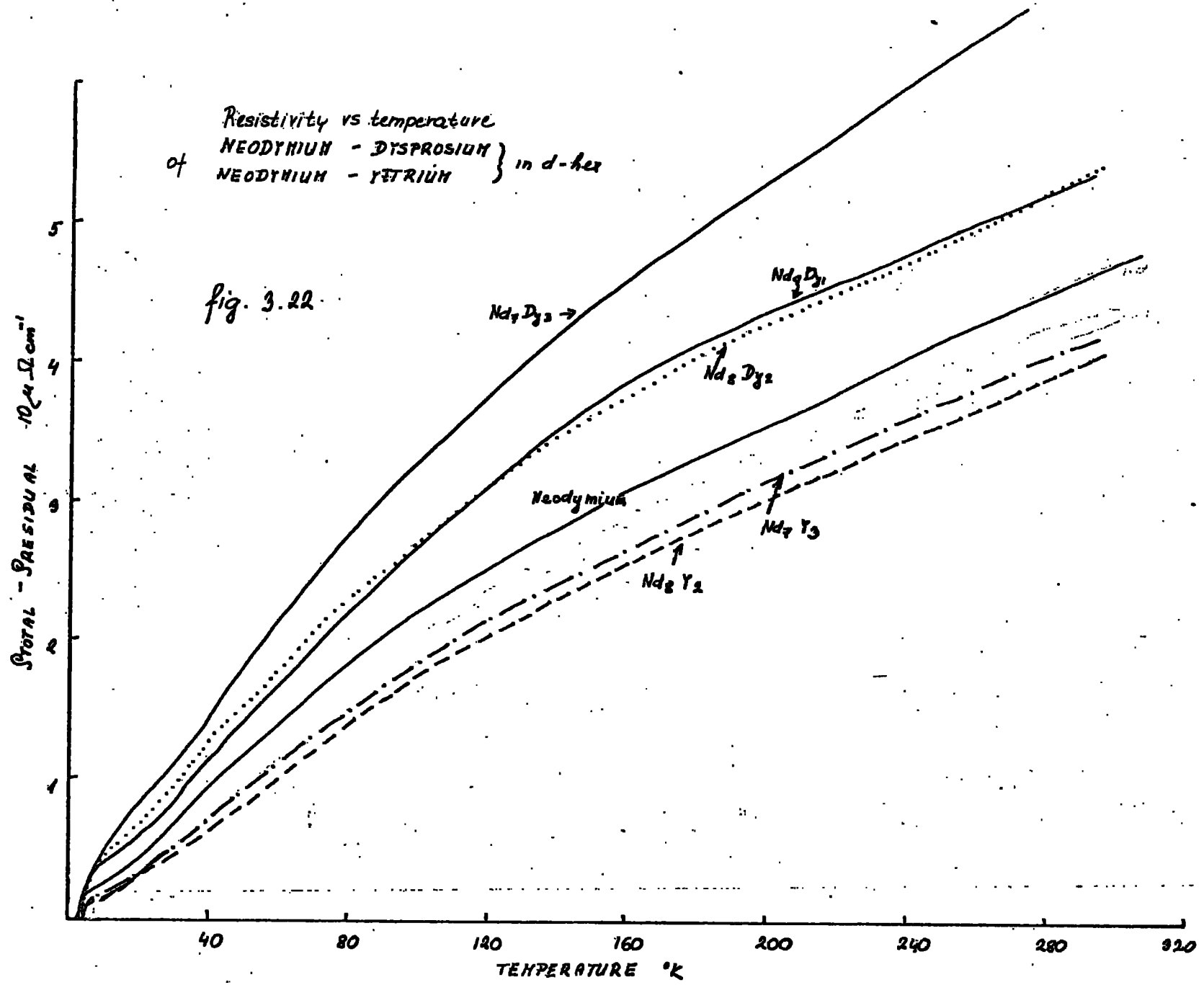

than the transition temperatures deduced from magnetic measurements(1-28,29). The $T_{N\text{-resistivity}}$ is generally lower than $T_{N\text{-mag.}}$ as is shown in table 3.7. The temperature related to the anomaly on the resistivity curve is likely to occur at the temperature at which long range magnetic ordering collapses, while if the short range ordering is strong the magnetization might show a maximum at temperature higher than the T_N value deduced from resistivity measurements. The definition of T_N and T_C must be different in the two cases mentioned (i.e. of electrical and magnetic measurements) from both a microscopic as well as thermodynamic point of view.

Sm-phase: The resistivity curve for both alloys in Sm phase, Dy_5Nd_5 and Dy_4Nd_6 show only a continuous curvature. The magnetic transitions for both are extremely difficult to identify independently, fig.3.20. The residual resistivity region no longer exists, but instead the resistivity is temperature dependent for all temperatures measured. At first the resistivity increases almost linearly, table 3.6, with temperature up to approximately T_N. This is more readily visible on a log-log graph, fig. 3.21 . In the paramagnetic region the increase is slower. The curved form of the resistivity curve might again suggest the presence of crystal field effects.

d-hex phase: The behaviour of the resistivity at very low temperatures indicates the presence of an anomaly at $\sim 6^{c}K$, fig.3.22 . This is particularly clear from the temperature dependance of $\rho(T)/T^2$ as the resistivity has approximately a T^2 dependence in this region if no anomaly is present, fig.3.23. Consequently the temperature region of constant

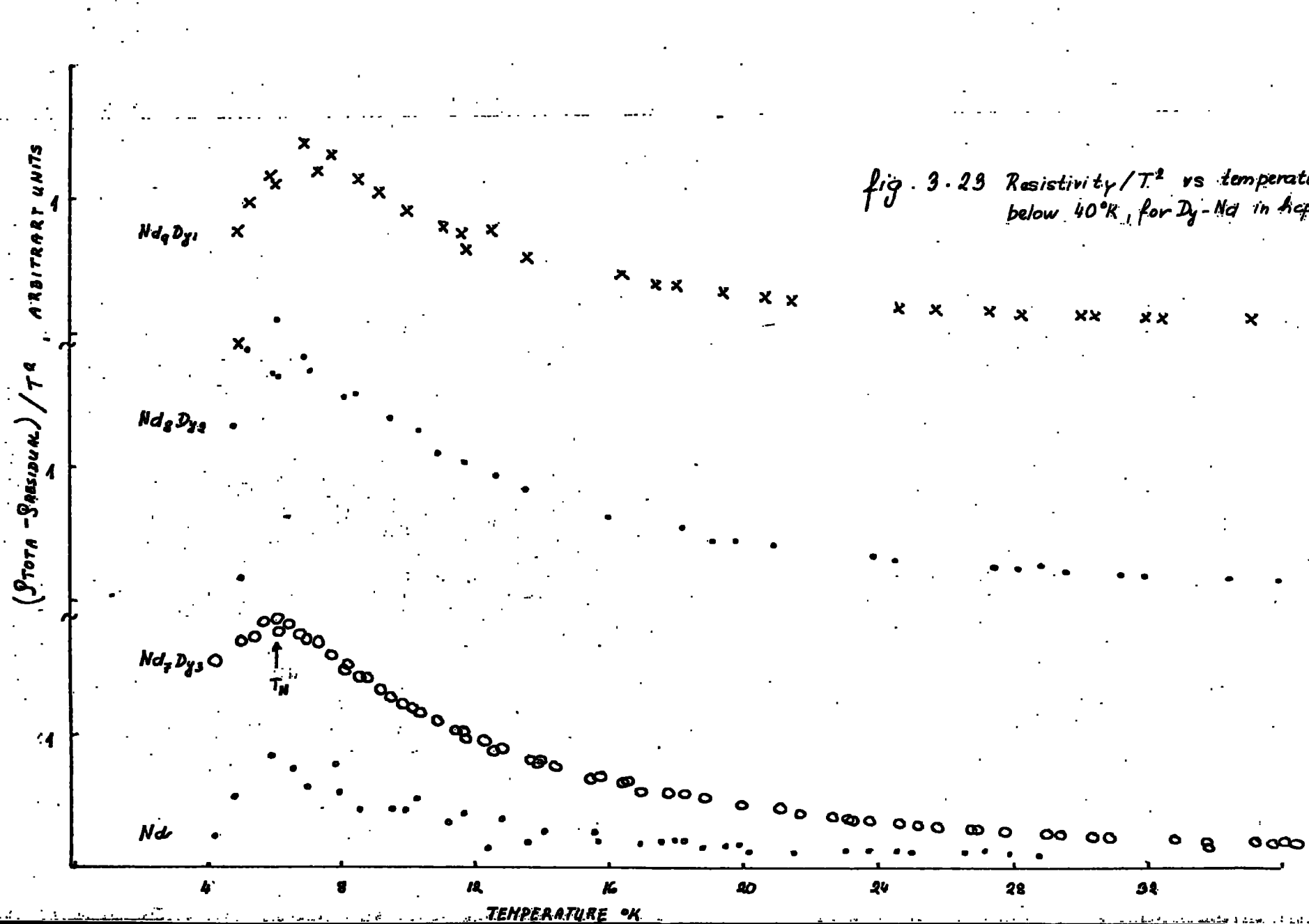

fig. 3.23 Resistivity / T^2 vs temperature, below 40°K, for Dy-Nd in hcp phase.

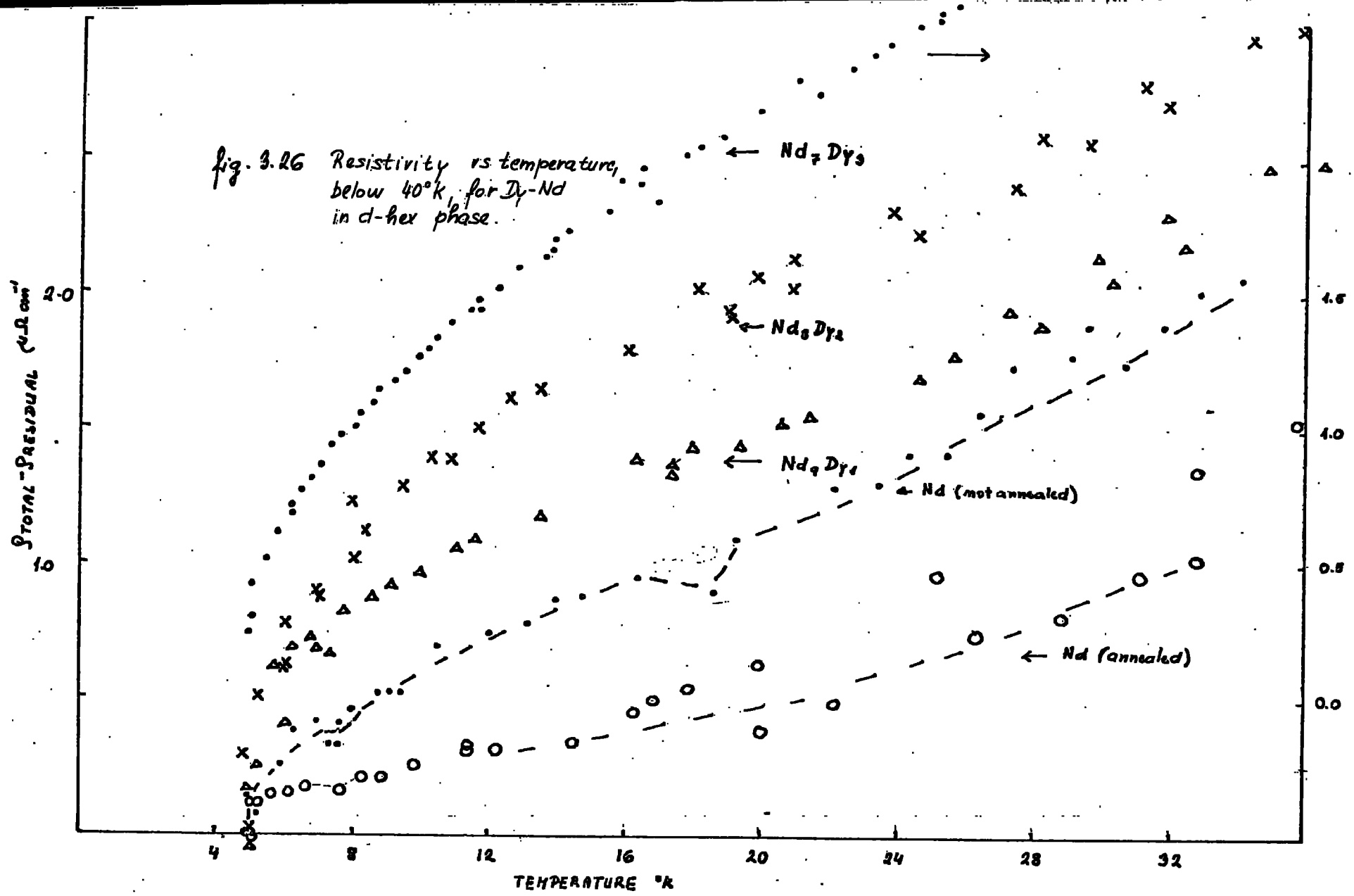
fig. 3.26 Resistivity vs temperature, below 40°K, for Dy-Nd in cl-hex phase.
← Nd₇ Dy₃
← Nd₈ Dy₂
← Nd₉ Dy₁
← Nd (not annealed)
← Nd (annealed)
ρTOTAL - ρRESIDUAL (μΩ cm)
TEMPERATURE °K
2.0
1.0
1.5
1.0
0.5
0.0
4
8
12
16
20
24
28
32

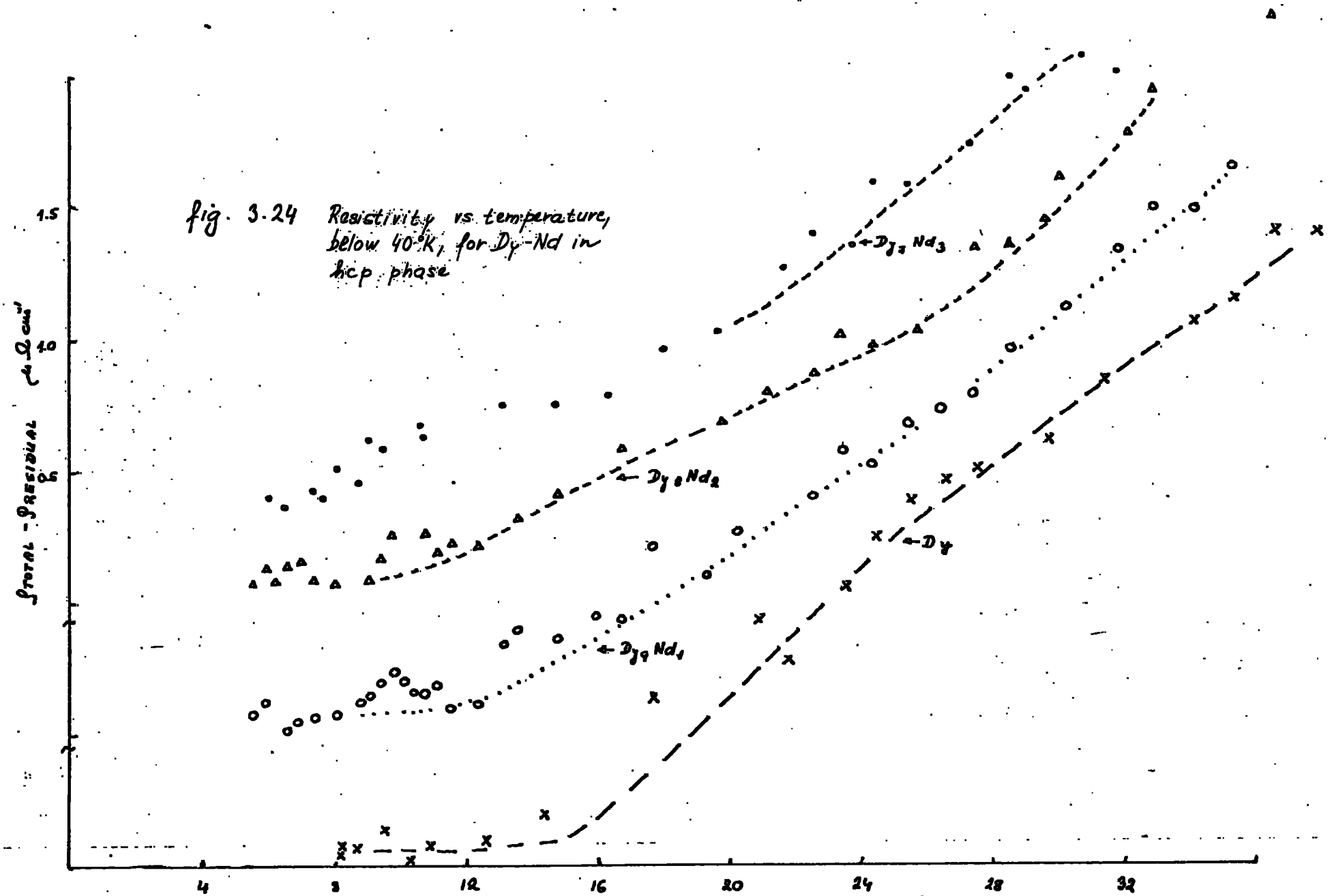

fig. 3.24 Resistivity vs temperature, below 40°K, for Dy-Nd in hcp phase

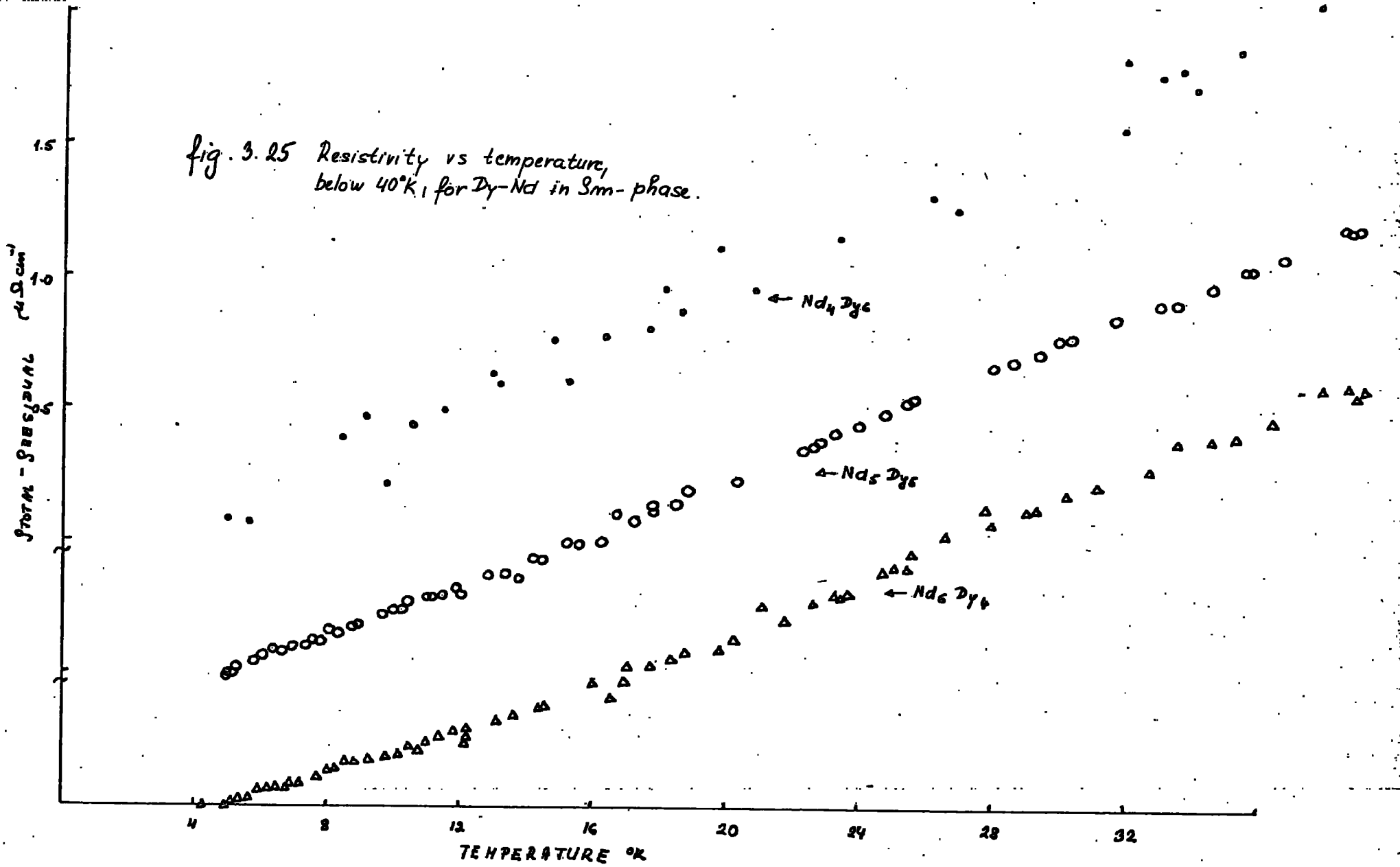

fig. 3.25 Resistivity vs temperature, below 40°K, for Dy-Nd in Sm-phase.

fig. 3.27 Resistivity vs temperature for Y-Nd in hcp - phase

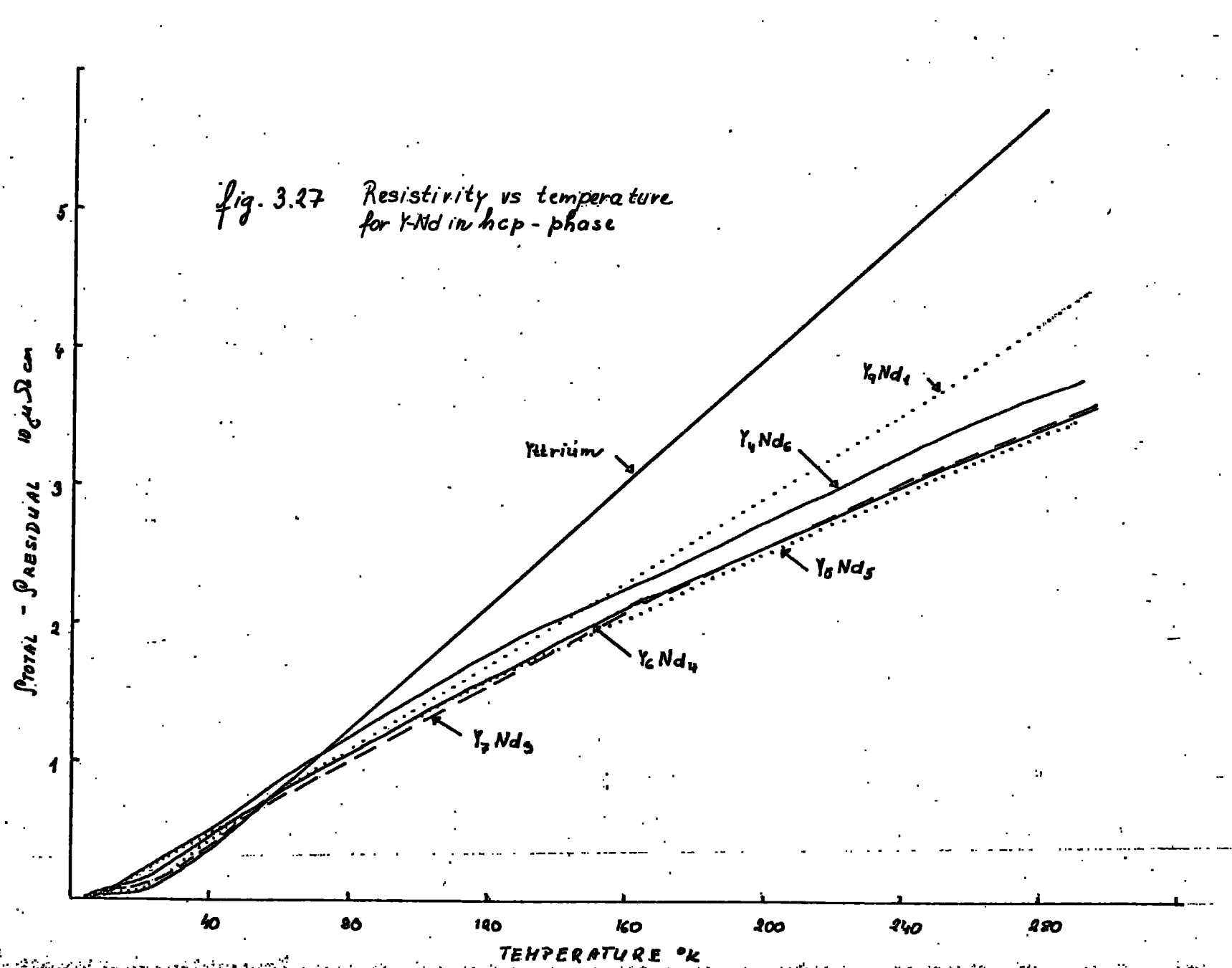

"residual resistivity" is absent. After the initial T^2 increase, the resistivity behaviour is governed by the existence of discrete crystal field levels as well as phonon scattering, although for these alloys it could not be described satisfactorily by any T^n dependence. Contrary to the Pr-Tb case $\varrho(T)$ increases with the addition of dysprosium, and in this case elemental Nd does not form a covering curve but rather is the lowest curve with Dy_3Nd_7 giving the covering curve.

3.44 Very low temperature region

The graphical display in an enlarged scale reveals clearly what has already been said about this temperature region, fig.3.24-26:

1) $\varrho(T)$ is temperature independent in the initial region for Dy (~18°K), Dy_9Nd_1 (13°K), Dy_8Nd_2 (12°K), Dy_7Nd_3 (8-10°K)

2) in Dy_6Nd_4, Dy_5Nd_5 and Dy_4Nd_6 there is no such region and the resistivity increases linearly from the lowest temperature measured;

3) $\varrho(T)$ exhibits the anomalous behaviour in the d-hex phase as mentioned above.

3.45 Neodymium-yttrium

This system was chosen as a complementary one to neodymium-dysprosium system. Yttrium is known to have many similar characteristics with the heavy rare earths. Especially it crystallises in an hcp structure and forms the same sequence of phases when alloyed with light rare earths (7) as those observed in the systems already discussed. Yttrium is not magnetic so that can hopefully separate the influences of the structure and strong magnetic moments (of Dy and Tb).

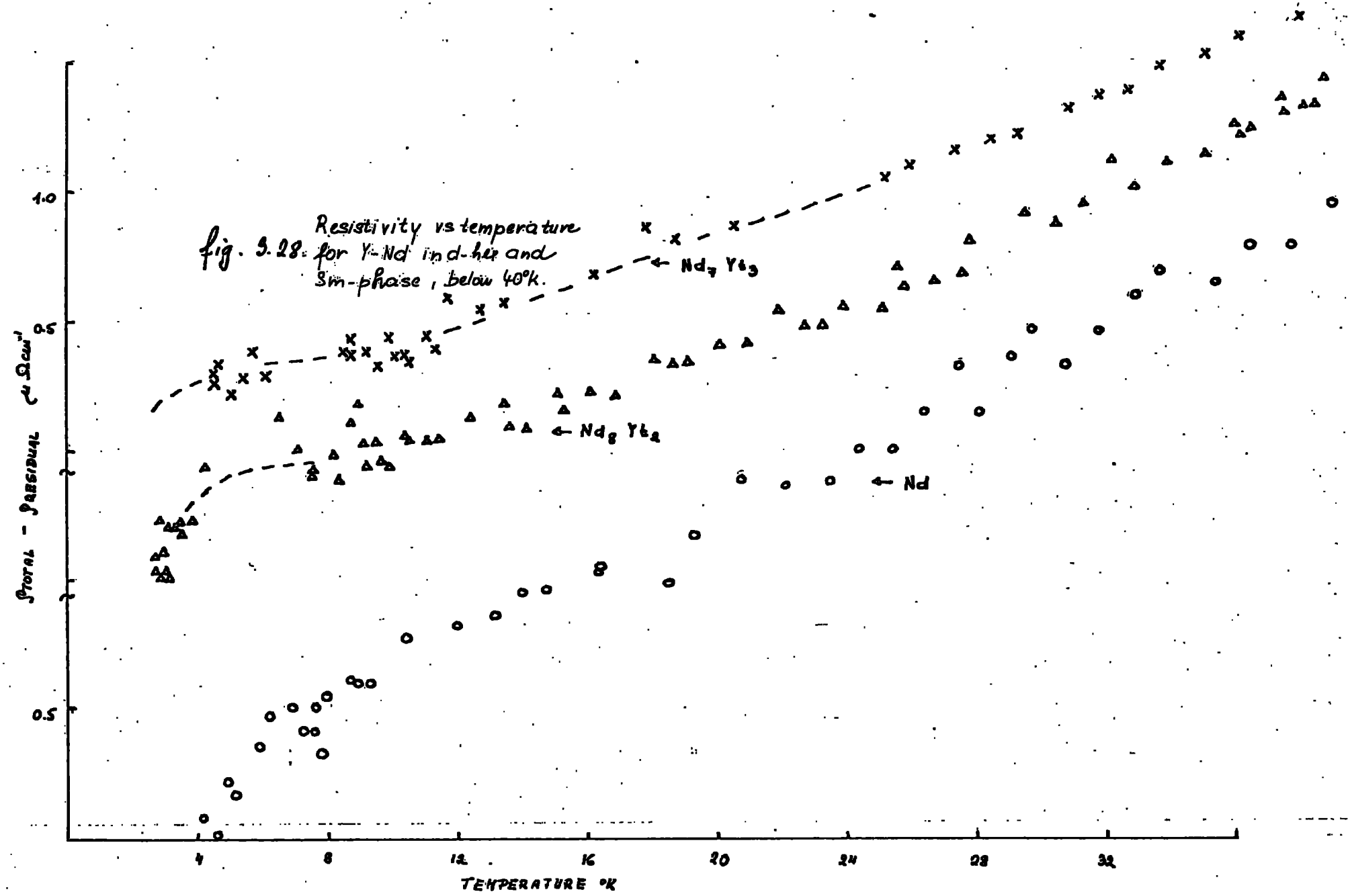

fig. 3.28. Resistivity vs temperature for Y-Nd ind-her and Sm-phase, below 40°k.

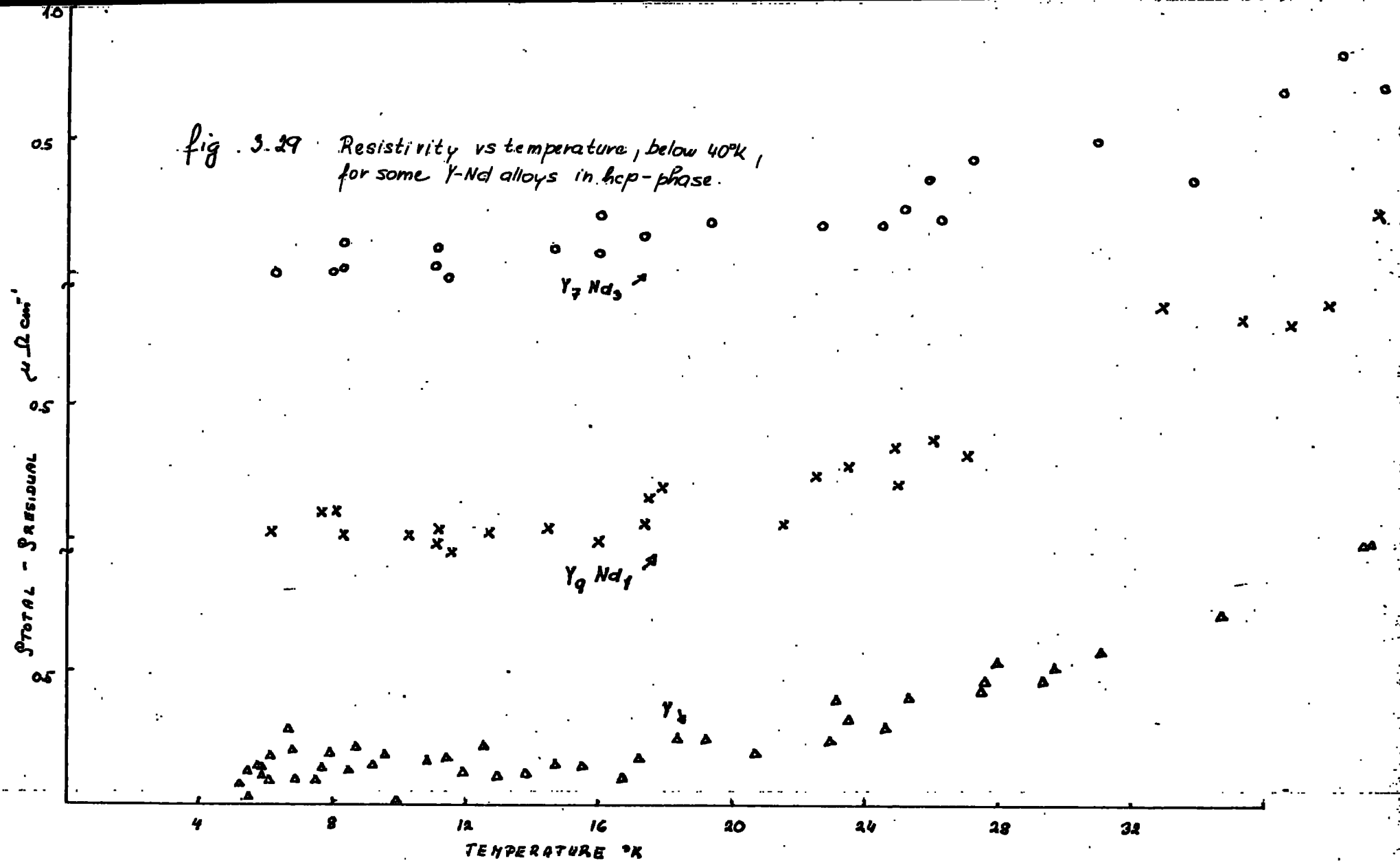

fig. 3.29 Resistivity vs temperature, below 40°K, for some Y-Nd alloys in hcp-phase.

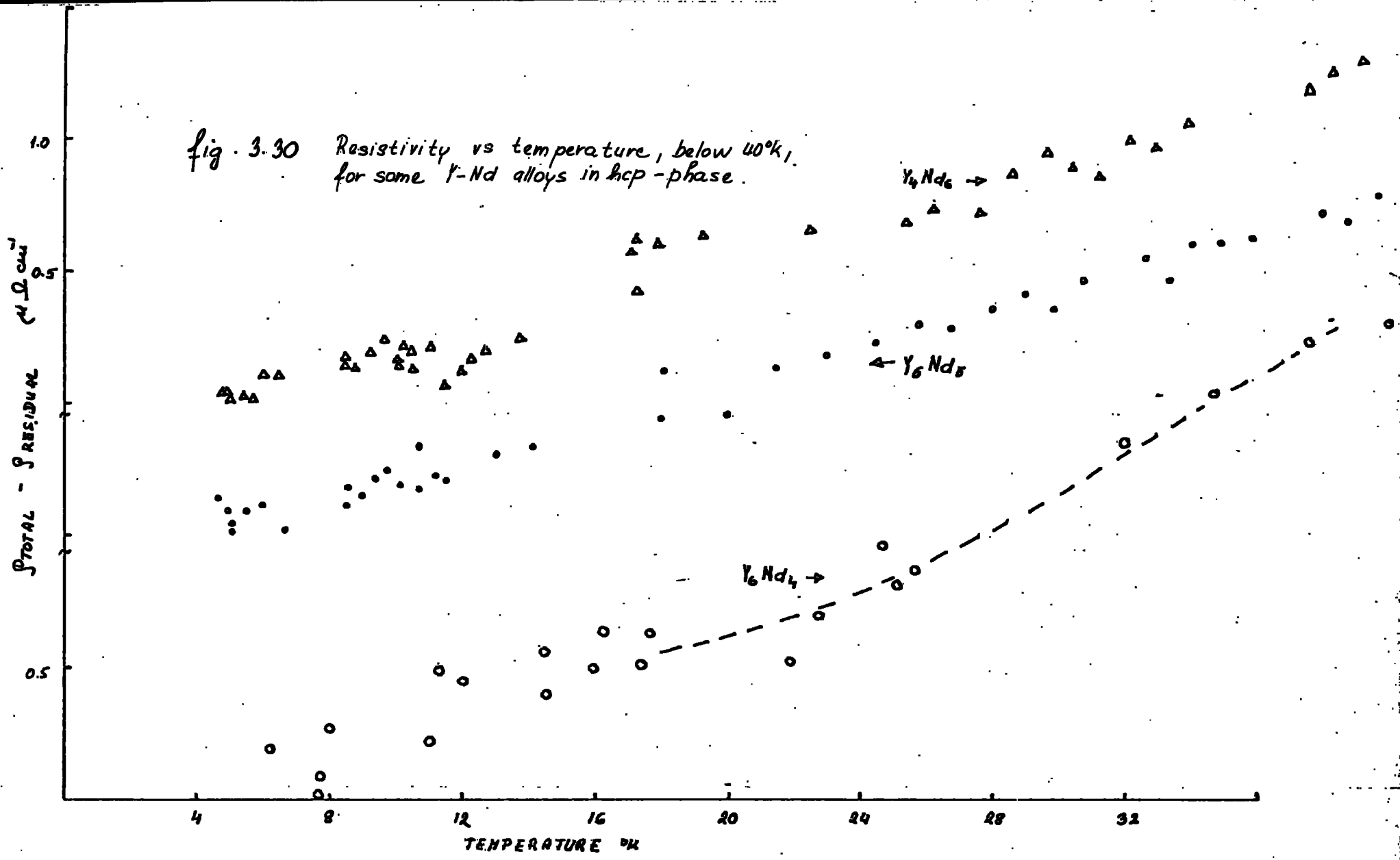

fig. 3.30 Resistivity vs temperature, below 40°K, for some Y-Nd alloys in hcp-phase.

hcp phase: The pattern of the resistivity variation with temperature in this phase for all compositions studied, pure Y, Y with 10, 30, 40, 50 and 60% of Nd, is similar. Y_9Nd_1 resembles the behaviour of pure Y. After the initial region of temperature independent residual resistivity increases monotonicaly in the temperature range studied (3°-320°K). As the Nd content increases the ρ-T increase becomes slower, table 3.8, and the residual resistivity becomes less obvious. The resistivity of the first three samples studied, Y, Y_9Nd_1 and Y_7Nd_3 varies with a similar power law, see table 3.8. This suggests that in these alloys the temperature variation of the resistivity could be explained by normal scattering mechanisms in nonmagnetic tri-valent metals. The influence of the magnetic atoms of Nd is very small even though there are obvious differences between pure Y and the alloys. In the resistivity variation of Y_6Nd_4, Y_5Nd_5 and Y_4Nd_6 the initial $\sim T^2$ dependence is missing, table 3.8, fig.3.27

Sm and d-hex phases: Y_3Nd_7 is a mixture of Sm and d-hex phases. In the latter as well as in Y_2Nd_8 there seems to be some evidence for the existence of scattering from crystal field levels. The $d\rho/dT$ variation with temperature is very sensitive to all the above features, fig. 3.44. There is also evidence of magnetic ordering in the region of very low temperatures similar to the behaviour of Dy-Nd, fig.3.28. The curves of Y_2Nd_8 and Y_3Nd_7 resemble the Nd curve, fig.3.22.

Crystal field effects are obviously present in the d-hex phase and are tracable in Y_3Nd_7 which is a mixture of the d-hex and Sm phases. From the $d\rho/dT$ curves the changes in the resistivity behaviour over the series are obvious.

fig. 3.31 Resistivity vs temperature in hcp phase.

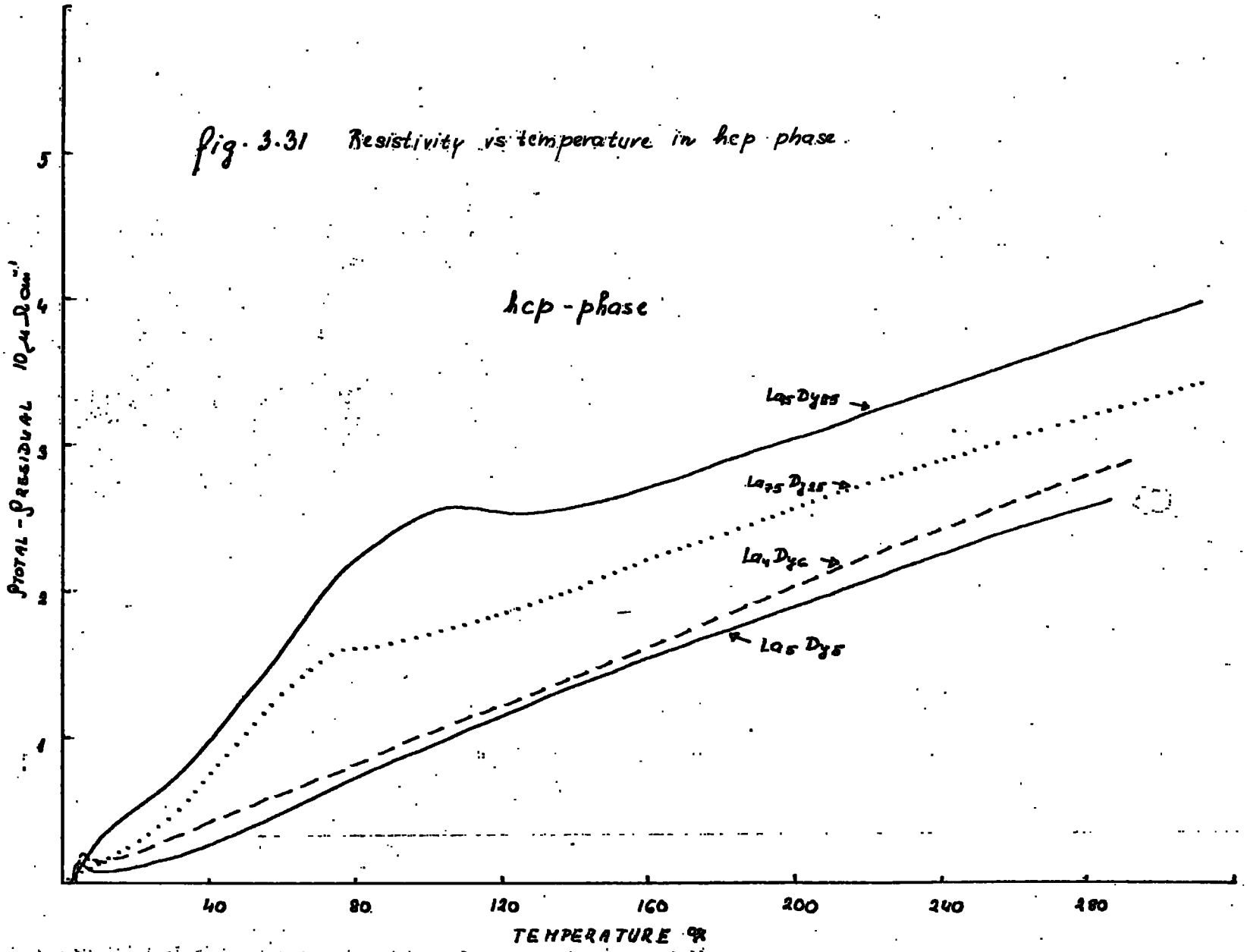

especially in the low temperature region. Whether this is because of the crystal field effects or not is still an open question. From resistivity measurements it is obvious that no long range ordering could be traced outside the d-hex phase.

3.46 Resistivity at very low temperatures

The residual resistivity occupies a wider temperature range (22-24°K) for Y, Y with 10 and 30%, fig.3.29-30, 10-12°K for Y with 40, 50 and 60% of Nd. The very low temperature resistivity of Y with 70% of Nd seems to be slightly temperature dependent to the lowest temperature measured and at 80% of Nd there is an obvious anomaly at 2.85°K which is attributed to some sort of magnetic ordering, fig. 3.28 (most probably antiferromagnetic as in the case of Nd). The anomaly is similar to the one observed in case od Dy-Nd in the d-hex phase but smaller.

3.47 Lanthanum-dysprosium

This alloy is a second complementary one to the Nd-Dy system where the magnetic atom Nd was replaced by nonmagnetic atom La. The purpose in using this series was to trace any difference in behaviour of the d-hex light rare earths when alloyed with heavy rare earths as the light rare earths are known to differ one from the other more than the heavy rare earths do. Lanthanum was also chosen as there is still considerable disputation going on relating to the extent to which it could be considered asarare earth by its physical properties.

hcp phase: The first three members of this phase Dy, $Dy_{85}La_{15}$ and $Dy_{75}La_{25}$ (ρvs T) have all the features described in

fig. 3.32 Resistivity v.s. temperature for La-Dy in Sm-phase.

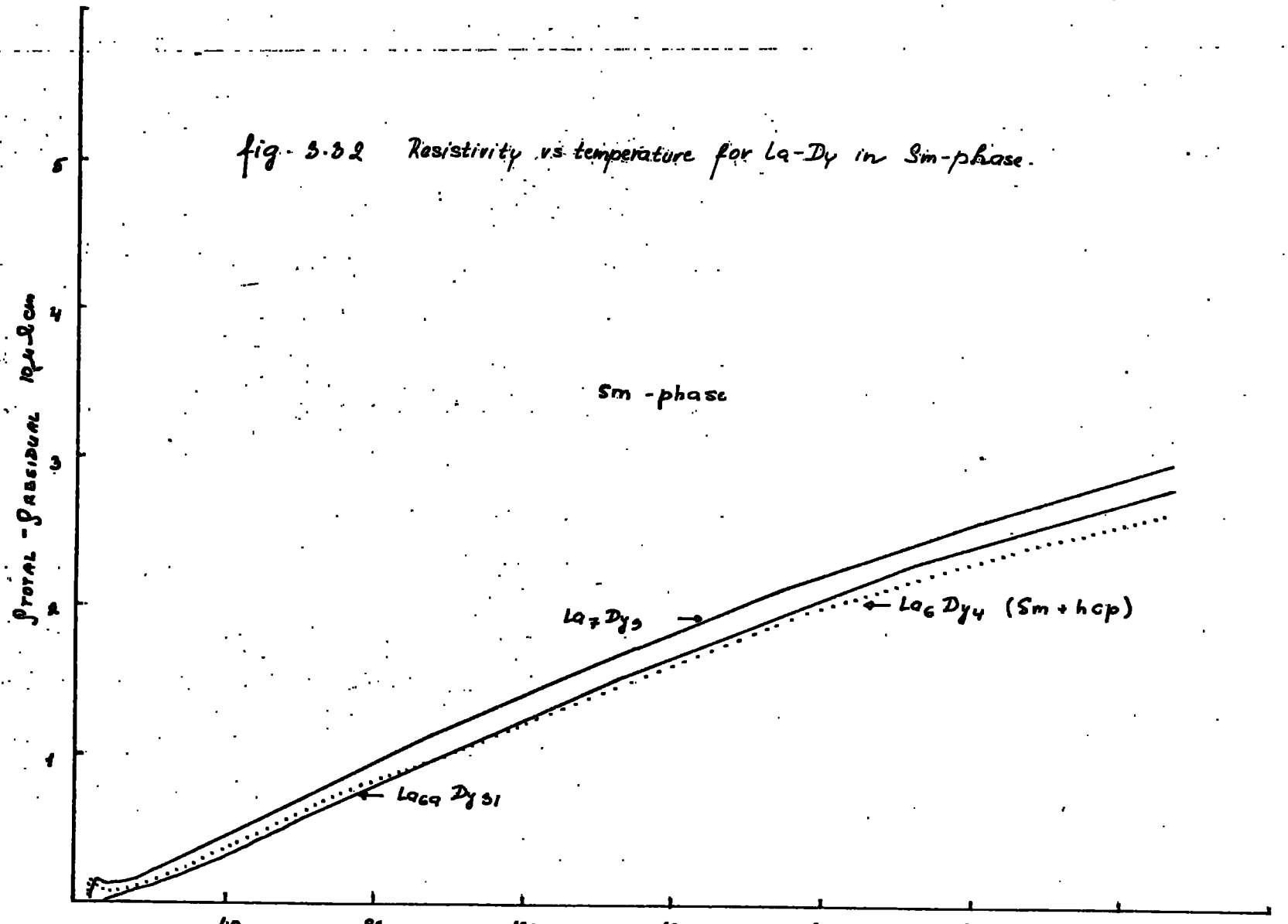

the introduction. A rather sharp increase in the temperature region, ~10°K - T_C,T_N, where the alloy is magnetically ordered. From (19) we know that Dy with 15 and 25% of La order only ferromagnetically. Near the Curie temperature T_C, there is an anomaly on the resistivity curve of the same type as that near T_N which was described for the hcp phase of the Dy-Nd alloys. If the resistivity variation with temperature above T_C in the paramagnetic phase is viewed as a power law ($\sim T^n$) than from the big difference between n=0.09 for pure Dy and n=0.7 for the alloys it is obvious that a different scattering mechanism should be present in addition to the phonon scattering in the case of the alloys. The resistivity variation with temperature of the remaining alloys in the hcp phase (La_4Dy_6, La_5Dy_5, La_6Dy_4) is rather untypical, fig. 3.31 for this phase as there is no anomaly above very low temperature and presumably no ordering.

The La_4Dy_6 behaviour could be described as $\varrho(T)\sim T^n$ where $n\simeq 1$ in the temperature region studied (e.g. 4-300°K), whereas in the case of La_5Dy_5 and La_6Dy_4 for the temperatures above 120°K n is smaller than 1 as the resistivity curve is already slightly curved suggesting that the behaviour resembles that of pure La.

Sm-phase: The resistivity curve of La_7Dy_3 and $La_{69}Dy_{31}$; fig.3 32, is very similar to the one of La_5Dy_5, La_6Dy_4 but the n's at higher temperatures (above 170°K) decrease with increasing La concentration.

d-hex phase: The approximation of $\varrho(T)\simeq T^n$ is not a very good one in this phase as scattering mechanisms of a different origin and character (e.g. crystal field influence and mechanism where the density of states $\eta(E)$ near E_F change)

fig. 3.33

Resistivity vs temperature for LANTHANUM - DYSPROSIUM in d-ka

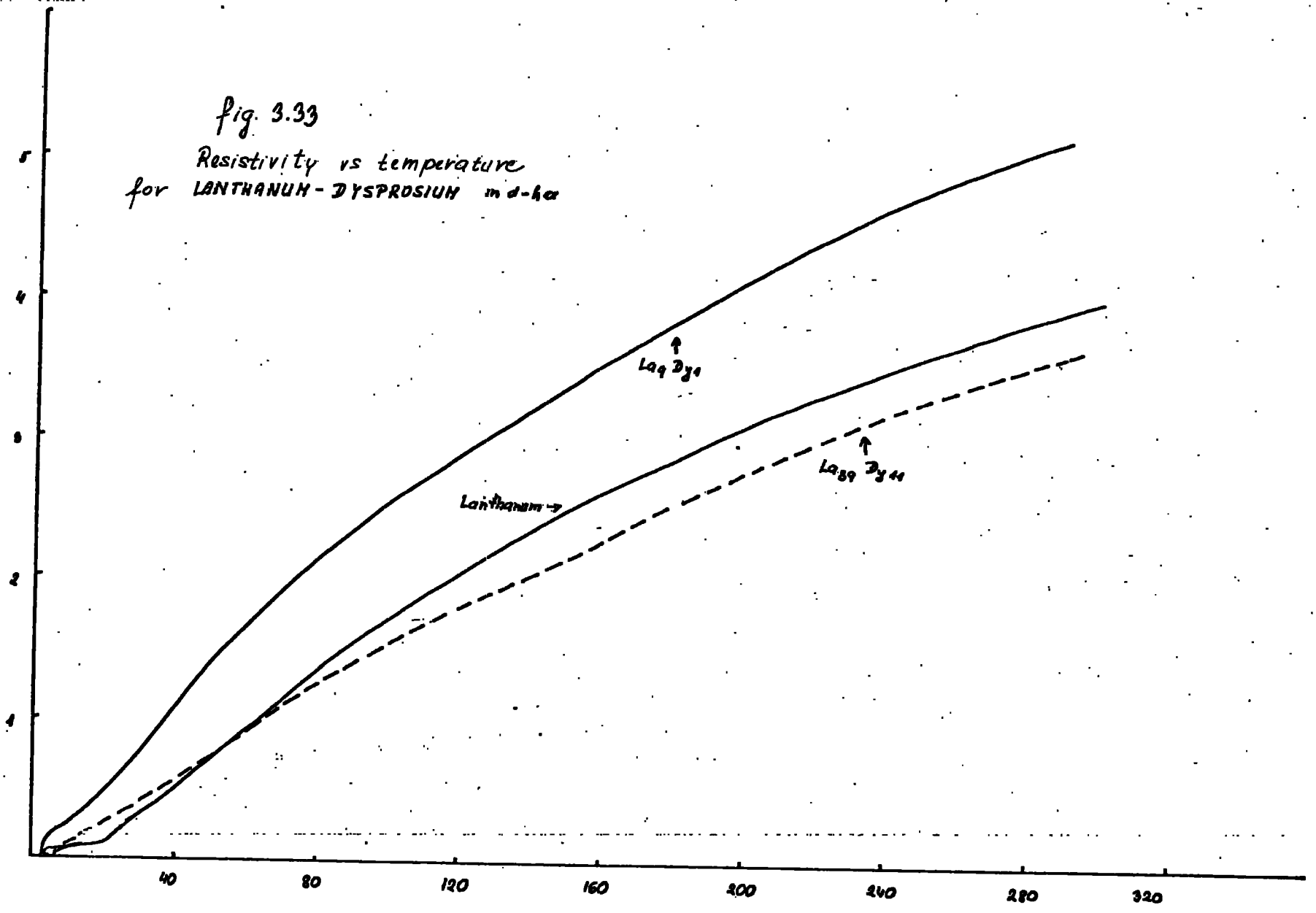

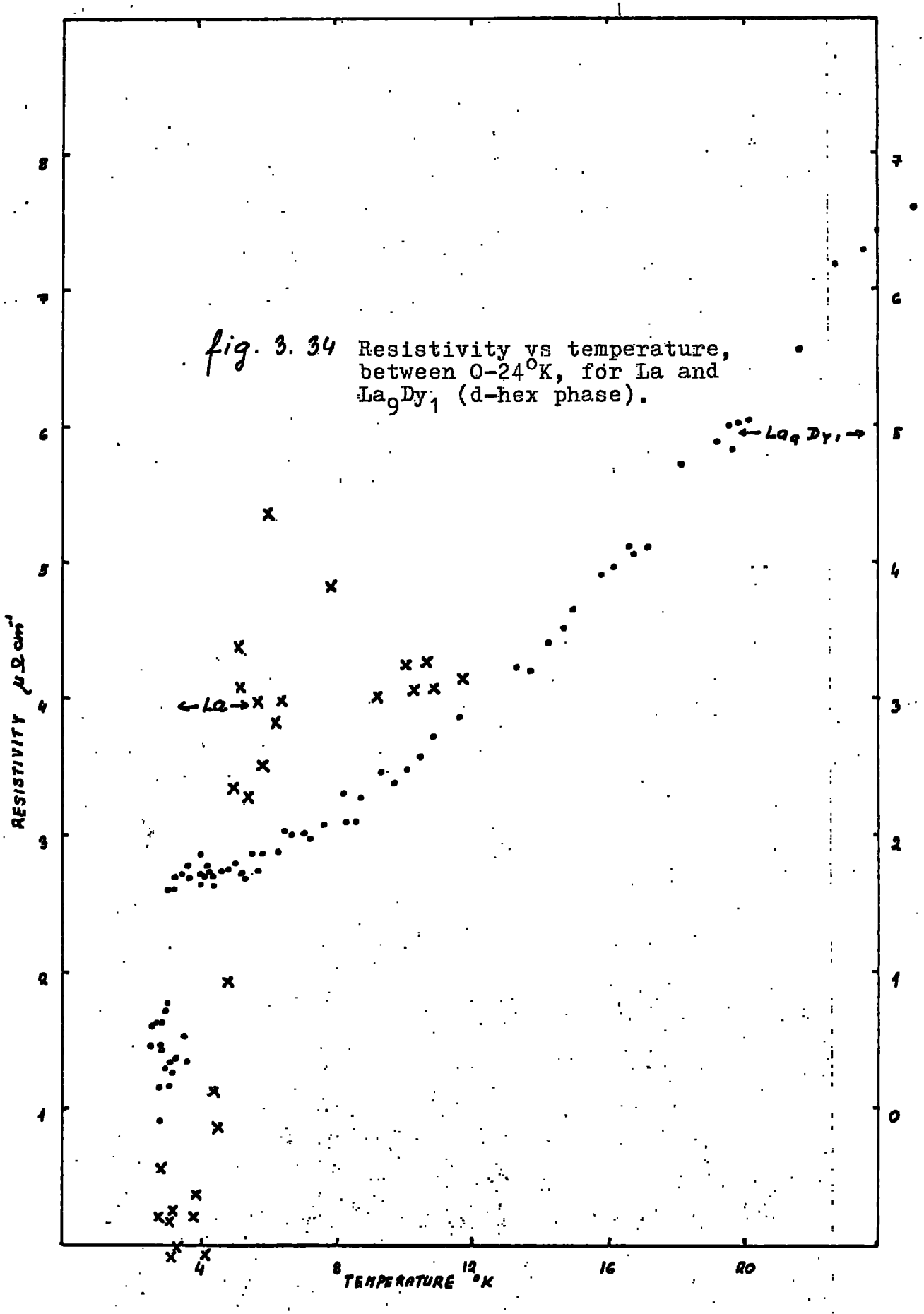

fig. 3. 34 Resistivity vs temperature, between 0-24°K, for La and La_9Dy_1 (d-hex phase).

are involved. In the case of La and La_9Dy_1, fig. 3.33, a superconducting transition has been found in the temperature region 4-5°K followed by a small temperature region of temperature independent resistivity, between ~16-20°K, equivalent to the residual resistivity in other alloys. Above 20°K the resistivity is steadily increasing but the 'slope' of increase is decreasing, table 3.10, with temperature.

3.48 Resistivity at very low temperature

La and La_9Dy_1 show superconducting transitions, fig. 3.34-35 La at 5.3-5.5°K, La_9Dy_1 at 4.5-4.7°K which verifies the assumption of the presence of both d-hex and cubic phase, made in the first part of this chapter and experimentaly observed on these specimens by (15). La with 11 and 30% of Dy show similar pattern in the resistivity variation below ~5°K, fig. 3.36, to the alloys described above, but in the temperature region measured, there is not sufficient evidence for superconducting transitions, fig. 3.37. The behaviour of La_6Dy_4 - La_4Dy_6 alloys is similar to the Nd-Dy alloys in Sm-structure. The remaining alloys $La_{25}Dy_{75}$ - Dy, as in the other alloys studied in the hcp phase, fig. 3.38, show clear sign of the residual resistivity region.

3.49 Conclusion

The conclusion concerning the form of the resistivity variation with temperature has been described to a great extent in the introduction to the second part of this chapter. Table 3.4 - 3.11 summarize some physical parameters obvious from the $\rho(T)$ vs T curves. Figure 5.29 represents the ρ_{res} variation with composition for all the alloys studied. In previously reported cases of Gd-Y (1-3), Gd-Lu, Tb-Lu (1-2) the curve was symmetric (maximum disorder was reached for ~50% concentration of both components). In

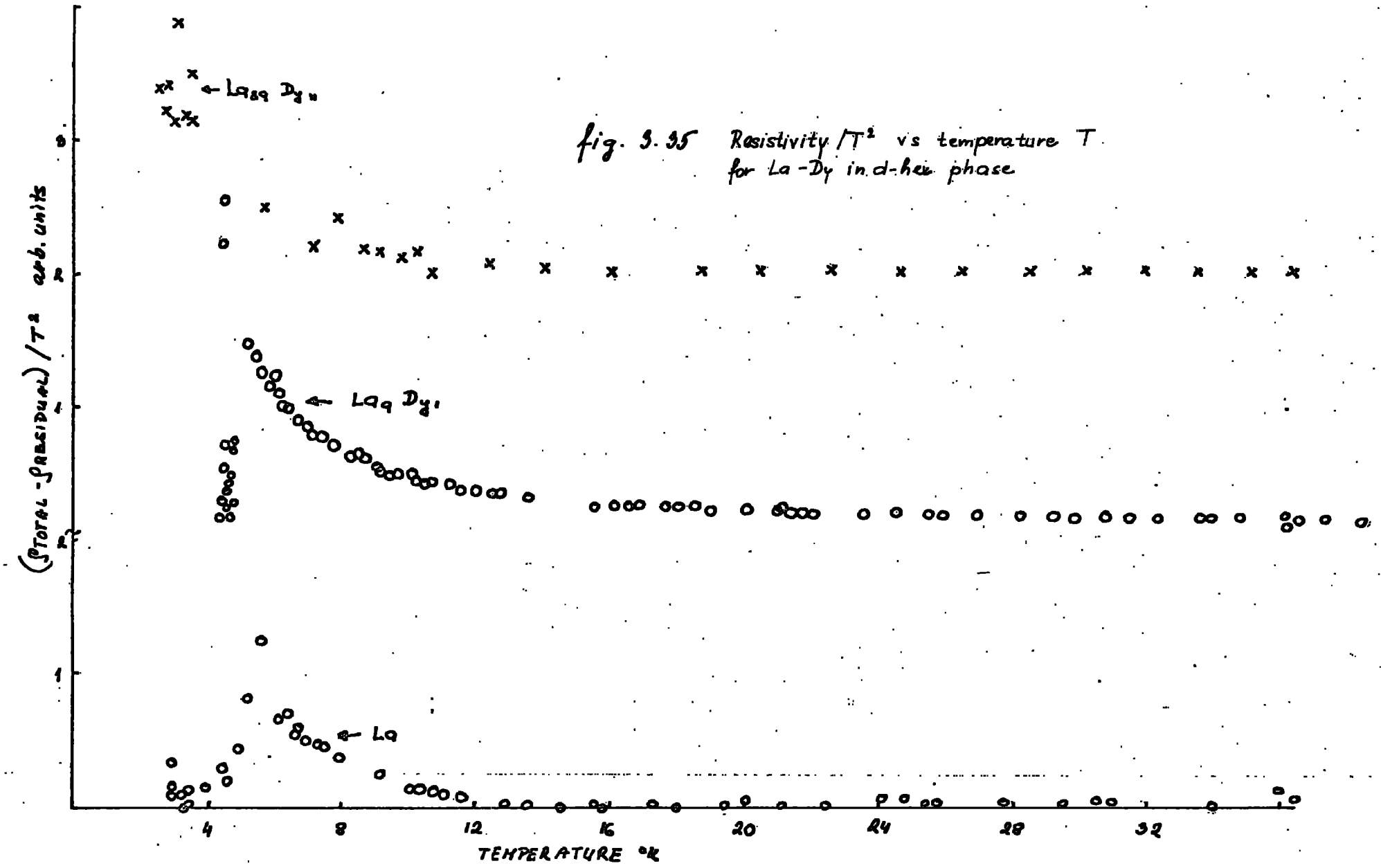

fig. 3.35 Resistivity / T^2 vs temperature T for La-Dy in d-hex phase

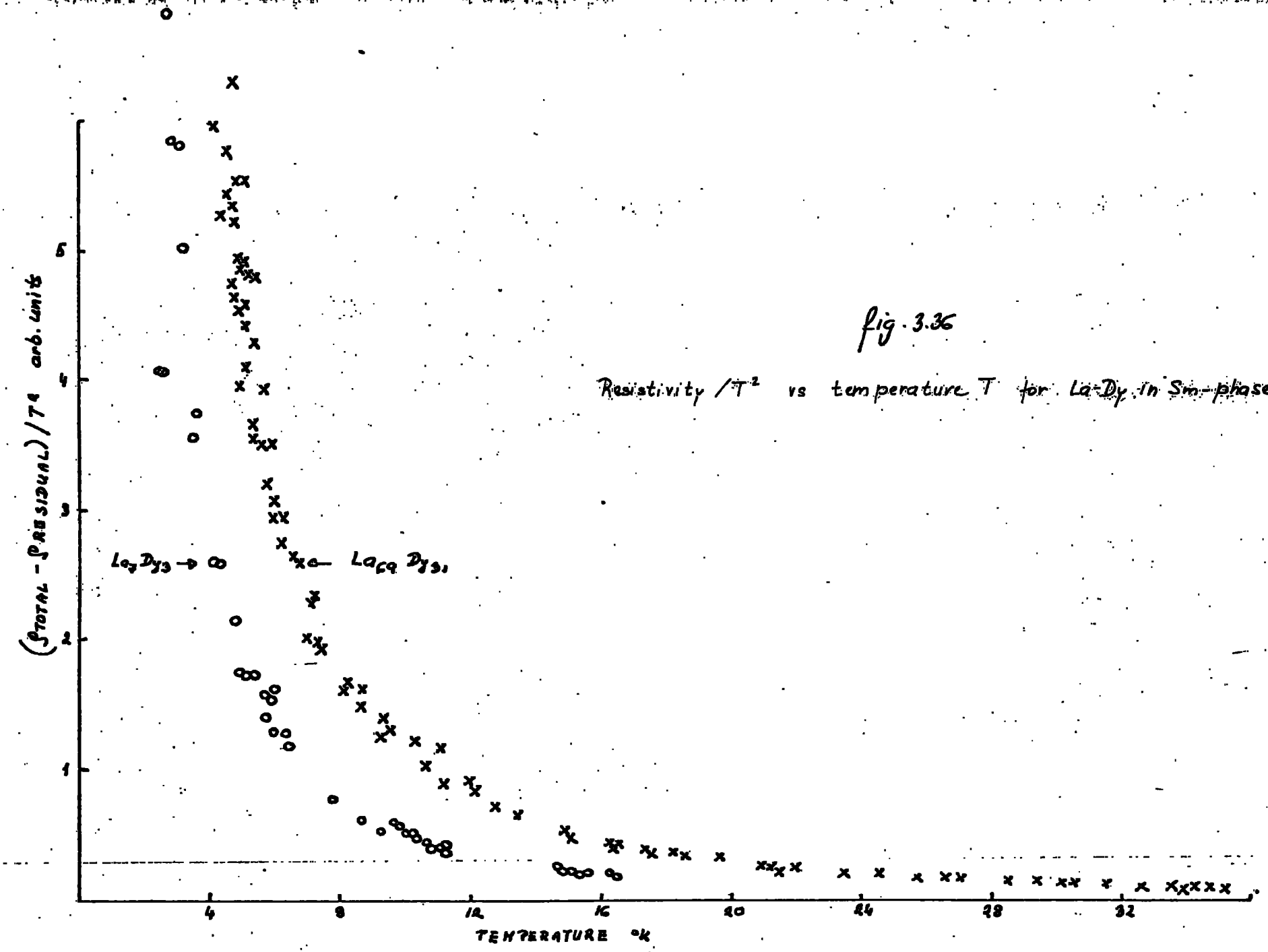

fig. 3.36

Resistivity $/T^2$ vs temperature T for La-Dy in Sm-phase.

fig. 3.37

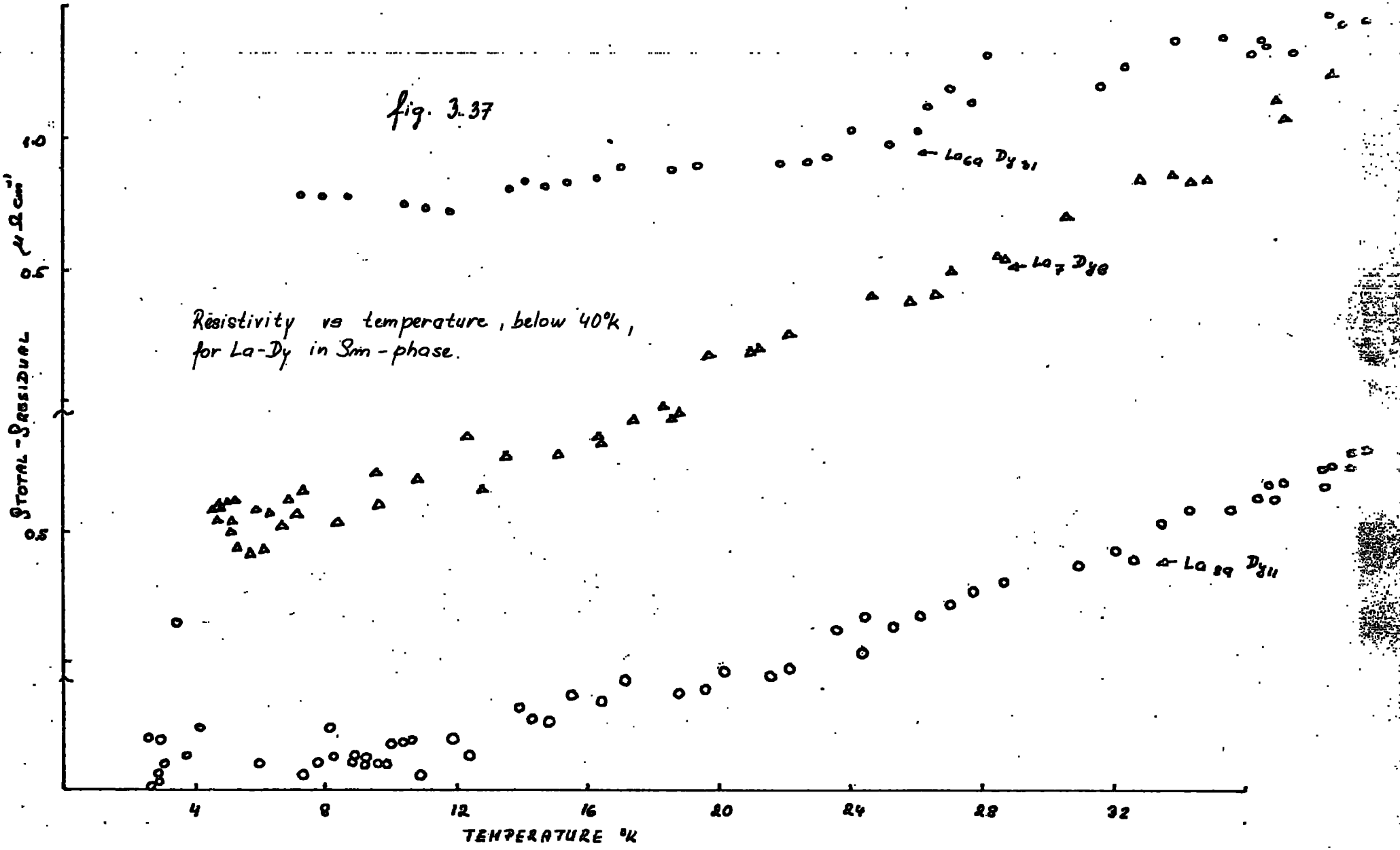

Resistivity vs temperature, below 40°k, for La-Dy in Sm-phase.

fig. 3.38 Resistivity vs temperature, below 40°K, for La-Dy in hcp phase.

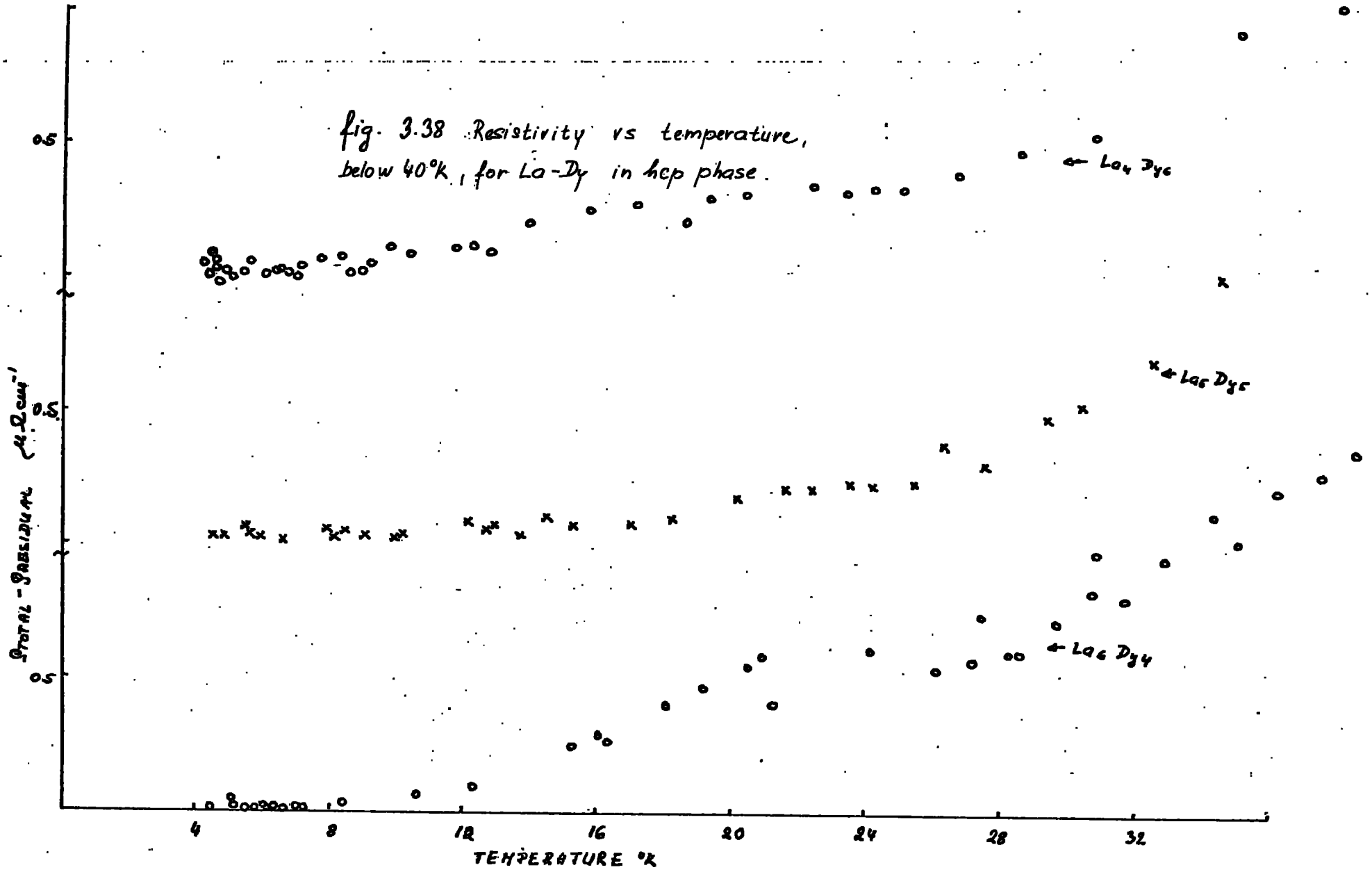

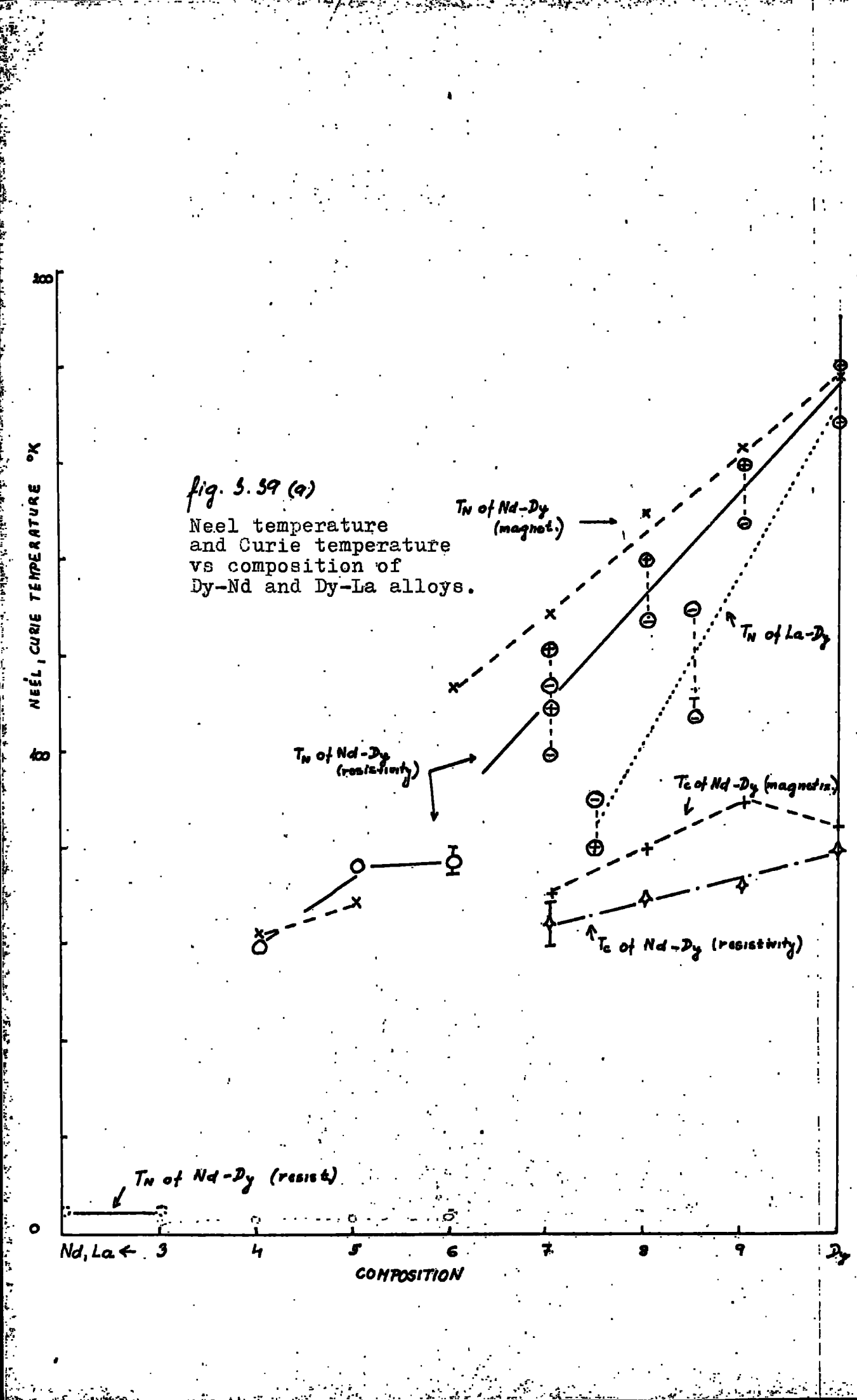

fig. 3.59 (a)

Neel temperature and Curie temperature vs composition of Dy-Nd and Dy-La alloys.

the case of Er-Gd (1-2) as well as in cases presented here, where one element is heavy rare earth or Y and the other is light rare earth the curve is asymmetric. The asymmetry seems to be smaller in the case of Y-Nd, than for the other systems measured. However the curve for Gd-Y(1-3) is known to be symmetric consequently when accounting for the asymmetry in the Y-Nd alloys the differences in the crystal structure should be considered in addition to the different magnetic properties of the light rare earths.

Figure 3.39 presents the variation of the Neel and Curie temperatures, with composition as deduced from electric and magnetic measurements. It does not follow any obvious law but clearly distinguishes the different crystallographic phases.

Figure 3.40-41 displays the variation of ρ_{spin} with the arithmetic combinations of the de Gennes factor $G_{\pm}$ where

$G_{\pm} = G_1 (1-c_2) \pm c_2 G_2$

c_2 are % of impurity (alloyed element), and

$G_i = (g_i-1)^2 J_i (J_i+1)$,

on a logaritmic scale. ρ_{spin} has been sub tracted in the generally accepted way, described in (20) , for instance. Contrary to the conclusion drawn on the basis of experimental results for heavy-heavy alloys or heavy-Y measured by (1-2,3) the variation of ρ_{spin} vs $G_{\pm}$ follows a power law in each phase but its variation is more complicated than previously thought. Alternatively the assumption of an effective G (here $G_{\pm}$) is too simple to account for the observations. The simple power law could be conserved, if $G_{ei} \leq G_{\pm}$ would be considered for alloys. The second explanation seems to be supported by the similarity in the behaviour of the rare earth alloys and pure elements.

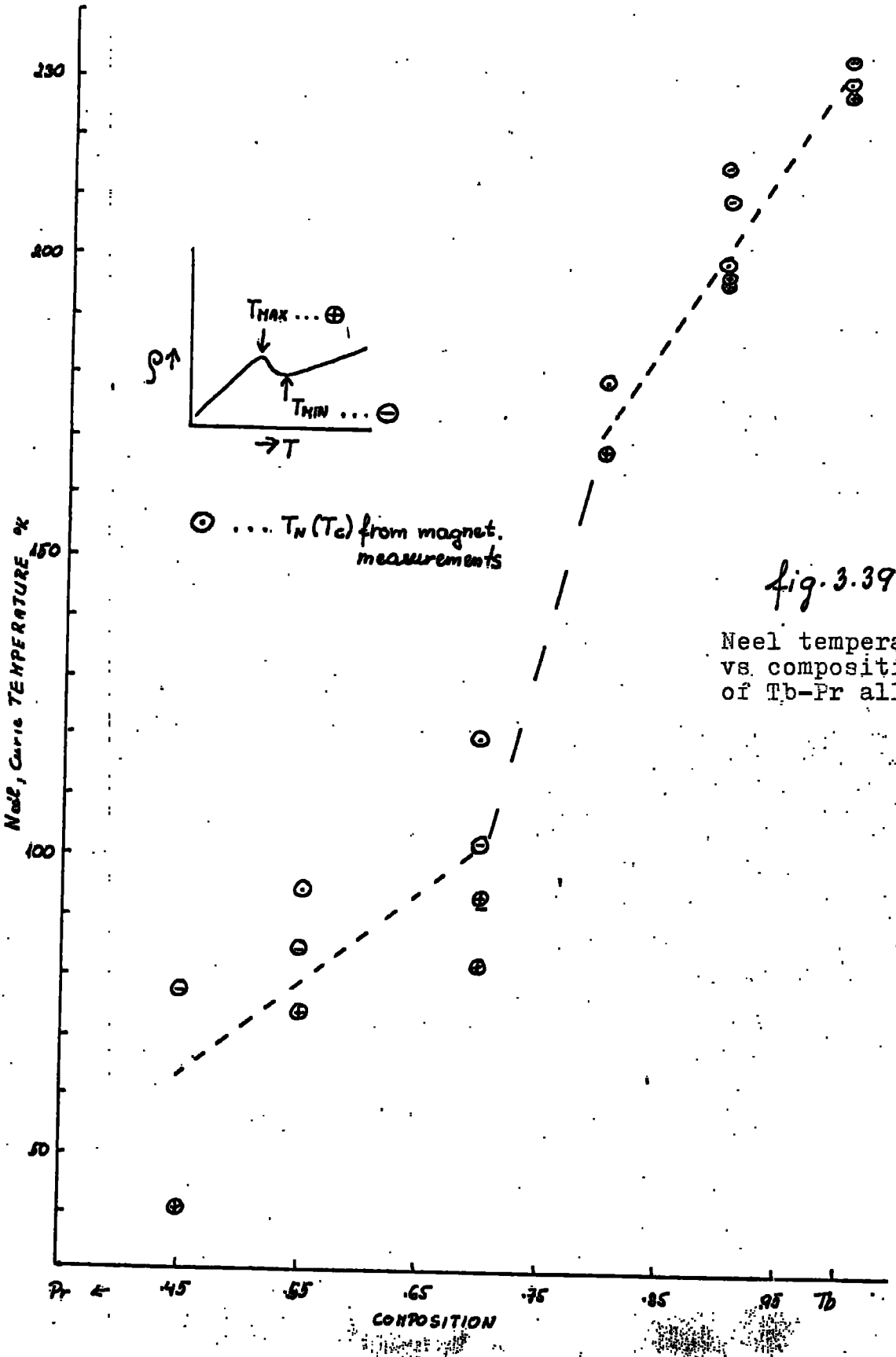

fig. 3.39 (b)

Neel temperature vs. composition of Tb-Pr alloys.

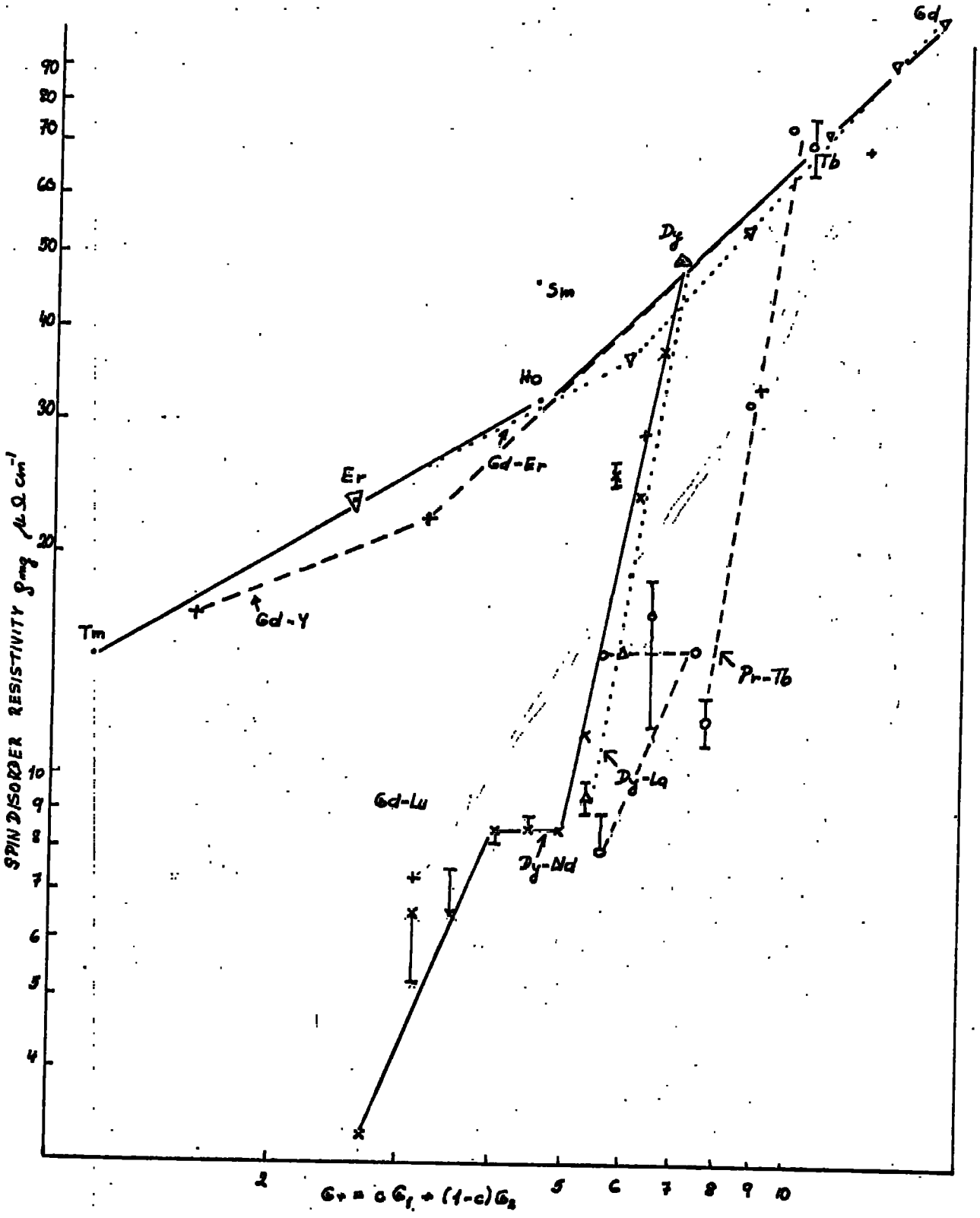

fig. 3.40 Spin-disorder resistivity vs de Gennes factor G for pure rare earths and vs reduced de Gennes gactor G+ for rare earth alloys.

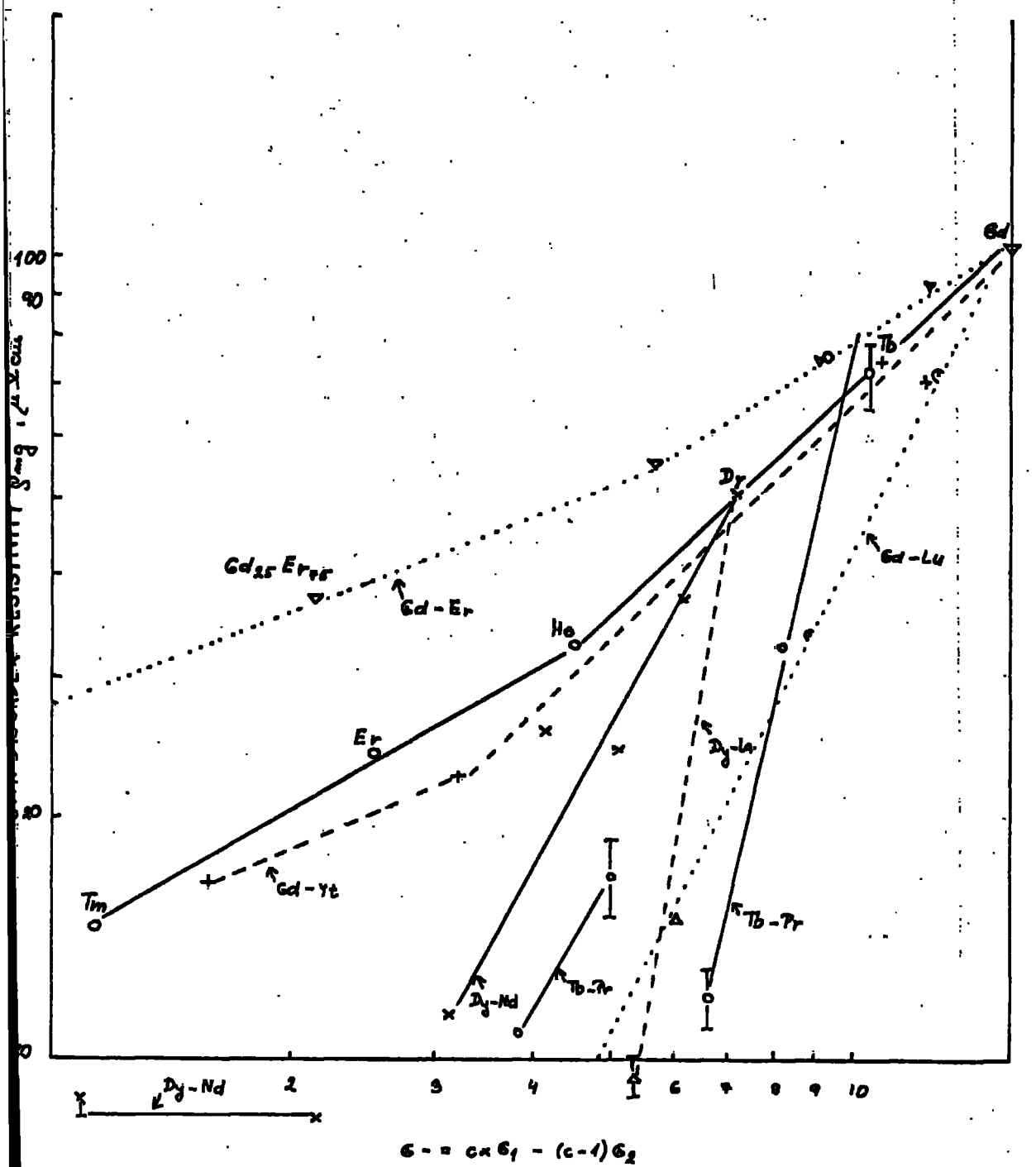

$$G- = c\alpha G_1 - (c-1)G_2$$

fig. 3.41 Spin-disorder resistivity vs de Gennes factor G for pure rare earths and vs reduced de Gennes factor G- for rare earth alloys.

fig. 3.42
(dρ/dT) vs temperature for Pr-Tb alloys

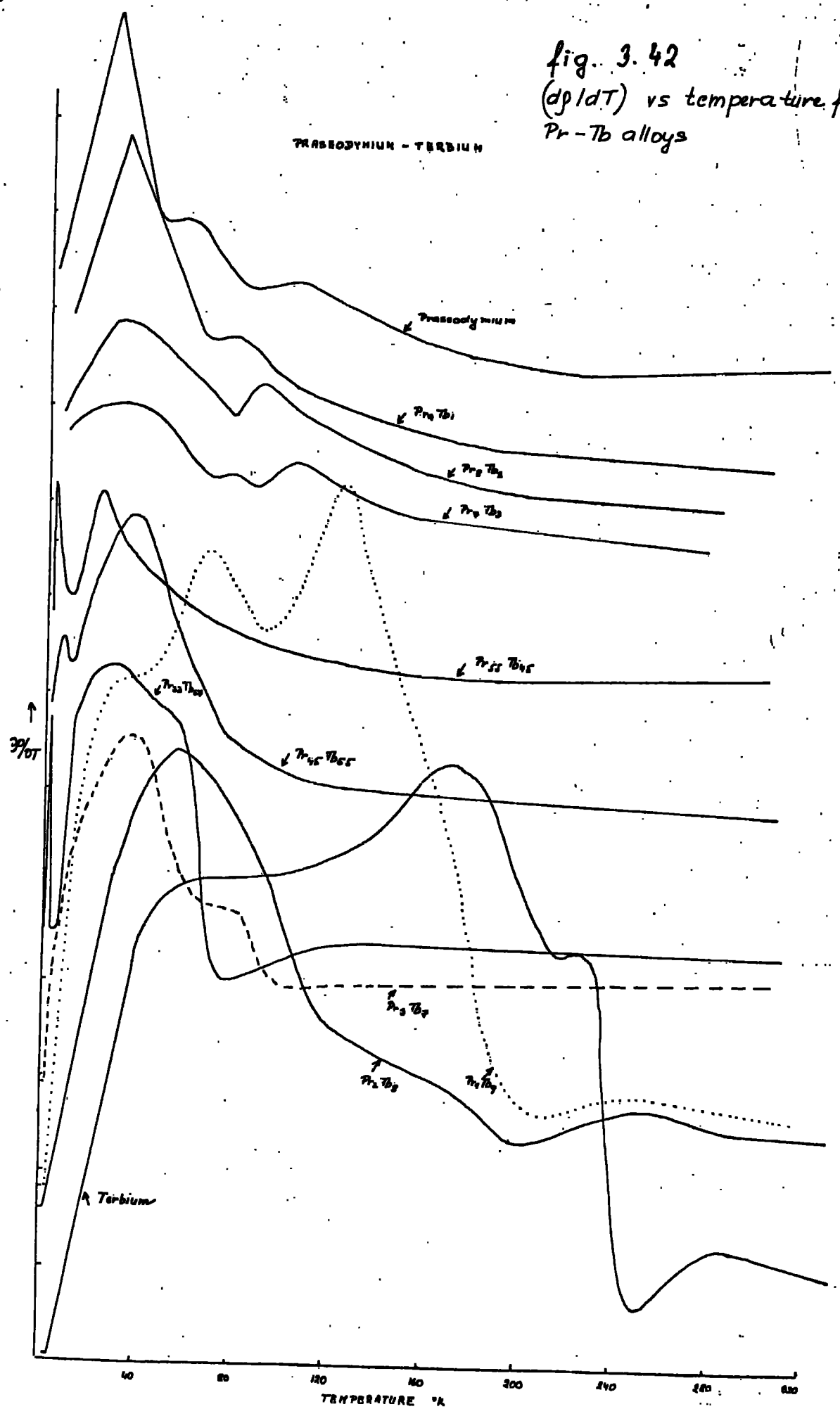

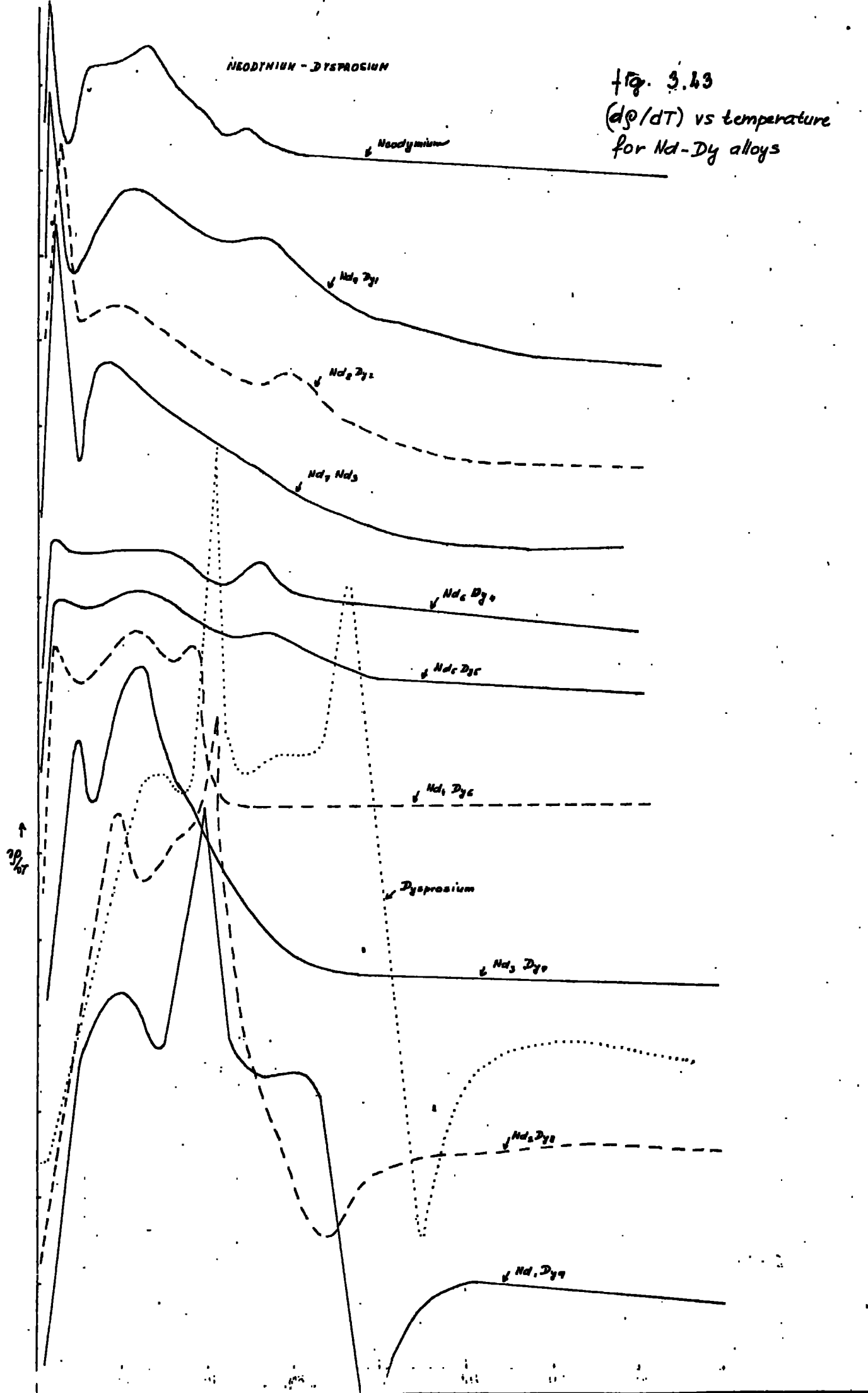

fig. 3.43
$(d\rho/dT)$ vs temperature
for Nd-Dy alloys

fig. 3.44
(dρ/dT) vs temperature
for Y - Nd alloys

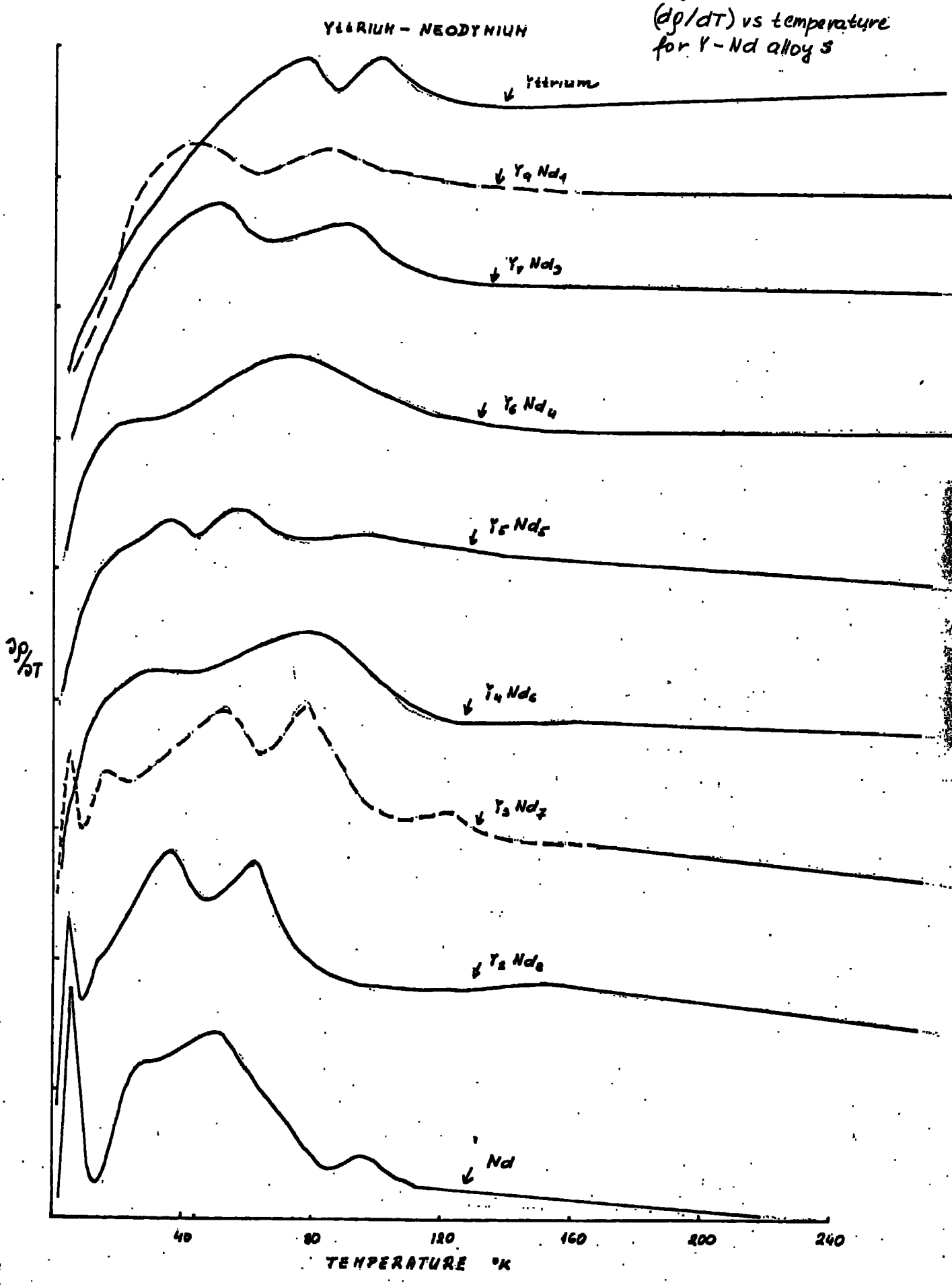

fig. 3.45

Lanthanum - Dysprosium

(dg/dT) vs temperature for La-Dy alloys

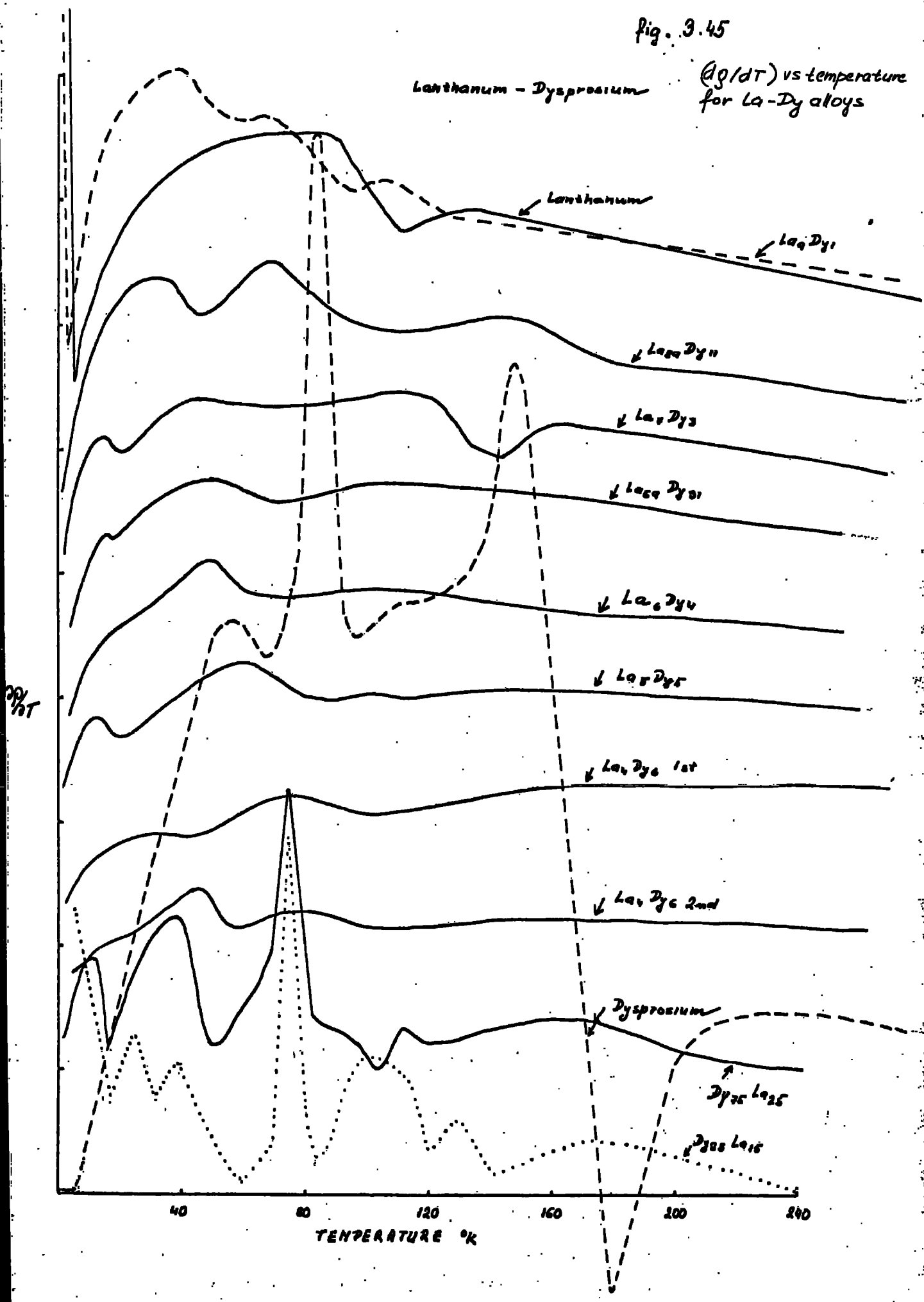

Tb_xPr_{1-x}	ρ_{res}	$\rho_{300°K}$ ($10\,\mu\Omega\,cm^{-1}$)	ρ_{s-f}	T_{N1}	T_{N2} °k	T_N mg	crystal structure
1.0	0.45	10.70	7.9	223	228	220,230	hcp
0.9	3.93	14.70	7.5	196	-	200	hcp
0.8	3.31	9.77	3.2	168	-	180	hcp
0.7	6.46	10.87	1.1	93	-	120	hcp
0.67	5.16	9.84	1.5	70	-		Sm
0.55	5.30	10.70	1 4	74	-	95	Sm
0.45	4.13	8.04	0.8	41	-		Sm
0.3	3.04	7.37	-	-	-	-	d-hex
0.2	1.66	7.00	-	-	-	-	d-hex
0.1	1.36	7.26	-	-	-	-	d-hex
0.0	0.23	5.00	-	-	-	-	d-hex

Table 3.5 Resistivity and magnetic data for Tb-Pr alloys.

Tb_xPr_{x-1}	T^oK	n	T^oK	n	T^oK	n
1.0	18-50	2.58	55-200	1.39	230-300	0.36
0.9			8-130	1.47		
0.8	20-50	2.32			120-300	0.41
0.7			16-55	1.72	110-300	0.70
0.67			10-35	1.25	60-300	0.52
0.55			8-40	1.38	55-300	0.61
0.45			8-40	1 37	55-300	0.72
0.3			10-50	1 09	100-300	0.73
0.2			15-60	1.22		
0.1			16-60	1.24		
0.0			10-35	1.52		

Table 3.4 Coefficient n for Pr-Tb alloys.

Dy_xNd_{1-x}	T^oK	n	T^oK	n	T^oK	n
1.0	16-80	1.54	130-180	0.97	180-300	0.09
0.9	18-55	1.97	65- 90	1.63	200-300	0.45
0.8	20-50	1.87	50- 82	1.46	150-300	0.53
0.7	13-60	1.53			75-300	0.48
0 .6	20-60	1.16			200-300	0.60
0.5	20-60	1.16			140-300	0.58
0.4	17-55	1.27			80-300	0.64
0.3	32-130	0.97				
0.2	5-50	0.60				
0.1	12-35	0.81				
0.0	8-45	1.16				

Table 3.6 Coefficient n for Nd-Dy alloys.

Dy_xNd_{1-x}	ρ res. ($10^{-4}\Omega cm^{-1}$)	ρ 300°K	ρ_{s-f}	T_C el	T_C mg	T_{N1} °K	T_{N2}	T_N mg	crystal structure
1.0	0.89	9.52	5.0	80	85	169	180	179	hcp
0.9	2.74	11.10	3.7	73	90	148	160	164	hcp
0.8	5.99	14.35	2.4	70	80	128	140	150	hcp
0.7	4.88	10.92	2.5	65	71	100	110	129	hcp
0.6	5.76	10.58	1.2	-	-	75	80	114	hcp+Sm
0.5	3.09	6.92	0.7	-	-	(76)	-	70	Sm
0.4	3.49	7.05	0.4	-	-	(60)	-	63	Sm
0.3	0.82	7.66	-	-	-	6	19	-	d-hex
0.2	0.93	7.30	-	-	-	6	23	-	d-hex
0.1	1.35	8.10	-	-	-	6	21	-	d-hex
0.0	1.21	6.05	-	-	-	7	19	7,19	d-hex

Table 3.7 Resistivity and magnetic data for Dy-Nd alloys.

Dy_xLa_{1-x}	T°K	n	T°K	n	T°K	n
1.0	16-80	1.54	130-180	0.97	180-300	0.09
0.85	8-25	1.18	45- 90	0.74	180-300	0.61
0 .75	3-45	1.25	90-300	0.74		
0.6	15-250	0.96				
0.5	20-100	1.41	100-250	0.97		
0.6	15-110	1.08	120-300	0.79		
0.3	16-170	1.40	170-300	0.67		
0.11	8-150	1.06				
0.1	35-130	1.05				
0.0	15-55	1.78				

Table 3.10 Coefficient n for La-Dy alloys.

Y_xNd_{1-x}	T°K	n	T°K	n	T°K	n
1.0	20-80	2.00	100-200	1.01		
0.9	25-50	2.15	55-140	1.22	140-300	0.85
0.7	23-55	2.50	55-160	1.10	160-300	0.75
0.6			16-150	1.24	150-300	0.85
0.5			16- 80	1.40	120-300	0.88
0.4	15-35	1.54	35-150	1.31	150-300	0.82
0.3			15-110	1.47	110-300	0.81
0.2	8-30	1.13	40-125	0.98	125-300	0.72
0.0	8-45	1.16				

Table 3.8 Coefficient n for Y-Nd alloys.

Y_xNd_{1-x}	ρ_{res} ($10\mu\Omega cm^{-1}$)	ρ_{300^oK}	$\rho_{c.f.}$ ($\mu\Omega cm^{-1}$)	crystal structure
1.0	2.88	8.77	0.0	hcp
0.9	4.03	8.65	0.0	hcp
0.7	6.09	9.61	3.0	hcp
0.6	6.25	9.71	5.5	hcp
0.5	6.39	9.96	5.5	hcp
0.4	4,89	8.77	5.7	hcp+Sm
0.3	4.03	8.35	9.0	Sm+d-hex
0.2	3.20	7.04	8.6	d-hex
0.0	1.21	6.05	13.2	d-hex

Table 3.9 Resistivity data for Y-Nd alloys.

Dy_xLa_{1-x}	ρ_{res} $10\,\mu\Omega\,cm^{-1}$	ρ_{300^oK}	ρ_{s-f}	T_C el °K	T_C mg	T_{N1}	T_{N2}	T_N mg	cryst. str.
1.0	0.89	9.52	5.0	80	85	169	180	179	hcp
0.85	7.01	10.67	1.5		-	104	120	135	hcp
0.75	7.59	10.90	1.0		-	80	91	105	hcp
0.6	7.20	10 25	0.2			(70)	-	68	hcp
0.5	6.15	8.89	(0.1)			-	-		hcp
0.4	5.20	8.08	(0.1)			-	-		hcp+Sm
0.3	3.83	7.17	-	-	-	-	-	-	Sm
0.11	2.71	6.45	-	-	-	-	-	-	d-hex
0.1	0.13	5.31	-	-	-	-	-	-	d-hex
0.0	0.03	4.40	-	-	-	-	-	-	d-hex

Table 3.11 Resistivity and magnetic data for Dy-La alloys.

CHAPTER FOUR

THEORETICAL PART

4.1 Introduction

The electronic properties of light-heavy rare earth alloys have been examined by means of measuring electric conductivity over a wide temperature range.

Any transport properties which arise either partly or entirely from electron motion in a solid are critically dependent upon the various types of electron scattering mechanism which exist within the solids. In normal non-ferromagnetic metals these can be considered to have two principal forms, namely phonon scattering due to the interaction of the electrons with thermal vibrations of the lattice, and impurity scattering. The first of these contributions is responsible for the linear dependence of the observed resistivity of a metal on temperature at normal temperatures and the second appears as a small temperature independent contribution to the total resistivity which is only appreciable at low temperatures and is responsible for the non-zero resistivity of all normal conductors at absolute zero. At low temperatures ($T<T_{Debye}$) the phonon scattering contribution changes from a simple proportionality to the temperature to a term of the form $\rho_{phonon} \sim T^5$ (Bloch-Grüneisen equation). Each of these scattering mechanisms contribute to the total resistivity, and its value at any temperature may be written, assuming Matthiessen's rule:

$$\rho_{total} = \rho_{residual} + \rho_{phonon} ,$$

where $\rho_{residual}$ is the resistivity arising from impurity

scattering and ρ_{phonon} is the temperature dependent scattering term due to lattice vibrations, the precise dependence being governed by the temperature of the lattice through the Bloch-Gruneisen equation.

In magnetically ordered metals there is a further contribution to the resistivity arising from disorder of the atomic moments. For a parallel alignment of all the moments its magnitude is zero, but with increasing deviation from this idealized picture, as happens for example, on raising the specimen temperature from absolute zero, the disorder scattering increases to a maximum constant value in the disordered paramagnetic state.

In addition to these scattering processes, any effect which changes the number of electrons available for conduction will also change the magnitude of the observed resistivity

In this chapter will be presented the theory of conductivity in metals especially with three specific solutions of the general Bloch equation in zero external magnetic field.

Generally heavy rare earths and alloys in the hcp phase are better characterized by a solution of the Bloch transport equation where elastic scattering plays the most important role. This solution will be described separately in this chapter.

Light rare earths and alloys in the d-hex phase do not seem to be well described by the approximation widely used for the heavy rare earths. Consequently the second part of this chapter will be devoted to the theory of electron scattering which we believe is taking part to a great extent in

normal light rare earths, and especially in Pr.

In the third part this solution of the scattering which is taking place in Pr for example, would be extended to magnetically ordered metals, e.g.Nd.

Finally since measurements on La-Dy and some alloys in the Sm-phase have been made, a simplified theory where the conductivity is affected by the abrupt changes in density of states in the vicinity of Fermi level will be presented as it is generally believed (1-11,1-42) that scattering mechanisms of this type are the most important in these cases.

4.2 Theory of resistivity in normal heavy rare earths

In the normal rare earths, the f-shell is deeply buried inside the electron cores, the unpaired f-electrons are localized on the particular atoms. Thus it has been suggested by (1) and (2) that the resistivity of the rare earth is determined largely by an exchange interaction between the conduction electrons and the localized spins. This interaction is modified by the crystal field (1-33) caused by the structural anisotropy. If the exchange interaction is sufficiently strong, disorder of the system will produce an appreciable contribution to the resistivity in the form of the spin disorder term (3). This is particularly true for magnetic metals and consequently for heavy rare earths and rare earth alloys having the hcp crystal structure.

The main differences between the heavy rare earths and say the transition metals are twofold;

1) as already mentioned one is the relatively big separation of 'magnetic' - 4f electrons belonging to the different atoms.

2) the second is due to the existence of a big anisotropy in the rare earths which significantly affects the transport properties.

In the basal plane (001) the resistivity decreases, with temperature as the magnetic order increases, in a way similar to that observed in ferromagnetic metals like Fe and Ni (11), and most of the anomalies in the transport properties are due to the behaviour along the c-axis.

All the observed antiferromagnetic orderings are such that the moments are the same for all the atoms in a plane and a wave variation occurs from plane to plane along the hexagonal axis. This suggests that the striking resistivity changes are associated with the effect of this order on the conduction electrons. Since the spin ordering has a periodicity different from that of the lattice, new Brillouin zone boundaries are introduced perpendicular to the c-axis.

Further the model is described which was first published by (11) to account for the resistivity behaviour of the heavy rare earths. As in most models where the transport properties are described we first should lay down simplifiing assumptions. In our case these are:

1) The f electrons are taken to be completely localized on each site, in the ground multiplet of the trivalent ion with total angular momentum J, and spin angular momentum S, given by Russell-Saunders coupling.

2) The conduction electrons are assumed to occupy a simple conduction band with energies $E(\bar{k})$.

3) The conduction electrons interact with the magnetic ions with energy

$h = 1/N \sum_n V\delta(\bar{r}-\bar{R}_n)\,\bar{S}_n\bar{\sigma}$ ... /1/

where V is an effective exchange energy between a conduction electron of spin $\bar{\sigma}$ and an ion centred at the lattice point $\bar{R}_n$. The δ-function is an approximation which gives a constant scattering cross section for all electron collisions.

4) The transport properties are explained in terms of a relaxation time τ (and Matthiessen's rule) where

$1/\tau = 1/\tau_i + 1/\tau_p + 1/\tau_s$ ... /2/

τ_i is due to residual impurity scattering and is taken to be independent of temperature, τ_p is due to phonon scattering and is given by a Grüneisen function ($\tau_p \sim T$ at $T \gg T_{Debye}$; $\tau_p \sim T^5$ at low temperatures), τ_s is due to spin disorder scattering via interaction /1/. (14) and (2) have shown that τ_s in the case discussed may be approximated as

$1/\tau_s \sim V^2 \left(1 - (\langle \bar{S} \rangle^2 / S(S+1))\right)$ ... /3/

i.e. it is proportional to the disorder in the magnetic moments. S_n^i could be defined as

$\langle S_n^z \rangle = MS \cos(\bar{q}\bar{R}_n + \phi)$ ... /4/ ... type I

$\langle S_n^x \rangle = M'S \cos(\bar{q}\bar{R}_n)$

$\langle S_n^y \rangle = M'S \sin(\bar{q}\bar{R}_n)$ ... /5/ ... type II

where $\bar{q}$ is parallel to the c axis and gives a wave like moment variation along this axis. For example the structure described by /4/ occurs in the high temperature phase of Er and Tm, eq. /5/ describes the high temperature phase of Tb, Dy and Ho etc.

With a combination of /4/ and /5/ electron states of wave vector $\bar{k}$ are coupled to those of $\bar{k}'$, by the matrix elements of /1/. As

$\bar{S}\bar{\sigma} = MS\,\sigma_z \cos(q_z + \phi) + 1/2\, M'S\,(\sigma_+ \exp(-iqz) + \sigma_- \exp(iqz))$

only the following matrix elements are non-zero:

$\langle \bar{k} \pm | H | \bar{k}' \pm \rangle = \pm 1/2\ VSM$ ... $\bar{k}-\bar{k}' = \bar{\tau} \pm \bar{q}$ ... /7a/

$\langle \bar{k} + | H | \bar{k}' - \rangle = VSM'$ ... $\bar{k}-\bar{k}' = \bar{\tau} + \bar{q}$ ... /7b/

$\langle \bar{k} - | H | \bar{k}' + \rangle = VSM'$ ... $\bar{k}-\bar{k}' = \bar{\tau} - \bar{q}$ ... /7c/

where $\bar{\tau}$ is an reciprocal lattice vector. The spin states of the conduction electrons $|\pm\rangle$ are defined relative to the z axis.

From /7a/ it is clear that ordering of type I mixes band states of the same spin polarization. This mixing is greatest when $E(\bar{k}) = E(\bar{k}')$, i.e. $\bar{k}=\bar{k}'=\pm 1/2\ (\bar{\tau} \pm \bar{q})$ ... /8/. This gives new zone boundaries in each spin sub-band, in a reduced zone picture, which are perpendicular to the c axis at $\pm 1/2\ q$ and the energy gap at the boundaries is VSM.

Ordering of the second type gives, from /7b/ and /7c/, a different result for two spins orientations. There is a strong mixing between $|1/2\ (\bar{\tau}+\bar{q}),+\rangle$ and $|-1/2\ (\bar{\tau}+\bar{q}\ ),-\rangle$ with a new zone boundary but there is no boundary for the other sub-band at this point, which has a boundary at $\pm\ 1/2\ (\bar{\tau}+\bar{q})$. So that in the reduced zone boundary there is plane $z=+1/2\ q$ for + spins and $z=-1/2\ q$ for - spins. The energy gap is 2VSM' in each case. Generally, if both types of ordering are present, a 4x4 secular determinant is involved (for the states $|\bar{k}, \pm\rangle$, $|\bar{k}+2\bar{L}, \pm\rangle$, where $2\bar{L}=\pm(\bar{\tau}+\bar{q})$ is the reciprocal vector associated with the new boundaries. The energy $E'(\bar{k})$ has than form:

$$E'(\bar{k}) = 1/2\ (E(\bar{k})+E(\bar{k}+2\bar{L}) \pm ((E(\bar{k})-E(\bar{k}+2\bar{L}))^2+V^2S^2M_{\pm}^2)^{1/2}) \quad .../9/$$

where $M_{\pm}^2 = M^2 + 2M'^2 \pm 2M'(M^2 + M'^2)^{1/2}$ ... /10/

and the gap $\Delta = VSM \pm$ ... /11/ so that for the first type of ordering: $M'=0$, $M^{\pm} = M$ and for the second type of ordering: $M=0$, $M^{\pm}=2M', 0$. Since

$$\sigma_{ij} = (e^2\tau/4\pi M) \int v_i\ dS_j \quad ... \quad /12/$$

is the expression for the conductivity tensor with $\bar{v}$ being

the group velocity vector defined as $\bar{v} \sim 1/\hbar\ (\partial E/\partial k)$, than it follows that the magnetic ordering causes a change in the energy bands by introducing new zone boundaries, and hence, a change in the Fermi surface.

If the scattering formula /3/ is extended to the case of general ordering following the procedure described in (11) for the idealized case of a spherical Fermi surface, we can get the following expression for the resistivity

$$\rho^{o}_{zz} = \alpha + \beta T + \gamma(1-1/2\ M^2 - M'^2) \quad \ldots \quad /13/$$

$$\rho^{o}_{xx} = \alpha + \beta' T + \gamma'(1-1/2\ M^2 - M'^2) \quad \ldots \quad /14/$$

If the new zone boundaries are not very close to the Fermi surface and $\delta \sim \Delta$, then

$$\delta = (\alpha + \beta T + \gamma(1-1/2\ M^2 - M'^2))/(1 - \Gamma'(M^2 + M'^2)^{1/2})$$

and similarly for ρ_{xx}, where α and β are parameters depending on the geometry of the Fermi surface.

4.3 Resistivity of nonmagnetic crystal with magnetic impurities

Van Peski-Tinbergen and Dekker (5) have derived a general expression for metal electrons suffering various kind of elastic and inelastic scattering under the following assumptions.

1) The matrix of the various scattering mechanisms are known.

2) The inelastic scattering is based on the interaction between the conduction electrons and the magnetic impurities . This is believed to give a good qualitative picture even in case of a paramagnet. Collisions of this type may or may not be elastic, depending in general on whether the collision proceeds without or with spin flip. So any energy transfer between the scattered electrons and scattering

centres should be taken into account. As spin-dependent scattering in general leads to different relaxation times for conduction electrons with magnetic quantum number $m_s = +1/2$ and $m_s = -1/2$ 'plus' and 'minus' electrons are normally considered separately. But in the case of zero external field these may be equated from the start.

3) A further assumption is that of a single conduction band for which the energy as a function of k (the wave vector of an electron) is assumed to be of the form

$$E(\bar{k}) = E_o + \hbar^2 k^2 / 2m^*$$

where m^* is an effective mass. In thermal equilibrium and in the absence of electric, or non-uniform magnetic fields, the fraction of the states occupied by electrons is given by the Fermi-Dirac distribution function:

$$f_o(E) = f_o(\bar{k}) = (\exp((\hbar^2 k^2/2m^* \pm \Delta E - E_F)/KT)+1)^{-1}$$

for $m_s = \pm 1/2$.

4) The electron densities $n_\pm$ differ from 1/2 n (n is the total electron density) only by a term of the order $\Delta E/E_F$ which is negligible for most of our purposes as long as the whole system is in thermal equilibrium. Though the electron densities are further considered to be constant .

In a state of steady electron current, under the influence of an electric field F_x along the x-axis, the density of electrons corresponding to $d\bar{k}$ is given by $(1/8\pi^3)\, f_\pm(\bar{k})d\bar{k}$. If e represents the charge of an electron, the rate of change $f_\pm(k)$ produced by the field F_x equals:

$$(\partial f_\pm/\partial t)_{field} = (eF_x \hbar k_x/m^*)(\partial f_{o\pm}/\partial E_\pm) \quad \ldots \quad /1/$$

If the rate of change $f_\pm$ due to scattering processes can be described by a relaxation time $\tau_\pm(\bar{k})$, we may write

$$(\partial f_{\pm}/\partial t)_{\text{collision}} = -(f_{\pm} - f_{o\pm})/\tau_{\pm} \quad \ldots \quad /2/$$

In a steady state the sum of /1/ and /2/ must vanish

$$f_{\pm} - f_{o\pm} = (-eF_x \hbar k_x \tau_{\pm})/m^* \, (\partial f_{o\pm}/\partial E) \equiv g_{\pm}(\bar{k}) \quad \ldots \quad /3/$$

Once the relaxation times $\tau_{\pm}$ are known the electrical conductivity, σ_e, follows directly from $\sigma_e = \sigma_{e+} + \sigma_{e-}$ and from

$$\sigma_{e\pm} = j_{x\pm}/F_x = (e/F_x) \int 1/(8\pi^3) \, d\bar{k} \, (f_{\pm} - f_{o\pm}) \, \hbar k_x/m =$$
$$= (-e^2/6\pi m) \int k^3 \tau_{\pm} \, (\partial f_{o\pm}/\partial E_{\pm}) \, dE_{\pm} \quad \ldots \quad /4a/$$

This transport equation could be generalized in terms of relevant matrix elements. If $P_i(\bar{k}_+ \rightarrow \bar{k}'_+)$ and $P_j(\bar{k}_+ \rightarrow \bar{k}'_-)$ denote transition probabilities for various elastic and inelastic processes, then

$$(\partial f/\partial t)_{\text{coll.}} = (1/8\pi^3) \int d\bar{k}'_+ \, (-\Sigma_i P_i(\bar{k}_+ \rightarrow \bar{k}'_+) \, f_+(1-f'_+) +$$
$$+ \Sigma_i P_i(\bar{k}'_+ \rightarrow \bar{k}_+) \, f'_+(1-f_+) +$$
$$+ (1/8\pi^3) \int d\bar{k}'_- (-\Sigma_j P_j(\bar{k}_+ \rightarrow \bar{k}'_-) \, f_+(1-f'_-) +$$
$$+ \Sigma_j P_j(\bar{k}_- \rightarrow \bar{k}_+) \, f'_-(1-f_+)) \quad \ldots \quad /4b/$$

In absence of field we can write

$$\Sigma_i P_i(\bar{k}'_+ \rightarrow \bar{k}_+) = \Sigma_i P_i(\bar{k}_+ \rightarrow \bar{k}'_+) \, f_{o+}(1-f'_{o+})/f'_{o+}(1-f_{o+}) \quad \ldots \quad /5/$$

and similarly for P_j. If we further consider only terms linear in g and the following simplifying relations

a) $f_{o\pm}(1-f_{o\pm}) = -k_B T \, (\partial f_{o\pm}/\partial E_{\pm}) \quad \ldots \quad /6/$ and

b) $f_{o+}(1-f'_{o+}) = -k_B T \, (\partial f_{o+}/\partial E_+)(1/(1-f_{o+}(1-\exp(-\varepsilon_j/k_B T)))) \quad /7/$

where $\varepsilon_j = E'_- - E_+ = -2\Delta E_+ + (\hbar^2/2m)(k'^2_- - k^2_+)$ and

$\varepsilon_i = E'_+ - E_+ = \hbar^2/2m \, (k^2_+ - k^2_-)$ than

using equation /3/,/6/ and /7/ we can get the following expression

$$(\partial f_+/\partial t)_{\text{coll.}} = -g_+((1/8\pi^3) \int dk'_+ \, \Sigma_i P_i(k_+ \rightarrow k'_+)(1-k'_x/k_x) x$$
$$(1/(1-f_o(1-\exp(-\varepsilon_i/k_B T))) +$$
$$+ (1/8\pi^3) \int dk'_- \, \Sigma_j P_j(k_- \rightarrow k'_-)(1-\tau_- k'_x/\tau_+ k_x) x$$
$$(1/(1-f_o(-\exp(-\varepsilon_j/k_B T))) \equiv -g_+/\tau_+ \quad \ldots \quad /8/$$

defining the relaxation time of the scattering involved.

Before another step is made it is necessary to make further limiting assumptions. They are the following:

1) The transition probabilities depend only on the magnitude of $\bar{k}'$ and $\bar{k}$ and on the angle of scattering θ.

$$P_i(k_+ \to k'_+,\theta) = (2\pi/\hbar)|M_i(k_+ \to k'_+,\theta|^2 N_i \delta(E'_+ - E_+ - \varepsilon_i) \quad \ldots /9/$$

M_i is the matrix element, corresponding to a single scattering center of type i and N_i as the number of scattering centers. If the volume element $d\bar{k}$ in k space is expressed as $2\pi \sin\theta d\theta k'^2 dk' = (2\pi m^*/\hbar^2) k' \sin\theta d\theta dE'$ equation /8/ has the form

$$1/\tau_+ = (mk/2\pi\hbar^3)\Big(\sum_i \int_0^{\pi} N_i |M_i(k_+ - k'_+,\theta)|^2 (1-\cos\theta)\sin\theta d\theta \times (1/(1-f_{o+}(1-\exp(-\varepsilon_i/k_BT))))+ + \sum_j \int_0^{\pi} N_j |M_j(k_+ - k'_-,\theta)|^2 (1-(\tau_-/\tau_+)\cos\theta)\sin\theta d\theta \times (1/(1-f_{o+}(1-\exp(-\varepsilon_j/k_BT)))) \quad \ldots /10/$$

and similarly for $1/\tau_+$. Substituting /10/ into /4a/ we get the general expression for the conductivity

$$\sigma_{e\pm} = j_{x\pm}/F_x = (e/F_x)\int (1/8\pi^3) d\bar{k} \, (f_\pm - f_{o\pm}) (\hbar k_x/m) = = -(e^2/6\pi^2 m)\int k^3 \tau_\pm (\partial f_{o\pm}/\partial E_\pm) \, dE_\pm \quad \ldots /11/$$

2) In the case of quasielastic scattering when the change in energy of electrons during a collision is small compared to k_BT the numerators $(1-f_o(1-\exp(-\varepsilon/k_BT)))$ in $1/\tau$ may be omitted.

3) The integral in equation /11/ may be approximated by the first member of the series evaluated in E_F if the higher terms of the series are smaller than the first one by powers of k_BT/E_F. That is when $\varepsilon_{i(j)} \ll k_BT$, $\varepsilon_{i(j)}$ being the energy levels of localized magnetic impurities.

This is so, and the approximation is acceptable only for heavy rare earths at high temperatures, and not in our case. (5) discussed the validity of this simplification at very low temperatures and found them plausible in most cases.

Applying the assumptions made above to equation /11/ we get the well known formula $\sigma_{e\pm} = (n_{\pm}e^2/m^*)\tau_F$ ... /12/ , where τ_F is the relaxation time for electrons with the Fermi energy:

$$1/\tau_F = (m^*k_F/\pi\hbar^3)(\sum_i N_i |M_i(k_{\pm} \rightarrow k'_{\pm})|^2 (2/(1+\exp(-\varepsilon_i/k_BT))) + \sum_j N_i |M_j(k_{\pm} - k'_{\pm})|^2 (2/(1+\exp(\varepsilon_i/k_BT))) \quad \ldots \quad /13/$$

and $k_F \sim (2m^*E_F/\hbar^2)^{1/2}$.

4) The equation /13/ is applicable only in the case of isotropic scattering when the term containing (τ_-/τ_+) in equation /10/ would disappear on integration and could be used in our case only for polycrystals of light rare earths.

4.4 Resistivity in light rare erths

Maranzana (6) and Watabe (4) further explored equation /10/ specifying the form of the matrix $M_i|k_{\pm} \rightarrow k'_{\pm}|$.

(6) have assumed a model consisting of a gas of charge carriers and a periodic array of spins with no interaction between them, that is, in the paramagnetic region. In this context spin means the total angular momentum. In the rare earths the total angular momentum results from the L–S coupling as the spin orbit interaction is much bigger than the spin spin interaction. J is a good quantum number . Both Pr and Nd have degenerate J states, the degeneracy being partially lifted by the presence of the crystal field interaction:

$$H_{mag} = N H_{c.f.} \quad \ldots \quad /14/$$

where N is the number of spins present in the crystal, $H_{c.f.}$ is the crystal field Hamiltonian corresponding to the symmetry of the site of the spin. The z-axis is taken as the axis of quantization of the array of spins. Diagonalizing H_{mag} we obtain the energy levels E_m. The charge cariers are described by creation and annihilation operators $a^{\pm}_{k\uparrow}$, $a_{k\uparrow}$,

$a^{+}_{\bar{k}}\downarrow$, $a_{\bar{k}}\downarrow$, $\bar{k}$ is the conduction electron wave vector the arrow indicating the direction of the spins with respect to the z-axis. As the magnetic system is paramagnetic the charge carriers of opposite spin reside in the same band which extends from $-E_1$ to E_1, defining $E_F = 0$. The perturbation Hamiltonian is the s-d Hamiltonian

$$H' = -(J/N)\sum_{\bar{k},\bar{k}',\gamma} \exp(i(\bar{k}-\bar{k}')\bar{R}_\gamma)\, x$$
$$(S^{\gamma}_{z}(a^{+}_{\bar{k}',\uparrow}a_{\bar{k}}\uparrow - a^{+}_{\bar{k}',\downarrow}a_{\bar{k}}\downarrow) + S^{\gamma}_{+}a_{\bar{k}',\downarrow}a_{\bar{k}}\uparrow + S^{\gamma}_{-}a_{\bar{k}',\downarrow}a_{\bar{k}}\downarrow)$$

The matrix elements of the perturbation H' calculated between the unperturbed states defined as a product of a Slater determinant of kets $|\bar{k},\uparrow\rangle$, $|\bar{k},\downarrow\rangle$ times the product of eigenfunction $|E^{\gamma}_{m}\rangle$ relative to the m-th energy level of the r-th ion are:

$$\langle \bar{k}',\uparrow\downarrow, E^1_{m1}, \ldots, E^r_{mr}, \ldots, E^N_{mN} | H' | \bar{k},\uparrow\downarrow, E^1_{m1}, \ldots, E^r_{mr}, \ldots, E^N_{mN}\rangle =$$
$$= -(J/N)(\pm 1)\exp(i(\bar{k}-\bar{k}')\bar{R}_\gamma)\langle E^{\gamma}_{m\gamma} | S^{\gamma}_{z} | E^{\gamma}_{m\gamma}\rangle, \quad \ldots \quad /15/$$

$$\langle \bar{k}',\uparrow, E^1_{m}, \ldots, E^r_{mr}, \ldots, E^N_{mN} | H' | \bar{k},\downarrow, E^1_{m}, \ldots, E^r_{mr}, \ldots, E^N_{mN}\rangle =$$
$$= -(J/N)\exp(i(\bar{k}-\bar{k}')\bar{R}_\gamma)\langle E^{\gamma}_{m'\gamma} | S^{\gamma}_{-} | E^{\gamma}_{m\gamma}\rangle, \quad \ldots \quad /16/$$

$$\langle \bar{k}',\downarrow, E^1_{m1}, \ldots, E^r_{mr}, \ldots, E^N_{mN} | H' | \bar{k},\uparrow, E^1_{m1}, \ldots, E^r_{mr}, \ldots, E^N_{mN}\rangle =$$
$$= -(J/N)\exp(i(\bar{k}-\bar{k}')\bar{R}_\gamma)\langle E^{\gamma}_{m\gamma} | S^{\gamma}_{+} | E^{\gamma}_{m\gamma}\rangle \quad \ldots \quad /17/$$

Considering the transition probabilities to the second approximation $W(a \to b) = W^{(1)}(a \to b) + W^{(2)}(a \to b)$ ... /18/

$$W^{(1)}(a \to b) = (2\pi/\hbar)\delta(E_a - E_b)H'_{ab}H'_{ba} \quad \ldots /19/$$

$$W^{(2)}(a \to b) = (2\pi/\hbar)\delta(E_a - E_b)\sum_{c=a}((H'_{ac}H'_{cb}H'_{ba}(E_a - E_c)^{-1} + \text{c.c.}) \quad /20/$$

where

$$W^{(1)}(\bar{k}\uparrow\downarrow, m \to \bar{k}'\uparrow\downarrow, m') = (2\pi/\hbar)(J/N)^2 \sum_{\gamma}\delta(E_k - E_{k'} + E^{\gamma}_{m\gamma} - E^{\gamma}_{m'\gamma})\, x$$
$$\langle E^{\gamma}_{m'\gamma} | S^{\gamma}_{z} | E^{\gamma}_{m\gamma}\rangle \langle E^{\gamma}_{m\gamma} | S^{\gamma}_{z} | E^{\gamma}_{m'\gamma}\rangle \quad \ldots \quad /21/$$

and similarly for $W^{(1)}(\bar{k}'\uparrow, m \to \bar{k}'\downarrow, m')$ and $W^{(1)}(\bar{k}\uparrow, m \to \bar{k}\uparrow, m')$

averaging them over the occupation of the initial state E_m, summing over the final state and taking into account that the states $|E_m^{\gamma}\rangle$ are the same for every γ we can write

$$W^{(1)}(\bar{k}\uparrow\downarrow \rightarrow \bar{k}\uparrow\downarrow) = (2\pi/\hbar)(J/N)^2 N(\sum_m \exp(-E_m/k_BT))^{-1} \times$$
$$\times(\sum_{m,m'} \exp(-E_m/k_BT)\,\delta(E_k-E_{k'}+E_m-E_{m'})\,|\langle E_{m'}|S_z|E_m\rangle|^2) \quad /22/$$

etc. Similarly in the second approximation. Using now equation /4/ and assuming isotropic scattering and the validity of Matthiessen's rule $1/\tau_{\bar{k}} = 1/\tau_{\bar{k}}^1 + 1/\tau_{\bar{k}}^2$ ... /23/ we get

$$1/\tau_{\bar{k}}^1 = (2\pi/\hbar)(J/N)^2 N\eta(E_F)(\sum_n \exp(-E_m/k_BT))^{-1} \times$$
$$\sum_{m,m'} ((1-f_k^o)\exp(E_m/k_BT)+f_k^o\exp(E_{m'}/k_BT))^{-1} \times$$
$$(|\langle E_{m'}|S_z|E_m\rangle|^2 + |\langle E_{m'}|S_+|E_m\rangle|^2)) \quad ... \quad /24/$$

and similarly for $1/\tau_{\bar{k}}^2$. The conductivity is then given by

$$\sigma \sim \int dE_k\, \tau_k\, (\partial f_k/\partial E_k) \quad ... \quad /25/$$

Watabe (4) used a more precise Hamiltonian

$$H = \sum_{n,q} (g-1)\, \bar{I}(\bar{q})\bar{\sigma}\bar{J}_n \exp(i\bar{q}(\bar{r}-\bar{R}_n)) + \sum_{i,q}(4\pi e^2/(q^2+q_o^2)\exp(-i\bar{q}(\bar{r}-\bar{R}_i)) =$$
$$= \sum_{n,q} (-(g-1)\bar{I}(\bar{q})\bar{\sigma}\bar{J}_n \exp(i\bar{q}(\bar{r}-\bar{R}_n)) +$$
$$+\sum_{i,l}\sum_{m=-l}^{l}(4\pi e)^2/(q^2+q_o^2)\; i^l Y_l^{m*}(\Omega_q) \exp(-i\bar{q}(\bar{r}-\bar{R}_n)) \times$$
$$\underline{j_l(q|R_i-R_n|)\; Y_l^m(\Omega_{R_i-R_n})} \quad ... \quad /26/$$

where they accounted for screening by the outer shells. This represents the potential underlined in equation /26/. This enables them, at least theoretically, to define two different relaxation times in a first approximation; one which is solely due to crystal field arising from an exchange type of interaction the other, underlined, is due to the quadrupole-quadrupole screening interaction:

$$1/\tau_{\bar{k}} = \sigma_{\bar{k}} N/4\pi^2 \hbar v_f^*) \sum_{\gamma,\gamma'} \int (d\Omega_{\bar{k}'}/4\pi)(|\bar{I}(\bar{q})|^2 (g-1)^2 \times$$

$$(|\langle \bar{\gamma}' | \Delta \bar{J}_z | \bar{\gamma} \rangle|)^2 + |\langle \bar{\gamma}' | \Delta \bar{J}_+ | \bar{\gamma} \rangle|^2 + (\alpha_J^2 (4\pi e)^4 (\hbar 2\pi)^2 / (q^2 + q_o^2)^2$$

$$\sum_m |Y_2^m(\Omega_{\bar{q}})|^2 |\langle \bar{\gamma}' | \Delta Y_2^m(J) | \bar{\gamma} \rangle|^2 W_{\bar{\gamma}} (1 - f_o(\epsilon_{\bar{k}} + \Delta_{\bar{\gamma}\bar{\gamma}'})) / (1 - f_o(\epsilon_{\bar{k}}) \quad /27/$$

(4) estimated that both of these effects are of approximately the same order of magnitude for Pr and Nd. In Pr the screening effect is bigger while in Nd the crystal field effect dominates. Because of the difficulty and so uncertainty in subdividing the total resistivity into differant scattering mechanisms in the light rare earths we have adopted the simpler mechanism described above and first used by (6). The crystal field effect was chosen on the basis of experimental evidence (1-14,1-36) in Pr and Nd.

4.5 Magnetically ordered light rare earths.

As this study deals also with light rare earths in which the ions are magnetic and show some sort of long range ordering (Nd) we should also include the theory for this case. Maranzana (10) imitated the calculation made by Kondo (15) for a periodic lattice (simple cubic) occupied by N magnetic ions in a crystal of volume V. The spins of the ions interact with one another through a Heisenberg interaction represented by a molecular field . Each spin is supposed to move in the presence of the temperature dependant molecular field independantly of other spins. The conduction of the system is accounted for by a Fermi sea of electrons residing in a single band extending from $-E_1$ to E_1 with a constant density of states, ie similar assumption to those in the previous section where the conduction model for a

metal with magnetic impurities was described. The Fermi level is taken as the zero energy, $E_f=0$.

The interaction of the 'conduction system' and'magnetic system' is presented by the well known s-f Hamiltonian:

$$H' = -(J/N)\sum_{kk'n} \exp(i(k-k')R_n)\ ((a^+_{k'\uparrow}a_{k\uparrow} - a^+_{k'\downarrow}a_{k\downarrow})S_{nz} +$$

$$+ a^+_{k'\uparrow}a_{k\downarrow}S_n - a^+_{k'\downarrow}a_{k\uparrow}S^+_n) \quad \ldots \quad /1/$$

In order to calculate appropriate conductivities the transition probabilities up to third order in J are calculated. Throughout the model only elastic scattering is considered, and processes of the type $\bar{k}\uparrow \rightarrow \bar{k}'\downarrow$ are neglected, on the basis of the fact that they are likely to contribute terms of the same order of magnitude and temperature dependence as the terms retained. This assumption does not exclude, in second order , processes of the type $\bar{k}\uparrow \rightarrow \bar{k}''\downarrow \rightarrow \bar{k}'\uparrow$ and the Kondo like processes.

If we assume the transition probability to be of the form given by standard perturbation theory ($t\cong$const) where in the matrix element of the hamiltonian /1/ $\langle\alpha'|H'|\alpha\rangle$, the ket $|\alpha\rangle$ represents a state given by $\bar{k}$ vectors and the spin σ of all conduction electrons, and by the magnetic quantum numbers of all the magnetic ions. Then the transition probability has the form:

a) in the first approximation

$$W_1(k'\uparrow,k\uparrow) = W_1(k'\downarrow,k\downarrow) = (2\pi/\hbar)\,\delta(E_k-E_{k'})$$

$$(-J/N)^2\sum_{nn'} m_n m_{n'} \exp(i(k-k')(R_n-R_{n'})) \quad \ldots \quad /2/$$

b)in second approximation

$$W_2(k'\uparrow\downarrow,k\uparrow\downarrow) = \pm(-J/N)^3\sum_{lmnk''} m_l m_m m_n \exp(i((k-k')R_l+(k''-k)R_m+$$

$$+(k'-k'')R_n))((1-f_{k''})/(E_k-E_{k''}+i\eta) + \text{c.c.}) +$$

$$\pm(-J/N)^3 \sum_{lmk''} m_l(S(S+1)-m_m(m_m\pm1)) \exp(i((k-k')R_l+(k'-k)R_m))$$
$$((1-f_{k''})/(E_k-E_{k''}+i\eta) +c.c.)\mp(-J/N)^3 \sum_{lmnk''} m_l m_m m_n \times$$
$$\exp(i((k-k')R_l+(k''-k)R_m+(k'-k'')R_n))(f_{k''}/(-E_k+E_{k''}+i\eta)+c.c.)+$$
$$\mp(-J/N)^3 \sum_{lmk''} m_l(S(S+1)-m_m(m_m\mp1)) \exp(i((k-k')R_l+(k'-k)R_m))$$
$$(f_{k''}/(-E_k+E_{k''}+i\eta)+c.c.)$$

The upper sign applies to the scattering of an electron with spin up and vice versa, the other notation is as usual (m_l- azimuthal quantum number of l-th spin, $((S(S+1))^{1/2}$ is the length of the spin).

In averaging these terms, there would be an obvious difference to the Kondo like treatment as he would reasonably assume that the magnetic impurities do not see one another while here we are dealing with the periodical lattice of magnetic atoms . In our case , for example, it should look like

$$\left\langle \sum_{ln} m_l m_n \exp(i((k-k')R_l+(k'-k)R_n)) \right\rangle = \sum_{ln} \langle m_l m_n \rangle \exp(i(k-k')R_l + (k'-k)R_n))$$

$$= N\langle m^2 \rangle + \langle m \rangle^2 \sum_{n=1} nl \exp(i((k-k')R_l+(k'-k)R_n)) =$$

$$= N\langle m^2 \rangle + \langle m \rangle^2 \ (-N+ \text{terms containing } \delta(k-k')) =$$

$$= N\langle (m-\langle m \rangle)^2 \rangle + \text{terms containing } \delta(k-k') \quad \ldots \quad /4/$$

From /4/ is obvious that the periodicity playes an essential role in this calculation as it allows the splitting of equation /2/ into a k-independent term and a contribution of the electron self energy (of no interest for the scattering). This is not possible if the model introduced by (16) is employed as he assumes that the magnetic atoms are distribited randomly throughout the lattice of the crystal. If we add a small amount of nonmagnetic atoms to the crystal the calculation would not be appreciably altered. Having

averaged the transition probability we get

ad a) $W_1(k'\uparrow,k\uparrow) = W_1(k'\downarrow,k\downarrow) = (2\pi/\hbar)\delta(E_k-E_{k'})(J/N)^2 N\langle(m-\langle m\rangle)^2\rangle$

ad b) $W_2(k'\uparrow\downarrow,k\uparrow\downarrow) = (2\pi/\hbar)\delta(E_k-E_{k'})(-2(-J/N)^3 N\langle(m-\langle m\rangle)^2\rangle$

$(1\pm 2\langle m\rangle)\sum_{k''}(1/(E_k-E_{k''}))+4(-J/N)^3 N\langle(m-\langle m\rangle)^2\rangle$

$\sum_{k''}(f_{k''}/(E_k-E_{k''}))$ ... /6/

The spin independent relaxation time is obtained by summing over k' and summing the relaxation times proper for electrons with spin up and spin down. Finally, the expression for the resistivity has a form:

$$\rho = (3\pi/2\hbar e^2)(VJ^2/Nv_f^2)\langle(m-\langle m\rangle)^2\rangle\,(1+(2J\eta(E_F)/N)(\ln\left|\frac{E_1}{E_2}\right| - 2\ln\left|\frac{E_1}{kT}\right|))$$

4.6 Models with $\eta(E)\neq$constant

So far we have been discussing different physical models to account for changes of the resistivity with temperature along the rare earth series with one overall assumption that the density of states $\eta(E)$ near the Fermi surface is constant. This simplification is perhaps justified in the case of the heavy rare earths (Elliot's model) and those light rare earths dealt with by the Maranzana model) where changes in the density of states is not a first order effect.

In the case of the anomalous rare earths this assumption is not possible to make (1-11) as is obvious from pressure experiments. Therefore we have to consider what is likely to be the effect of a changing density of states $(\partial\eta/\partial T)$ on the transport properties, in this case the resistivity.

The simplified model has been outlined by (17-21) as follows;

Let us assume that the conduction electrons are in the form of a degenerate gas. The conductivity is than given by

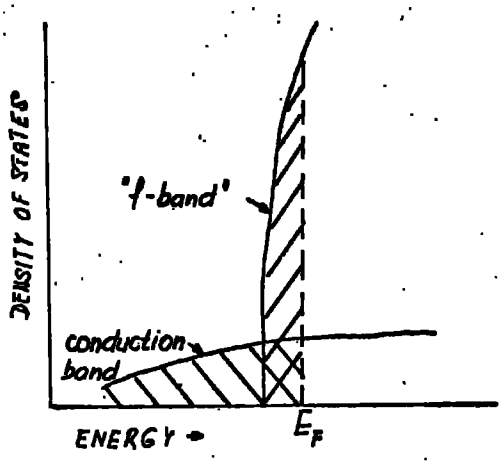

Fig. 4.1 Standard band structure

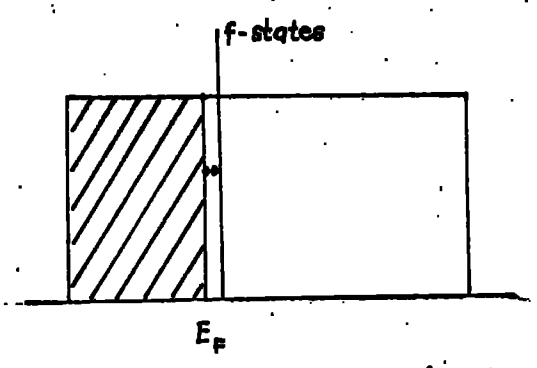

Fig. 4.2. Density of states for electrons (localized) and itinerant holes and electrons

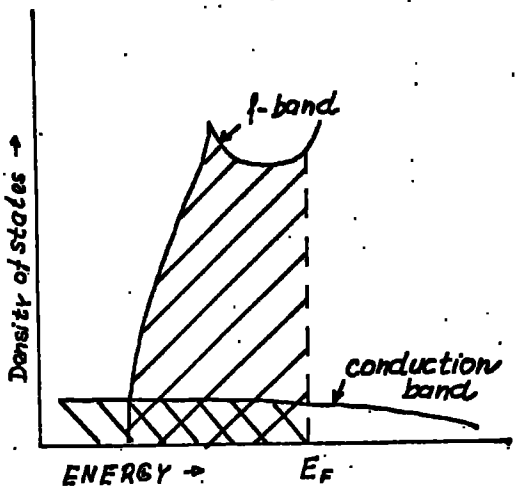

Fig. 4.3 One of the possible band structures for the metal-insulator model

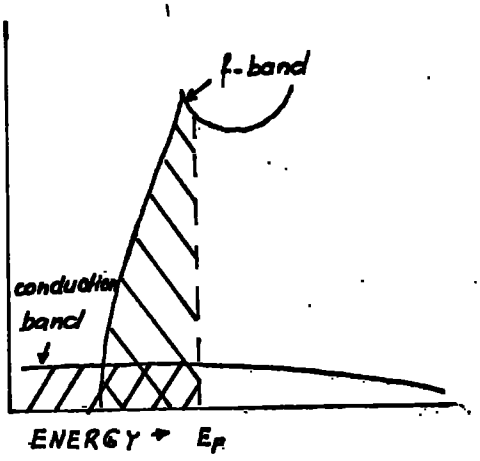

Fig. 4.4 A second band structure for the metal-insulator model

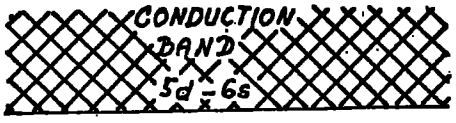

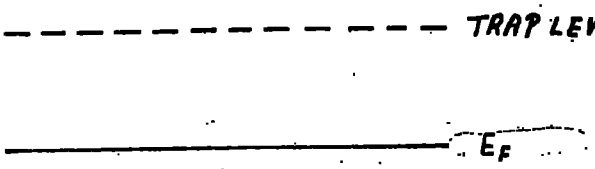

Fig. 4.5 Schematic model of the band structure for the metal-semiconductor model

$$\sigma = -\int_0^\infty \sigma(E)\,(\partial f_0/\partial E)\,dE = \sigma(\eta) + (\pi^2/6)(kT)^2(\partial^2\sigma(E)/\partial E^2)_{E=\eta} \quad /1/$$

where $\sigma(E)=(e^2/12\pi^2\hbar^3)(\tau(E)\langle v_c(E)\rangle^2 N_c(E))$ ... /2/

$N_c(E)$ is the density of final states for scattering processes which limit the conductivity, Q is a factor containing a variety of factors such as the number of defects, transition probabilities etc. For simplicity we will consider elastic scattering only.

In normal metals it is the variation of Q with temperature that is responsible for the usual Bloch-Grüneisen temperature dependance of the resistivity. Departures from this law could arise from causes which we may classify as follows:

1) An explicitly temperature dependent scattering mechanism (eg. change in phonon spectrum) leading to an anomalous variation of Q with T.

2) A variation of $N_f(E)$ with E so rapid as to make the second term on the right -hand side of equation /1/ significant (19).

3) A dependence of the band structure on temperature leading to an anomalous variation of $N_f(E)$, $N_c(E)$ and/or $v_c(E)$ with temperature.

So far we have been discussing case ad1) for a few different models suitable for rare earths.

One of the simpler models of type 2) suggested by (19) assumes that near the Fermi energy there are two overlaping bands (fig. 4.1). One of them, the conduction band, is broad, having an effective mass of the electron roughly equal to that of the free electron. The second is assumed to be narrow. The density of states $\eta(E)$ in the narrow band greatly exceeds that in the conduction band at the Fermi

energy. Consequently N(E) is a sensitive function of energy. So we may further assume that the density of states near the Fermi surface $N_f(E)$ is the only function exhibiting a rapid variation with energy near E_F. Further simplifying assumptions are: the effective mass in this narrow band is so large that the current is carried almost exclusively by electrons (or holes) in the broad conduction band. Then the resistivity has a form :

$$\rho(T) = \rho(N_{F(T=0^oK)},T)(1-(\pi kT)^2/6(3(N'_f/N_f)-(N''_f/N_f))) \quad .../4/$$

Each prime(') denotes a differentiation with respect to E and all quantities in the brackets are to be evaluated at $N_{F(T=0^oK)}$. Along with (19) we have retained in the equation only terms of order $(N'_f/N_f)^2$ and have neglected terms with $(N_f/N_{F(0)}N_f)$ and $(1/N_{F(0)})^2$. If we further assume that the f-band is of'standard' form, see fig. 4.1, equation /3/ will simplify to

$$\rho(T) = \rho(N_{F(0)},T)(1-\pi^2/6\ (KT/\Delta E)^2) \quad ... \quad /5/$$

ΔE is the energy difference between the Fermi energy at $T=0^oK$ and the edge of the f-band. Due to the above mentioned simplification, defined by $N'_f/N_f \gg 1/N_{F(o)}$ the $\Delta E \ll N_{F(0)}$. This model could be extended and improved in different ways. First it seems unlikely that if $N(E_F)$ changes very rapidly the band structure would remain unaffected. But as these effects are technically difficult to account for at the same time then models with different 'band structures' have been proposed.

The metal-insulator model described in (22) specially suitable for Ce assumes

1) an extended band of hybridized s-and d-like Bloch states, with a constant density of states,

2) a set of localized f-like states with an energy $E_f, E_f > 0$, where E_{Fermi} is again taken equal to zero.
These states are highly localized and correlated admitting only one electron per atom. The energy necessary to place a second electron in the same localized f-state is one order of magnitude larger than E, see fig. 4.2. Fig. 4.2 shows schematically the density of states of this model. The aim of the model is to account, under simplifying assumptions, for the temperature dependence of the density of states of various contributions.

If the crystal contains N atoms, and $n_e(E)$, $n_h(E)$, and $n_c(E)$ are the occupation probabilities for conduction electrons, holes and localized electrons respectively than we have the following relations

$$Nn_a \cong \int_0^{We} D(E)n_e(E)\,dE \quad \ldots /6/$$

$$Nn_b \cong \int_0^{Wh} D(E)n_h(E)dE \quad \ldots /7/$$

$$n_c = n_b - n_a \quad \ldots /8/$$

where Nn_c is the number of occupied f-levels, D(E) is the density of states function which could be simply expressed (for instance for Ce) by:

$$D(E) = 12N/W \quad \ldots /9/$$

12 being the number of states per atom. The excitation energy Σ of a given many-electron state consists of two terms, $E_{ex} = E_1 + E_2$ where E_1 is the single-quasiparticle contribution and E_2 is the quasi-quasiparticle interaction.

$$E_1 = \int_0^{We} ED(E)n_e(E)dE + \int_0^{Wh} ED(E)n_h(E) + NEn_c \quad \ldots /10/$$

In order to express E_2 we make the following assumptions:
1) All interactions are short range

2) The interaction between two electrons in f levels in the same atom is considered to be infinitely large.

3) The interaction -G of the f-electron with either electrons or holes in the conduction band is assumed to be constant, independent of E. Then

$$E_2 = -NGn_c(n_b-n_a) \quad .... \quad /11/ \quad \text{or} \quad E_2 = -NGn_c^2 \quad ... \quad /12/$$

The interaction G could also be accounted for thermodynamically. If E is the energy of one isolated electron moving in a lattice whose potential is set up by a collection of n+ ions and neutralizing charge, E+G would be the energy of the same electron in the same lattice but with ions of (n-1)+ charge and neutralizing charge. The equilibrium values of the occupation functions $N_e(E)$, $N_h(E)$ and N_c are obtained by minimizing the expression for the systems free energy with respect to them.

The free energy F=E-TS where the entropy is given

$$S = -k_B\int_0^{We} D(E)(n_e(E)\ln n_e(E) + (1-n_e(E))\ln(1-n_e(E)))dE -$$

$$-k_B\int_0^{Wh} D(E)(n_h(E)\ln n_h(E) + (1-n_h(E))\ln(1-n_h(E)))dE -$$

$$-Nk_B(n_c\ln n_c + (1-n_c)\ln(1-n_c)) + Nk_Bn_c\ln(2J+1) \quad ... \quad /13/ .$$

The first term in equation /13/ represents itinerant electron entropy, the second itinerant hole entropy, the third localized electron entropy and the fourth represents the ionic spin entropy. With respect to the constrain (8) we can write further

$$n_e(E) = (a^{-1}\exp((E-E_{ex}+2Gn_c)/k_BT)+1)^{-1} \quad ... \quad /14/$$

$$n_h(E) = (a^{-1}\exp((E+E_{ex}-2Gn_c)/k_BT)+1)^{-1} \quad ... \quad /15/$$

where $a=n_c/(2J+1)(1-n_c)$, $n_c=(12k_BT/W)\ln\left|\frac{(A_1+\exp(-Q_1))(A_o+1)}{(A_o+\exp(-Q_o))(A_1+1)}\right|$

$A_o \equiv 1/A_1 \equiv a\exp((E-2Gn_e)/K_BT)$, $Q_o = W_h/k_BT$, $Q_1 = W_e/k_BT$

k_B being the Boltzman factor. The equilibrium value of n_e is given by a temperature dependent implicit equation (17) which depends also on the parameters of the system W_e, W_h, G and J. For a given temperature T (15) may yield one or three solutions. Of those three solutions one is a maximum and the other two are local minima so that numerical evaluation is necessary.

This model could be improved by a more realistic D(E), density of states function, see fig 4.3 and 4.4, or by adding a hybridization term, mixing f and conduction states. This way an infinitely narrow f band becomes (24) a resonant level and the occupation of these states is never zero, even at T=0. Also interaction between itinerant quasiparticles should be taken into account, as well as the effects of the long range part of the quasiparticle interaction.

The metal-semiconductor model (23) was first used (and developed) for pressure induced transitions and the 4f electron delocalization evidence comes from studies of SmTe.

Figure 4.5 represents schematically the band picture at atmospheric pressure and room temperature, As the pressure increases the conduction band continuously approaches the 4f states as we assume that E_f and 4f states do not move, until they merge which then delocalizes the 4f electrons.

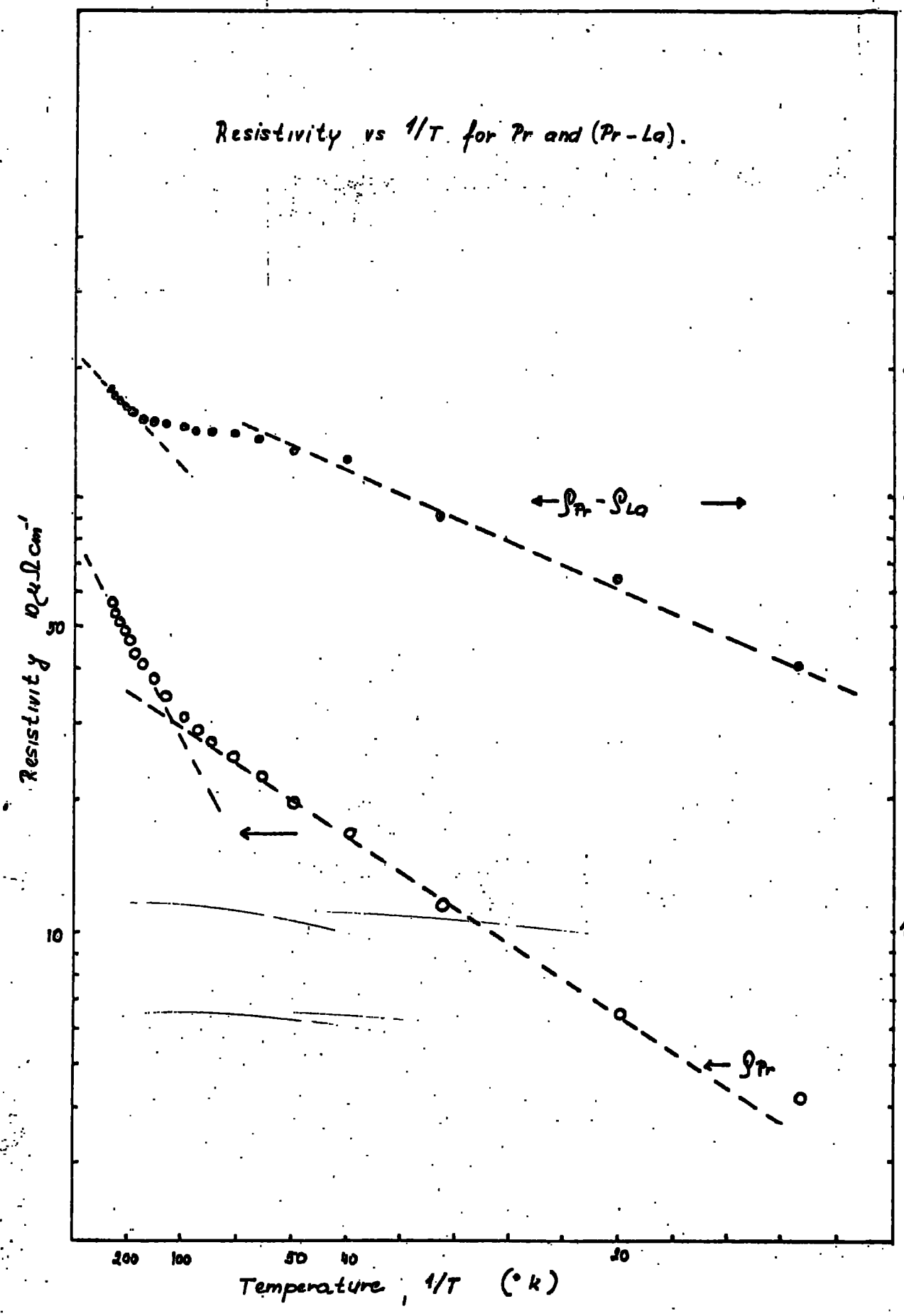
Resistivity vs 1/T for Pr and (Pr-La).
$\rho_{Pr} - \rho_{La}$
ρ_{Pr}
Resistivity ρ $\mu\Omega cm^{-1}$
20
10
1
10
200
100
50
40
30
Temperature, 1/T (°k)

Fig. 5.1

C H A P T E R F I V E

DISCUSSION

5.1 The resistivity variation of some light rare earths and light-heavy rare earth alloys in the d-hex phase

In chapter four the M-B-W-K (4-4,6) method was described. This method accounts for the resistivity variation with temperature, in metals which are not magnetically ordered, but contain magnetic moments. It is assumed that strong crystal field intaractions cause a splitting of the degenerate low lying electron energy states, the electrons concerned being localized in the unfilled 4f shell.

The temperature variation of the resistivity of the alloys formed between light and heavy rare earths in the d-hex phase has a common feature: a logarithmic increase in ρ with temperature, fig.5.1 which may be attributed to the crystal field effect.

Light rare earths have non zero magnetic moment due to the unfilled f-electron shell. They are magnetically ordered only in the region of very low temperature (Ce,Nd) or not at all (Pr). This indicates a rather weak exchange interaction which allows the crystal field to split the 4f electron energy levels. This plays an important role in the physical properties of light rare earths, as is well known.

The f-electron energy levels lie in the vicinity of ($\sim$KT) the Fermi energy and overlap with the conduction band. f-electrons consequently interact strongly with the conduction electrons and any changes in the position and probability of occupation of the f-levels show up on the resistivity curve. This was first discussed in detail by (4-4,6) as refered to in the theoretical chapter of this thesis. In the present

discussion Pr will be considered in detail first since only for Pr of all the light rare earths is enough information available for the M-B-W-K type of calculations.

Pr-Tb alloys will be discussed in a similar way to pure Pr. The effect of Tb 'impurities' in the Pr lattice was approached basically in two different ways.

1) Since the atoms of Tb are smaller than the atoms of Pr we can assume that the Tb atoms cause a distortion of the Pr lattice so that the crystal field energy levels will be shifted.

2) We also know that presence of Tb atom in the Pr lattice above a certain concentration is responsible for magnetic ordering of the alloy through the exchange interaction between Pr and Tb atoms. A similar effect may be caused by the action of an applied magnetic field on Pr atoms in the d-hex lattice. Consequently we have calculated the resistivity of Pr in a magnetic field of 400KOe which is slightly smaller than the internal field necessary for ordering.

Nd,Nd-Dy and Nd-Y alloys we believe could be explained similarly if the crystal field energy levels for Nd were known. The resistivity contains in addition to the crystal field term a magnetic ordering term whose character will be discussed as well. An attemp to make an independent estimate of ρ_{phonon} and $\rho_{c.f.}$ in Nd using the results from the Nd-Y alloys is discussed also.

La and La-Dy alloys represented a different problem since La and La_9Dy_1 are superconducting. Also the f-electron energy levels in La lie above E_F which weakens the s-f interaction in comparison to Pr and Nd. An attempt has been made to explain La resistivity behaviour using Jones'(2) model where the most rapid variation with temperature is expected from the density of states function $\eta(E)$.

Fig. 5.2 Crystal field energy levels for Pr in zero magnetic field as proposed by (1-44 and 1-14)

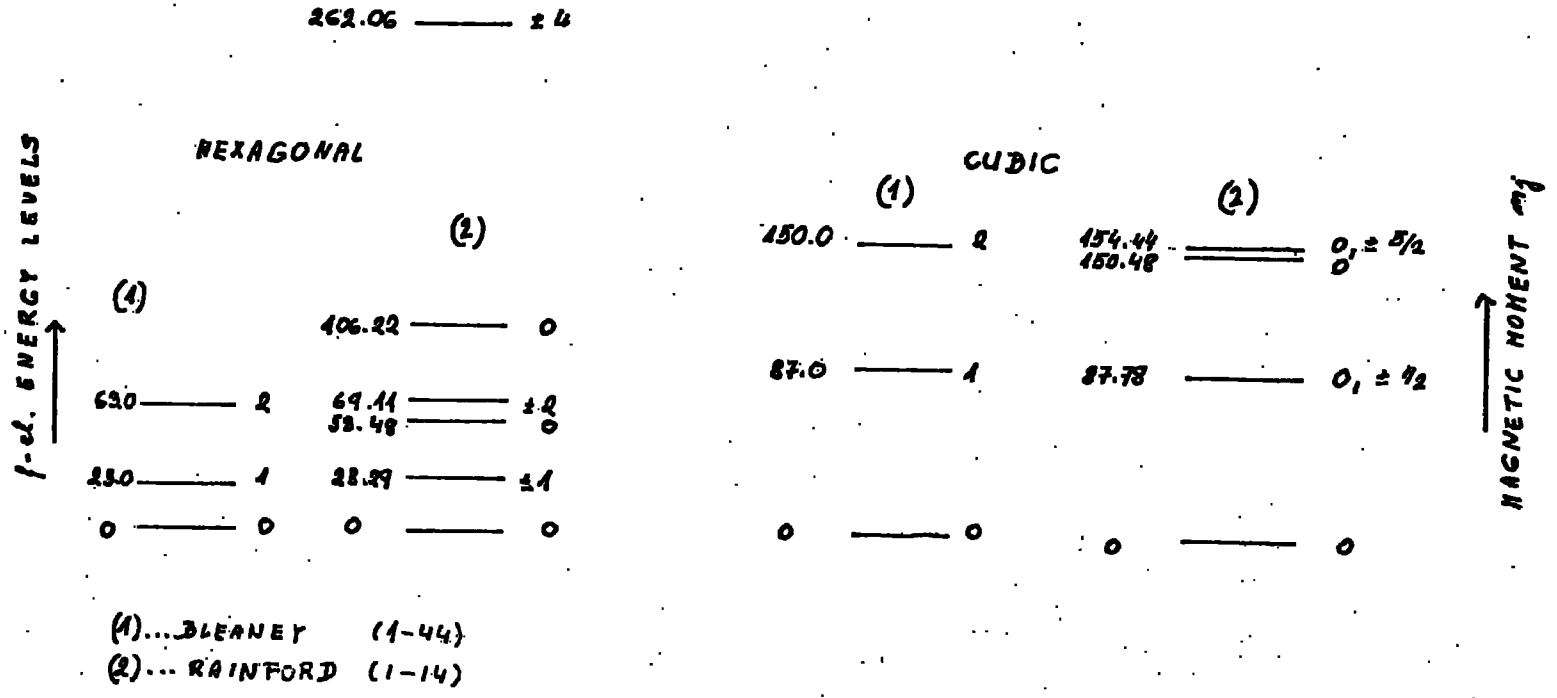

(1)... BLEANEY (1-44)
(2)... RAINFORD (1-14)

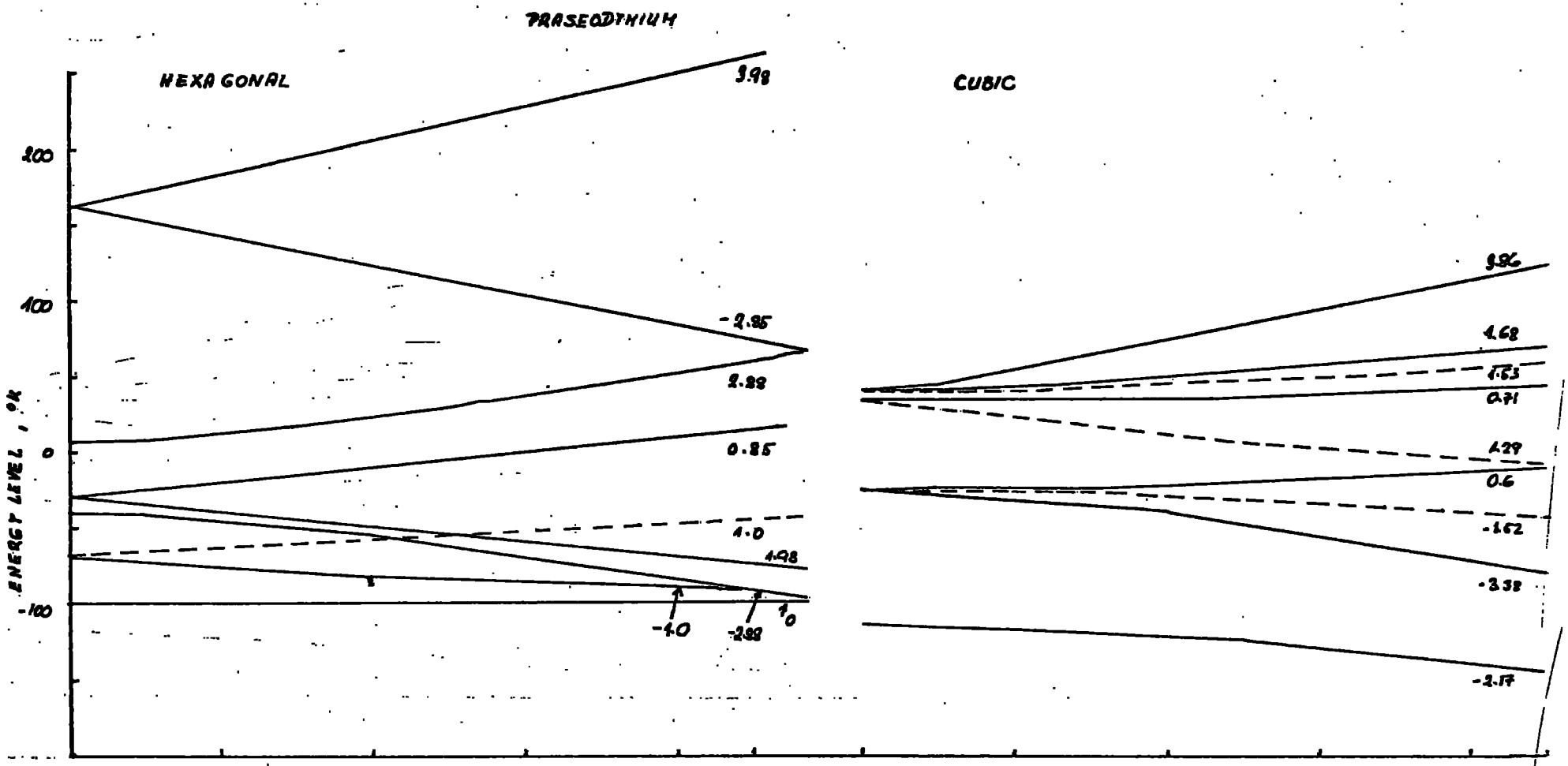

Fig. 5.3

Crystal field energy levels of Pr in hexagonal and cubic environments vs H_z

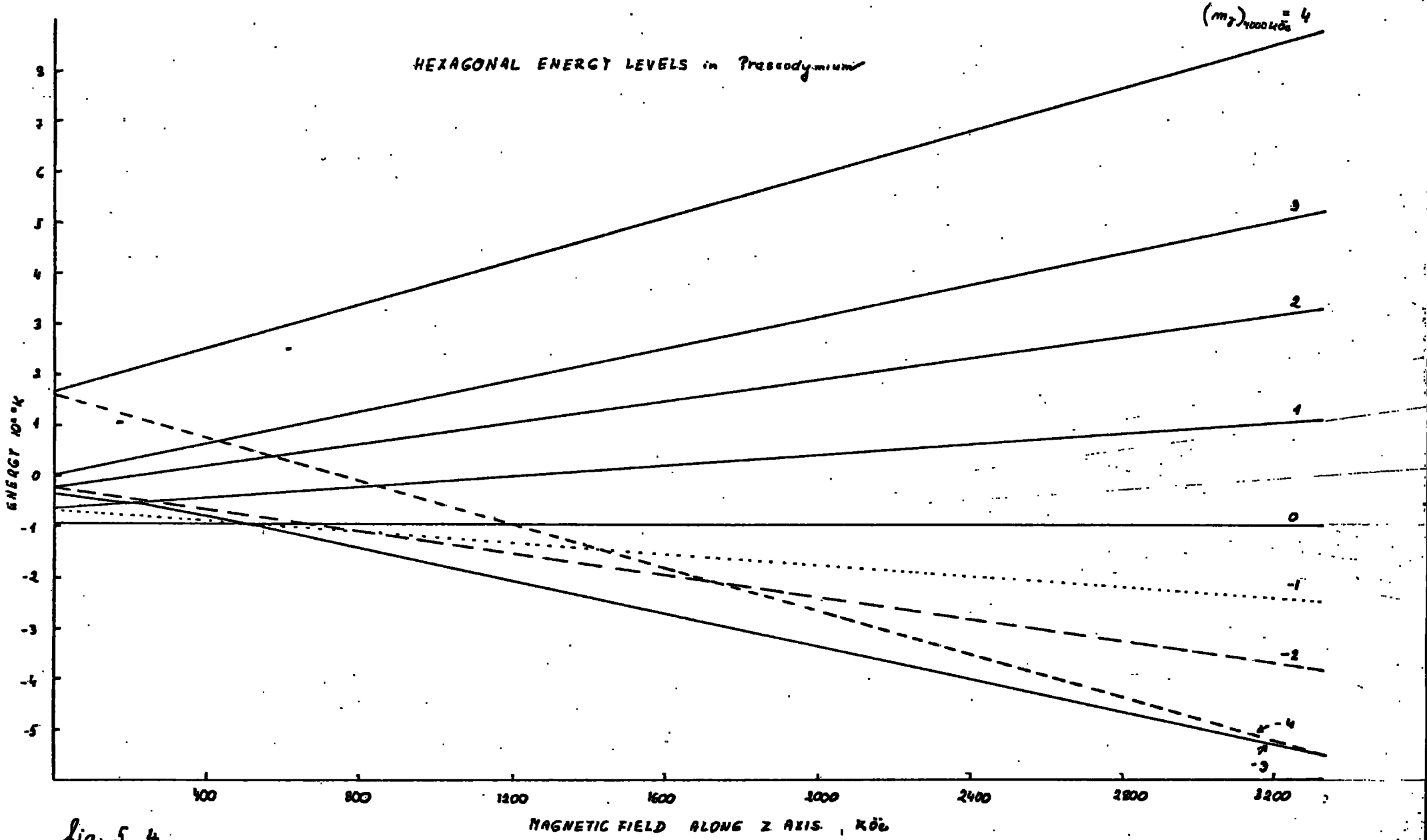

fig. 5.4

Crystal field energy levels of Pr in hexagonal environment vs H_z

5.2 Praseodymium

Plotting log $\rho(T)$ of Pr vs 1/T gives well defined straight lines, fig.5.1. This suggests excitations between well defined energy levels with an energy separation ΔE_i of the order of KT. This agrees remarkably well qualitatively with both the theoretical assesment of ΔE_i by Bleaney (1-44) and the experimentally based values of Rainford (1-51), fig.5.2.

The calculations presented here are based on both the assesment of the c.f. energy levels done by (1-44) and (1-51) as well as by (5-1). Later autors (1-51, 5-1) have made an allowance for the nonideal lattice by using the c/a ratios typical for Pr.

According to (5-1) in zero magnetic field in the hexagonal environment only three out of the nine states are pure eigen states while in a cubic environment there are none. This is contrary to the Ce case in which all levels are eigenstates and is consequently rather exeptional. A magnetic field of the order of 400kOe, applied along the z-axis of Pr is required to order Pr, due to the crossing of the nonmagnetic (singlet) graund state (H=0) by an excited magnetic state, fig. 5.3-4

In order to simulate theoretically the curves for the Pr and some Pr-Tb alloys we have closely followed the M-B type of calculations made originally for Ce-Al alloys. To calculate the expression for $\tau(1)$ the equation /4-24/ from the theoretical chapter was used along with the values of the magnetic moment m_{ji} and E_i obtained from the calculation of crystal field energy levels made by (1-44, 51, 5-1) fig.5.2. The conduction band was considered to be of a parabolic form. The integral over the Fermi function being taken over 5KT (=4200°K) in order to keep the computation time within reasonable limits and also to conserve the character of the

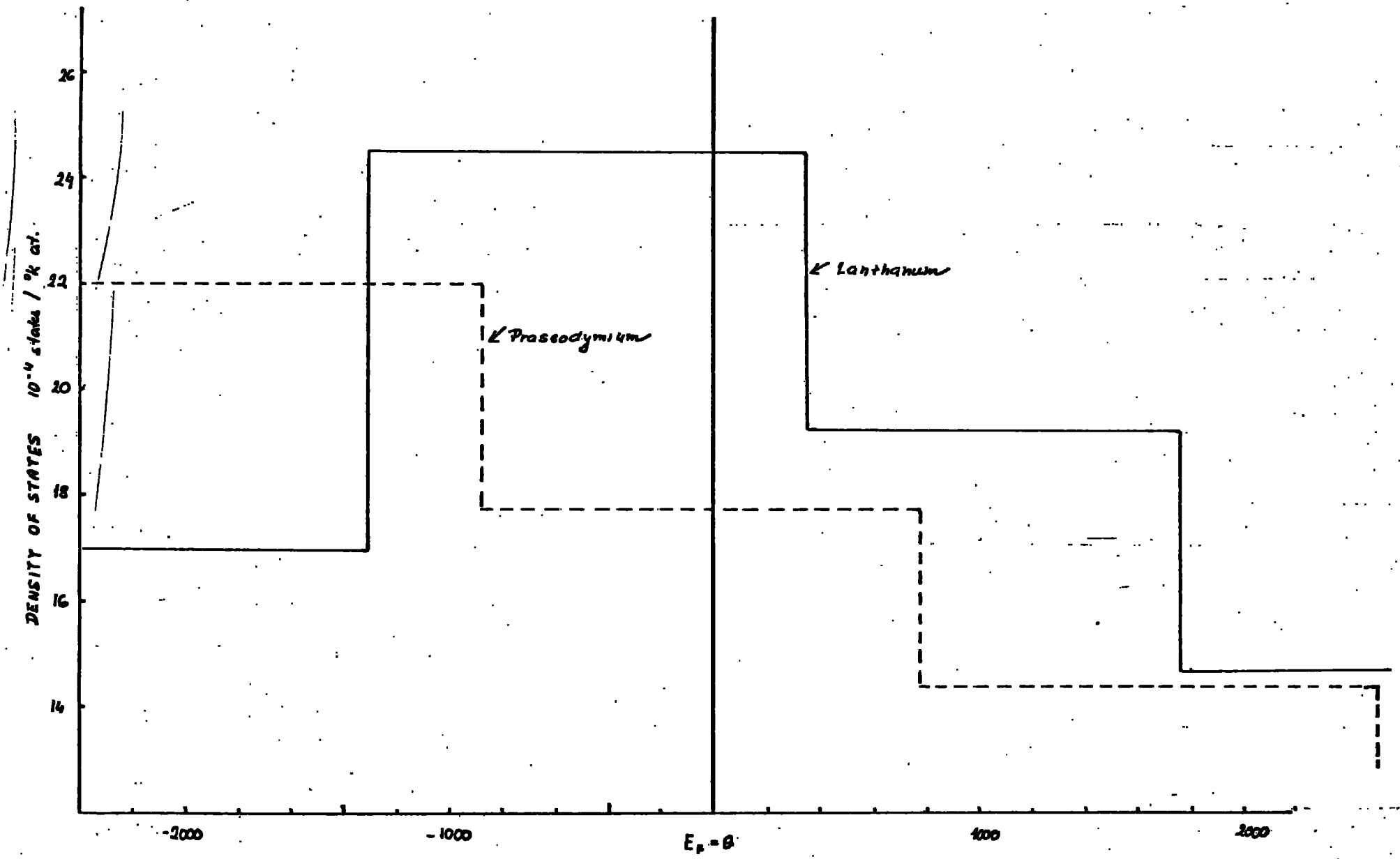

Fig. 5.5

Density of states function vs energy for Pr and La as calculated by (1-34)

Fermi-Dirac statistics function. The Fermi energy was assumed to lie in the middle of the conduction band. As the density of states $\eta(E)$ we used the function calculated by Miron and Liu (1-34), fig.5.5. The results obtained under this assumption and under the assumption of $\eta(E)=\eta(E_F)$ (i.e. constant density of states) are very similar. This result is not surprising and is presumably due to the rather narrow conduction band considered. Calculations for the cubic and hexagonal environments were made separately because values of E_i and m_{ij} are known only for the hexagonal and cubic lattices respectively.

Obviously should we accept the assumption that the resistivity in the light rare earths has its main contribution from an sf scattering mechanism of the type described above the result of the proposed calculation of $\rho(T)$ depends greatly on the choice of crystal field energy levels. The parameters used in this thesis were obtained theoretically from calculations based on a point charge model which were fitted to the experimental curves for specific heat and magnetization. Complementary to this indirect evidence, there is also some direct information about their position.

The position of crystal field energy levels, their anisotropy and dispersion relations could be followed from the neutron diffraction results (1-14) graphicaly presented in fig.1.11. Rainford (1-51) tentatively assigned the upper mode to the Γ_1 to Γ_4 transitions on the cubic sites, assuming thus that the axial crystal terms $b_2(c)$ is small and not zero as is commonly thought. There is no a priori evidence for this assumption and it is only based on the similarity with the fcc Pr neutron diffraction data.

The lower branches were assigned by (1-14,51) to the transition ($|0\rangle \rightarrow |\pm 1\rangle$), between the singlet ground state of the hexagonal sites and first excited doublet state. This assumption is supported by independant magnetization measurements. The splitting of the lower mode has been partly explained by dispersion relations calculated on the basis of pseudo-boson theory and is partly attributed to an anisotropic exchange or electric quadrupole interaction. The magnitude of the splitting in the Γ M direction would indicate that the anisotropic interactions in Pr are of the same order of magnitude as the isotropic exchange. This leads to a similar estimate of these two interactions in Pr as was made by (4-4) on the basis of the resistivity variation with temperature measured by (1-16) using parameters (such as specific heat, radius of Fermi sphere etc.) typical of the heavy rare earths. It is obvious, from (1-14) experiments on Pr single crystals, that the ΔE_i, the crystal field splitting of the energy levels represents only the mean values of ΔE_i or E_{mi} characteristic for polycrystaline Pr. With regard to the above discussion of crystal field splitting of the cubic and hexagonal energy levels the following rules were observed in fitting the theoretical curve to the experimental one.

a) The problem with fitting a theoretical curve (M-B-W-K) to the experimental one (Pr) are as follows:

The experimental curve contains essentially more information than just the contribution due to the crystal field $\rho_{c.f.}$. It also includes the phonon contribution ρ_{phonon} and the residual contribution ρ_{res} apart from other possible terms, e.g. due to quadrupole and exchange interaction (4-4). The

residual resistivity which is not temperature dependent is easy to obtain from measurements made at 4.2°K or below. The phonon contribution to the resistivity may be estimated (at least its lower limit) from the high temperature behaviour if the resistivity curve is resonably linear at high temperature (e.g. $T > T_{Debye}$). For example see the resistivity curve of the heavy rare earths and alloys in the hcp structure, presented in this study, (Chapter three). We can, having in mind the Bloch-Gruneisen theoretical equation for $\rho_{phonon}(T)$, assume that $\lim_{T\to\infty}(\partial\rho/\partial T)$ is the smallest gradient of the phonon contribution in the temperature region $T<T_{Debye}$, then

$$\rho(T)_{scattering} \geq \rho(T)_{tot} - (\rho_{res.} + \rho_{phonon}(T)) \quad \ldots /1/$$ where

$$\rho(T)_{phonon} \geq T(\lim_{T\to\infty}(\partial\rho/\partial T) \quad \ldots /2/$$

$\rho(T)_{scattering}$ then represents the resistivity due to other scattering mechanisms, for instance that due to crystal field effects.

In the resistivity variation of Pr with temperature, measured in this study, in the temperature region up to 300°K it is not possible to define this high temperature limit. From measurements made by (1-13) up to ~880°K it might be possible to estimate $\rho_{phon.}$ this way since $\rho_{tot.}(T)$ is almost linear from 450°K to the transition temperature, giving $\Delta\rho/\Delta T = 5.23\times10^{-2}(\mu\Omega\,deg^{-1})$. Even this value should be viewed with some scepticism however because of the nature of the curve.

Another problem represents the classification and choice of the fitting criterion. What is the criterion for a good fit of the theoretical curve to the experimental one. Maranzana et. al. (4-8, 9) as well as Watabe and Kasuya (4-4) were more concerned with the general form of the resistivity curve.

Assuming localized energy levels with a separation of the order of $10^{\circ}K$ and with the $\rho_{phon.}$ generally governed by the Bloch-Gruneisen relation it seems more sensible to be more concerned with a fit in the temperature region up to $T_{D.} \sim 170^{\circ}K$ (1-20) than with the region approaching room temperature, $300^{\circ}K$, as here there is likely to be a significant phonon contribution.

Maranzana et. al. (4-8,9) were dealing with alloys and compounds of Ce-Al where the form of the resistivity curve is such that the $\rho_{phon.}$ contribution cannot be obtained in the way described above and consequently they neglected $\rho_{phon.}$ completely in order to understand and explain the general form of $\rho(T)$.

Watabe and Kasuya (4-4) made an allowance for the $\rho_{phon.}$ contribution assuming it has the same form as the resistivity of La, which should be mainly due to the phonon contribution. Lanthanum is in many aspects similar to the rare earths (specially light rare earths), e.g. with respect to the crystal structure, mechanical and chemical properties etc. but at the same time is believed not to have any f-electrons and consequently has zero magnetic moment. The main contribution to the resistivity should then be in the form of a residual resistivity and the phonon scattering. There are, or might be other mechanisms because a) the metal is superconducting at low temperatures and b) at high temperatures there might be non zero occupation of the 4f states which lie above E_F, but we assume, these make a qualitatively smaller contributuion to the resistivity and may be neglected.

The similarity between La and Pr results in our assumption (2) that $\rho_{phon.}$ of Pr might be given by $\propto \rho_{La}$

where α is almost constant with temperature since T_D for La and Pr are close to one another (1-20). Then we can write

$$\rho_{c.f.}(T) = \rho_{Pr}(T) - \alpha\rho_{La} \quad \ldots \quad /3/$$

as a better estimate of the scattering due to the crystal field rather than taking $\rho_{tot.}(T) = \rho'_{c.f.}(T)$. Which one of these approaches will give the best fit between the theoretical and the experimental curves depends in general, as we see it, on the experimental conditions. The above relation is most likely to be a good approximation providing the material used is of reasonable purity. It is generaly known that the resistivity drastically decreases with purity and even the form of the resistivity curve could be altered by a change in purity of the material. For instance in the case in question: the experimental curve of Pr presented here is similar in shape with results of (1-16b) but not with (1-16a). The resistivity of Pr and La measured in this work lie below those measured previously by (1-16,a,b) presumably due to having specimens available of better purity compared to the samples used ten or fifteen years ago when those measurements were made. Also, see discussion in Chapter two, differences associated with the different laboratories supplying the metals in question are responsible for slightly different properties . The need of good purity samples is even more obvious in the case of the Pr and La resistivity curves used by W-K(4-4) as a bases for their theoretical discussion since the La curve lies above the Pr one. This brought about unreasonably small α values (/3/) and the whole discussion presented by them could be viewed only as a qualitative and not a quantitative one. The experimental

SIMLE MODEL FOR f-el. EN.LEVELS , FIRST APPROXIMATION

Fig . 56 Resistivity vs temperature for Pr
(experimental curve - full line)
(predicted broken line)

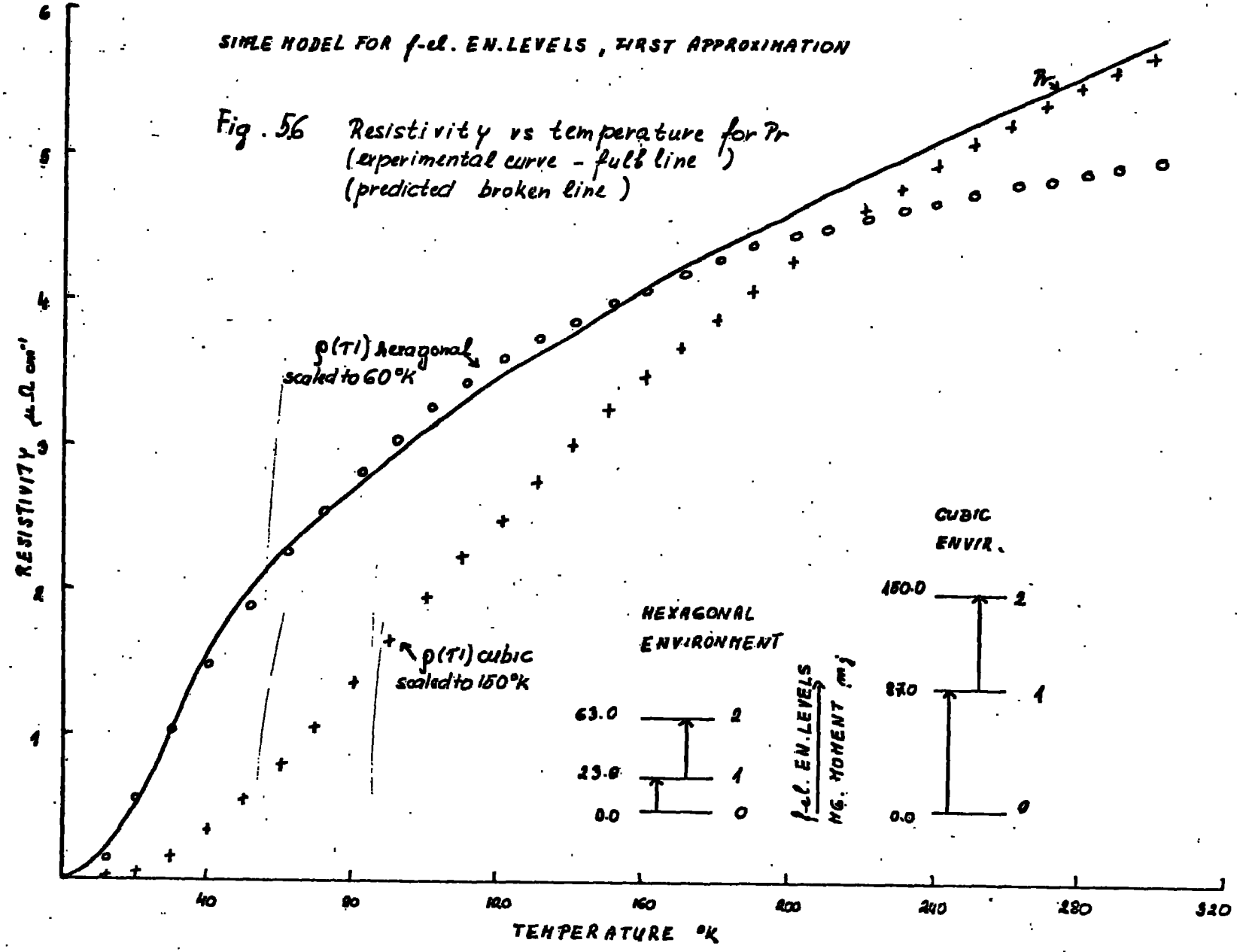

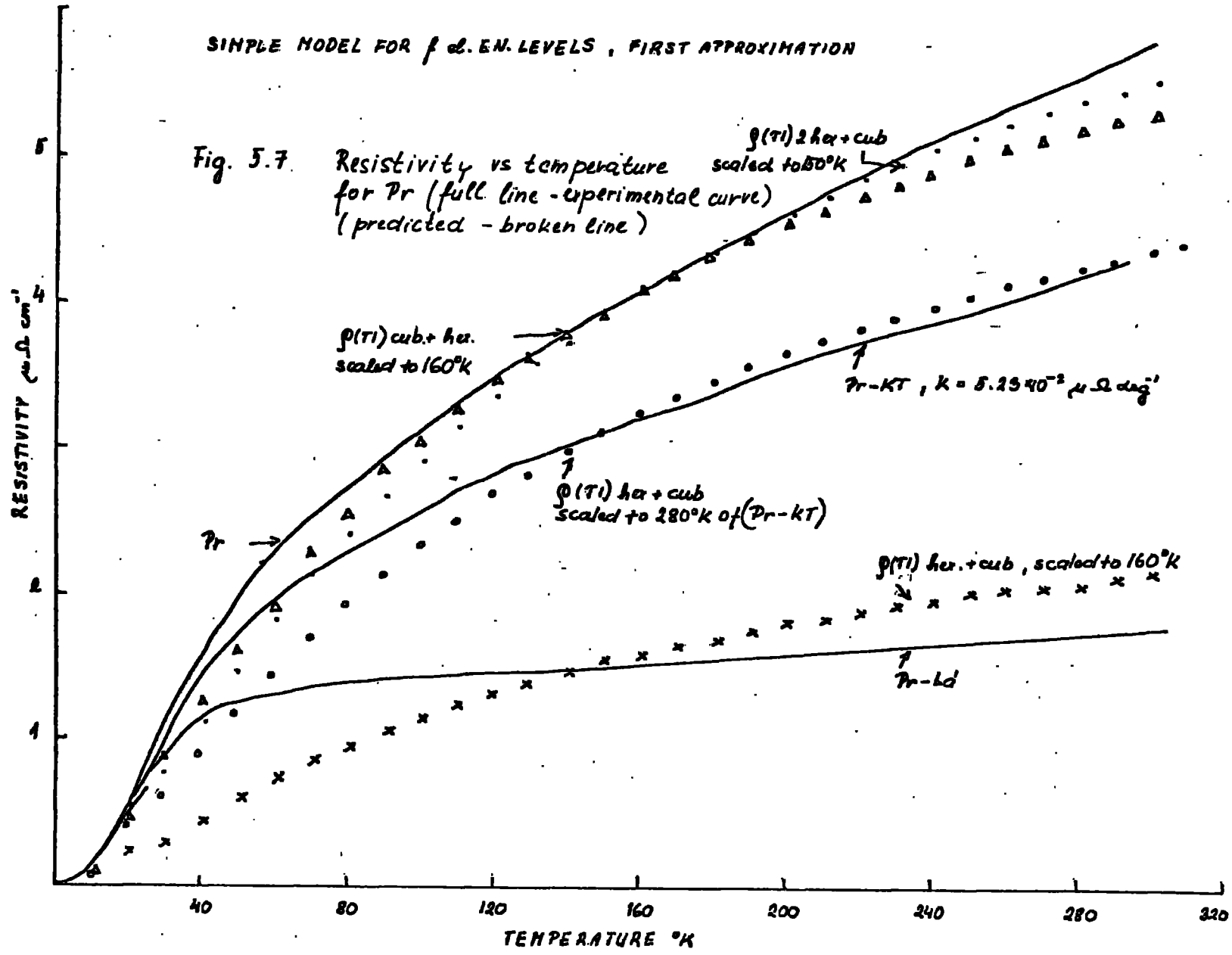

Fig. 5.7 Resistivity vs temperature for Pr (full line - experimental curve) (predicted - broken line)

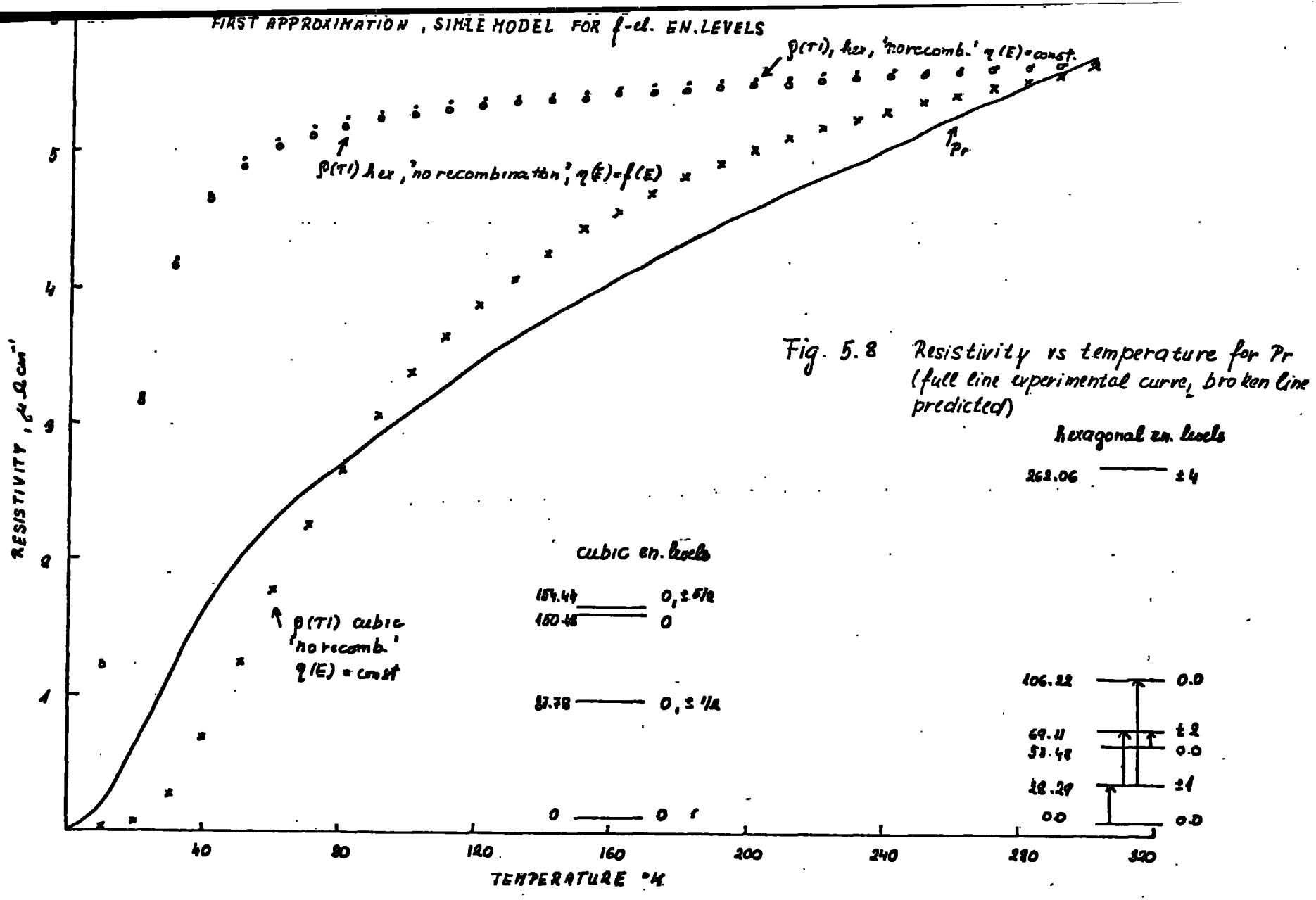

Fig. 5.8 Resistivity vs temperature for Pr (full line experimental curve, broken line predicted)

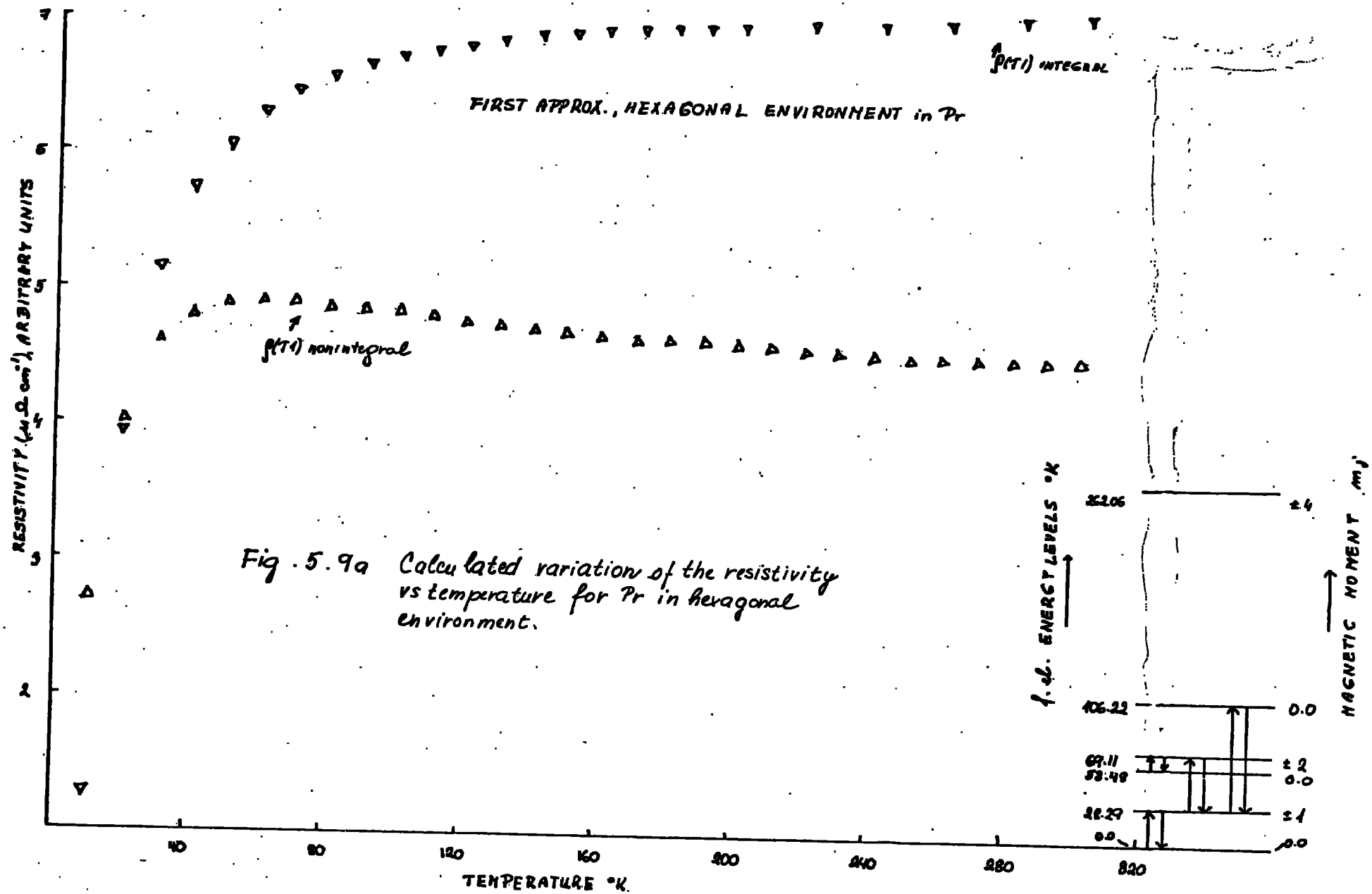

Fig. 5.9a Calculated variation of the resistivity vs temperature for Pr in hexagonal environment.

FIRST APPROXIMATION , CUBIC ENVIRONMENT in Pr

Fig. 5.9b Calculated variation of the resistivity vs temperature for Pr in cubic environment.

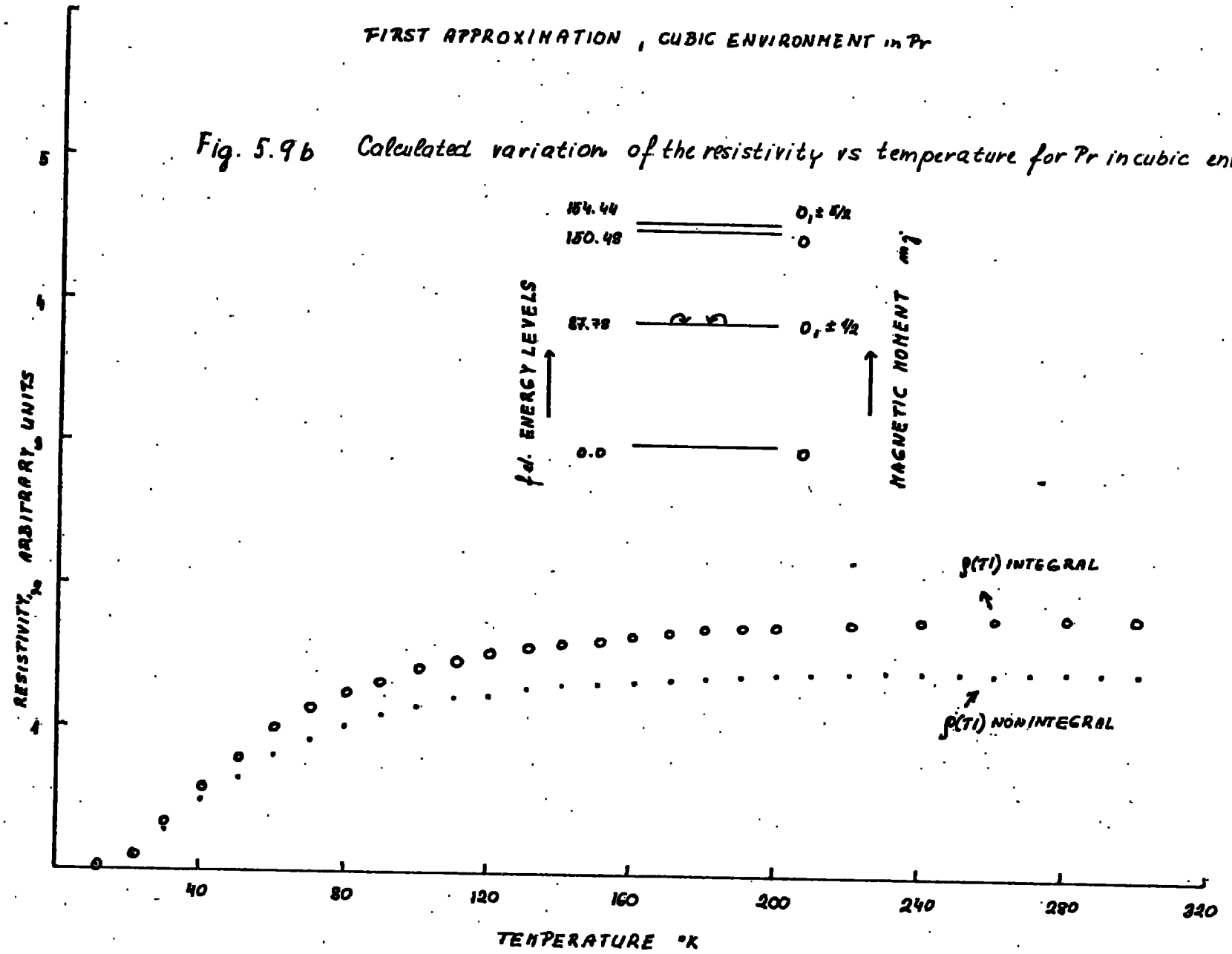

Fig. 5.9c

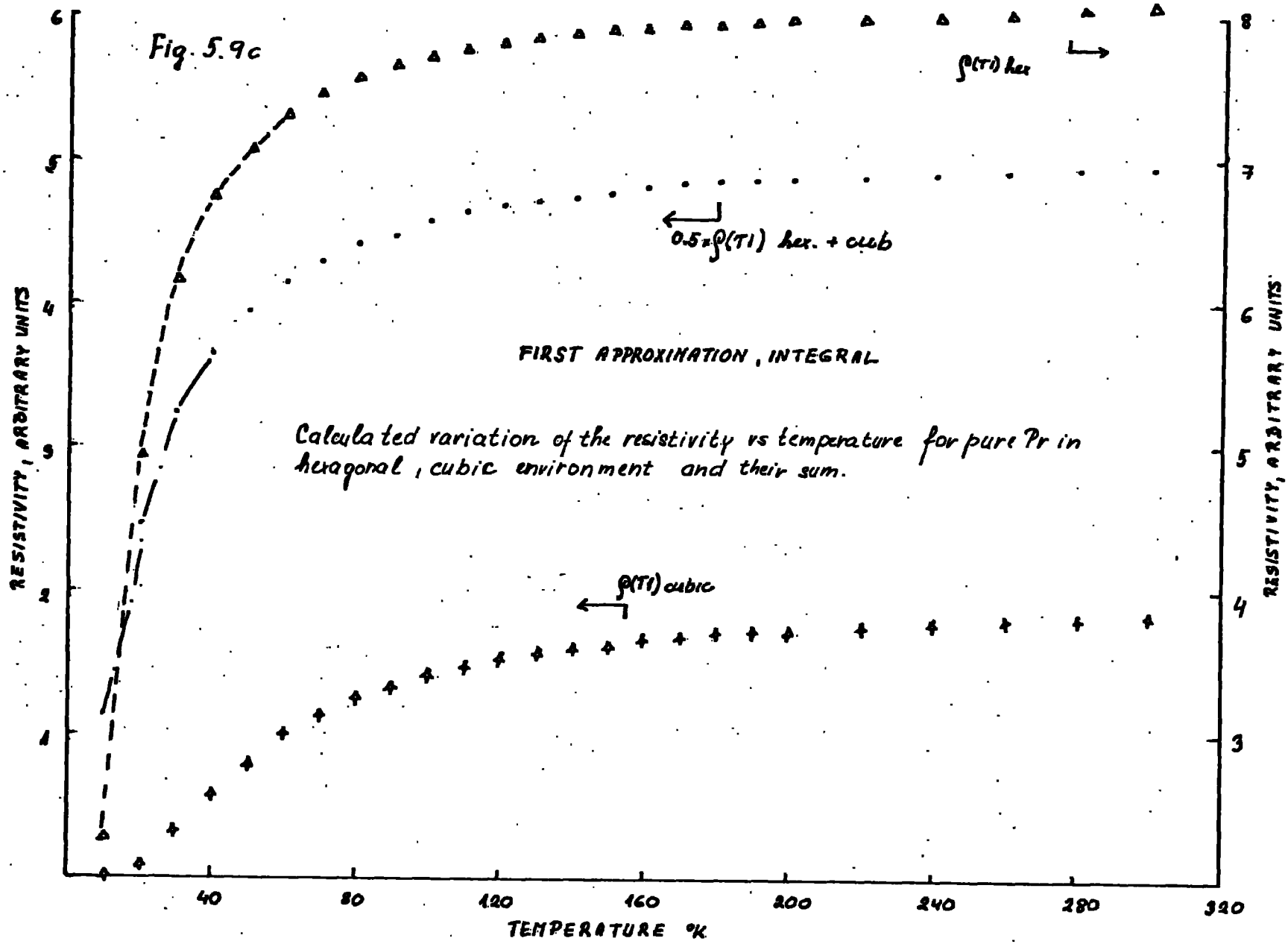

Calculated variation of the resistivity vs temperature for pure Pr in hexagonal, cubic environment and their sum.

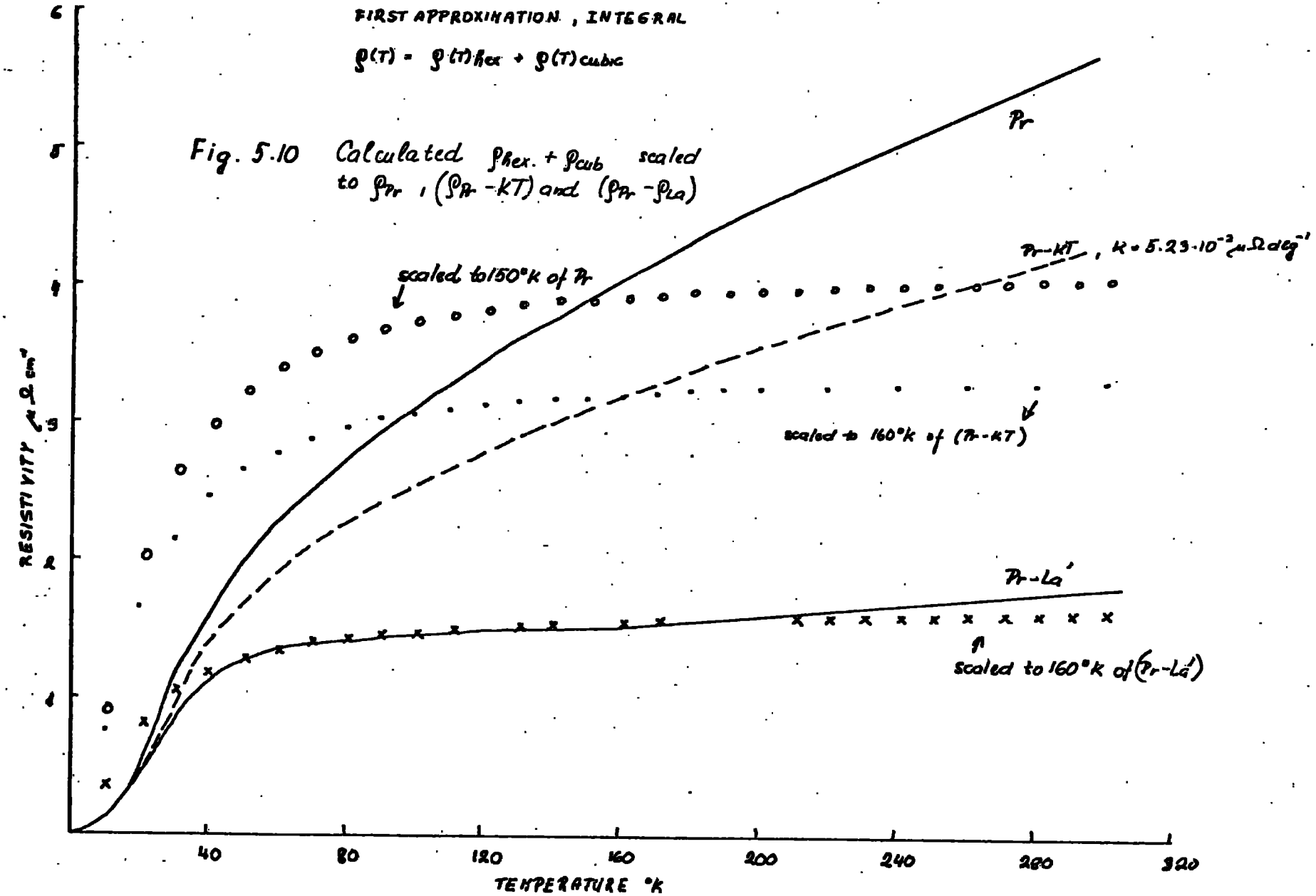

Fig. 5.10 Calculated $\rho_{hex.} + \rho_{cub}$ scaled to ρ_{Pr}, $(\rho_{Pr} - kT)$ and $(\rho_{Pr} - \rho_{La})$

results presented here enable a better start in this aspect since our resistivity of La is smaller then the resistivity of Pr. But as is obvious from fig. 5.7 ,5. 10 and the following discussion, unambiguous approval for this method of approach is not gained in our case either.

The experimental data for the resistivity of Pr and the Pr-Tb system were approached in all the three ways mentioned above.

1) The total resistivity (corrected for ρ_{res}) was considered to be mainly due to crystal field scattering

2) The total resistivity (corrected for ρ_{res}) was dealt with as if it consists mainly of two components $\rho_{phon.}$ and $\rho_{c.f.}$. Where

a) $\rho_{phon.}$ is of the same form as ρ_{La}

b) $\rho_{phon.}$ is linearly increasing with the temperature.

The resistivity due to crystal field scattering was calculated , as mentioned above, on the bases of M-B(4-6) theory for the hexagonal and cubic environments separately. An extention of the Matthiessen's rule was assumed

$$\rho(\tau_1)_{d\text{-}hex} = \alpha\rho(\tau_1)_{hex} + \beta\rho(\tau_1)_{cub}$$

In fig. 5.6 -5.10 are presented the results of the calculation. The theoretical contribution from the hexagonal and cubic environment are given separately in fig. 5.6 for a three level system (1-44) the theoretical curve being scaled to the Pr resistivity curve. These levels are shown in fig. 5.6, and were assumed to be eigenstates. The fit of the hexagonal contribution in the low temperature region ($\leq 160^{\circ}K$) is rather good as also is the fit for the cubic contribution in the high temperature region ($200\text{-}320^{\circ}K$)

suggesting that the sum of the hexagonal and cubic contributions to the $\rho_{c.f.}$ should provide a reasonable explanation of the resistivity behaviour of Pr. This is presented in the next fig. 5.7 . The best fit obtained to the total ρ_{Pr} is provided by the sum of ρ_{hex} and ρ_{cub}. Also shown in the figure is the total resistivity corrected for a phonon contributions, either assuming $\rho_{phonon} \sim KT$ or ρ_{La}.

In all three of the experimental curves presented there is an obvious deviation in the low temperature region. It may originate from a quadrupole term which has so far been neglected or alternatively if Matthiessens rule ceases to be valid at too low temperatures. The curve $\rho_{Pr}-\rho_{La}$ is obviously not fitted by this theoretical curve at all. Since it cannot give a good fit for ρ_{tot} corrected for ρ_{phon}. we will look more thoroughly at the system.

The results of the $\rho_{c.f.}$ calculation for all the crystal field energy levels calculated by (1-51,5-1) are presented on fig.5.8 and 5.9a-c. The calculations have assumed that recombination may be neglected, as has been done in the above to ensure that the form of the curve does not become substantially altered, i.e. that it still represents the crystal field scattering for a given set of energy levels. Figure 5.8 represents ρ_{hex} and ρ_{cub} where recombination was neglected along with $\rho_{hex}(\eta(E)=\text{const.})$ and $\rho_{hex}(\eta(E)=f(E))$. Both of which give almost identical results. Also there is only a small variation in the low temperature region between the curves where recombination was neglected, fig.5.8 and was considered fig. 5.9a-c. The sum of $\rho_{hex}+\rho_{cub}$, fig.5.9c reveals the fact that all transitions between all possible

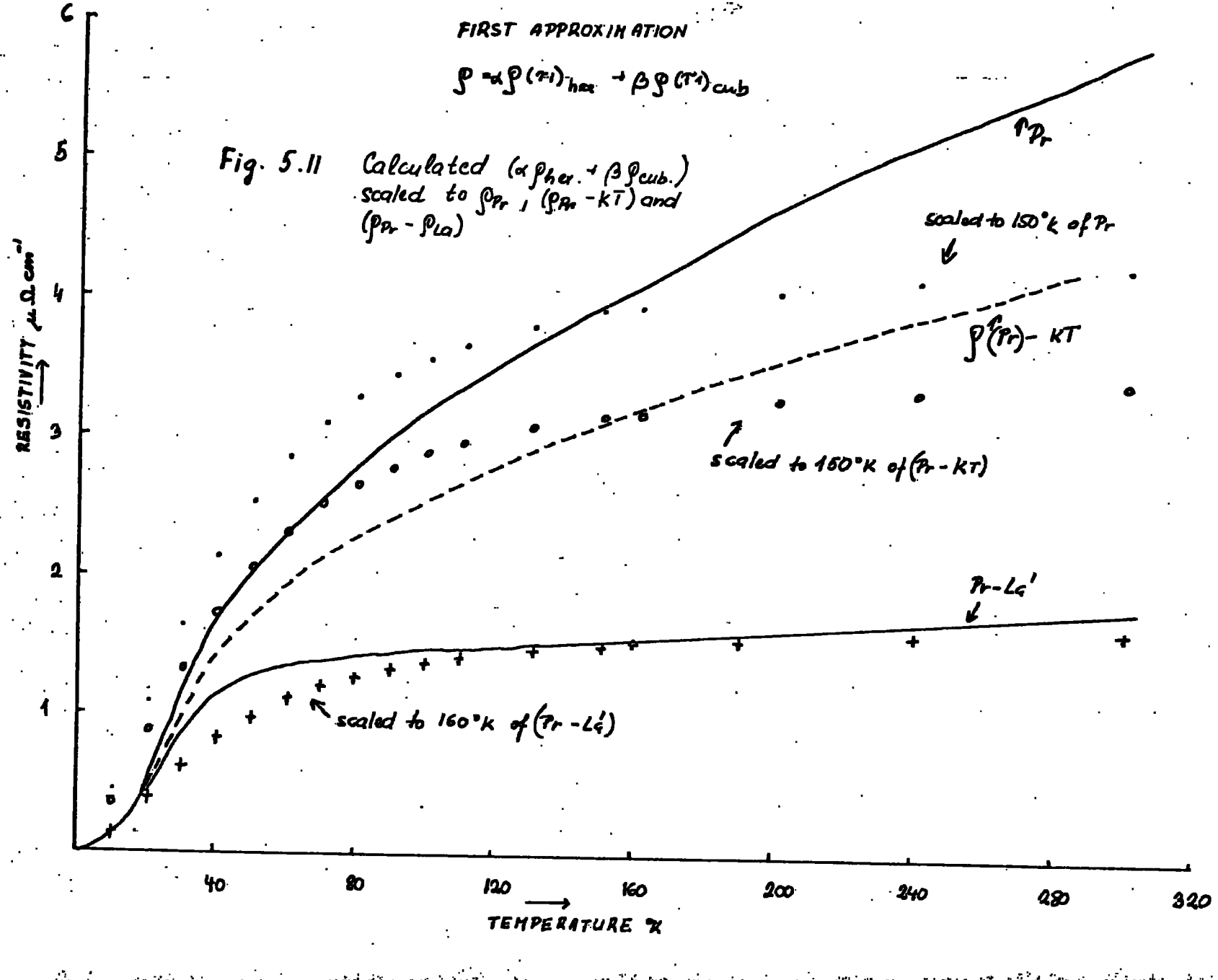

Fig. 5.11 Calculated ($\alpha \rho_{hex.} + \beta \rho_{cub.}$) scaled to ρ_{Pr}, $(\rho_{Pr} - KT)$ and $(\rho_{Pr} - \rho_{La})$

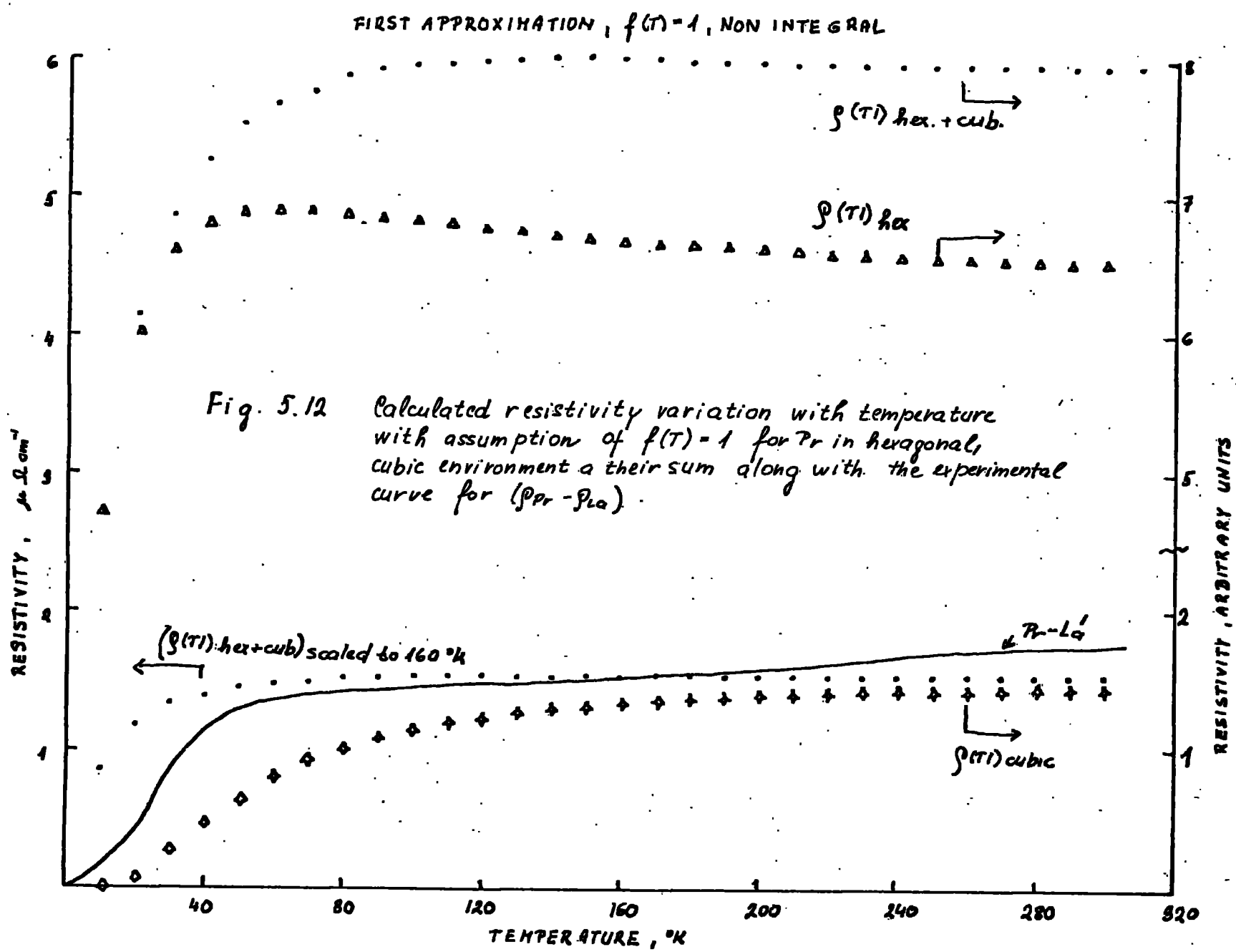

Fig. 5.12 Calculated resistivity variation with temperature with assumption of $f(T) = 1$ for Pr in hexagonal, cubic environment a their sum along with the experimental curve for $(\rho_{Pr} - \rho_{La})$.

energy levels (1-51,5-1) are considered ρ_{hex} is much bigger then ρ_{cub} so that ρ_{hex} essentially determines the character of $\rho_{c.f.}$ in Pr. The scaled sum of ρ_{hex} and ρ_{cub} from fig. 5.9c to the ρ_{Pr}, ρ_{Pr-KT}, and $\rho_{Pr} - \rho_{La}$ is presented in fig. 5.10. The best fit is obviously obtained for the case of $\rho_{Pr} - \rho_{La}$. Since the theoretical curve is scaled to the higher temperature (160°K), the theoretical curve predicts a faster rise at low temperature than is actually observed. This may be understood perhaps if the resistivity due to quadrupole scattering was considered (4-4) since this is believed to be strong in the case of Pr. Further, according to some experimental evidence, polycrystaline Pr is believed to be ordered up to ~20°K and if this is so then in fig.5.10 the $\rho_{c.f.}$ should be considered only from 20°K onwards, where as may be seen the fit is good. The small deviation at high temperatures can be attributed to the difference between $\rho_{Pr-phon.}$ and ρ_{La}.

The weighted sum $\alpha\rho_{cub} + \beta\rho_{hex}$ scaled as above to ρ_{Pr}, ρ_{Pr-KT} and $\rho_{Pr} - \rho_{La}$ is presented on fig 5.11. The fit to any of the experimental curves is poor in comparison to the fit obtained in fig 5.10 for $\rho_{Pr} - \rho_{La}$ and consequently we can than take $\rho_{c.f.} = \rho_{hex}(T) + \rho_{cub}(T)$. Fig.5.12 shows the same calculation for the energy levels used in the above with assumption that the Fermi-Dirac distribution function is $f(T)=1$ and the integral resistivity could be expressed as

$$\rho_{c.f.}(T) = \tau(1) \times \text{constant} \quad \ldots \quad /4/$$

Again the cubic contribution is smaller than the hexagonal. The biggest deviation from the integral results, fig.5.9, are obviously at low temperatures. In the hexagonal case $\rho(T)$

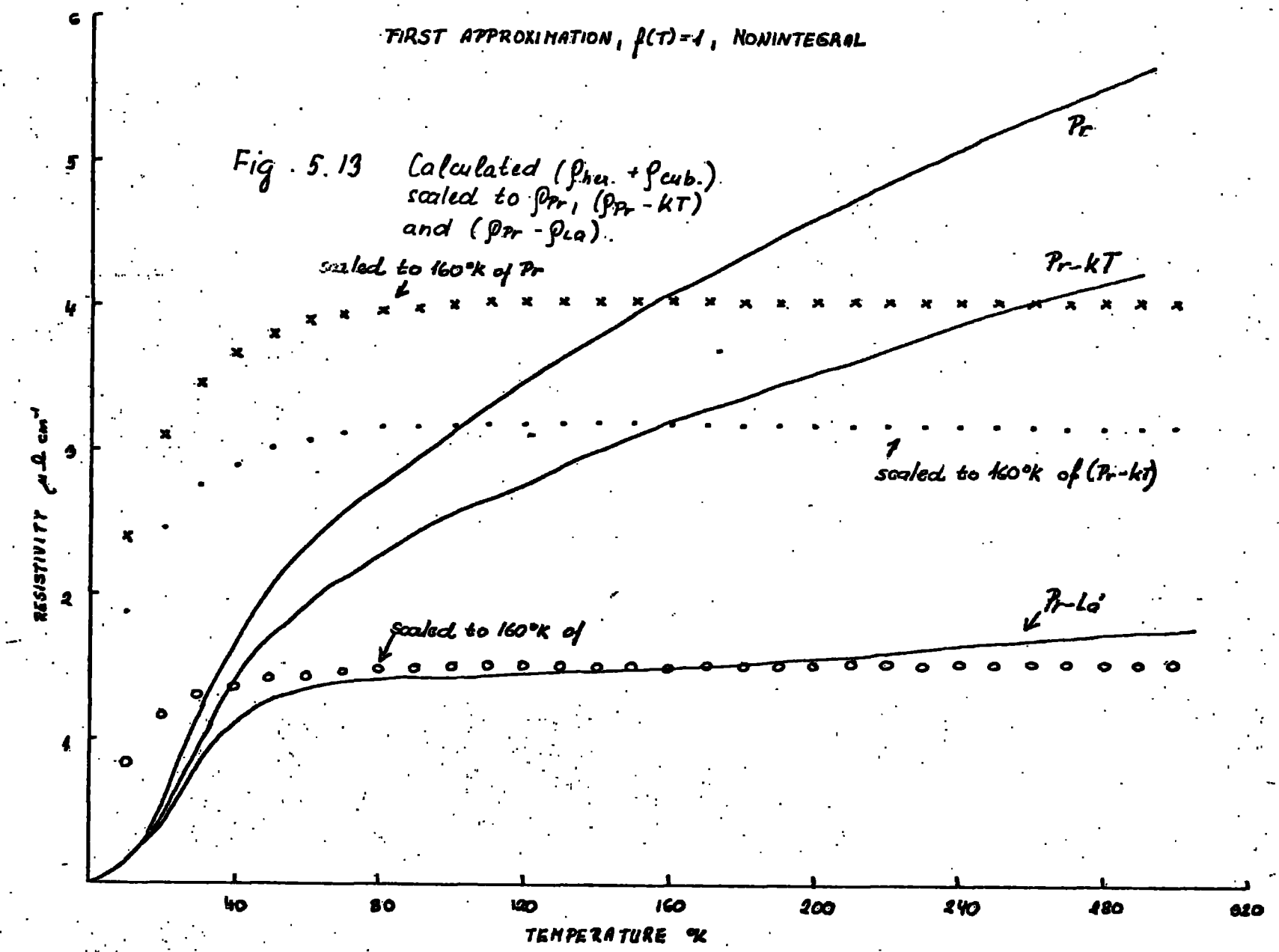
FIRST APPROXIMATION, f(T)=1, NONINTEGRAL
Fig. 5.13 Calculated ($\rho_{hex.} + \rho_{cub.}$) scaled to ρ_{Pr}, ($\rho_{Pr} - kT$) and ($\rho_{Pr} - \rho_{La}$).
scaled to 160°K of Pr
Pr
Pr-kT
scaled to 160°K of (Pr-kT)
Pr-La
scaled to 160°K of
RESISTIVITY $\mu\Omega$ cm
TEMPERATURE °K
40
80
120
160
200
240
280
320
1
2
3
4
5
6

is decreasing with temperature, after reaching a maximum at ~40°K. This shows the necessity for carrying out a complete calculation for the case where $\Delta E_i \sim KT$. The fit of this curve to the experimental $(\rho_{Pr}-\rho_{La})$ values is obviously worse than in fig.5.10, mainly at low temperatures. and can be only regarded as a zero approximation to the problem. This conclusion is also supported by the results shown in fig.5.13 which may be discussed(in zero approximation) in a similar way to the discussion concerning fig.5.10.

5.3 Praseodymium-terbium in the d-hex phase

The temperature variation of the resistivity of Pr-Tb alloys in the d-hex phase has been approached in a similar way to the case of pure praseodymium. In general these alloys do not show any evidence for long range ordering, but neutron diffraction results(5-1,1-36) show that some short range order occurs. This is a minimum for the 10% Tb specimen and increases with increasing terbium, until at 30% Tb magnetic measurements show a very broad peak at 20°K in the χ-T curve (fig.5.14) and deviations from a Curie Weiss behaviour for temperatures below about 70°K. This latter temperature coincides with the disappearance of the broad, short range order sattelite peaks in the elastic neutron scattering data.

The magnetic behaviour of the 30% Tb specimen is believed to result from an assembly of ions in which the ration of the crystal field to magnetic exchange interactions is very close to the critical value for spontaneous ordering (12,13).

It is known from crystal field calculations (1) and magnetic measurements(1-51)that an internal field of 500KOe is necessary to induce the magnetic ordering of Pr .; Consequently it would appear that in the 30% Tb alloy the effect of the

Fig. 5.14 Susceptibility variation with temperature for Pr_9Tb_1.

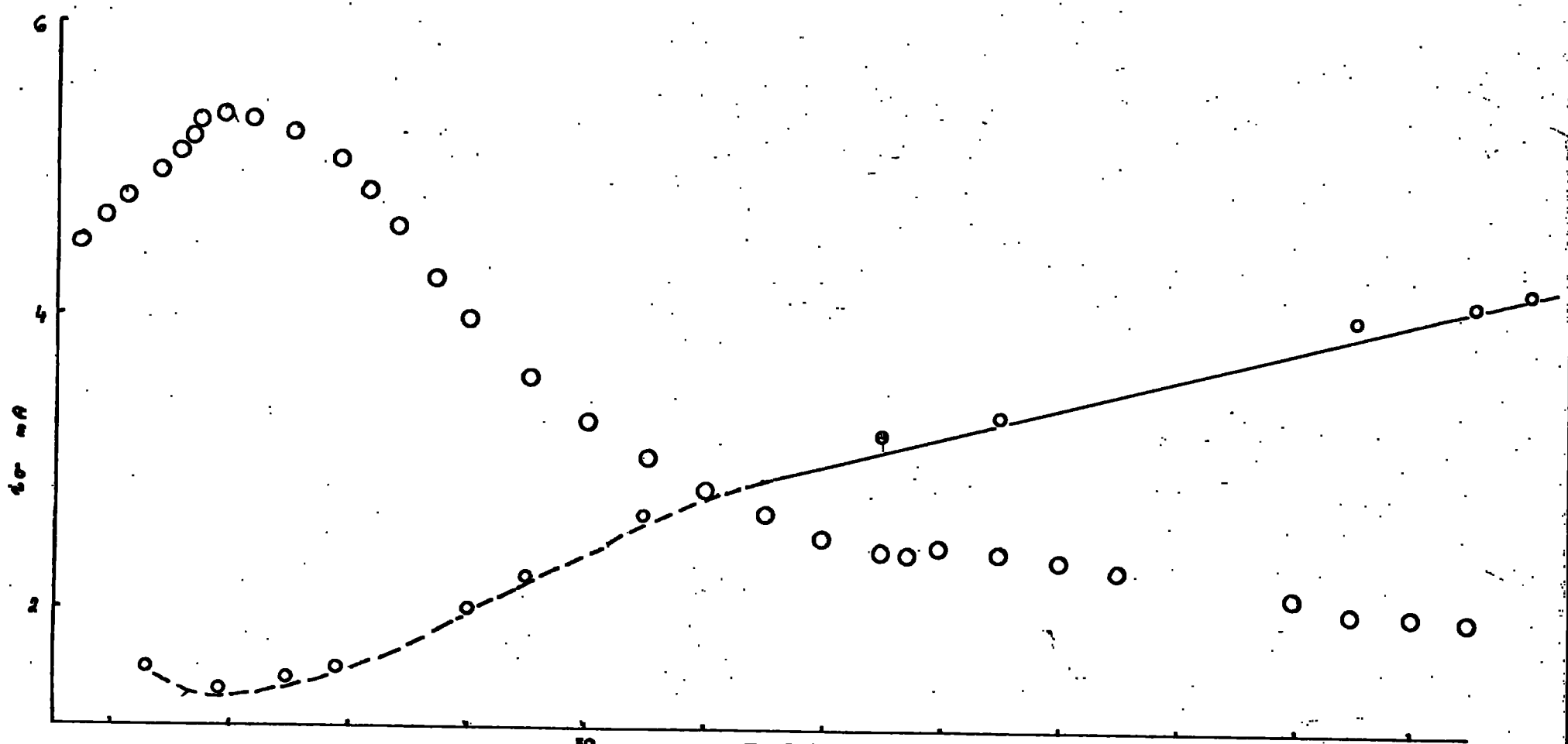

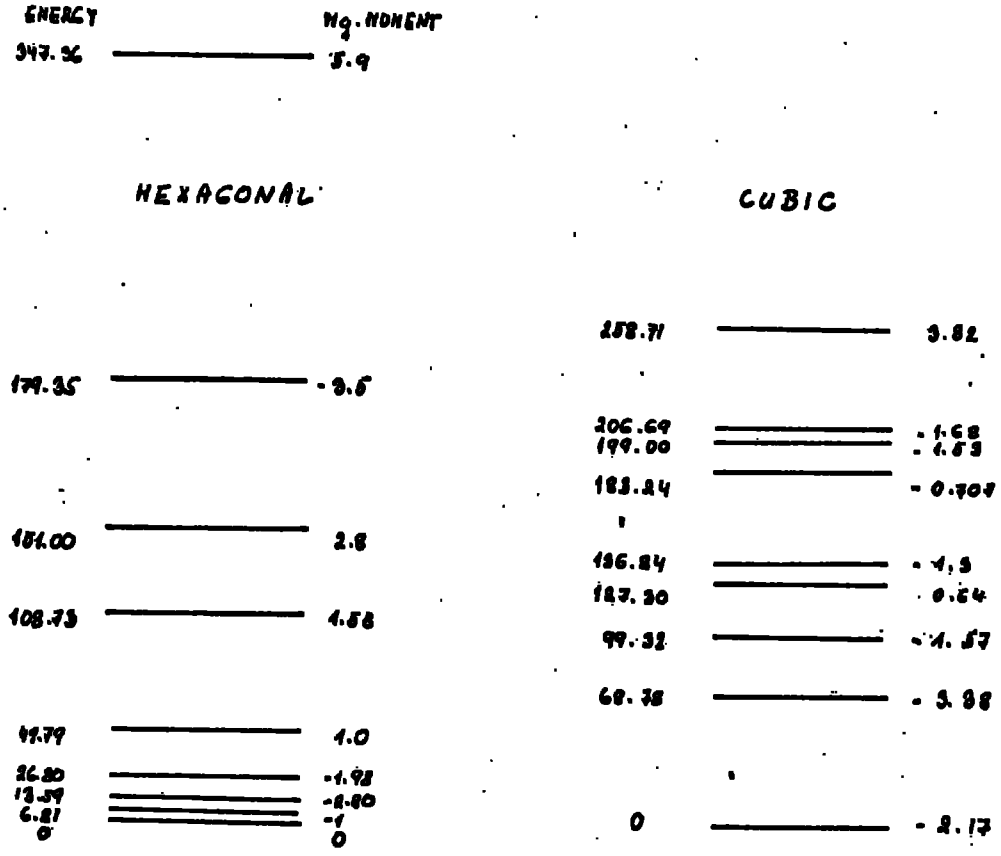

ENERGY LEVELS OF PRASEODYMIUM IN $(H_{HC})_E$ 400 KOe

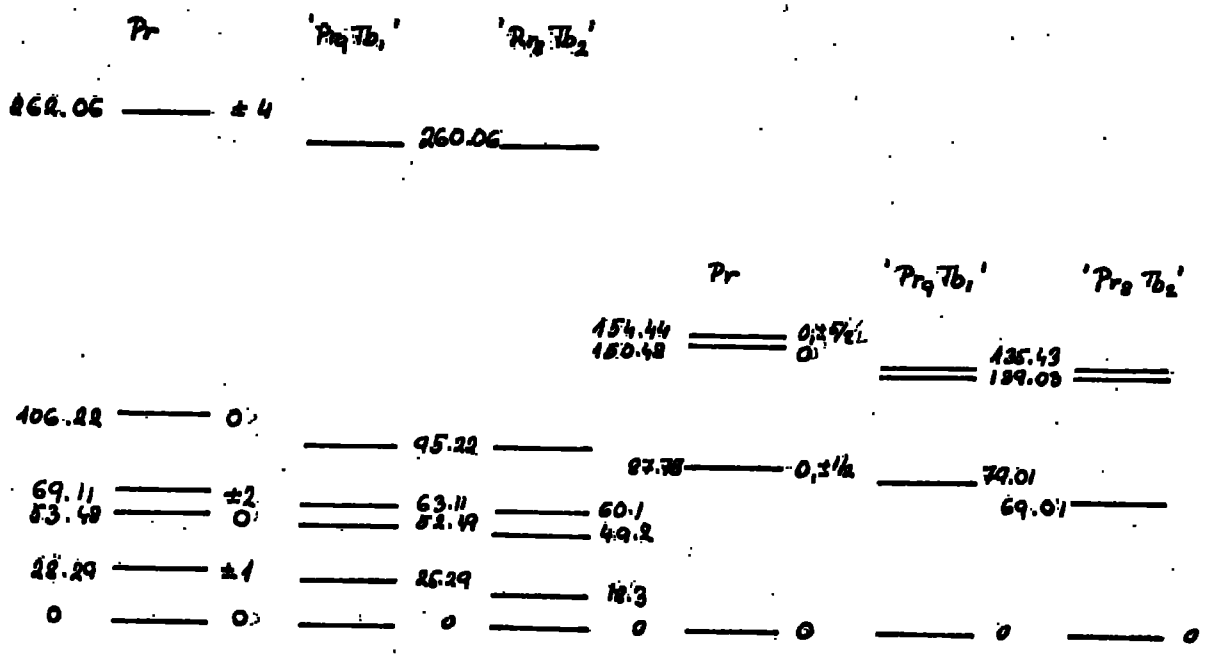

Fig. 5.15

Various distributions of the crystal field energy levels for Pr in magnetic field.

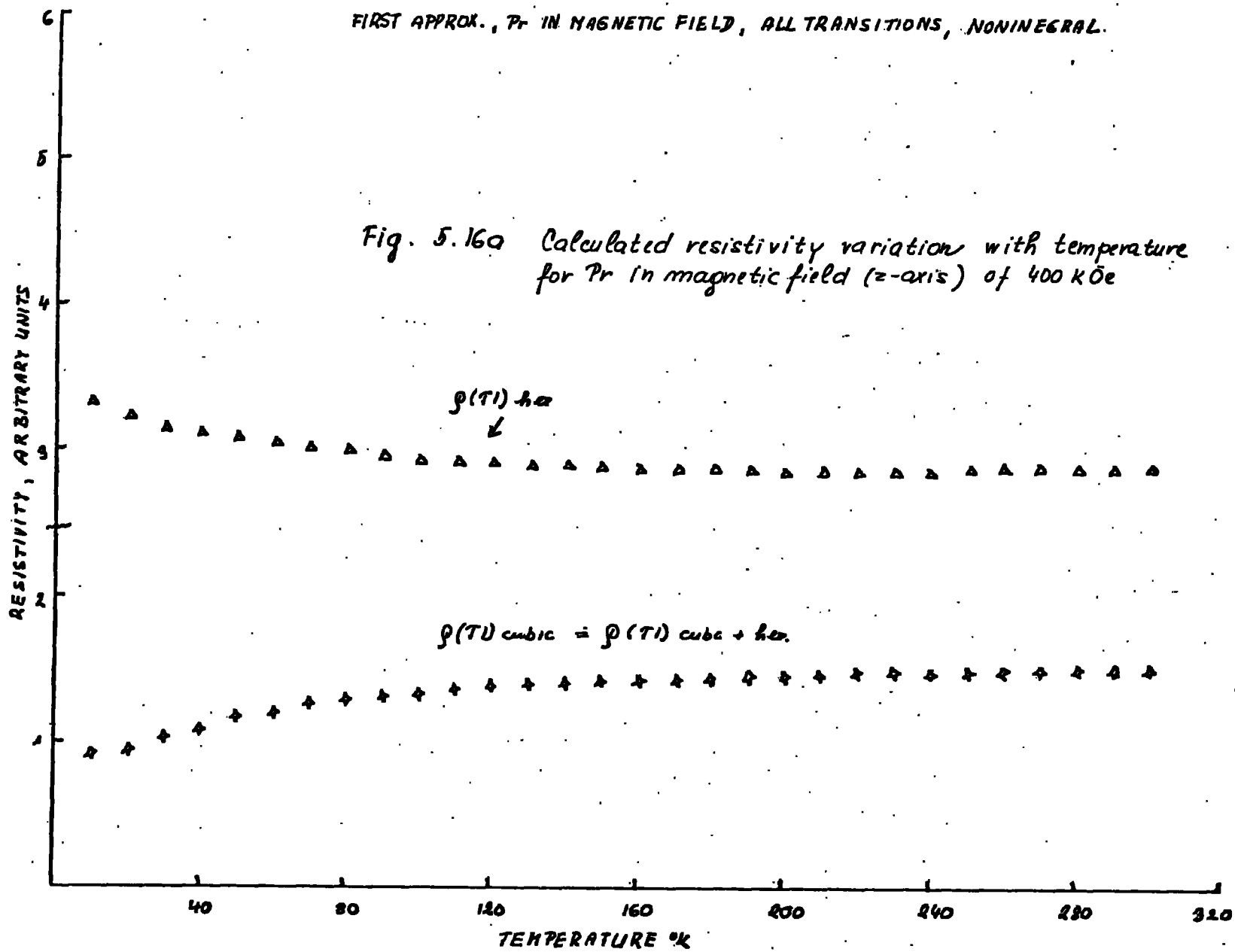

Fig. 5.16a Calculated resistivity variation with temperature for Pr in magnetic field (z-axis) of 400 kOe

Fig. 5.16 b Calculated resistivity variation with temperature for Pr in magnetic field of 400kOe

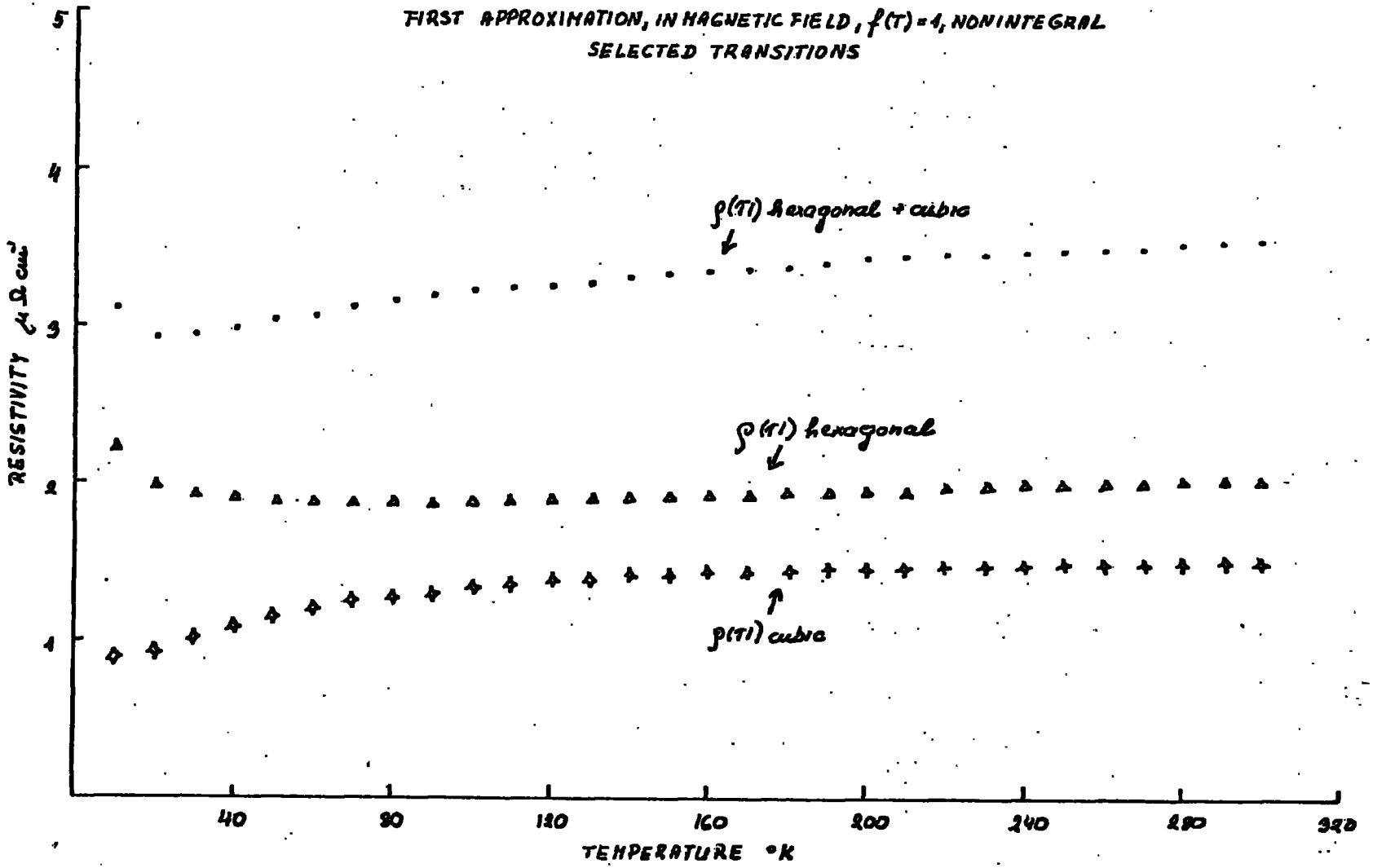

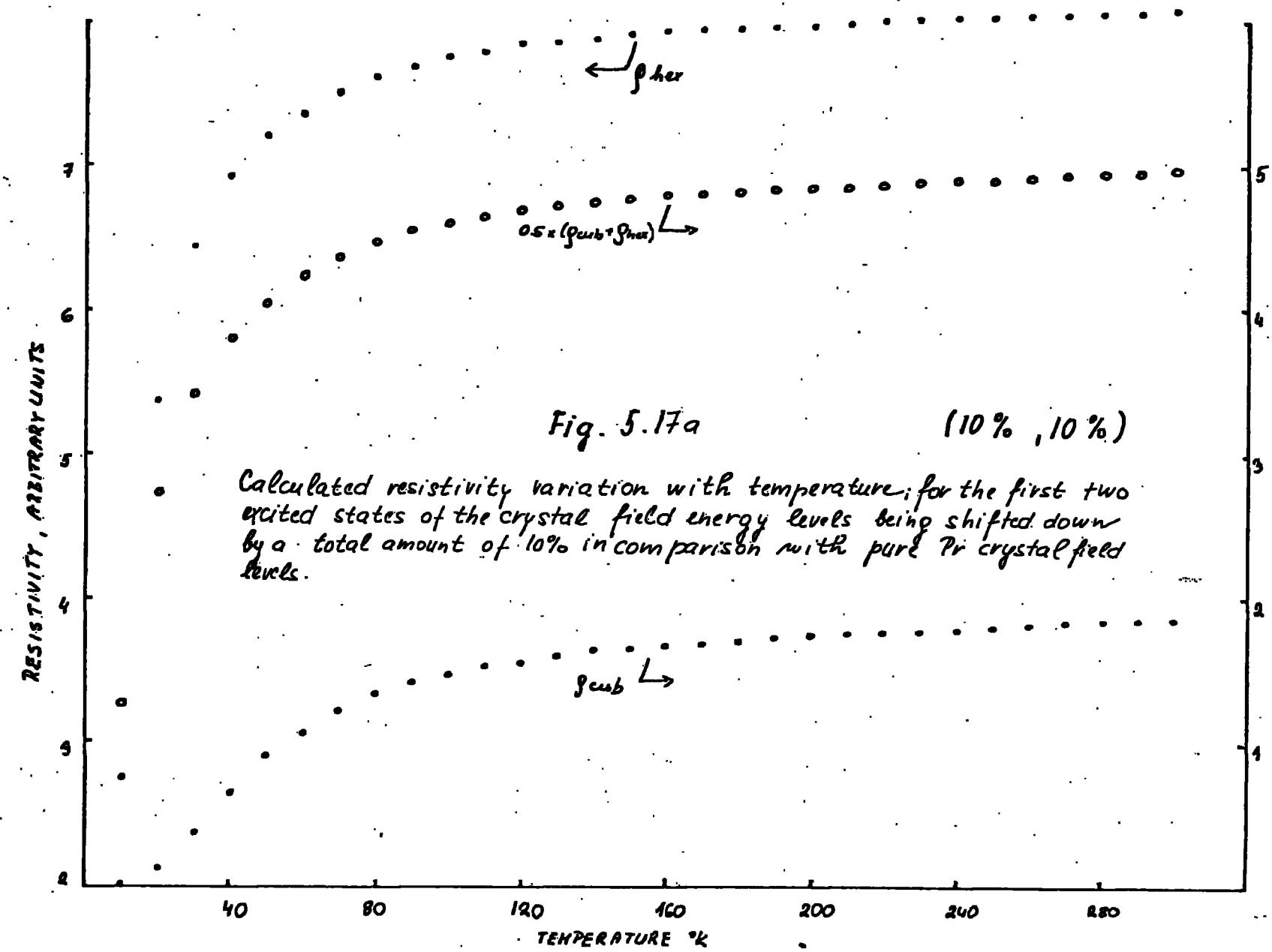

Fig. 5.17a (10 %, 10 %)

Calculated resistivity variation with temperature; for the first two excited states of the crystal field energy levels being shifted down by a total amount of 10% in comparison with pure Pr crystal field levels.

Fig. 5.17b

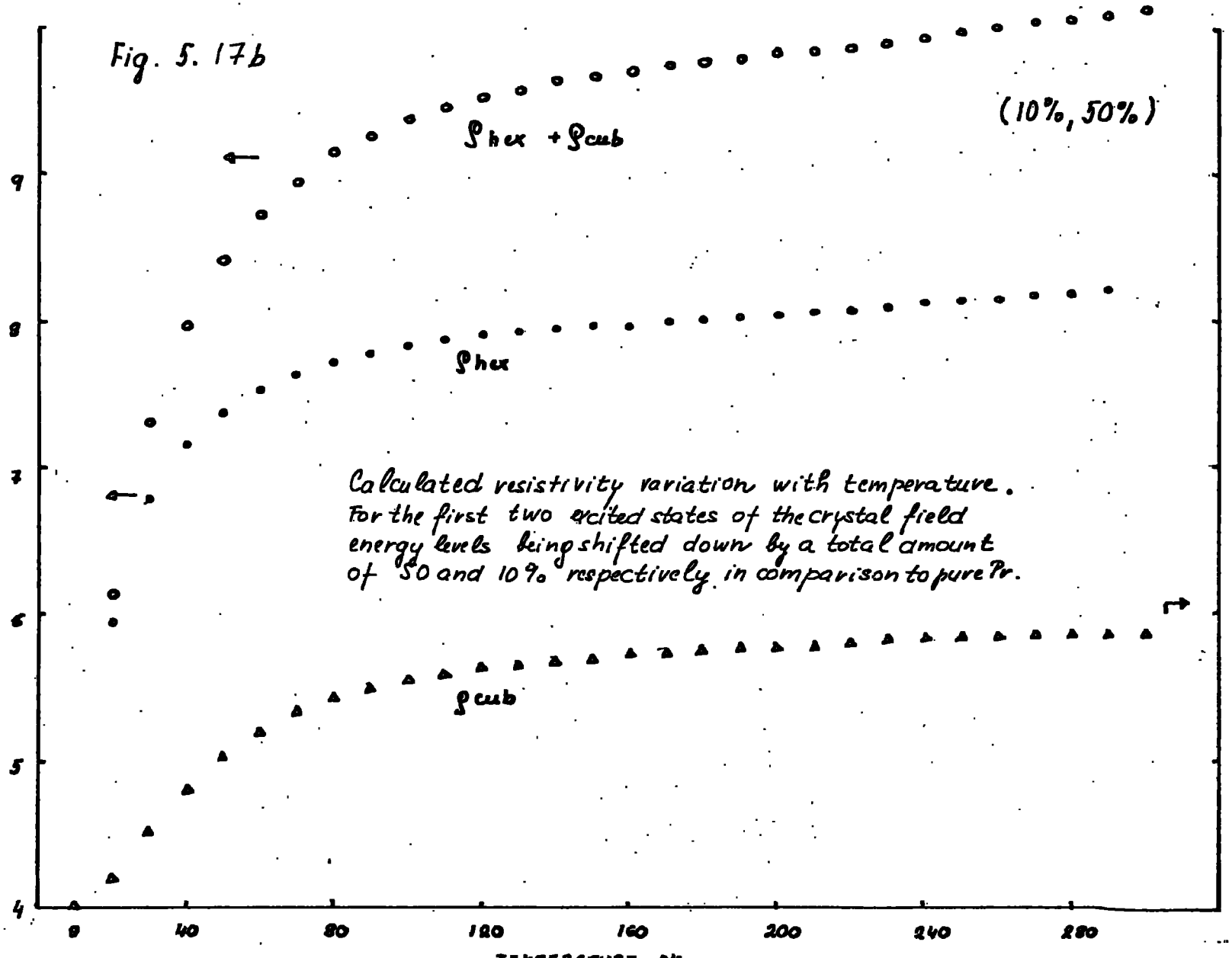

Calculated resistivity variation with temperature. For the first two excited states of the crystal field energy levels being shifted down by a total amount of 50 and 10% respectively in comparison to pure Pr.

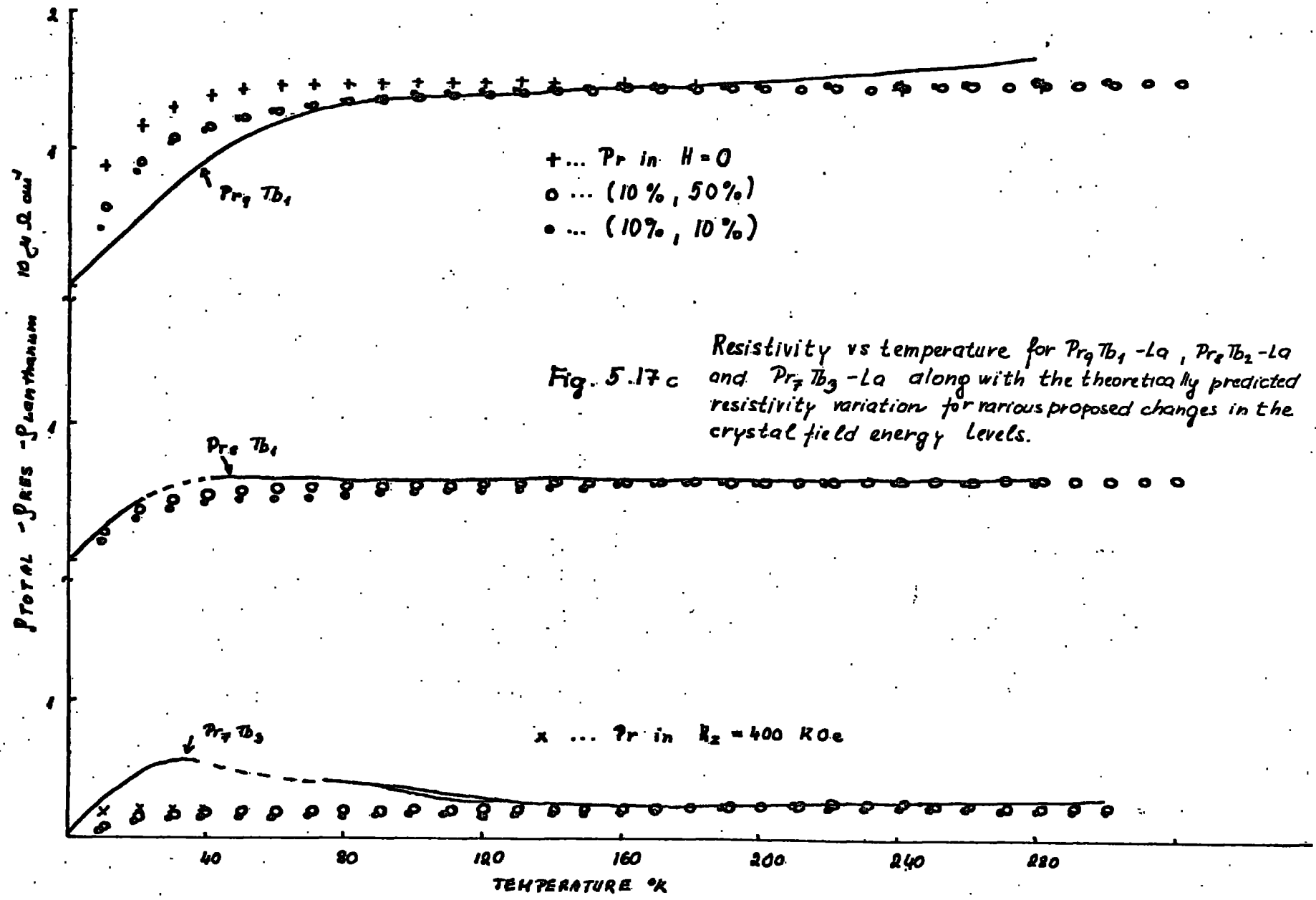

Fig. 5.17c Resistivity vs temperature for Pr_9Tb_1-La, Pr_8Tb_2-La and Pr_7Tb_3-La along with the theoretically predicted resistivity variation for various proposed changes in the crystal field energy levels.

exchange interactions may be expected to lie slightly below this figure . For lower terbium concentrations the effect of the exchange will correspond to lower field values and in the limit the addition of Terbium may simply distort the praseodymium crystal field resulting in slight shifts of the levels involved. Some evidence for this effect has already been observed (1) for the range 5-15% Tb using inelastic neutron scattering.

If we take the effect of the exchange interactions in the 30% Tb sample to correspond to 400KOe, crystal field calculations give the level structure shown in fig 5.15 for the two sites. Evaluation of the temperature dependence of the resistivity are then straightforward, and may be carried out as for pure praseodymium. The results of this calculation are shown in fig. 5.16a,b under the assumption that $f(T)=1$, ie neglecting the effects of the change in the Fermi-Dirac function with increasing temperature.

Fig. 5.17a shows the total crystal field contribition to the resistivity compared with the experimentally obtained variation of the "magnetic" resistivity for the 30% Tb alloy. The experimental values are given by

$$\rho_{c.f} = \rho_{tot.}(30\%tb) - \rho_{res.} - \alpha\rho_{La}$$

and the theoretical curve is normalized to $\rho_{c.f}$ at T=160°K. Above about 100°K the fit is reasonably good as might be expected, however below this temperature the experimental values show a broad peak with a maximum at about 30°K. This is similar to the susceptibility observations and we assume that this additional resistivity is associated with the presence of short range ordering in the specimen. If this ordering is antiferromagnetic then the additional resistivity

can be expected to be in excess of the crystal field only values because of the local superzone effects arising from the difference in the periodicity of the spin structure and the atomic structure of the alloys.

An examination of the resistivity with temperature for the 10 and 20% terbium samples showed that the former is remarkably similar to pure praseodymium exept for an in increase in the residual resistivity. The latter has a decreased contribution to the magnetic resistivity at all temperatures compared with pure praseodymium and in addition at low temperatures ($<40^{o}K$) shows some evidence of the effect of short range order.

If we assume that there is little or no short range order in the 10% Tb sample, as seems likely from the neutron scattering data, then the resistivity variation should be capable of interpretation in the same way as pure Pr. Assuming that the Tb impurities contribute only the increase in the residual resistivity the praseodymium contribution will then be given by a dilution correction to the pure Pr results. This is shown in fig.5.17c compared with the experimental data and as may be seen there is a considerable error at low temperatures. As suggested previously, inelastic neutron scattering data shows that the magnetic excitation levels in Pr-Tb alloys are sensitive to the addidtion of Tb, the 8-9meV and 2-4mev levels decreasing with increasing Tb, fig. 5.18a,b(13,17) .The upper level is known to decrease by approximately 10% while the lower level, which is much more difficult to resolve, moves to lower energies by an amount between 10-50%. Using a set of crystal field levels to which corrections of this type have been made, the predicted

resistivity variation moves towards the experimental form. These results are shown in fig. 5.17a,c,c for shifts of(10%,10%) and (10%,50%) in the 8-9mev and 2-4mev levels.

It is evident that by allowing for changes of the detailed crystal structure it is possible to obtain a reasonable understanding of the resistivity variation in this alloy. In order to obtain a complete fit however, it will be necessary to know the changes in all the levels rather than only the lowest two. As this data is not likely to be available in the near future from experimental observations, and since it is probably not possible to obtain a unique set of crystal field levels to give a best fit we have taken the above results as an indication that the observed effects in dilute Pr-Tb alloys may be attributed, at least to a first approximation, to the effects of changes in the crystal field caused by the addition of Tb. In a complete fit, of course, it will also be necessary to allow for the temperature dependence of the scattering from the Tb ions.

The 20% Tb alloy is obviously intermediate between the 10 and 30% Tb alloys and in order to obtain a complete understanding of the observed resistivity both the crystal field and the exchange interactions must be known. This is not the situation at present and only crude theoretical estimates are possible by combining the results of the 10 and 30% Tb specimens. Fig 5.17c shows the experimental data for this alloy, and a variety of predicted crystal field combinations. It is evident that there is little to choose between these curves. In conclusion, for these d-hex structure Pr-Tb alloys, the variation in the ρ-T curves with concentration may be understood in terms of a continuous

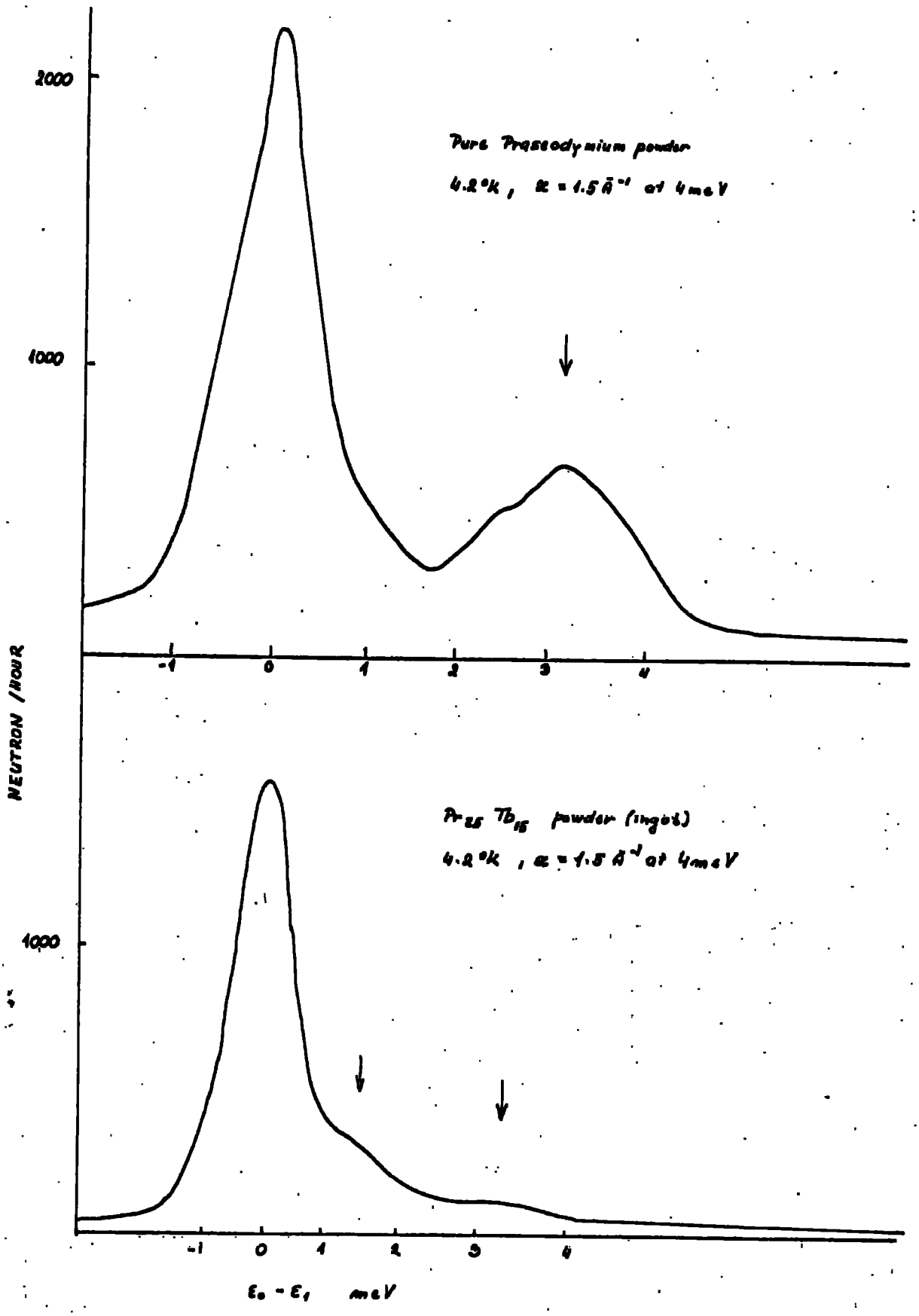

Fig. 5.18 a Neutron diffraction results for the Pr powder at 4.2°K

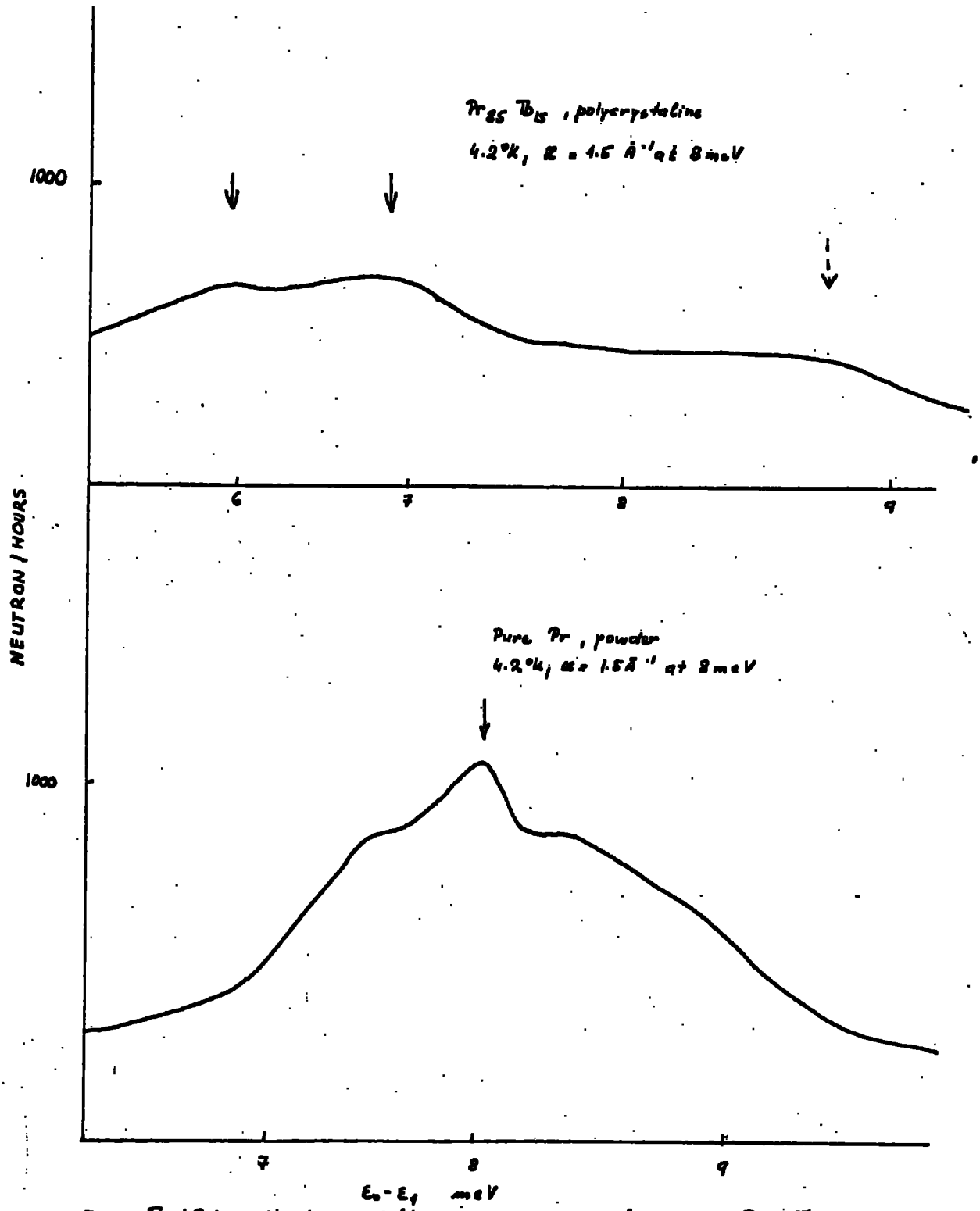

Fig. 5.18 b Neutron diffraction results for the $Pr_{85}Tb_{15}$ polycrystal at 4.2°K

change in the crystal field levels with increasing terbium and an increasing amount of short range order in the specimen. Whether the short range order contributes to the resistivity through a normal term (14, 6) of the form

$(g-1)^2 J(J+1)$ (or $S(S+1)$)

or by means of critical fluctuations (3) is not yet clear.

5.4. Neodymium-Dysprosium and Neodymium-Yttrium alloys in the d-hex phase

It appears likely that the resistivity variation of these two alloy systems may be considered in terms of four contribitions, the total resistivity being written

$$\rho_{tot}(T) = \rho_{res} + \rho_{c.f}(T) + \rho_{s-f}(T) + \rho_{phon.} \quad \ldots \quad /5/$$

Again, the residual resistivity is taken as $\rho(4.2^{\circ}K)$ and the phonon scattering may be approximated to by ρ_{La}. To define the form of the scattering due to the crystal field it is necessary to know the eigenvalues and eigen functions describing the sublevels of the J=4 ground state of the Nd ion in the alloys. Unfortunately these are not known with any degree of accuracy at the present time and a less detailed understanding must result in consequence. The problem is further complicated by the presence of magnetic ordering in pure Nd which gives rise to the spin disorder resistivity term $\rho_{s-f}(T)$. It is well known that this contribution varies rapidly with temperature up to the ordering temperature ($T_N \tilde{=} 7\ ^{\circ}K$) (15) above which it gives an essentially constant contribution to the resistivity, which in terms of the RKKY theory has a magnitude $\rho_{s-f}(T>T_N) = A(g-1)^2 J(J+1)$. If we assume that the constant term can be normalized to the value obtained for elemental Gd, this contribution would be expected to be of magnitude approximately 18 $\mu\Omega$cm. As we

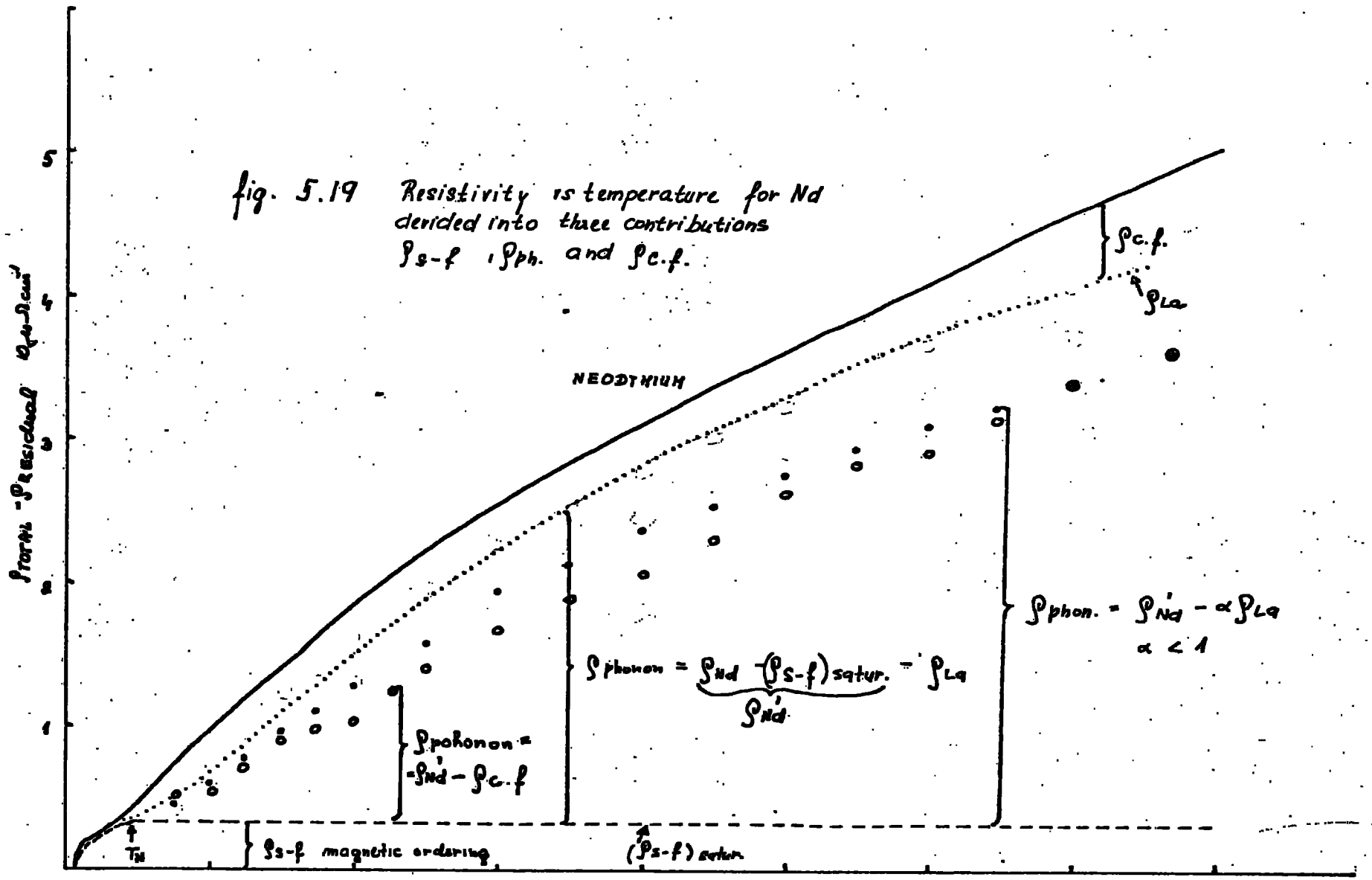

fig. 5.19 Resistivity vs temperature for Nd devided into three contributions ρ_{s-f}, $\rho_{ph.}$ and $\rho_{c.f.}$

can see from fig.5.19 the total resistivity is less than this value at 20°K, so that it is evident that the free electron picture is inadequate to describe the observations even qualitatively. Since it is known (4-4) that the exchange interaction is comparable to that of Gd, in the d-hex structure, the differences are undoubtely associated with the differences between the real Fermi surfaces of the two elements (these are of course primarly concerned with the two different structures of Gd and Nd). Similar the variation of ρ_{s-f}. with temperature gives mechanism(1-13,36)desribed in chapter 4.5 where the presence of the crystal field levels is taken into account and consequently we believe this model is more suitable for the light rare earths.

Following earlier workers(4-4,) we can discuss the behaviour of Nd (and also the Nd-Dy, and Nd-Y alloys) as indicated in fig. 5.19. Here, the spin disorder resistivity ρ_{s-f} is shown dashed, reaching a saturation value above about 20°K. The absolute value of the saturation value of ρ_{s-f} is difficult to establish, as discussed above, however as the only other temperature dependent contribution to the resistivity below 20°K will arise from $\rho_{phon.}(T)$, which is expected to be small at these temperatures we have assumed that it corresponds to a value slightly less than $(\rho_{tot}-\rho_{res.})(20°K)$.

The remaining resistivity corresponds to the crystal field contribution (T>20°K) and the phonon resistivity. The latter may be taken proportional to ρ_{La} as was done in the Pr alloys or alternatively it may be qualitatively estimated by assuming that the substitution of Y serves merely to dilute $\rho_{c.f.}$ in the d-hex phase, and extrapolating to pure Y, so giving an effective d-hex yttrium behaviour.

Obviously this is a long extrapolation and the result can only be taken as a guide to th emagnitude of $\rho_{phon.}$. These two contribution obtained in this way are shown in fig.5.19. As may be seen , the phonon contribution differs appreciably from the resistivity of the pure La,particularly in the mi-middle temperature region, although this is probably to be expected in view of the alloys under consideration. The crystal field resistivity however, is typical of the behaviour observed in the Pr series,and for electron scattering from crystal fields in general. If we take the knee as being a crude guide to the splitting of the first two doublet states in the Krammer's ion this will correspond to a value of about 100°K which is the correct order of magnitude for neodymium in a hexagonal environment. It must be remembered however, that 50% of the atomic sites in the d-hex lattice have cubic symmetry, for which the crystal field splitting in metals is known(1-47) to be nearer to 20°K. This will be discussed later in this section.

If we return to the Nd-Y alloys, the discussion may be based on equation / 5 /. The results of fig.3.22 show that at low temperatures (<10°K) there is a rapid fall in total resistivity which may be associated with a magnetic transition, or alternatively with an increase in crystal field scattering. This change is also evident in pure Nd and is normally associated with the magnetic ordering of the cubic sites which occurs at 6°K.

In either case, above this temperature one can assume that with Y dilution, the magnitude of this contribution to $\rho_{tot.}$ will fall off as the Nd concentration, fig.5.20.

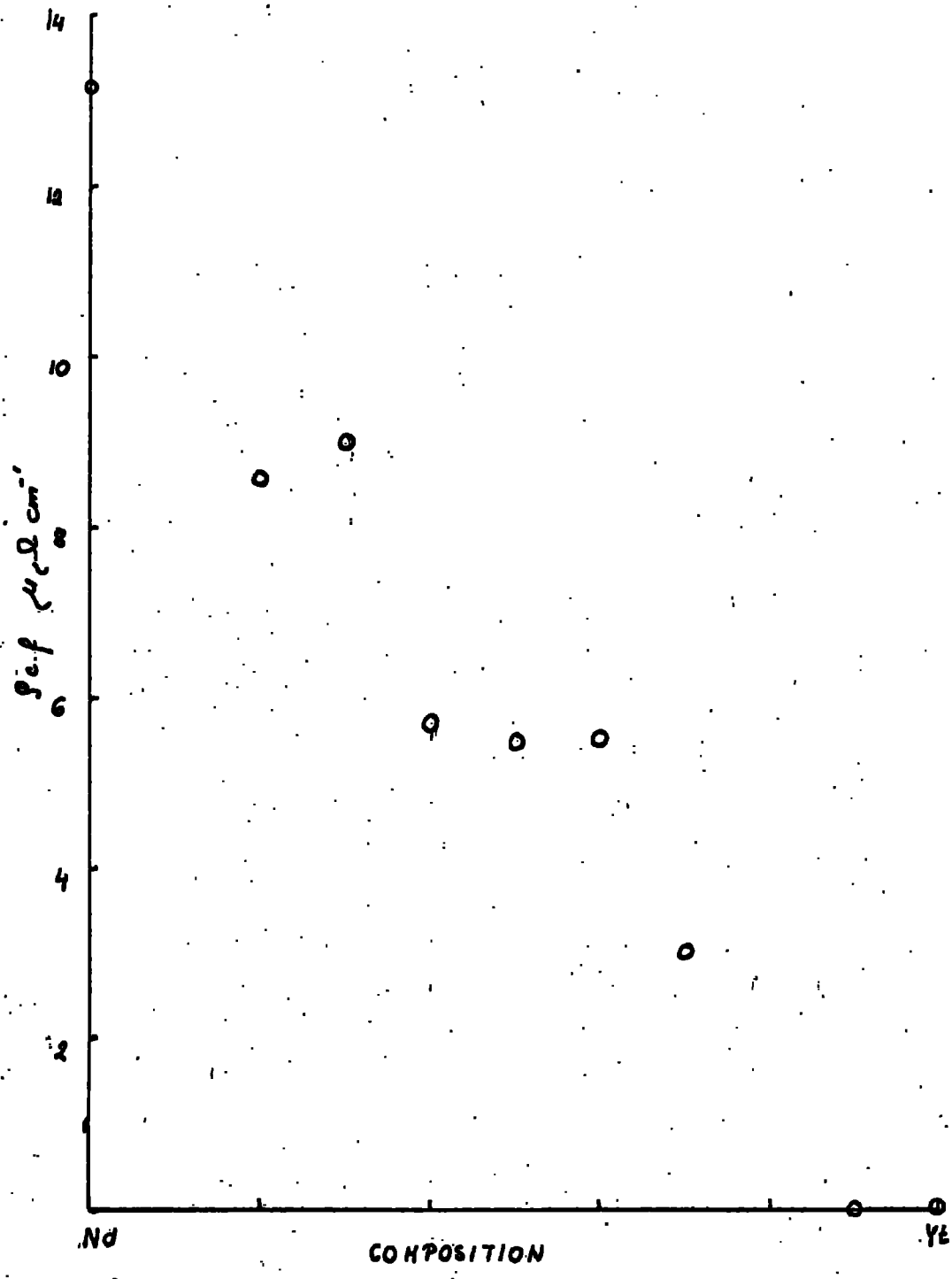

fig. 5.20 $\rho_{c.f.}$ vs composition for Nd-Y alloys.

Similarly, as has been discussed earlier in this section the crystal field contribution to the resistivity above 20°K will be concentration dependent. Consequently, we may write $\rho_{tot.}(T) = \rho_{res.} + x\rho_{s-f}(T) + \rho_{phonon}$ where $\rho_{res.}$ can be expected to depend on concentration as $x(1-x)$ through the scattering from the potential mismatch in the alloy system and ρ_{s-f} includes both the crystal field and spin disorder terms where the latter is relevant. This term will of course be constant at high temperatures.

As may be seen from fig.3.22 above 120°K, $\rho_{tot} \propto T$ consequently the saturation value of ρ_{s-f} may be obtained in the normal way by extrapolating the high temperature resistivity variation to T=0. The values obtained in this way are shown in fig.5.20 for the entire alloy system, and as may be seen there is an approximately linear decrease with increasing yttrium content. This decrease in the magnetic term is very evident from the resistivity results of figs.3.22,27, where it is also clear that the form of $\rho_{s-f}(T)$ is the same for all the series. Since those figures refer to materials in the d-hex, the samarium and the hcp phases this is rather interesting as the relative percentage of cubic and hexagonal sites change appreciably from one to another. This result leads to two possibilities, either

a) the contribution to the total resistivity from the two types of site are identical in form and magnitude, which seems unlikely in view of the radically different crystal fields at the two environments or

b) the cubic sites make 1) a relatively small contribution to the resistivity and 2) this contribution reaches its

$(d\rho/dT)_{high\ temp.}$ vs composition for Nd-Y, Nd-Dy, La-Dy and Pr-Tb.

Fig. 5.21 ($\rho(T)$ was approximated by T^m).

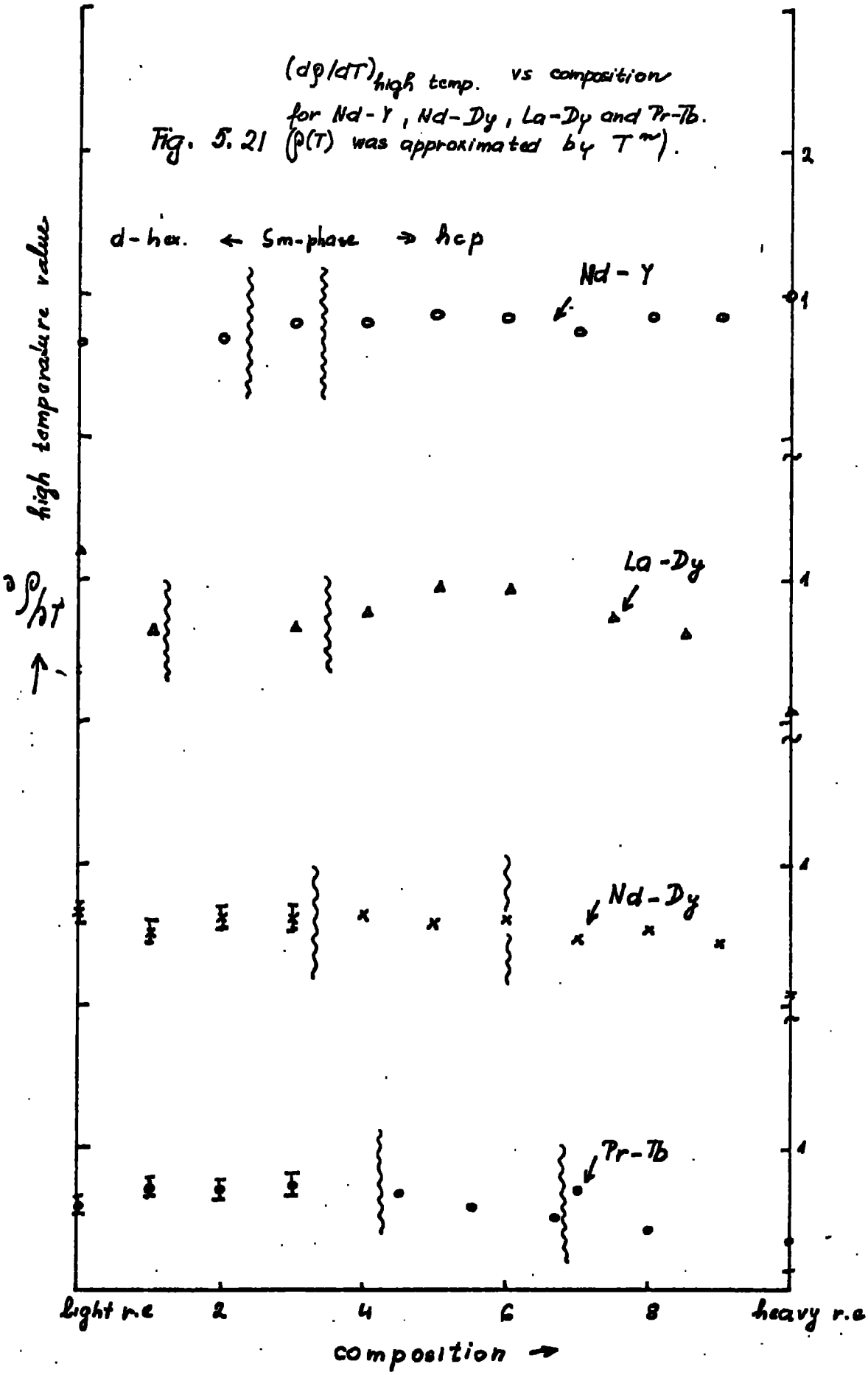

maximum value at low temperatures. The previous work on the Pr-Tb system suggests that 1) may be true at least in the d-hex structure and the small cubic splitting associated with the neodymium ions would result in the conclusion under 2).

The remaining ρ_{phonon} term in ρ_{total} shows a remarkable similarity over most of the alloy system. Fig.5.21,3.44 indicates the gradient $d\rho/dT$ for $T>150^{o}K$ in the region in which ρ_{phonon} is believed to be the only temperature dependent term and as may be seen this is constant over the d-hex and Sm phase region, increasing in the hcp phase to a maximum at pure yttrium.

To a first approximation, the gradient of a normal phonon contribution to the resistivity in the i direction in a metal is given by $d\rho_{ph}/dT \sim \sum_{\text{Fermi surface}} dS_i$ and in our case, with polycrystalline samples we have approximately

$$d\rho_{ph}/dT\Big|_{poly.} \propto 1/3\ (2\sum dS_{(i)\ basal} + \sum dS_{(i)\ c\text{-}axis})$$

The results then suggest that in the complex hexagonal phases there is either relatively little change in the form of the Fermi surface from one structure to another, or alternatively that the changes which do occur are complementary, leaving the average unchanged.

In the simple hcp structure however, $(2\sum dS_{basal} + \sum dS_{c\text{-}axis})$ evidently increases with increasing yttrium. This is much harder to understand than the behaviour in the more comlex phases, but must result from either detailed changes in the shape of the Fermi surface (S_{eff}) due to the differences in atomic species in the alloy, and/or to the changes in the Debye temperature across the alloy series.

If we assume with (2) that we can express the resistivity in the zero approximation as

$\rho = m^*/(n^* e^2 \tau)$

and can expect Matthiessen's rule to be valid at high temperatures $1/\tau = 1/\tau_{phonon} + 1/\tau_{c.f.}$ ... /6/

then the phonon contribution may be expressed (14) by

$1/\tau = (N\Omega/4\pi^3\hbar)\int |U_{k'k}|^2 ((\sin(E'-E)/\hbar)/(E'-E)) \times (1-\chi(\bar{k}')/\chi(\bar{k})) (dE'dS'/\nabla E(\bar{k}'))$ ... /7/

which after integration and substitution for $U_{k'k}$ with

$|U_{k'k}|^2 = (9\pi/2)^{2/3}(\hbar^2/Nr_s^2)(T/Mk\theta_D^2)(V_o(r_s)-E_o)^2$ ... /8/

and neglecting conduction in any other but the conduction band has the form

$1/\tau_{ph})_{\text{conduction band}} = (48\pi^2)^{1/3}(k_o m r_s/h)(T/Mk\theta_D^2)(V_o(r_s)-E_o)^2$ /9/

From fig.5.20 we know, in the zero approximation that $\rho_{c.f.}$ is zero for Y_9Nd_1 and Y. From fig.521 we know that $d\rho/dT$ is biggest for Y, Y_9Nd_1 and smallest for the alloys in the d-hex phase at high temperatures. From Y, Y_9Nd_1 and Y_7Nd_3, fig.5.21, 3.44, it can be seen that $(d\rho/dT)_{\text{high temp.}}$ decreases with composition but is almost constant with temperature while in the d-hex phase in Y_3Nd_7 $d\rho/dT$ decreases with temperature as well as with composition. If we assume that the $\rho_{c.f.}$ contribution is linearly dependent on concentration, it means that it decreases with Nd concentration. Then the negative contribution to $d\rho/dT$ of Nd, Nd_8Y_2 and Nd_7Y_3 must come from the $\rho_{c.f.}$ term and $d\rho_{c.f.}/dT$ must have a non zero contribution even at the high temperatures.

In Y_4, Y_5 and Y_6-Nd the $\rho_{c.f.}$ contribution is approximately one half of $\rho_{c.f.}$ in Nd, fig.5,21, and the $d\rho/dT$ is constant above ~80°K which means that $d\rho/dT$ does not

contribute appreciably above this temperature. It is interesting to notice the difference between ρ vs T of Y, Y_9Nd_1 and Y_7Nd_3 where the $\rho_{c.f.}$ is zero. Consequently the total resistivity is due to ρ_{phonon} and may be given by equation/7,9/ (for polyvalent metals).

The transition matrix depends on $T/Mk\Theta_D^2$ as well as other parameters which we assume to be constant in our case. In addition to the transition matrix the total relaxation time (and hence the resistivity) depends on the effective density of the states of the conduction slectrons, the effective Fermi surface and the band structure near the Fermi energy.

M, the atomic weight, changes substantially , from 88.9 at Y to 144.24 at Nd which gives a 6.25% drop in the total value of the resistivity for every 10% increase of the Nd concentration. Θ_D the Debye temperature changes from $\sim 220^{\circ}K$ for Y to $160^{\circ}K$ in Nd and brings about an increase of 5.97% in the resistivity for 10% Nd increase. Consequently these contributions partially cancel and can not give the changes in the resistivity. The changes must then be due to the changing Fermi surface and its effective surface area. The form of the Y Fermi surface is believed to be similar to the other heavy rare earths (1-1). The form of the Nd Fermi surface is partially known but it is clear that its details are different from the Fermi surface of the heavy rare earths. The changes in the effective Fermi surface and/or the changes in the electron band structure might explain the pohonon resistivity behaviour of the Y-Nd series. This hypothesis may be supported by the experimental evidence (1-3) of the Ziman parameter R calculated from the experimental data for the alloy series Y-Gd where it is found that R drops substantially on going

from Y to Gd. This has been explained (1-3) by using the following approximate equation

$$R = 8.125\times10^{9}\left[(M\Theta^{2}\rho_{1})/(DT)\right] \quad \ldots \quad /10/$$

where ρ_1 is the resistivity due to the lattice vibrations and D the Debye radius. This equation is equivalent to

$$R \cong na^{2/3}\,(S_{free}/S)^{2} \quad \ldots \quad /11/$$

where na is the number of the conduction electrons per atom and S and S_{free} the actual and free-electron Fermi surface areas respectively. From /9/ and /10/ we get

$$\rho_1 \sim na^{2/3}\,(S_{free}/S_{eff})^{2}(DT/M\Theta^{2})\ \text{const.} \quad \ldots \quad /12/$$

In this expression we can safely estimate that there should be a decrease of approximately 5% due to the $D/M\Theta$ term. To explain the experimental results by ρ_{phonon} either na, the effective number of the conduction electrons per atom, is going to increase or/and the effective Fermi surface. In view of the stability of the trivalent state of the rare earth elements it seems more likely that it is the latter term which is important in these measurements.

5.5 Dysprosium-neodymium alloys

As discussed previously, the alloys with up to 30 at%Dy crystallize in the d-hex phase. This is in agreement with the results of (3-9) who also reported that there was no evidence for magnetic ordering in this phase above 4.2°K. The resistivity observations at low temperatures however, show a rapid fall in the resistivity with decreasing temperature below about 6°K as may be seen from fig.3.26. The form of the resistivity variation below about 20°K is somewhat similar to that of elemental neodymium (fig.3.26) in which the rapid change in resistivity at 6-7°K corresponds to the ordering temperature for the atoms on the

cubic sites. On raising the temperature this is followed by a region of low $d\rho/dT$ to about 20°K above which the resistivity rises continuously and smoothly in a manner which suggests that we are observing the temperature dependence of the sum of a crystal field and phonon resistivity as was the case in the praseodymium alloys. If we take the change in slope at 20°K as being due to the disordering of the hexagonal sites then it would appear that the alloys do in fact show some evidence for magnetic ordering and that this proceeds in two steps as in the case for neodymium. The transition temperatures for the alloys obtained in this way are given in the table 3.7. As may be seen the upper transition temperature shows a slight increase with increasing Dy content and at the same time the effective spin disorder resistivity, which we can only define as $\rho_{tot} - \rho_{res}$. in this situation ($\rho_{tot}=\rho$ at the upper transition temperature) increases appreciably.

In general, as we have seen, we can expect the saturation value of the temperature dependent part of the spin disorder resistivity for the alloy system to be given by $\rho_{sat} = A(x(g_a-1)^2 J_a(J_a+1) f_a^2 + (1-x)(g_b-1)^2 J_b(J_b+1) f_b^2)$ where a and b refer to Nd and Dy respectively, the remaining symbols having their usual meaning. Since f_a and f_b are known to be of comparable magnitude the value of ρ_{sat} should vary simply as the average de Gennes factor $\bar{G}$ for the alloy system. While the variation is approximately linear in $\bar{G}$ (table 3.7), the rate of increase of ρ_{sat} with Dy concentration is faster than might have been anticipated by scaling to pure Nd data. Consequently it would seem that we may be involved with a concentration dependence of

$A(=3\pi^2 Nm^*/2\hbar q^2 E_F)$ and therefore of m^* and/or E_F since N likely to remain constant.

The rise in resistivity above the upper ordering temperature is similar to that observed in the Y-Nd alloys and presumably represents the crystal field and phonon contributions as mentioned earlier. As with the Y-Nd alloys $d\rho/dT$ becomes constant above about 120°K, and if we take this high temperature gradient as an indication of the temperature dependence of the phonon resistivity it will also provide an indication of the behaviour of the average cross section of the Fermi surface taken over all orientations. As fig.5.22 shows, $d\rho/dT$ increases rapidly at 30 at% Dy, beyond which the structure changes to the more complex Sm phase. This increase in $d\rho/dT$ corresponds to a decrease in the Fermi surface area, and it is interesting to speculate whether or not this change is associated with the structural change in these materials.

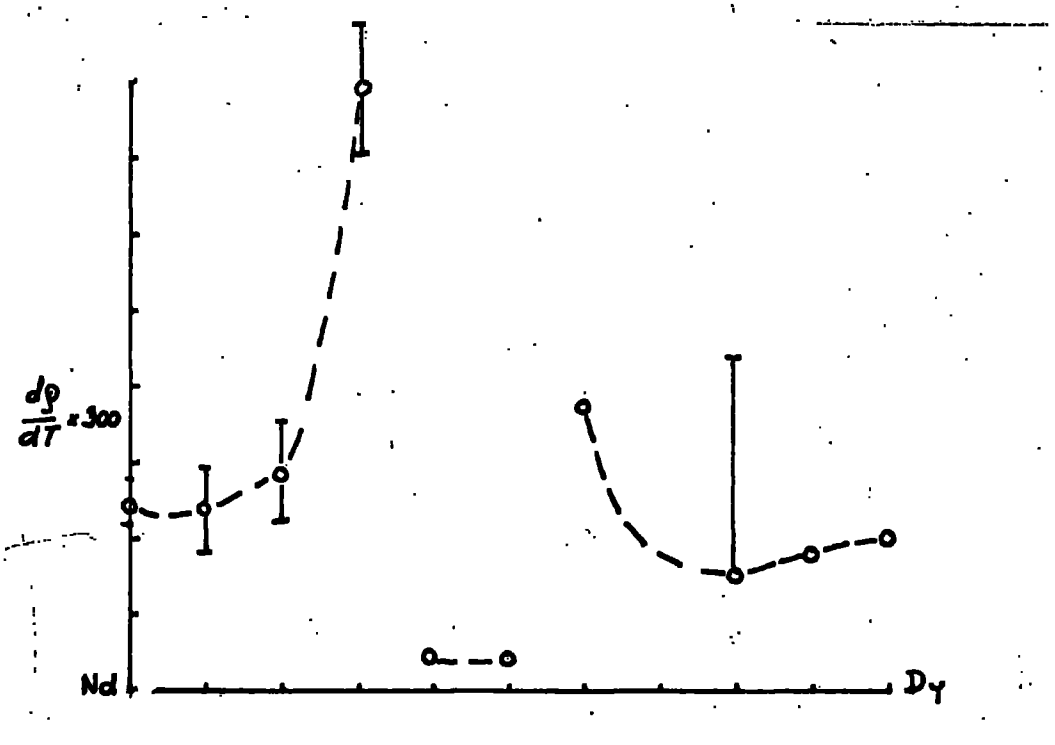

Fig.5.22

$(d\rho/dT)$ vs composition for Nd-Dy alloys.

Fig. 5.23 Resistivity and ρ_{La}/T vs temperature T for ρ_{La} and $\rho_{La} - \rho_{res}$.

LANTHANUM

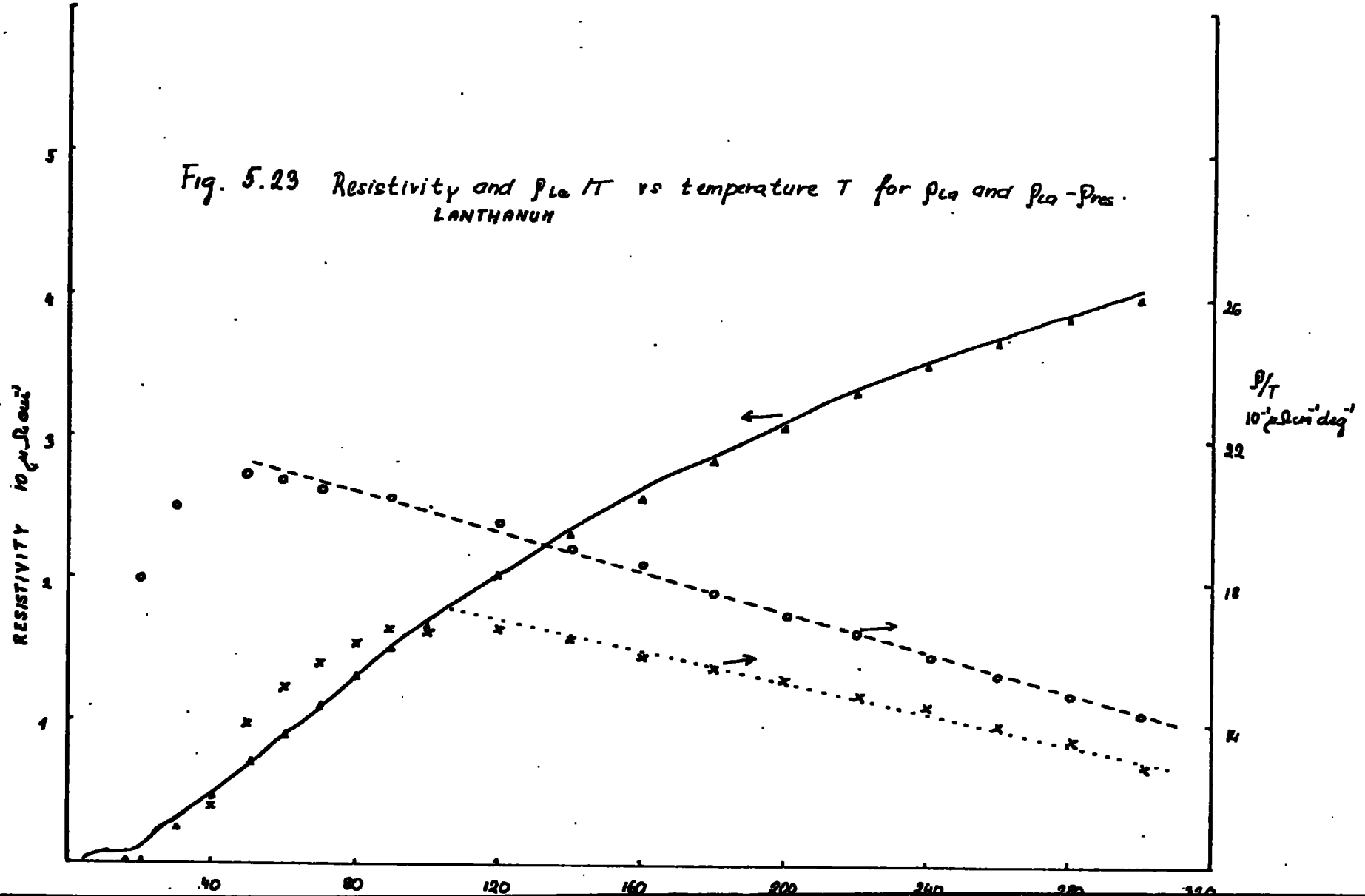

5.6 Lanthanum-dysprosium in d-hex

5.61 Lanthanum

As already stated La is nonmagnetic having no f-electrons. Consequently its resistivity should be given by

$$\rho(T) = \rho_{resid.} + \rho_{phonon}(T)$$

where we assume that only ρ_{phonon} is temperature dependent and the variation of $\rho(T)$ with temperature, fig.3.33, arises only from this phonon contribution.

In order to understand this behaviour let us to a first approximation assume that there are no f-electrons. It is likely that the Debye temperature θ_D will change with temperature by analogy with the other rare earth metals for which the variation of θ_D with temperature has been measured(1-20).Consequently the only temperature dependent part of the resistivity in La will be associated with the thermal variation of the lattice and the following relation between ρ,T and θ_D should hold $\rho/T \sim \theta_D^2$ or by using thermodynamics: $\rho/T = \text{const.}(1+2\alpha\gamma T)$ where $\alpha = 1/v(\partial V/\partial T)$ and $\gamma = (d\log\theta_D/d\log V) = (\alpha V/\varkappa_t c_v)$, c_v being the specific heat, $\varkappa = (-1/V)(\partial V/\partial p)$ is the isothermal compresibility.

Since $\rho(T)$ is convex upwards at high temperatures the value of $2\alpha\gamma$ should be negative for La and from fig.5.23 would have a value -4 to -5×10^{-4} $\mu\Omega\,cm^{-1}deg^{-1}$. The magnitude of this term is similar to that of normal metals, e.g. copper ($2\alpha\gamma = 1.9\times10^{-4}$) although the sign is different.

Since thereis still some dispute about the existence of occupied 4f states in La it is interesting to consider the situation where the lowest 4f state lies just above E_F, the Fermi energy (4). Then, because the density of states function will have a much bigger value near E_F, in the

f-band than it has in the conduction band, the density of states $\eta(E)$ would be the most rapidly varying function with temperature T (and concentration of the diluting atom). Then the resistivity will have the form (2):

$$\rho(T) = \rho(E_{F_o},T)(1-(\pi KT)^2/6(3(1/\eta\,(d\eta/dE))^2-1/\eta(d^2\eta/dE^2))_{E_{F_o}}$$

Fig.5.5 represents the density of states function as was calculated by(1-34)for La (and Pr) using APW techniques. The function has a maximum near the Fermi energy, which would lead to a decrease in $d\rho/dT$ with increasing temperature as is observed in La.

Since no theoretical calculations heve been done to support either of the proposed explanations, we cannot rule out the possibility that in pure lanthanum there also exists a crystal field term since the 4f states may lie close enough to the Fermi level to be occupied at some temperatures. It seems most likely that all of these contributions may be present and only detailed calculations will allow us to define the extent of each.

5.62 Lanthanum-Dysprosium alloy in the d-hex phase

This phase in our study is represented only by two samples La and La_9Dy_1, since $La_{89}Dy_{11}$ should be disregarded as will be discussed below. La and La_9Dy_1 are both superconducting with a transition temperature, table 3.11, which suggests that they are both almost exclusively in the d-hex structure. In the sample of $La_{89}Dy_{11}$ the superconducting transition was not observed but this sample lies very closely to the Sm → d-hex phase boundary and we suspect that the heat treatment was inadequate to stabilize the phase structure. Consequently it is probably a mixture of d-hex and S phases, see chapter 3.24 and may be disregarded. This assumption is thought

to be supported by the difficulties in defining lattice parameters a and c for this sample and their large deviations from the values of the remaining alloys of this series. From the behaviour of La and La_9Dy_1, fig.3.33 it seems that Dy behaves as it did in the Nd-Dy series and increases the resistivity due to its big scattering power. We can assume then that the resistivity of the alloy in this phase can be expressed as:

$$\rho(T) = \rho_{res} + \rho_{phonon}(T) + x(\rho_{Dy-(s-f)})$$

where ρ_{phonon} we again assume to have the form of the La resistivity for all the alloys in this phase. x is the concentration of the Dy and by $\rho_{Dy-(s-f)}$ is meant ρ_{s-f} of this element which in this rough estimate is true. More experimental evidence would be necessary to prove it but from the parallel with Y-Nd alloy it seems reasonable to accept this assumption.

5.7 Comparison of the various alloy series in the d-hex phase

At first sight it is somewhat surprising to find that the resistivity $(\rho_{total} - \rho_{res})$ of the Pr_9Tb_1 to Pr_7Tb_3 alloys are lower than those of praseodymium when the similar series of Nd-Dy alloys exhibit a continuous increase in the resistivity with increasing dysprosium concentration. Both terbium and dysprosium might be expected to have a similar behaviour when alloyed with either of the light rare earth metals praseodymium or neodymium.

As we have seen however, the fall in resistivity with increasing terbium may be understood in terms of electron scattering between the set of crystal field levels of the praseodymium ions, the detailed splitting parameters

changing from specimen to specimen. Since the ground state level is a singlet at both the cubic and hexagonal sites, the energy gap to the first excited state is probably the most important variable. By allowing this level to decrease relative to the ground state we have been able to produce a theoretical fit to the most of the observed resistivity variation. This shift in the position of the excited states has also been confirmed using inelastic neutron scattering techniques. It is not yet clear whether the change in the crystal field paremeters arises as the result of local distortions due to the substitution of the terbium ions, or to the effects of interionic exchange and dipole-dipole interactions.

In the case of Pr-Tb, it was assumed that, because of the large splitting of the lowest ionic energy levels of the non Kramers terbium ions (singlet ground state), to first order terbium would act simply as a diluent for the $\rho_{c.f.}$ term. In the Nd-Dy alloys however, the ground state of the Dy ions is a doublet at both sites and consequently spin flip scattering at these ions will be significant at all temperatures.

It is also possible that in both alloy series, there may be significant changes in the Fermi surface which will affect the overall behaviour of the resistivity. This is clearly evident in the transition from the d-hex to the Sm phase where the magnitude of $\rho(T)$ falls appreciably for relatively small composition changes. To make quantitative estimates of these changes it is necessary to make observations of $d\rho/dT$ at temperatures far above those

at which the crystal field effects are changing with temperature. Unfortunately the present work was limited to $T \lesssim 300^{o}K$ and it is felt that this type of analysis is presently unjustified.

The behaviour of the Y-Nd series is readily understandable in terms of dilution by the yttrium ions, and no change in the crystal field is necessary, to first order, because of the degenerate ground state of the Nd ions. Similarly, the La-Dy alloys show an increase in $\rho(T)$ which arises solely from the additional scattering due to the presence of the magnetic Dy ions in the lanthanum matrix.

5.8 Sm-phase

In Y-Nd alloys the resistivity behaviour in this phase, can be described in terms of a dilution of the crystal field scattering from the magnetic Nd atom. The character of the yttrium scattering appears only through the phonon contribution and any Fermi surface changes. The form of $\rho_{c.f.}$ in the Sm phase is, of course, generally different from $\rho_{c.f.}$ in the d-hex phase. This way we explain the $(\rho_{c.f.})_{Sm\text{-}phase}$ being bigger than the $\rho_{c.f.}$ in the d-hex phase, fig.3.22. This is of course true only if the assumption that ρ_{phonon} in both the Sm and d-hex phases, can be expressed in terms of ρ_{La}. The general expression for the resistivity ρ_{tot} in this phase, as in the d-hex phase, can be split into four contributions:

$$\rho_{tot}(T) = \rho_{res} + \rho_{phonon}(T) + \rho_{c.f.}(T) + \rho_{s\text{-}f}(T)$$

where $\rho_{s\text{-}f}$ accounts for the small contribution caused by the magnetic ordering at very low temperature, which is obvious in Nd_7Y_3, fig.3.28.

La-Dy is similar to Y-Nd in many ways. It shows some evidence of magnetic ordering at very low temperatures, fig. 3.36-7, which unfortunately has not yet been confirmed from magnetic measurements. The total resistivity can be viewed as a sum of four contributions:

$$\rho_{tot}(T) = \rho_{res} + \rho_{phonon}(T) + \rho_{s-f}(T) + x(\rho_{s-f})_{Dy}$$

From a comparison of ρ_{tot} in the d-hex phase and in the Sm phase it is obvious that ρ_{phonon} in the Sm-phase is less than ρ_{phonon} in the d-hex phase, presumably again due to Fermi surface changes. ρ_{s-f} has been roughly estimated and is presented in table 3.11 and fig.3.40. It is intersting to note its dependence on J which agrees well with the other alloys studied in the Sm-phase, within the experimental error.

In Pr-Tb in the Sm-phase, the effect of long range order (Sm-magnetic structure) prevails up to the region of 40-80°K. Also detecteble is the influence of short range order at the cubic sites, which was estimated from neutron diffractim experiments to be present up to ~350°K. This is, most probably, the reason for the nonlinear behaviour of the resistivity above T_N in this system. In addition to the results from magnetic experiments, there is also some evidence of long range order with transition temperature ~4°K. The resistivity behaviour in this low temperature region is similar to the behaviour of the Nd-Dy alloys in the d-hex phase over the same temperature region. ρ_{tot} could be expressed in this case by the sum of six terms:

$\rho_{tot}(T) = \rho_{res} + \rho_{phonon} + \rho_{c.f.} + \rho_{s-f} + \rho_{s.r.} + \rho_{mg.}$

where ρ_{res} should be the resistivity value where, according to the third law of thermodynamics, ρ_{tot} becomes constant with temperature. This value may not heve been reached in this study, fig.3.17.

ρ_{phonon} can most likely be expressed by the Gruneisen law for polyvalent metals since the assumption of linear ρ with T at high temperatures seems quite reasonable, from fig. 3.14. $\rho_{c.f.}$, we believe, could show up in the absence of long range order, e.g in $Tb_{45}Pr_{55}$. The nature of $\rho_{c.f.}$ would be the same as in the d-hex phase, the only differences occuring because of the different concentrations of the hexagonal and cubic environments in the Sm structure than d-hex. ρ_{s-f}, the long range spin disorder term, is most likely governed by the RKKY interaction, where the effective moment and the dependence on the light rare earth concentration has not yet been established. From fig.3.40-1 it is obvious that ρ_{s-f} deviates strongly from ρ_{s-f} vs $\bar{G}$ which holds for the heavy rare earths and heavy -heavy rare earth alloys. ρ_{mg} is the magnetic contribution at very low temperatures, whose origin is not yet obvious. $\rho_{s.r.}$ is the spin-disorder contributuion from the short range order appearing at the cubic sites. This should be a statistical average of the resistivities of small ordered clusters of Pr-Tb in the cubic crystal field, presumably again of the RKKY type.

Dy-Nd: Dy_5Nd_5 and Dy_4Nd_6 can be compared with $Pr_{55}Tb_{45}$ since no long range magnetic ordering takes place in this alloy in the Sm-phase. Consequently

$$\rho_{tot}(T) = \rho_{res} + \rho_{phonon}(T) + \rho_{c.f.} + \rho_{s.r.}$$

where the symbols have the same meaning as above. Contrary to Tb-Pr no magnetic transitions have been observed to the lowest temperature measured, but $\rho_{tot.}(T)$ was never constant with T, suggesting that ρ_{res} is smaller than the values quoted in tha table 3 .7.

ρ_{phonon}, we assume, can be discussed in a similar way to the Pr-Tb case, as well as $\rho_{c.f.}$ and $\rho_{s.r.}$, for which we lack the supporting evidence from neutron difraction experiments since Dy, due to its high cross section is not easily studied by this technique .

From the high temeperature value of $d\rho/dT$ it is obvious that there is a reduction in the effective Fermi surface area, as we have already proposed for the Pr-Tb and Nd-Dy alloys.

5 .9. hcp -phase

Because of their similarity in behaviour the Dy-Nd, Tb-Pr and Dy-La alloys may be discussed together. We can again divide ρ_{tot} as follows:

$$\rho_{tot}(T) = \rho_{res} + \rho_{phonon}(T) + \rho_{s-f}(T) + \rho_{s.r.}(T) \quad \ldots \quad /13/$$

where ρ_{res} is well defined in most of the alloys. ρ_{phonon} can be well approximated by a linear relationship above T_N which suggests that the Gruneisen law is obeyed for this contribution and consequently we can anticipate some power law for ρ_{phonon} at low temperatures, table 3.6. ρ_{s-f} is given by the RKKY interaction, where, due to the presence of the light rare earths we should expect substantial changes in the band structure, Fermi surface, magnetostriction effects and consequently in $J_{eff.}$ This effect can

be followed from the dependence of ρ_{s-f} vs $\bar{G}$, T_N vs $\bar{G}$ and T_N vs composition, fig.3.39-41, which all behave similarly. The behaviour is consistent with the observations made earlier for some light-heavy rare earths in the hcp phase as summarized in (3-19).

From the increasing high temperature values of $d\rho/dT$ when going from pure heavy rare earths towards light rare earths in the hcp phase it appears that the effective Fermi surface decreases . This fits into the observed behaviour in the Sm-phase.

$(\rho_{s-f})_{saturation}$ decreases with addition of light rare earths far more rapidly than it does for the heavy rare earths and heavy-heavy rare earth alloys. In La-Dy(3-19) reported on interesting behaviour of T_N which increases on adding La to Dy for the first 15 % of Lanthanum substitution before the abrupt decrease takes place in T_N and ρ_{s-f}, which we saw making the study for all the La-Dy series, fig. 5.24-8. In Pr-Tb which has not been previously reported, we can trace this behaviour, namely for ρ_{s-f}, but only over a limited range, since only Tb_9Pr_1 seems to have $\rho_{s-f} = (\rho_{s-f})_{Tb}$. In Dy-Nd, for 10,20 and 30% of Nd no such a behaviour could be resolved however.

The abrupt decrease of ρ_{s-f} in the hcp phase is slowed down in the Sm-phase, presumably due to the abrupt changes in the band structure and hence the effective Fermi surface, due to the crystallographic change.

T_N, the Néel temperature, behaves almost identically to ρ_{s-f}, fig. 3.39, 5.24. Only T_C, the Curie temperature seems to be very little effected by alloying. It appears as if the ferromagnetic state prevails in an almost unchanged

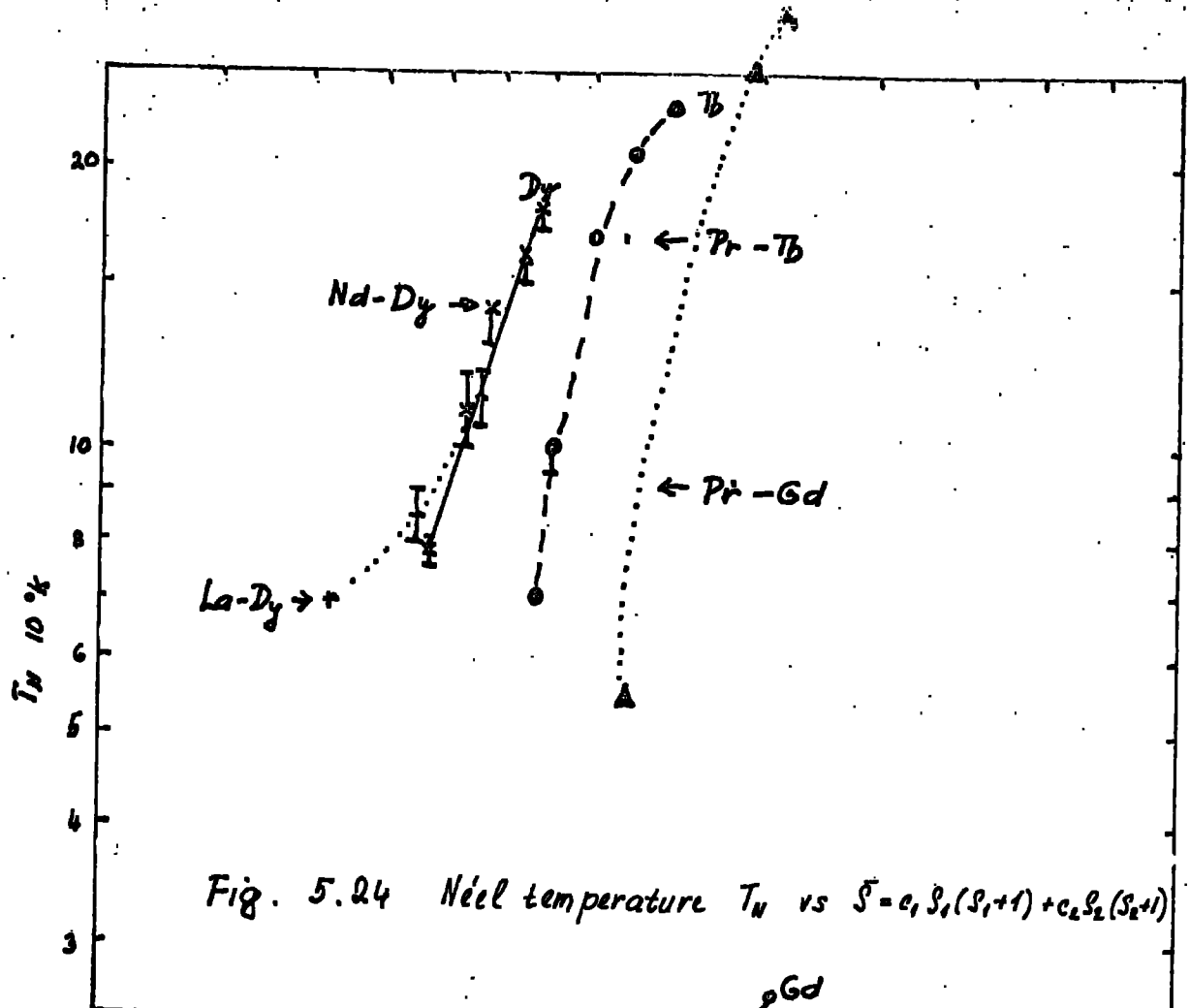

Fig. 5.24 Néel temperature T_N vs $\bar{S} = c_1 S_1(S_1+1) + c_2 S_2(S_2+1)$

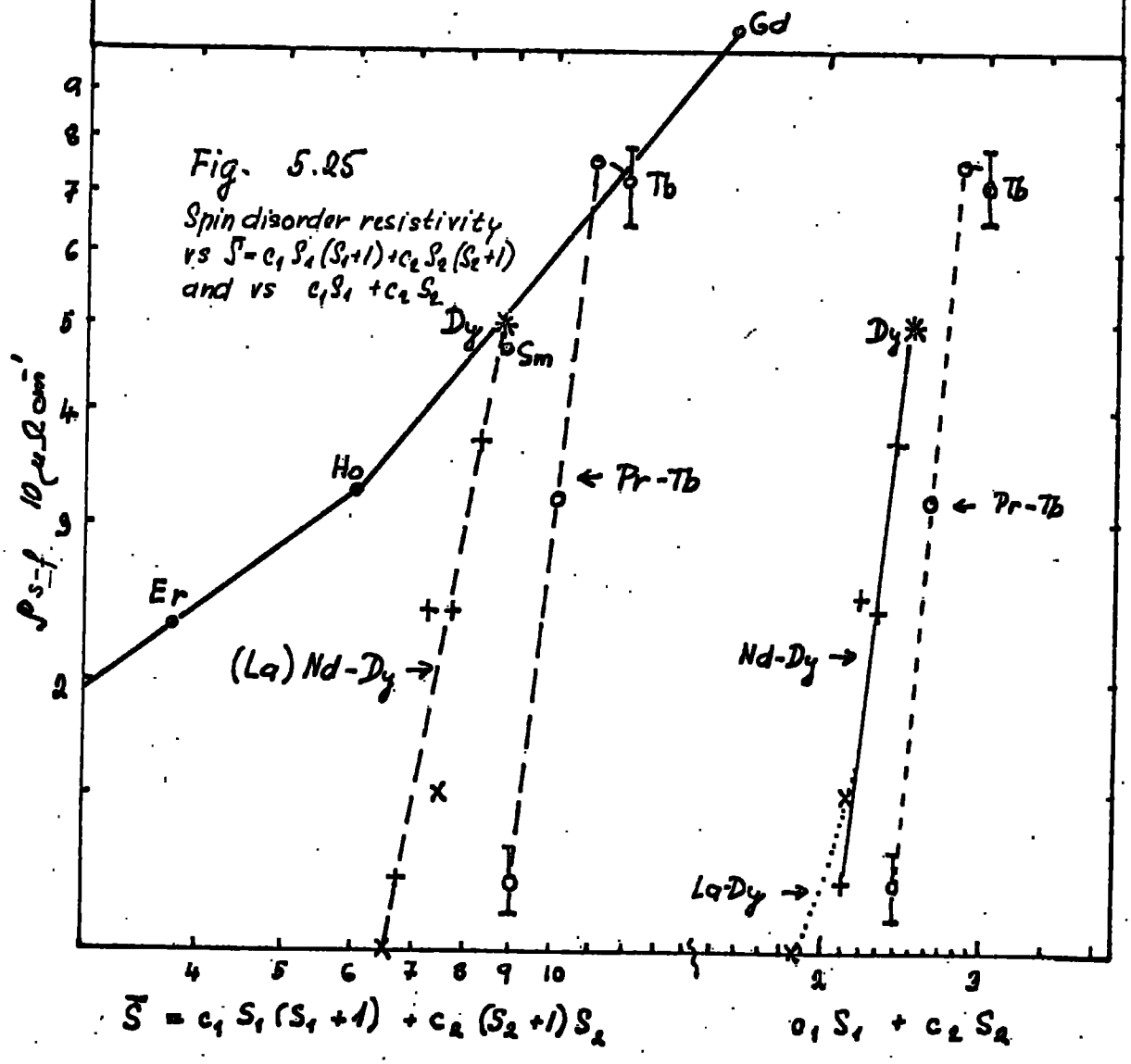

Fig. 5.25
Spin disorder resistivity
vs $\bar{S} = c_1 S_1(S_1+1) + c_2 S_2(S_2+1)$
and vs $c_1 S_1 + c_2 S_2$

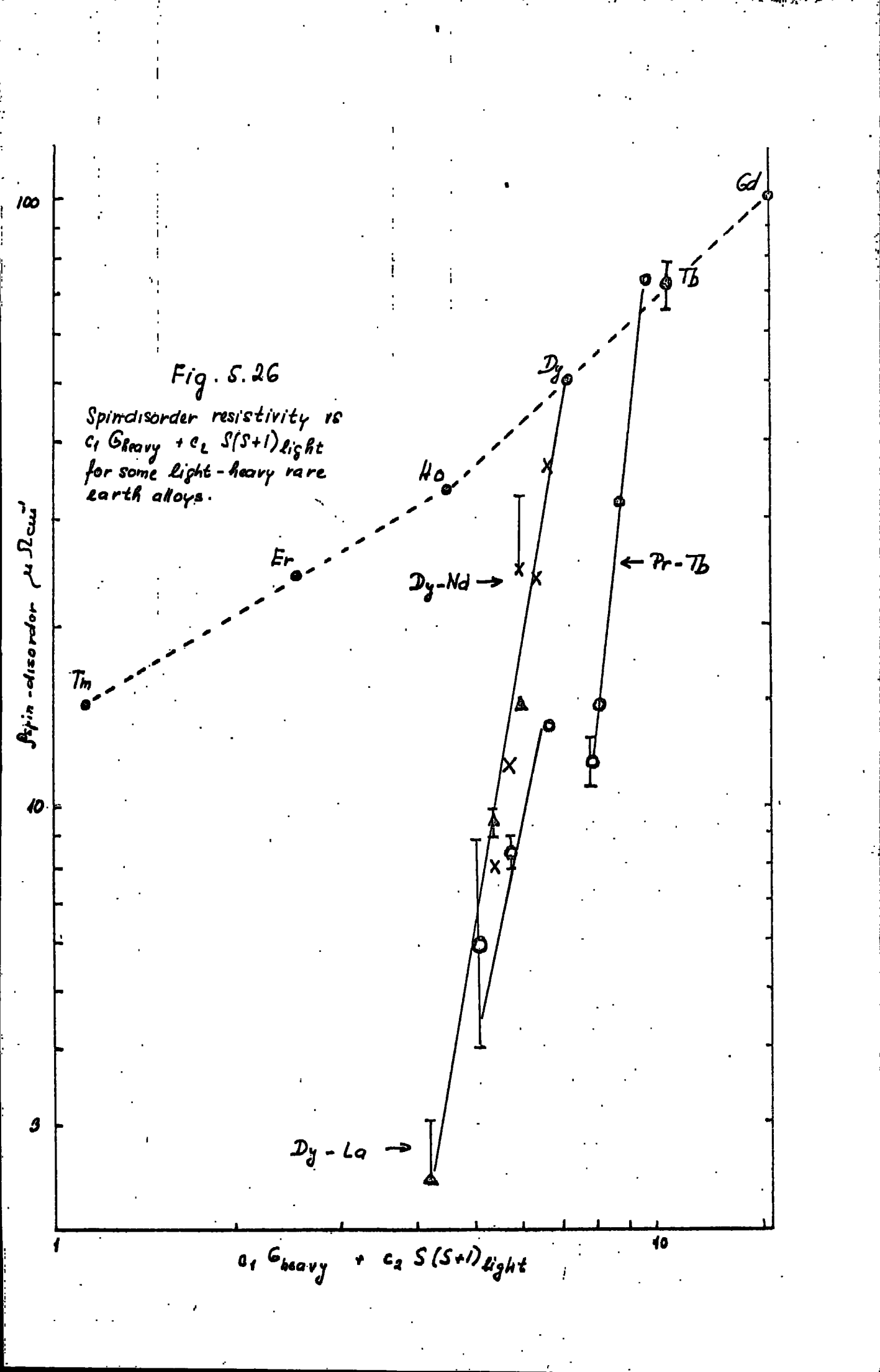

Fig. 5.26

Spindisorder resistivity vs $c_1 G_{heavy} + c_L S(S+1)_{light}$ for some light-heavy rare earth alloys.

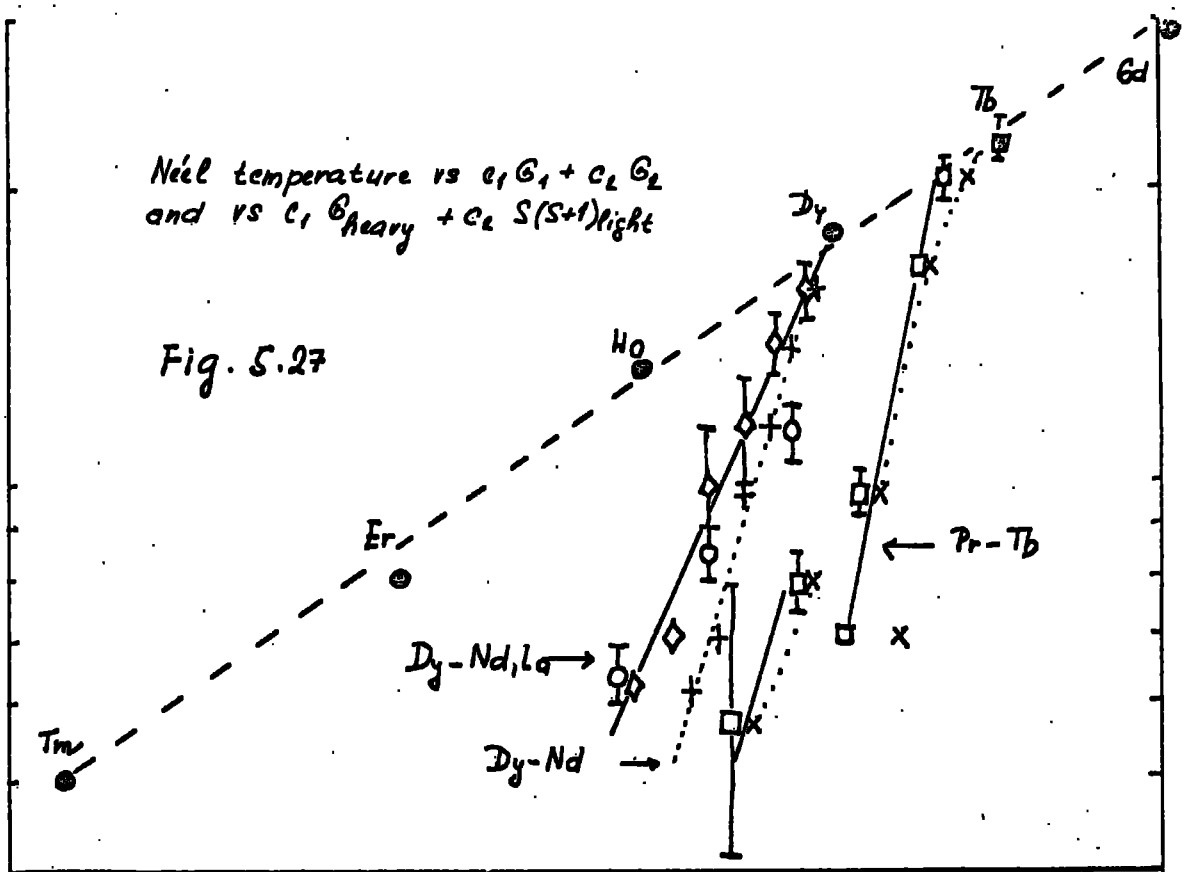

Fig. 5.27

$c_1 G_1 + c_2 G_2$ (ful line) , $c_1 G_{heavy} + c_2 S(S+1)_{light}$ (doted line)

Fig. 5.28 Néel temperature vs $(c_1 S_1 (S_1+1) + c_2 S_2 (S_2+1))$

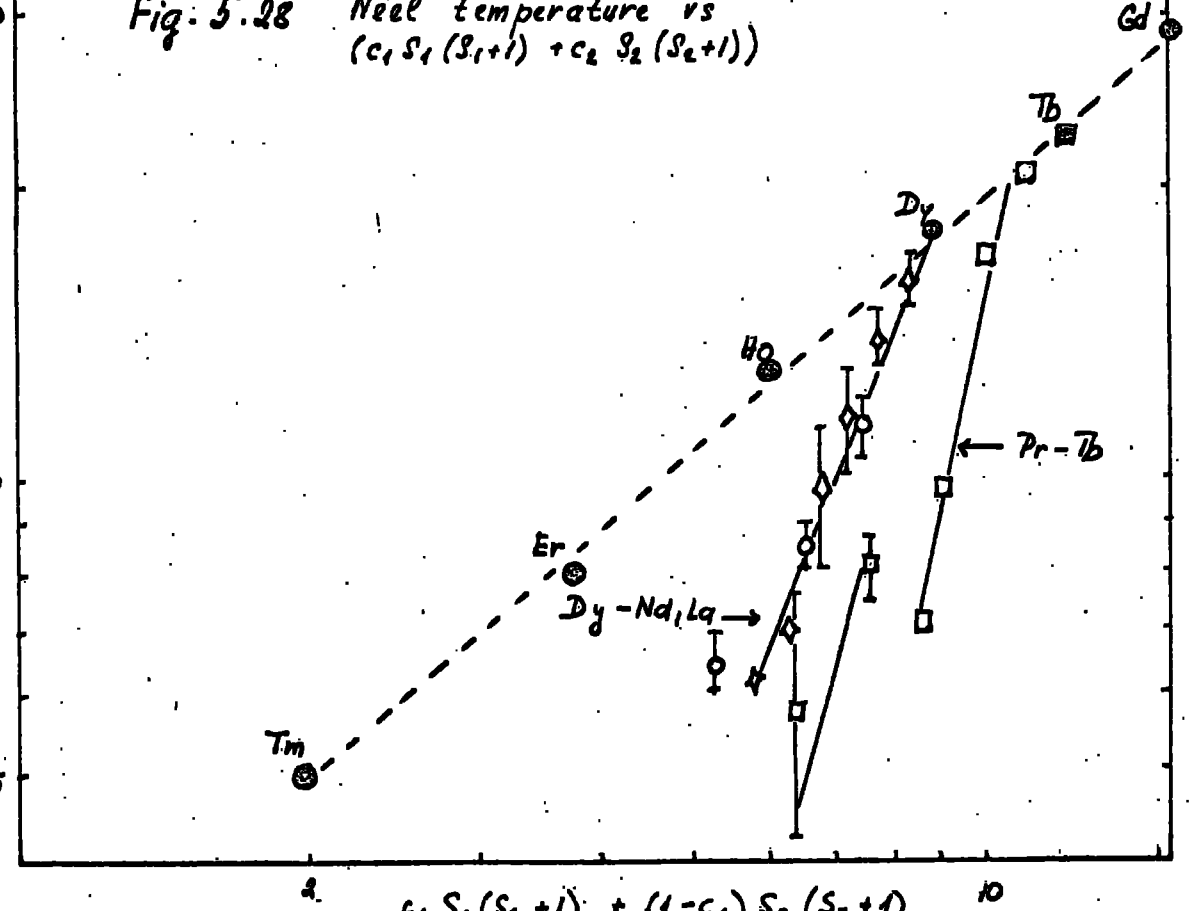

form until the ferromagnetic state vanishes or is taken over by the antiferroamgnetic state which is usually connected with the crystallographic transitions from the hcp to the Sm phase.

The spin disorder resistivity, ρ_{s-f} and the Néel temperature, T_N are obviously dependent on spin and the total magnetic moment of the rare earth atoms. ρ_{s-f} and T_N of heavy rare earths and heavy-heavy rare earth alloys are well described by the dependence on de Gennes factor (1-1). ρ_{s-f} of the light-heavy rare earth alloys deviate from this dependence, figs.3.40-3.41. Consequently we have tried to find some 'parameter' as a function of S,J or G, in figs.5.24-28, which would be most suitable for desribing these alloy systems.

The alloys which do not show any sign of ordering, i.e. Y-Nd, could be described by the following equation:

$$\rho_{tot}(T) = \rho_{res} + \rho_{phonon}(T) + \rho_{c.f.}(T)$$

ρ_{res} is well defined in the Y-Nd series. ρ_{phonon} is most likely a contribution of ρ_{phonon} of Y and Nd of the form:

$$\rho_{phonon}(T) = \alpha(\rho_{ph})_Y + \beta(\rho_{ph})_{Nd\text{-}hcp}$$

and $\rho_{c.f.}$ in this series appears to have the form:

$\rho_{c.f.} \cong \gamma(\rho_{c.f.})_{Nd\text{-}d\text{-}hex}$ where $\gamma(<1)$ is proportional to the concentration of Nd.

From the resistivity measurements La_4Dy_6 appears to be ordered up to 6^oK, however magnetic susceptibility measurements show evidence for ordering (antiferromagnetic) up to 68^oK. Careful examination of the $\rho(T)$ behaviour shows that any change in the resistivity in this area is comparable to the exparimental scatter and consequently the spin disorder resistivity at this composition must be very small($2.5\pm1.0\,\mu\Omega cm^{-1}$) and can be discussed in the same way as for the other magnetically ordered alloys in the hcp phase, using equation/13/.

Residual resistivity vs composition for Nd-Dy, Nd-Y, Dy-La and Pr-Tb alloys

Fig. 5.29

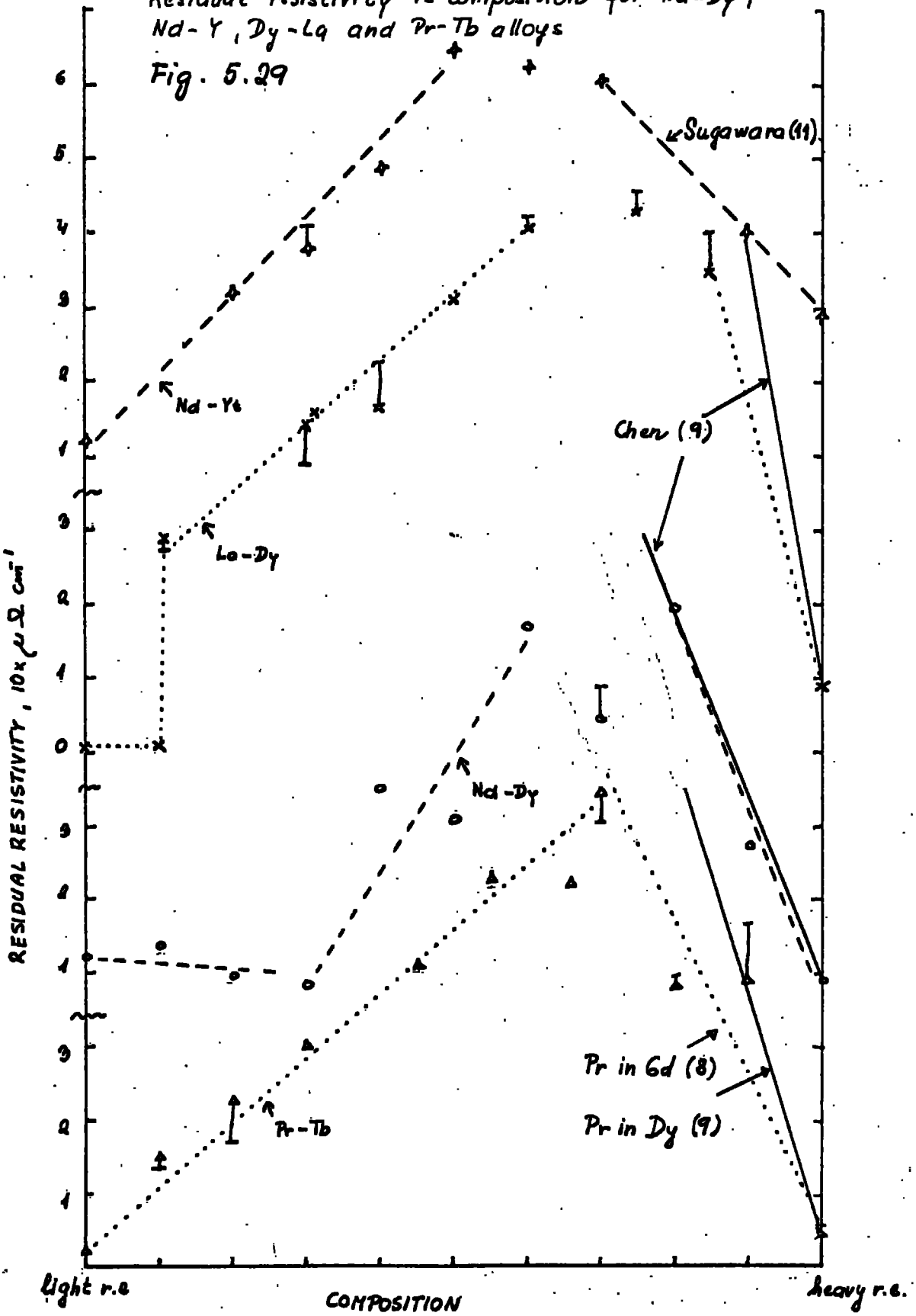

Fig. 5.30

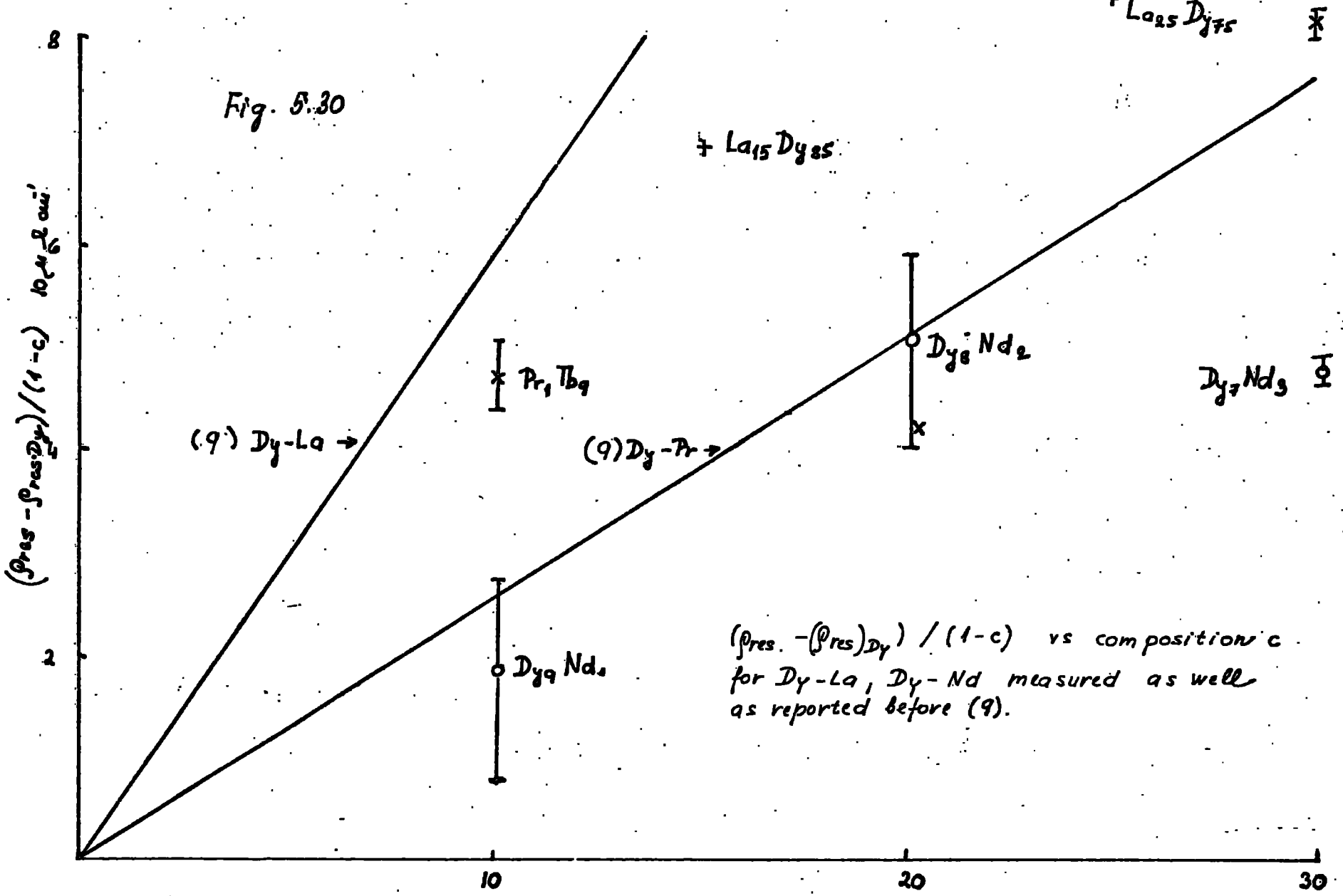
8
2
10
20
30
CONCENTRATION %
$(\rho_{res} - \rho_{res\,Dy})/(1-c)$ $10^{-6}\,\Omega$ cm
+ $La_{25}Dy_{75}$
+ $La_{15}Dy_{85}$
(9) Dy-La →
(9) Dy-Pr →
Pr_1Tb_9
Dy_8Nd_2
Dy_7Nd_3
Dy_9Nd_1
$(\rho_{res.} - (\rho_{res})_{Dy}) / (1-c)$ vs composition c for Dy-La, Dy-Nd measured as well as reported before (9).

5.10 The residual resistivity

Besides the difficulty of estimating ρ_{res} in many of the alloys studied, we think that we can make, within the experimental error quite interesting conclusions.

From fig.5.29 it is obvious that the residual resistivity variation with composition is strongly assymetric with a maximum on the heavy rare earths side, which is not surprising since ρ_{res} of the magnetic material contains a spin-disorder contribution ρ_{s-f} (6 -10) arising from the statistical distribution of the two types of atoms in the alloy. The residual resistivity rises sharply in the hcp phase, especially so when the ferromagnetic phase is present. In the region where light rare earths could be regarded as a perturbation ρ_{res} follows the, theoretical curve, fig 5.30 (8,9).

The Sm phase is so narrow that no definite statements can be made as to the behaviour of ρ_{res}, but it seems likely that no abrupt change takes place and ρ_{res} is almost constant, or perhaps shows a slight decrease to the light rare earths end.

In the d-hex phase, which in our study is represented well by the Pr-Tb alloys a moderate increase takes place with increase in the Tb concentration. The same is most likely true about Nd-Y, even with the rather insufficient experimental evidence available. Nd-Dy and La-Dy behave anomalously. Nd-Dy, owing to the form of the resistivity behaviour with temperature at very low temperatures, did not allow us, to define a 'proper' ρ_{res} and ρ_{res} (at 4.2°K) vs composition in the the d-hex phase is found to be constant

since Nd-Dy orders magnetically in the temperature range ~5°K. The ρ_{res} quoted would not contain the $\rho_{spin-disorder}$ term which is present for instance in Pr-Tb, which might explain this anomaly. La-Dy presents a 'similar' problem due to the superconducting state.

5.11 General behaviour of the spin disorder resistivity

As we have seen from fig.3.39-41 and 5.24-28 the ordering temperature (T_N) and the magnetic contributions to the total resistivity did not show a unique dependence on the angular momentum parameters $S(=S(S+1))$ or $G(=(g-1)^2J(J+1))$ or averages of these for the two ions as might have been anticipated from the observed behaviour of alloys of the heavy rare earths. There is some evidence however, that alloys involving a single heavy rare earth do form a single curve, independent of the light rare earth partner, and that form of this dependence on averages of S or G are similar for different series.

If we examine the relations in the RKKY theory which give ρ_{s-f} and θ_p then we have:

$$\rho_{s-f} = (k_F m^{*2} \pi^2)/(4\pi\hbar^2 q^2 Z)\ J(J+1)(g-1)^2$$

$$\theta_p = m^*/(6\pi^3 k_B \hbar^2)\ \pi^2 J(J+1)(g-1)^2 \Sigma F(2k_F R_n)$$

where $J(J+1)(g-1)^2$ may be replaced by linear combinations of the component G's on alloying, or even combinations of G and S. Assuming that the combination used will be the same for both ρ_{s-f} and θ_p, then this will disappear from the ratio

$$\rho_{s-f}/\theta_p = (k_F m^*)/(\Sigma F(2k_F R_n)\ (3\pi^2 K_B)/(2\pi q^2 Z)$$

Consequently, any changes in the ρ_{s-f}/θ_p ratio must occur as the result of changes in either k_F, m^*, or $\Sigma F(2k_F R_n)$.

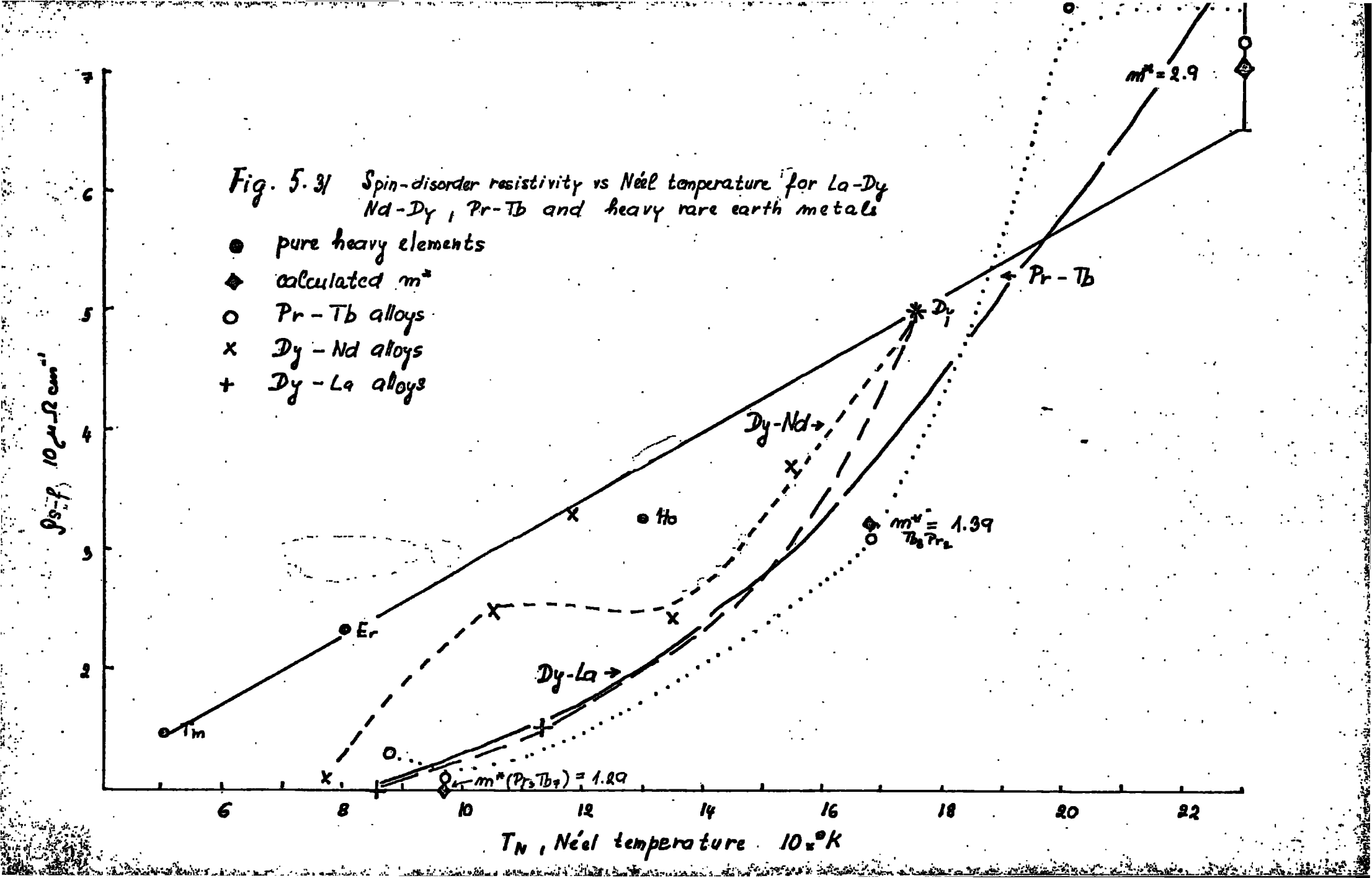
Fig. 5.31 Spin-disorder resistivity vs Néel temperature for La-Dy Nd-Dy, Pr-Tb and heavy rare earth metals
pure heavy elements
calculated m*
Pr-Tb alloys
Dy-Nd alloys
Dy-La alloys
$m^* = 2.9$
Pr-Tb
Dy
Dy-Nd
Ho
$m^*_{Tb_3Pr_2} = 1.39$
Er
Dy-La
Tm
$m^*(Pr_3Tb_7) = 1.29$
ρ_{s-f} 10 μΩ cm
T_N, Néel temperature 10 °K

As figure 5.31 shows, the magnitudes of the ratios for all the alloys studied can be crudely described by a single curve which shows a sixfold decrease in ρ_{s-f}/θ_p as the light elements are alloyed with any heavy rare earth element.

It is unlikely that either k_F or $\Sigma F(2k_F R_n)$ will change by this amount within a single crystallographic phase (hcp as in fig.5.31), and the lattice parameter variation would suggest that $k_F/\Sigma F(2k_F R_n)$ will remain essentially constant because of the behaviour of $\Sigma F(2k_F R_n)$ as a function of k_F (16). Consequently it is more likely that the changes in ρ_{s-f}/θ_p observed on alloying, arise from changes in the details of the Fermi surface which are replaced in the the effective mass contribution to the ratio.

On this basis, the effective mass variation has been calculated using the theoretical values of $\Sigma F(2k_F R_n)$ and k_F corresponding to the heavy rare earth partner of any alloy series (17) together with the experimental values of ρ_{s-f} and T_N(taken $\equiv \theta_p$ for this calculation). Typical values of m* obtained this way are shown on fig.5.31 for the average curve drawn through the data. While there are considerable deviations from this general curve, particularly for the Dy-Nd series, it is evident that the overall behaviour may be approximately represented by this approach. It is likely that a better fit would be obtained by using more realistic values for k_F and hence for $\Sigma F(2k_F R_n)$, but unfortunately the errors involved in trying to estimate these values are very great in a view of the calculated shapes of the Fermi surface in the pure elements and because as yet no successful Fermi surface calculations have been performed for random alloy systems.

C H A P T E R S I X

CONCLUSION

The relative values of the different scattering contributions to the resistivity for the rare earth elements has been estimated by means of a study of various light-heavy rare earth alloys.

The resistivity of the heavy rare earths have been investigated previously in great detail and the RKKY theory has been used to account for the anomalies observed. The theory is probably also applicable to the light-heavy rare earth alloys in the hcp phase but our knowledge of parameters such as the band structure variation with substitution of the light rare earths, the combined changes in the Fermi surface (S_{eff}) and the exchange interactions is limited essentially to guesswork . Consequently we can make, on the basis of the resistivity results, only qualitative conclusions in most cases.

1) The rate of change of the effective Fermi surface within one crystallographic phase is small compared to the changes from phase to phase, namely hcp → Sm and Sm → d-hex phase transitions.

2) The changes of J_{eff} (S_{eff}) with ρ_{s-f}, and T_N follows the same power law within one phase for all the alloys, regardless of the constituent atoms.

3) The changes of the Curie temperatures, are small with the exception of La-Dy, where T_C first rises before falling abruptly below 65% of Dy.

The Sm-phase results serves to form a bridge between the resistivity behaviour in the hcp and d-hex phases. Some of

the alloys, presumably with $J_{eff} > J_{critical}$, show ordering effects not unlike those in the hcp phase. The alloys for which $J_{eff} < J_{critical}$ show only crystal field and short range order effects, which because of its statistical character is difficult to formulate theoretically.

The crystal field contribution to the resistivity is very important to both the d-hex and Sm-phases. Its temperature dependence has been succesfully calculated theoretically for the case of Pr and Pr-Tb alloys in the d-hex phase, where the crystal field energy levels are known, or can be estimated. Its total value was found comparable in magnitude to the phonon contribution, decreasing with increasing Tb concentration.

In Nd, Nd-Dy and Nd-Y the crystal field contribution has been estimated and found to be of the same order as in Pr contrary to the earlier findings of Watabe and Kasuya. The ρ_{cf} values increased with increasing Dy concentration which we believe is due to the high scattering power of Dy. Yttrium as might be expected has only a dilution effect on Nd.

Abrupt changes in the density of states in La near the Fermi level seems to account for the La resistivity behaviour, which we believe is to a certain extent present even in the light rare earths such as Pr and Nd.

It would be interesting to make experimental observations of the resistivity and both magnetoresistance on single crystals and correlate them with magnetic experiments and theoretical calculations on the basis of the point-charge crystal field calculations , which have been so far used to estimate the crystal field energy level splitting for all the light rare earths.

R E F E R E N C E S

CHAPTER ONE:

1-1 Taylor,K.N.R., Darby M.I., Physics of Rare Earth Solids edit. Chapman & Hall, 1972

1-1a Taylor,K.N.R., Contemp. Phys., 11, (1970),pp.423

1-2 Smidt,F.A., Daane,H., J.Phys. Chem. Solids, 24, (1963), pp.361

1-3 Popplewell,J., Arnold,P.G., Davies,P.M., Proc.Phys.Soc., 92, (1967), pp.177

1-4 Boys,D.W., Legvold,S., Phys.Rev., 174, (1968), pp.377

1-5 Nira, Kazuo, Phys.Rev., 117, (1960), pp129

1-6 Alstad,J.K., Colvin,R.V., Legvold,S., Phys.Rev. 123, (1961), pp.418

1-7 Hennephof,J., Phys.Letts. 11, (1964), pp.273

1-8 Lodge,F.M.K., Taylor, K.N.R., Colloquium Int., no 180, (1969), pp.531

1-9 Barson,F., Legvold,S., Spedding,F.H., Phys.Rev., 105, (1957), pp.418

1-10 Stager,R.A., Drickamer,H.G., Phys.Rev., 133, (1964), pp.A 830

1-11 Coqblin,B., Conference, Rare Earths and Actinides, Durham(1971),pp.117

1-12 Parkinson,D.H., Simon,F.E., Spedding,F.H., Proc.Roy.Soc.(London), A 207, (1951), pp.137

1-13 Herrmann,K.W., Daane,A.H., Spedding,F.H., Report No. ISC 702
Spedding,F.H., Daane,A.H., Herrmann,K.W., J.Metals, 9, (1957), pp.897

1-14 Rainford,B.D., Houmann,J.G., Conf.,Rare Earths and Actinides, Durham (1971), pp.40

1-15 Behrendt,D.R., Legvold,S., Spedding,F.H., Phys.Rev., 106, (1957), pp.723

1-16 Alstad,J.K., Colvin,R.V., Legvold,S., Spedding,F.H., Phys.Rev., 121, (1961), pp.1937 1637
James,N.R., Legvold,S., Spedding,F.H., Phys Rev., 88, (1952), pp.1092

1-17 Lounasmaa,O.V., Sudstrom,J.L.,
Phys. Rev., 158, (1967), pp.591

1-18 James,N.R., Legvold,S., Spedding,F.H.,
Phys.Rev., 88, (1952), pp.1092

1-19 Rosen,M.,
Phys.Rev., 174, (1968), pp.504

1-20 Rosen,M.,
Phys.Rev., 180, (1969), pp.540

1-21 Speight,J.D., Harris,I.R., Raynor,G.V.,
J.Less-Common Met., 15, (1968), pp.317

1-22 Beaudry,B.J., Michel,M., Daane,A.H., Spedding,F.H.,
Rep. No. 1470, (U.S.Atomic En. Commision)

1-23 Finnemore,D.K., Williams,L.J., Spedding,F.H., Hopkins,D.C.,
Phys.Rev., 176, (1968), pp.712

1-24 Sugavara,T., Eguchi,H.,
J.Phys.Soc.Japan, 21, (1966), pp.725

1-25 Mc Ewen, K.A.,
Conf., Rare Earths and Actinides, Durham (1971), pp.35

1-26 Bucher,E., Andres,K., Maita,J.I., Hull Jr.,G.W.,
Helvetica Phys.Acta, 41, (1968), pp.723

1-27 Anderson,G.S., Legvold,S., Spedding,F.H.,
Phys.Rev., 109, (1958), pp.243

1-28 Krizkova,H., Chatterjee,D., Taylor,K.N.R.,
9th Rare Earth Conf., (1971)

1-29 Chatterjee,D., Taylor,K.N.R., Stringfellow,M.W.,
Conf.,Rare Earths and Actinides, Durham (1971), pp.22

1-30 Chatterjee,D., Taylor,K.N.R.,
J.Phys. F 2, (1972), pp.151

1-31 Griffel,M., Skochdopole,R.E., Spedding,F.H.,
J.Chem.Phys., 25, (1956), pp.75

1-32 Spedding,F.H., Daane,A.H., Herrmann,K.W.,
Acta Cryst., 9, (1956), pp.599

1-33 Elliot,R.J., Wedgwood,F.A.,
Proc.Phys.Soc., 81, (1963), pp.846

1-34 Myron,H.W., Liu,S.H.,
Phys.Rev., B 1, (1970), pp.2414

1-35 Keeton,S.C., Loucks,T.L.,
Phys.Rev., 168, (1968), pp.672

1-36 Kjems,J.,
Private communication

1-37 Lebech,B., Rainford,R.D.,
J. de Phys., 32, (1971), pp.C1-370

1-38 Bucher,E., Chu,C.W., Maita,J.P., Andres,K., Cooper,A.S., Buehler,E., Nassau,K.,
Phys.Rev.Letts., 22, (1969), pp.1260

1-39 Lock,J.M.,
Proc.Phys.Soc., B 70, (1957), pp.566

1-40 Ramirez,R., Falicov,L.M.,
Phys.Rev., B 3, (1971), pp.2425

1-41 Jayaraman,A., Narayanamurti,V., Bucher,E., Maines,R.G.,
Phys.Rev.Letts., 25, (1970), pp.368

1-42 Blatt,F.J.,
J Phys.Chem.Solids, 17, (1961), pp.177

1-43 Liu,S.H.,
Private communication

1-44 Bleaney,B.,
Proc.Roy.Soc., 276, (1963), pp.38

1-45 Watabe,A., Kasuya,T.,
J.Phys.Soc.Japan, 26, (1969), pp.64

1-46 Johanssan,T., Mc Ewens,K.A., Touborg,P.,
J.Phys., 32, (1971), pp.C1-372

1-47 Primavesi,G.J.,
Ph.D.Thesis, (1972), Durham University

1-48 Ray,D.K.,
Conf., Rare Earths and Actinides, Durham(1971), pp.15

1-49 Vedernikov,M.V.,
Conf., Rare Earths and Actinides, Durham(1971), pp.44

1-50 Elliot,R.J., Wedgwood,F.A.,
Proc.Phys.Soc., 84, (1964), pp.63 and ref. therein

1-51 Rainford,B.D.,
AIP Conf. Proc., 5, Magnetism and Magnetic Materials, (1971), pp.591

CHAPTER TWO

2-1 Stephens,A.E., Macket,H.J., Sybert,J.R.,
J.Appl.Phys., 42, (1971), pp.2592

2-2 Ehrlich, J.Appl.Phys., 42, (1971), pp.2598

CHAPTER THREE

3-1 Spedding,F.H., Valletta,R.N., Daane,A.H.,
Trans.A.S.M., 55, (1962), 483

3-2 Nachman,J.F., Lundin,C.E., Rauscher,C.B.,
Tech.Rep,No.1, Cont.No.Nonr. 3661(02), (1963)

3-3 Burov,I.V., Chechernikov,V.I., Sovitskii,E.M., Iulin,Pop,
Russ.J.Anorg.Chem., 9, (1964), pp.1401

3-4 Harris,I.V., Koch,C.C., Raynor,G.V.,
J.Less-Common Met., 11, (1966), pp.436

3-5 McWhan,D.B., Stewens,A.L.,
Phys.Rev., 139, (1965), A 682

3-6 Jayaraman,A., Scherwood,R.C., Williams,H.J., Corenzwit,E.,
Phys.Rev., 148, (1966), pp.502

3-7 Beaudry,B.J., Michel,M., Daane,A.H., Spedding,F.H.,
Cont. No. 1470, (1960)

3-8 Speight,J.D., Harris,I.R., Raynor,G.V.,
J.Less-Common Met., 15, (1968), pp.317

3-9 Chatterjee,D., Taylor,K.N.R.,
J.Phys. F 2, (1972), pp.151

3-10 Lundin,C.E.,
Acta Met., 13, (1966), pp.149

3-11 Taylor,K.N.R., Harris,I.R.,
Private communication

3-12 Spedding,F.H., Daane,A.H., Herrmann,K.W.,
Acta Cryst., 9, (1956), pp.559

3-13 Barson,F., Legvold,S., Spedding,F.H.,
Phys.Rev., 105, (1957), pp.418

3-14 Krizkova,H., Chatterjee,D., Taylor,K.N.R.,
9th Rare Earth Conf.,(1971)

3-15 Taylor,K.N.R.,
Contemp.Phys., 11, (1970), pp.423

3-16 Mc Lennan, , Mc Kay,
Trans.Roy Soc.Canada, 24, (1930), pp.33

3-17 Quill,L.L.,
Z.Anorg.Chem., 208, (1932), pp.275

3-18 Coles,B.R.,
Private communication

3-19 Koehler,W.C.,
J.Appl.Phys., 36, (1965), pp.1078

3-20 Lodge,P.M.K., Taylor,K.N.R.
PPrivate communication

3-21 Chatterjee,D., Taylor,K.N.R.,
Private communication

CHAPTER FOUR

4-1 Kasuya,T.,
Prog.Theor.Phys.Japan, 16, (1956), pp.58

4-2 De Gennes,P.G., Friedel,J.J.,
Phys.Chem.Solids, 4, (1958), pp.71

4-3 Coles,B.R.,
Phil.Mag.Suppl., 7, (1958), pp.40

4-4 Watabe,A., Kasuya,T.,
J.Phys.Soc.Japan, 26, (1969), pp.64

4-5 Van Peski-Tinbergen,T., Dekker,A.J.,
Physica, 29, (1963), pp.917

4-6 Maranzana,F.E., Bianchessi,P.,
Phys.Status Solidi, 43, (1971), pp.601

4-7 Mader,H.K., Swift,W.M.,
J.Phys.Chem.Solids, 29, (1968), pp.1759

4-8 Bushow,K.H.J., Van Daal,H.J., Maranzana,F.E., Van Aken,P.B.,
Phys.Rev., B 3, (1971), pp.1662

4-9 Van Daal,H.J., Maranzana,F E., Buschow,K.H.J.,
J. de Phys., 32, (1971), pp.C1-424

4-10 Maranzana,F.E.,
J.Phys.Chem.Solids, 31, (1970), pp.2245

4-11 Elliott,R.J., Wedgwood,F.A.,
Proc.Phys.,Soc., 81, (1963), pp.846

4-12 Machintosh,A R.,
Phys.Rev.Letts., 9, (1962), pp.90

4-13 Miwa,H.,
Prog.Theor.Phys.Japan, 28, (1962), pp 208

4-14 Kasuya,T.,
Prog.Theor.Phys.Japan, 16, (1956), pp.58

4-15 Kondo,J.,
Prog.Theor.Phys., 32, (1964), pp.37

4-16 Abrikosov,A.A.,
Physics, 2, (1965), pp.61

4-17 Blatt,F.J.,
J.Phys.Chem.Solids, 17, (1961), pp.177

4-18 Chandrasekhar,B.S., Hulm,J.K.,
J.Phys.Chem.Solids, 7, (1958), pp.259

4-19 Jones,H.,
Handbuch der Physik, 19, (1956), pp.227

4-20 Friedel,J.,
J.Phys.Chem.Solids, 1, (1956), pp.175

4-21 Ziman,J.M.,
Proc.,Roy.Soc., A 252, (1959), pp.63

4-22 Ramirez,R., Falicov,L.M.,
Phys.Rev., B 3, (1971), pp.2425

4-23 Jayaraman,A., Narayanamurti,V., Bucher,E., Maines,R.G.,
Phys.Rev.Letts., 25, (1970), pp.368

4-24 Coqblin,B., Blandin,A.,
Advances in Physics, 17, (1968), pp.281

4-25 Abrikosov,A.A., Gorkov,L.P., Dzaloshinski,I.E.,
Methods of the Quantum Theory of Fields in Statistical Physics, Moscow (1962)

CHAPTER FIVE

5-1 Curry,D., Taylor,K.N.R.,
Private communication

5-2 Jones,H.,
Handbuch der Physik, 19, (1956), pp.227
(Springer Verlag Berlin)

5-3 Taylor,K.N.R.,
Private communication

5-4 Liu,S.H.,
Private communication

5-5 Johnson,D.J., Finnemore,D.K.,
Phys.Rev., 158, (1967), pp.376

5-6 Dekker,A.J.,
J.Appl.Phys., 36, (1965), pp.906

5-7 Chen,C.W., Ashkin,M., Takei,W.J.,
Phys.Letts., 21, (1966), pp.243

5-8 Chen,C.W.,
Solid State Communications, 3, (1965), pp.231

5-9 Chen,C.W.,
J.Appl.Phys., 37, (1966), pp.1026

5-10 Mackintosh,A.R., Smidt Jr.,F.A.,
Phys.Letts., 2, (1962), pp.107

5-11 Sugawara,T.,
J.Phys.Soc.Japan, 20, (1965), pp.2252

5-12 Trammell,G.T.,
J.Appl.Phys.Suppl., 31, (1961), pp.3623

5-13 Cooper,B.R., Vogt,O.,
J. de Phys., 32, (1971), pp.C1-958
and ref. therein

5-14 de Gennes,P.G.,
J. de Phys. et le Radium, 23, (1962), pp.510

5-15 Wiess,R.J., Marotta,A.S.,
J.Phys.Chem.Solids, 9, (1959), pp.302

5-16 Darby,M.I., Taylor,K.N.R.,
J.Appl.Phys., 37, (1966), pp.1442

5-17 Yosida,K.,
Progress in Low Temperature Physics (Academic Press Inc., New York, 1964), Vol.4, p.265

5-18 Tissot,I., Blaise,A.,
J.Appl.Phys., 41, (1970), pp.1180

LIST OF FIGURES

5.6 Resistivity vs temperature for Pr, experimental and predicted from simple model for crystal field energy levels (1)(in the first approximation).

5.7 Resistivity vs temperature for Pr, experimental and predicted from simple model(1).

5.8 Resistivity vs temperature for Pr,,experimental and predicted using (2) set of crystal field energy levels together with assumption of $\eta(E)$=const and 'no recombination'.

5.9a Calculated variation of the resistivity vs temperature for Pr in hexagonal environment. Fermi-Dirac function f(T) was assumed to be temperature dependent as well as equal to one.

5.9b Calculated variation of the resistivity vs temperature for Pr in cubic environment under the same assumptions as in fig 5.9a.

5.9c Calculated variation of the resistivity vs temperature for Pr in hexagonal, cubic environment and their sum.

5.10 Sum of ρ_{hex} and ρ_{cub}, from fig 5.9 scaled to Pr, Pr-KT and Pr-La.

5.11 Sum of $\alpha\rho_{hex}$ and $\beta\rho_{cub}$, from fig.5.9 scaled to Pr, Pr-KT and Pr-La.

5.12 Calculated resistivity variation with temperature with assumption of f(T)=1 (nonintegral calculation) for Pr in hexagonal, cubic environment and their sum also scaled to Pr-La, experimantal curve.

5.13 Sum of ρ_{hex} and ρ_{cub}, from fig 5.12 scaled to Pr, Pr-KT and Pr-La.

5.14 Susceptibility variation with temperature for Pr_9Tb_1.

5.15 Various distributions of the crystal field energy levels for Pr in a magnetic field of various strength from 0-400KOe, used in the resistivity calculations.

5.16a Calculated resistivity variation with temperature for Pr in hexagonal and cubic environment in $(H_{mg})_z$=400KOe considering maximum transitions.

5.16b Calculated resistivity variation with temperature for Pr in $(H_{mg})_z$ considering few transitions.

5.17a Calculated resistivity variation with temperature for the first two excited states of the crystal field energy levels being shifted down by a total amount of 10% in comparison to the crystal field energy levels in pure Pr.

5.17b Calculated resistivity variation with temperature For the first two excited states of the crystal field energy levels beeing shifted down by a total amount of 50 and 10% respectively in comparison to the crystal field energy levels in pure Pr.

5.17c Resistivity vs temperature for Pr_9Tb_1-La, Pr_8Tb_2-La and Pr_7Tb_3-La along with the predicted resistivity variation for the various proposed changes in the distribution of the crystal field energy levels.

5.18a Neutron diffraction results for the Pr powder at 4.2°K.

5.18b Neutron diffraction results for the $Pr_{85}Tb_{15}$ polycrystal at 4.2°K.

5.19 Resistivity vs temperature for Nd devided into three contributions, ρ_{s-f}, $\rho_{ph.}$, $\rho_{c.f.}$

5.20 $\rho_{c.f.}$ vs composition for Nd-Y alloys.

5.21 $(d\rho/dT)_{high\ temp.}$ vs composition for Nd-Y, Nd-Dy, La-Dy, Pr-Tb alloys where $\rho(T)$ was approximated as T^n.

5.22 $(d\rho/dT)$ vs composition for Nd-Dy alloys.

5.23 Resistivity and ρ_{La}/T vs temperature T for ρ_{La} and $\rho_{La}-\rho_{res}$.

5.24 Néel temperature T_N vs $\bar{S}=c_1S_1(S_1+1) + c_2(S_2+1)S_2$ for La-Dy, Nd-Dy, Pr-Tb and Pr-Gd (18) alloys.

5.25 Spin-disorder resistivity vs $\bar{S}=c_1S_1(S_1+1)+c_2S_2(S_2+1)$ and vs $(c_1S_1+c_2S_2)$ for pure heavy rare earths and light-heavy rare earths measured.

5.26 Spin-disorder resistivity vs $c_1G_{heavy} + c_2S(S+1)_{light}$ for heavy rare earths and light-heavy rare earth alloys measured in this work.

5.27 Néel temperature vs $c_1G_1+c_2G_2$ and vs $c_1G_{h.r.e.}+c_2S(S+1)_{l.r.e.}$ for heavy rare earths and light-heavy rare earth alloys.

5.28 Néel temperature vs $(c_1S_1(S_1+1)+c_2S_2(S_2+1))$

5.29 Residual resistivity vs composition for Nd-Dy, Nd-Y, Dy-La, Pr-Tb alloys.

5.30 $(\rho_{res}-\rho(\rho_{res})_{Dy})/(1-c)$ vs composition c for Dy-La, Dy-Nd measured here as well as reported before(9).

5.31 Spin-disorder resistivity vs Néel temperature for La-Dy, Nd-Dy, Pr-Tb and heavy rare earth metals.

LIST OF TABLES

A P P E N D I C E S

1. Programm for calculating d-values from X-ray powder diffractogramm.

2. Programm calculating the lattice parameters a and c and atomic volume V for hexagonal lattice from given ($\bar{h}kl$) values and θ values.

3. Programm for calculating resistivity $\rho_i(T)$ from the measured values of voltage V and current I. the pragramm also does the plotting of the resistivity vs temperature curves.

4. Programm for numerical calculation of the derivatives of the resistivity $\rho(T)$ with temperature for a given set of $\rho(T)$ and T values .

5. Programm for the calculation of the theoretical resistivity variation with the temperature, using model (4-6).

Appendix 1

Programm for calculating d-values from X-ray powder diffractogramm.

```
S (LA34-0046)
sig phr4 pw=hana
*LAST SIGNON WAS: 15:51.41   09-20-72
USER "PHR4" SIGNED ON AT  16:03.58 ON 09-20-72
l x-ray
     1            DIMENSION E(50),H(50),A(50),B(50),C(90),S(50),(50),G(50)
     2            READ(5,100)W
     3            READ(5,101)N
     4            WRITE(6,200)
     5            DO 1 I=1,N
     6            READ(5,102)(A(I),B(I))
     7            E(I)=ABS(B(I)-A(I))/2
     8            C(I)=3.1428*(E(I)/180)
     9            S(I)=SIN(C(I))
    10            D(I)=W/(S(I))
    11            G(I)=ALOG(D(I))
    12            H(I)=G(I)/2.303
    13             WRITE(6,201)(I,E(I),S(I),D(I),G(I),H())
    14          1 CONTINUE
    15        100 FORMAT(F10.5)
    16        101 FORMAT(I2)
    17        200 FORMAT('1','LINE',6X,'ANGLE',6X,SIN(A)',6X,'D-VALU',6X,LOG-D'
    18        102 FORMAT(2F6.2)
    19        201 FORMAT(1H ,I2,7X,F.2,6X,F6.4,6X,F64,6X,F6.4,6X,6.4)
    20            READ(5,101)M
    21            DO 2 I=1,M
    22            READ(5,102)(A(I),B(I))
    23            E(I)=180.0-ABS(B(I)-A(I))/2
    24            C(I)=3.1428-(3.1428*ABS((B(I)-A(I))/360))
    25            S(I)=SIN(C(I))
    26            D(I)=W/(S(I))
    27            G(I)=ALOG(D(I))
    28            H(I)=G(I)/2.303
    29             WRITE(6,201)(I,E(I),S(I),D(I),G(I),H())
    30          2 CONTINUE
    31            STOP
    32            END
END OF FILE
```

Appendix 3

Programm for calculating resistivity from the measure values of voltage and current.

```
G COMPILER        MAIN              07-13-72        13:41.02        PAGE 0001

C       HANA K.
      DIMENSION V(3,1000),A(3,1000),T(3,1000),R(3,1000),RC(3,1000),E(3),
     3TT(3,1000),B(3,1000)
      F(A,B,C,D,E)=E*(A+B)/(C+D)
      READ 103,N
  103 FORMAT(I4)
      READ 102,E
  102 FORMAT(3F10.0)
      PRINT 203,E
  203 FORMAT(1H  ,3F10.5)
      PRINT 201
  201 FORMAT('1',15X,'TEMPERATURE',2X,'SAMPLE NO1',15X,'TEMPERATURE',2X,
     5'SAMPLE NO2',15X,'TEMPERATURE',2X,'SAMPLE NO3')
      DO 1 I=1,N,2
      READ 104,V(1,I),A(1,I),V(2,I),A(2,I),V(3,I),A(3,I),T(1,I),V(1,(I+1
     8)),A(1,(I+1)),T(2,I),V(2,(I+1)),A(2,(I+1)),T(3,I),V(3,(I+1)),A(3,(
     9I+1))
  104 FORMAT(5X,F7.0,F8.0,5X,F7.0,F8.0,5X,F7.0,F8.0,12X/F5.0,F7.0,F8.0,F
     15.0,F7.0,F8.0,F5.0,F7.0,F8.0,12X)
      R(1,I)=F(A(1,I),A(1,(I+1)),V(1,I),V(1,(I+1)),E(1))
      R(2,I)=F(A(2,I),A(2,(I+1)),V(2,I),V(2,(I+1)),E(2))
      R(3,I)=F(A(3,I),A(3,(I+1)),V(3,I),V(3,(I+1)),E(3))
    1 CONTINUE
      WRITE(6,200)(T(J,1),R(J,1),J=1,3)
      DO 2 I=3,N,2
      RC(1,I)=R(1,I)-R(1,1)
      RC(2,I)=R(2,I)-R(2,1)
      RC(3,I)=R(3,I)-R(3,1)
      WRITE(6,200)(T(J,I),RC(J,I),J=1,3)
    2 CONTINUE
  200 FORMAT(18X,F6.1,5X,F9.3,18X,F6.1,5X,F9.3,18X,F6.1,5X,F9.3)
      L=N+1
      M=L/2-1
      CALL PLTOFS(0.0,0.3,-1.0,0.3,1.0,0.5)
      CALL PLGAXS(1.0,0.5,'T (S)',-5,9.0,0.0,0.0,0.33333)
      CALL PLGAXS(1.0,0.5,'RESIST',6,9.0,90.0,-1.0,-0.33333)
      CALL PLGGRD(1.0,0.5,3.0,9.0,9.0,0.0)
      CALL PLGGRD(10.0,0.5,3.0,9.0,9.0,90.0)
      CALL PLTLOG(3)
      CALL PLINE(T(1,3),RC(1,3),M,6,-1,4,99.9)
      CALL PLINE(T(2,3),RC(2,3),M,6,-1,2,99.9)
      CALL PLINE(T(3,3),RC(3,3),M,6,-1,11,99.9)
      CALL PLTEND
      STOP
      END

MORY REQUIREMENTS 0150AA BYTES
RMINATED
```

Appendix 4. Programm for numerical calculation of the derivatives

```
COMPILER        MAIN            04-28-73        11:21.52        PAGE 0001

C       HANA K.
      DIMENSION T(3,100),R(3,100),RC(3,100),E(3),DRC(3,100),DRC1(3,100),
     1DT(3,100)
      READ 103,N
  103 FORMAT(I4)
      READ 102,E
  102 FORMAT(2F10.0)
      PRINT 203,E
  203 FORMAT(1H  ,2F10.5)
      PRINT 201
  201 FORMAT('1',15X,'TEMPERATURE',2X,'SAMPLE NO1',15X,'TEMPERATURE',2X,
     5'SAMPLE NO2',15X,'TEMPERATURE',2X,'SAMPLE NO3')
      DO 2 I=1,N,1
      READ 101,T(1,I),R(1,I),R(2,I)
  101 FORMAT(3F10.2)
      T(2,I)=T(1,I)
    2 CONTINUE
      WRITE(6,200)(T(J,1),R(J,1),J=1,2)
      DO 1 I=2,N,1
      DO 3 J=1,2,1
      RC(J,I)=R(J,I)-R(J,(I-1))
      IF (T(J,I)-T(J,(I-1)))5,6,5
    5 DRC(J,I)=ABS((RC(J,I)-RC(J,(I-2)))/(T(J,I)-T(J,(I-2))))
      GO TO 7
    6 DRC(J,I)=0.000
    7 DT(J,I)=(T(J,I)+T(J,(I-2)))/2
      DRC1(J,I)=DRC(J,I)*100
    3 CONTINUE
      WRITE(6,200)(T(J,I),RC(J,I),J=1,2)
      WRITE(6,200)(DT(J,I),DRC1(J,I),J=1,2)
  200 FORMAT(18X,F6.1,5X,F9.3,18X,F6.1,5X,F9.3)
    1 CONTINUE
      M=N
      CALL PLTOFS(1.0,40.0,0.1,1.0,1.0,0.5)
      CALL PAXIS(1.0,0.5,'TEMPERATURE',-11,10.0,0.0,0.0,40.0,1.0)
      CALL PAXIS(1.0,0.5,'RESISTIVITY',11,10.0,90.0,0.0,1.0,1.0)
      CALL PLINE(T(1,3),RC(1,3),M,3,-1,1,1)
      CALL PLINE(T(2,3),RC(2,3),M,3,-1,2,1)
      CALL PLINE(DT(1,3),DRC1(1,3),M,3,-1,1,1)
      CALL PLINE(DT(2,3),DRC1(2,3),M,3,-1,2,1)
      CALL PLTEND
                $
IEY015I NO END CARD

Y REQUIREMENTS 0022BE BYTES

RY FOR PROGRAM MAIN   0001 0000 0000
```

Appendix 5a. Hexagonal envirinment, $H_{mag.}=0$

```
OMPILER        MAIN              03-29-73        18:54.53        PAGE 0001

     DIMENSION Y1(2080),Y2(2080),R(6,302),CO(2),EN(6),T(302),U(302),S(6
    1),Y3(2080),Y4(2080),V(302),ET1(2080),X20(2081),X21(2081),X30(2081)
    2,X31(2081),X40(2081),X41(2081),X50(2081),X51(2081)
     F(J,I)=1.0/(EXP(FLOAT(J)/FLOAT(I))+1.0)
     READ(5,100)CO
     READ(5,101)EN
     READ(5,102)N
     READ(5,103)M
     WRITE(6,204)(EN(1),EN(2),EN(3),EN(4),EN(5),EN(6),CO(1),CO(2),N,M)
 204 FORMAT(' ',8E15.5,2I10)
     DO 1 I=12,N,10
     A=EXP(-EN(2)/I)
     B=EXP(-EN(3)/I)
     C=EXP(EN(2)/I)
     D=EXP(EN(3)/I)
     B1=EXP(-EN(4)/I)
     C1=EXP(EN(4)/I)
     B2=EXP(-EN(5)/I)
     C2=EXP(EN(5)/I)
     B3=EXP(-EN(6)/I)
     C3=EXP(EN(6)/I)
     E=1.0/(1.0+A+B+B1+B2+B3)
     WRITE(6,207)(A,B,C,D,E,B1,B2,B3,C1,C2,C3)
 207 FORMAT(1H   ,11E10.5)
     F2=80.0/C+26.0/D+32.0/C2+20.0+20.0/C1+20.0/C3
     V(I)=E*F2*CO(1)/CO(2)
     WRITE(6,206)(F2,V(I))
     DO 2 J=1,M
     K=J+2080
     L=-J+2080
     X00=1.0+F(J,I)*(C-1.0)
     X01=1.0+F(-J,I)*(C-1.0)
     X10=C+F(J,I)*(D-C)
     X11=C+F(-J,I)*(D-C)
     X60=C+F(J,I)*(C1-C)
     X61=C+F(-J,I)*(C1-C)
     X70=C+F(J,I)*(C3-C)
     X71=C+F(-J,I)*(C3-C)
     X20(J)=C+F(J,I)*(1.0-C)
     X30(J)=D+F(J,I)*(C-D)
     X40(J)=C1+F(J,I)*(C-C1)
     X50(J)=C3+F(J,I)*(C-C3)
     X21(J)=C+F(-J,I)*(1.0-C)
     X31(J)=D+F(-J,I)*(C-D)
     X41(J)=C1+F(-J,I)*(C-C1)
     X51(J)=C3+F(-J,I)*(C-C3)
     IF(X20(J))10,7,10
   7 X20(J)=X20(J-1)
  10 IF(X30(J))12,6,12
   6 X30(J)=X30(J-1)
  12 IF(X40(J))14,8,14
   8 X40(J)=X40(J-1)
  14 IF(X50(J))40,18,40
  18 X50(J)=X50(J-1)
  40 Y3(J)=E*(2.0/C+8.0/D+32.0/C2+20.0/X00+18.0/X10+20.0/X20(J)+18.0/X3
```

```
    10(J)+20.0/X40(J)+20.0/X50(J)+20.0/X60+20.0/X70)
      IF(X21(J))13,42,13
   42 X21(J)=X21(J-1)
   13 IF(X31(J))15,80,15
   80 X31(J)=X31(J-1)
   15 IF(X41(J))17,41,17
   41 X41(J)=X41(J-1)
   17 IF(X51(J))43,44,43
   44 X51(J)=X51(J-1)
   43 Y4(J)=E*(2.0/C+8.0/D+32.0/C2+20.0/X01+18.0/X11+20.1/X21(J)+18.0/X3
     11(J)+20.0/X41(J)+20.0/X51(J)+20.0/X61+20.0/X71)
      IF(ABS(Y3))29,20,29
   20 Y3(J)=1.0
   29 IF(J-780)30,30,31
   30 ET1(J)=17.76
      GO TO 19
   31 ET1(J)=14.44
   19 Y1(J)=CO(2)*(FLOAT(K)**0.5)*F(J,I)*(1.0-F(J,I))/(Y3(J)*FLOAT(I)*CO
     1(1))*ET1(J)
      IF(ABS(Y4))23,22,23
   22 Y4(J)=1.0
   23 IF(-J+950)34,33,33
   33 ET1(J)=17.76
      GO TO 21
   34 ET1(J)=22.00
   21 Y2(J)=CO(2)*(+(FLOAT(L)**0.5))*F(-J,I)*(1.0-F(-J,I))/(Y4(J)*FLOAT(
     11)*CO(1))*ET1(J)
      IF(MOD(J,200).EQ.0) WRITE(6,209)(Y3(J),Y4(J),Y1(J),Y2(J),J)
  209 FORMAT(1H  ,4E15.5,I5)
    2 CONTINUE
      CALL QSF(1.0,Y1,Y1,2080)
      CALL QSF(1.0,Y2,Y2,2080)
      WRITE(6,206)(Y1(2080),Y2(2080))
  206 FORMAT(1H  ,2E15.5)
      Z12=Y1(2080)+Y2(2080)
      IF(Z12)4,5,4
    5 Z12=1.0
      GO TO 4
    4 Z34=Y1(2080)-Y2(2080)
      U(I)=1.0/Z12
      WRITE(6,200)(I,U(I),Z12,Z34,V(I),F2)
    1 CONTINUE
      S(1)=5.7/U(302)
      S(2)=3.9/U(152)
      S(3)=2.3/U(62)
      S(4)=5.7/V(302)
      S(5)=3.9/V(152)
      S(6)=2.3/V(62)
      DO 3 I=12,N,10
      T(I)=FLOAT(I)
      R(1,I)=U(I)*S(1)
      R(2,I)=U(I)*S(2)
      R(3,I)=U(I)*S(3)
      R(4,I)=V(I)*S(4)
      R(5,I)=V(I)*S(5)
```

Appendix 5a. (cont.)

```
OMPILER        MAIN            03-29-73        18:54.53        PAGE 0003

      R(6,I)=V(I)*S(6)
      WRITE(6,205)(I,R(1,I),R(2,I),R(3,I),R(4,I),R(5,I),R(6,I))
  205 FORMAT(1H   ,15X,I3,10X,6E15.5)
    3 CONTINUE
  100 FORMAT(2E8.1)
  101 FORMAT(6F10.0)
  102 FORMAT(I4)
  103 FORMAT(I6)
  200 FORMAT(' ',15X,I3,5X,E15.9,5X,E15.9,5X,E15.9,5X,E15.9,5X,E15.9)
      CALL PLTOFS(0.0,40.0,0.0,1.0,1.0,0.5)
      CALL PAXIS(1.0,0.5,'TEMPERATURE',-11,10.0,0.0,0.0,40.0,1.0)
      CALL PAXIS(1.0,0.5,'RESISTIVITY',11,10.0,90.0,0.0,1.0,1.0)
      CALL PLINE(T(1),R(1,12),N,10,-1,4,99.9)
      CALL PLINE(T(1),R(2,12),N,10,-1,4,99.9)
      CALL PLINE(T(1),R(3,12),N,10,-1,4,99.9)
      CALL PLTEND
      STOP
      END

 REQUIREMENTS 01E6E4 BYTES
ATED
```

Appendix 5b. Cubic environment, $H_{mag.}=0$.

```
MPILER      MAIN            05-01-73        11:22.3)        PAGE 0001

      DIMENSION Y1(2080),Y2(2080),P(6,802),CO(2),EN(4),T(802),U(802),S(6
     1),Y3(2082),Y4(2082),V(302),ET1(2082),ET2(2082)
      EQUIVALENCE(EN2,EN(2)),(EN3,EN(3)),(EN4,EN(4))
      F(J,I)=1.0/(EXP(FLOAT(J)/FLOAT(I))+1.0)
      READ(5,100)CO
  00  FORMAT(2E8.1)
      READ(5,101)EN
  01  FORMAT(4F10.0)
      READ(5,102)N
  02  FORMAT(I4)
      READ(5,103)M
  03  FORMAT(I6)
      WRITE(6,204)(EN(1),EN(2),EN(3),EN(4),CO(1),CO(2),N,M)
 204  FORMAT(1H ,6E15.5,2I10)
      DO 1 I=12,N,10
      A=EXP(-EN(2)/I)
      B=EXP(-EN(3)/I)
      C=EXP(EN(2)/I)
      D=EXP(EN(3)/I)
      B1=EXP(-EN(4)/I)
      C1=EXP(EN(4)/I)
      E=1.0/(1.0+A+B+B1)
      WRITE(6,207)(A,B,C,D,E,B1,C1)
 207  FORMAT(1H  ,7E10.5)
      F2=20.25/C+12.5/C1
      V(I)=E*F2*CO(1)/CO(2)
      WRITE(6,206)(F2,V(I))
      DO 2 J=1,M
      K=J+2080
      L=-J+2080
      Y3(J)=E*F2
      Y4(J)=Y3(J)
  29  IF(J-780)30,30,31
  30  ET1(J)=17.76
      GO TO 19
  31  ET1(J)=14.44
  19  Y1(J)=CO(2)*(FLOAT(K)**0.5)*F(J,I)*(1.0-F(J,I))/(Y3(J)*FLOAT(I)*CO
     1(1))*ET1(J)
      IF(ABS(Y4))23,22,23
  22  Y4(J)=1.0
  23  IF(-J+950)34,33,33
  33  ET2(J)=17.76
      GO TO 21
  34  ET2(J)=22.00
  21  Y2(J)=CO(2)*(+(FLOAT(L)**0.5))*F(-J,I)*(1.0-F(-J,I))/(Y4(J)*FLOAT(
     1I)*CO(1))*ET1(J)
      IF(MOD(J,200),EQ.0) WRITE(6,209)(Y3(J),Y4(J),Y1(J),Y2(J),J)
 209  FORMAT(1H  ,4E15.5,I5)
   2  CONTINUE
      CALL QSF(1.0,Y1,Y1,2080)
      CALL QSF(1.0,Y2,Y2,2080)
      WRITE(6,206)(Y1(2080),Y2(2080))
 206  FORMAT(1H  ,2E15.5)
      Z12=Y1(2080)+Y2(2080)
      IF(Z12)4,5,4
```

Appendix 5b. (cont.)

```
OMPILER        MAIN            05-01-73        11:22.31        PAGE 0002

   5 Z12=1.0
     GO TO 4
   4 Z34=Y1(2080)-Y2(2080)
     U(I)=1.0/712
     WRITE(6,200)(I,U(I),Z12,Z34,V(I),F2)
   1 CONTINUE
     S(1)=5.7/U(302)
     S(2)=3.9/U(152)
     S(3)=2.3/U(62)
     S(4)=5.7/V(302)
     S(5)=3.9/V(152)
     S(6)=2.3/V(62)
     DO 3 I=12,N,10
     T(I)=FLOAT(I)
     R(1,I)=U(I)*S(1)
     R(2,I)=U(I)*S(2)
     R(3,I)=U(I)*S(3)
     R(4,I)=V(I)*S(4)
     R(5,I)=V(I)*S(5)
     R(6,I)=V(I)*S(6)
     WRITE(6,205)(I,R(1,I),R(2,I),R(3,I),R(4,I),R(5,I),R(6,I))
205  FORMAT(1H ,15X,I3,10X,6F15.5)
   3 CONTINUE
00   FORMAT(' ',15X,I3,5X,E15.9,5X,E15.9,5X,E15.9,5X,E15.9,5X,E15.9)
     STOP
     END

REQUIREMENTS 0138CE BYTES
TED
```

Appendix 2. Program for calculating lattice parameters for hexagonal lattice from (hkl) and θ values.

```
G PH4R
AST SIGNON WAS: 12:46.19   06-18-73
ER "PH4R" SIGNED ON AT  04:10.05 ON 06-20-73
E -P
LE "-P" HAS BEEN CREATED.
MBER
MBER
ST -P
  1        HEXSOLV:PROCEDURE OPTIONS(MAIN);
  2        DCL(G1,G2,G3,G4,G5,A(3,3),B(3),X(3),THETA(50),A0,C0,W)FLOAT;
  3        DCL(Y,V)FLOAT;
  4        DCL(S,I,J,M,N,H(50),K(50),L(50))FIXED BINARY;
  5        DCL NAME CHARACTER (50) VARYING;
  6       GJM : PROCEDURE(A,B,X,NA)RETURNS(FLOAT);
  7       /* SOLVES A SET OF NA SIMULTANEOUS EQ. FOR X AX=B SEE
  8         HAWGOOD NUMERICAL ANALYSIS FOR ALGOL VERSION,GAUSS JORDAN METHOD.*/
  9       DECLARE(A(*,*),B(*),X(*),PIVOT,PIVPROD,MULT,COMP)FLOAT,
 10       (PIVROW(NA),PIVCOL(NA),I,JC,IA,JA,IC,IO,JO,N)FIXED BINARY;
 11         DCL (J)FIXED BINARY ;
 12       PIVPROD=1;
 13       DO I=1 TO NA;
 14       PIVROW(I), PIVCOL(I) = I ;
 15       END;
 16       DO N=1 TO NA;
 17       PIVOT=A(PIVROW(N),PIVCOL(N));
 18       IO,JO=N;
 19       IA=PIVROW(N); JA=PIVCOL(N);
 20       DO I = N TO NA ;
 21       DO J=N TO NA;
 22         IC=PIVROW(I);  JC=PIVCOL(J);
 23       COMP=A(IC,JC);
 24       IF ABS(COMP)>ABS(PIVOT) THEN DO;
 25       PIVOT=COMP;
 26       IA=IC; IO=I;
 27       JA=JC; JO=J;
 28       END;
 29       END;
 30       END;
 31       PIVROW(IO)=PIVROW(N);
 32        PIVCOL(JO)=PIVCOL(N);
 33       PIVROW(N)=IA; PIVCOL(N)=JA;
 34       B(IA)=B(IA)/(PIVOT);
 35       PIVPROD=PIVPROD*PIVOT;
 36       DO J=N+1 TO NA;
 37       JC=PIVCOL(J);
 38       A(IA,JC)=A(IA,JC)/PIVOT;
 39        END;
 40       DO I=1 TO NA ;
 41       IF I¬= IA THEN DO ;
 42       MULT=A(I,JA);
 43       B(I)=B(I)-B(IA)*MULT;
 44       DO J=(N+1) TO NA;
 45       JC=PIVCOL(J);
 46       A(I,JC)=A(I,JC)-A(IA,JC)*MULT;
 47        END;
 48        END;
 49       END;
 50       END;
 51       DO I=1 TO NA;
 52       X(PIVCOL(I))=B(PIVROW(I));
```

Appendix 2. (cont.)

```
53        END;
54        RETURN(PIVPROD);
55        END GJM;
56         GET LIST(S);
57         DO I=1 TO S ;
58         GET LIST (NAME);
59         PUT SKIP(3) ;
60         PUT LIST (NAME);
61         PUT SKIP;
62         GET LIST(W);
63         GET LIST(M);
64         A=0; B=0;
65         DO J=1 TO M ;
66          GET LIST( THETA(J),H(J),K(J),L(J));
67         THETA(J)=THETA(J)/(57.296);
68         G1 = H(J)**2 + K(J)**2 +K(J)*H(J);
69         G2 = L(J)**2 ;
70         G3=(SIN(2*THETA(J)))**2;
71         G3=G3*5*(1/SIN(THETA(J)) +1/(THETA(J)));
72         A(1,1)= A(1,1) +G1**2;
73         A(2,1),A(1,2) = A(1,2)+ G1*G2;
74         A(3,1),A(1,3) = A(1,3)+ G1*G3;
75          A(2,2) =A(2,2) + G2**2;
76          A(3,2),A(2,3) =A(2,3)+G2*G3 ;
77         A(3,3) = A(3,3) +G3**2 ;
78          G4=(SIN(THETA(J)))**2;
79         B(1) = B(1) + G1*G4;
80          B(2) = B(2) + G2*G4;
81         B(3) = B(3) + G3*G4;
82         END;
83          N=3;
84           G5 = GJM (A,B,X,N);
85           AO = (W**2)/(3*X(1));
86           AO = SQRT(AO);
87           CO= W/(2*SQRT(X(2)));
88           PUT SKIP;
89           PUT DATA(AO);
90           PUT DATA(CO);      PUT SKIP DATA(X);
91         Y=CO/AO;
92         V=(AO**2)*CO*(SQRT(3))/2;
93         PUT SKIP DATA (Y);
94         PUT DATA (V);
95           END;
96           END HEXSOLV ;
OF FILE
```